

Doctorate Dissertation

博士論文

Constraining primordial black holes with  
gravitational microlensing effect

( 重力マイクロレンズ観測による原始ブラックホールの制限 )

A Dissertation Submitted for Degree of Doctor of Philosophy

December 2018

平成30年12月 博士（理学）申請

Department of Physics, Graduate School of Science,

The University of Tokyo

東京大学大学院理学系研究科物理学専攻

Hiroko Niikura

新倉 広子



# Abstract

This thesis describes observational studies of dark matter (DM) as compact objects in the Universe. While the presence of DM has been verified by observations, the nature of dark matter is still a mystery. Gravitational lensing is a very powerful tool to test the presence of DM, and especially the time-variable magnification phenomenon, known as gravitational microlensing effect, is very powerful to test compact DM objects. In this thesis, we search for microlensing events caused by primordial black holes (PBHs) that are one of viable DM candidates. We show the two observational results, where all DM in the Galactic halo region is made of either PBHs at particular mass scale (I) in the range  $[10^{-11}, 10^{-6}]M_{\odot}$ , or (II) of Earth-mass ( $10^{-6}M_{\odot}$ ) scales.

In Part (I) of this thesis, we investigate microlensing events for stars in the Andromeda Galaxy (M31). In particular we focus on an unexplored mass window of PBHs,  $M_{\text{PBH}} = [10^{-14}, 10^{-9}]M_{\odot}$ , which could occupy the halo region of our Milky Way galaxy. However, frequent photometry of many stars has been challenging, which prevent us from probing microlensing event with time scale shorter than 30 minutes. Here we propose microlensing search by taking advantage of a large number of stars in M31, as well as the large field-of-view of the Subaru Hyper Suprime-Cam. We developed the image difference technique to detect time-variable objects, and succeeded to detect more than 10,000 transient candidates. From microlensing analysis of these data, we set the stringent upper limit on the abundance of PBHs in  $M_{\text{PBH}} = [10^{-11}, 10^{-6}]M_{\odot}$ . Our results give the upper limit on PBH abundance over the previously-unexplored mass window of  $M_{\text{PBH}} = [10^{-11}, 10^{-9}]M_{\odot}$ , and give tighter upper bounds for a PBH scenario with an extended mass spectrum when combined with other constraints.

In Part (II) of this thesis, we study microlensing events with longer timescale than we did in Part (I). Here, to constrain the PBH scenario, we use 2622 microlensing events obtained from the 5-years Optical Gravitational Experiment (OGLE) data that is the long-term monitoring observation of  $5 \times 10^7$  stars in the Galactic bulge region. A majority of the OGLE microlensing events, peaked at the microlensing timescale of 10 days, can be fairly well explained by microlensing due to brown dwarfs, main-sequence stars, and stellar remnants (white dwarfs, neutron stars, and black holes). The OGLE data also indicates another popu-

lation of microlensing events in the short timescales of  $\sim 0.1$  days, whose origin is advocated to be due to wide-orbit planets or free-floating planets of Earth-like masses. First we derive the upper bound on the PBH abundance in the mass range  $M_{\text{PBH}} = [10^{-7}, 10^{-1}]M_{\odot}$  assuming the null PBH hypothesis in the OGLE data: there is no PBH microlensing event in the OGLE data. Secondly, we discuss that the 6 OGLE events of short timescales can be well explained by PBHs of Earth mass-scale, which is consistent with both the HSC results and the long timescale OGLE events. This might be a hint of PBH existence, and a further study will be worth to explore.

# Contents

<b>Abstract</b>	<b>i</b>
<b>Contents</b>	<b>ii</b>
<b>List of figures</b>	<b>vi</b>
<b>List of figures</b>	<b>ix</b>
<b>Acknowledgement</b>	<b>xi</b>
<b>1 Introduction</b>	<b>1</b>
1.1 The origins of cosmological structure . . . . .	3
1.1.1 The standard cosmological model . . . . .	3
1.1.2 Structure formation . . . . .	10
1.2 Relics of cold dark matter . . . . .	14
1.2.1 Observational evidences of cold dark matter . . . . .	14
1.2.2 WIMPs as dark matter . . . . .	17
1.2.3 Dark matter as astrophysical compact objects . . . . .	19
1.3 Primordial black hole as dark matter . . . . .	20
1.3.1 Formation mechanism . . . . .	20
1.3.2 Theoretical properties . . . . .	22
1.3.3 Possible observational imprints . . . . .	23
1.3.4 Brief history of observational constraints . . . . .	26
1.4 Objective of this thesis . . . . .	30
<b>2 Gravitational lensing</b>	<b>32</b>
2.1 Theory . . . . .	32
2.1.1 Light path in the unperturbed metric . . . . .	32
2.1.2 Light path in the perturbed metric . . . . .	35

2.2	Observational characteristics . . . . .	42
2.3	Microlensing basics . . . . .	43
2.3.1	Point source approximation . . . . .	43
2.3.2	Finite source size effect . . . . .	46
2.3.3	Wave effect . . . . .	48
<b>3</b>	<b>Microlensing constraints on primordial black holes with the Subaru/HSC Andromeda observation</b>	<b>53</b>
3.1	Introduction . . . . .	53
3.2	Event rate of PBH microlensing for M31 stars . . . . .	55
3.2.1	Microlensing basics for M31 observation . . . . .	55
3.2.2	Microlensing event rate . . . . .	57
3.2.3	Light Curve characterization in pixel lensing regime . . . . .	62
3.3	Data Analysis and Object Selection . . . . .	63
3.3.1	Observations . . . . .	63
3.3.2	Data reduction and Sample selection . . . . .	65
3.4	Statistics and Selection Criteria . . . . .	72
3.4.1	Photometric errors of the light curve measurement . . . . .	72
3.4.2	Microlensing model fit to the light curve data . . . . .	73
3.5	Results: Upper bound on the abundance of PBH contribution to dark matter	79
3.5.1	Efficiency Calculation: Monte Carlo simulation . . . . .	80
3.5.2	Estimation of star counts in M31 . . . . .	82
3.5.3	Expected number of PBH microlensing events . . . . .	86
3.5.4	Experimental limits on the abundance of PBHs . . . . .	87
3.6	Discussion . . . . .	89
<b>4</b>	<b>Reobserving Andromeda for Microlensing: Improved constraints on PBH abundance</b>	<b>92</b>
4.1	Introduction . . . . .	92
4.2	Data analysis and Object Selection for 2017 observation . . . . .	94
4.2.1	Observation . . . . .	94
4.2.2	Data reduction and Sample selection . . . . .	94
4.3	Statistics and Selection Criteria for 2017 observation . . . . .	97
4.3.1	Photometric errors of the light curve measurement . . . . .	97
4.3.2	Microlensing model fit to the light curve data . . . . .	98
4.4	Result 1: Time-variability of one microlensing candidate . . . . .	100

4.4.1	Archival observation of the M31 with the Subaru/HSC . . . . .	101
4.4.2	Light curves of one remaining candidate from archival data . . . . .	103
4.4.3	Test of time-variability . . . . .	103
4.5	Result 2: Tighter Upper bound on the abundance of PBHs . . . . .	105
4.5.1	Efficiency Calculation: Monte Carlo simulation of observation in 2017 . . . . .	105
4.5.2	Expected number of PBH microlensing events . . . . .	106
4.5.3	Experimental limits on the abundance of PBHs from two-night observations . . . . .	107
4.6	Discussion and future prospects . . . . .	108
<b>5</b>	<b>Earth-mass black holes? – Constraints on primordial black holes with 5-years OGLE microlensing events</b>	<b>110</b>
5.1	Introduction . . . . .	110
5.2	Microlensing for bulge stars . . . . .	112
5.2.1	Microlensing optical depth and event rate for a star in the Galactic bulge . . . . .	112
5.3	Models of Galactic disk and bulge and Milky Way dark matter . . . . .	116
5.3.1	The mass density distribution . . . . .	117
5.3.2	Mass spectrum of astrophysical lensing objects . . . . .	122
5.4	Results . . . . .	125
5.4.1	OGLE data . . . . .	125
5.4.2	Event rate of microlensing . . . . .	129
5.4.3	Comparison with the 5-years OGLE data . . . . .	129
5.4.4	Upper bound on the PBH abundance under null hypothesis . . . . .	131
5.4.5	A possible detection of Earth-mass scale PBHs from short-timescale OGLE data . . . . .	136
5.5	Discussion and Conclusion . . . . .	138
<b>6</b>	<b>Summary and Conclusion</b>	<b>141</b>
	<b>Appendix</b>	<b>143</b>
<b>A</b>	<b>Properties of transient candidates detected in HSC-M31 observation</b>	<b>144</b>
A.1	Properties of variable stars . . . . .	144
A.2	Flare events . . . . .	148
A.3	Binary stars with short period . . . . .	151
A.4	Eclipsing binary stars . . . . .	155

<b>B</b>	<b>Reduction of imaging data targeting dense stellar field using hscPipe</b>	<b>157</b>
----------	--	------------

# List of Figures

1.1	Temperature power spectrum of CMB by Planck satellite . . . . .	6
1.2	Imprint of baryon acoustic oscillation probed by the clustering of galaxies . .	8
1.3	Observational constraints on the $(\Omega_M, \Omega_\Lambda)$ parameters . . . . .	9
1.4	Mass maps of the Bullet Cluster . . . . .	16
1.5	Constraints on annihilation cross section on WIMPs . . . . .	17
1.6	The 95% C.L. upper bound on the PBH mass fraction to DM from previous studies . . . . .	29
2.1	Configuration of lensing system in the unperturbed metric . . . . .	33
2.2	Configuration of lensing system in the perturbed metric . . . . .	35
2.3	Shear patterns in the background galaxies . . . . .	42
2.4	Illustration of lensing system in microlensing scheme . . . . .	44
2.5	Example of theoretical light curves for microlensing events . . . . .	46
2.6	Example of light curves with finite source size effect . . . . .	47
2.7	Diffraction effect on microlensing magnification . . . . .	51
3.1	The optical depth of PBH microlensing effect on a single star in M31 . . . . .	58
3.2	Configurations of a lensing PBH and a source star in M31 in the lens plane .	59
3.3	The differential event rate of PBH microlensing for a single M31 star . . . . .	61
3.4	Configuration of 104 CCD chips and “patch” regions of the Subaru/HSC camera	64
3.5	The seeing size of each exposure as a function of time for our observation . .	65
3.6	An example of the image subtraction technique for a variable star candidate	67
3.7	Examples of detected objects in the difference image . . . . .	69
3.8	Examples of light curves for real variable stars identified in our observation .	71
3.9	Distribution of secure variable star candidates detected from our analysis . .	72
3.10	The photometric error used for the light curve measurement . . . . .	73
3.11	Example of light curves of candidates that are rejected by our selection criteria for a microlensing event . . . . .	75

3.12	Light curves for fake events that are caused by a spike-like image around a bright star or an asteroid . . . . .	76
3.13	One remaining candidate that passed all the selection criteria . . . . .	79
3.14	The detection efficiency estimated from light curve simulations . . . . .	80
3.15	A justification of the detection efficiency estimation, based on the different method using the fake image simulations . . . . .	81
3.16	An example image of the distribution of peaks identified in a small region of the reference image . . . . .	82
3.17	The total number of detected peaks in each patch region . . . . .	83
3.18	The peaks counts of HSC data in different regions of M31; two disk regions and the halo region . . . . .	83
3.19	The luminosity function of M31 stars in the HST PHAT catalog and that of the peaks in the HSC image . . . . .	85
3.20	The 95% C.L. upper bound on the PBH mass fraction to DM derived from our microlensing search of M31 stars . . . . .	88
3.21	The event rate of PBH microlensing for a single star in M31 when taking into account the effect of finite source size . . . . .	89
3.22	The 95% C.L. upper bound when taking into account the effects of finite source size on the event rate of microlensing . . . . .	90
4.1	The seeing size of each exposure as a function of time for 2017 observation . . . . .	95
4.2	Distribution of secure variable star candidates detected from 2017 data . . . . .	97
4.3	The photometric error used for the light curve measurement . . . . .	98
4.4	Magnitude of one remaining microlensing candidate from reference image . . . . .	102
4.5	Light curves of one remaining microlensing candidate and the seeing conditions . . . . .	102
4.6	The excluded region of periodicity for one remaining microlensing candidate . . . . .	104
4.7	The detection efficiency estimated from light curve simulations on the 2017 observation . . . . .	106
4.8	The 95% C.L. upper bound on the PBH mass fraction to DM derived from 2014 and 2017 observations . . . . .	107
5.1	The initial and final mass functions of each stellar component . . . . .	123
5.2	The expected differential number of microlensing events for a single star in the Galactic bulge region . . . . .	126
5.3	The relative contributions of main-sequence stars in the bulge and disk regions to the total event rates of microlensing . . . . .	127

5.4	The detection efficiency, $\epsilon(t_E)$ , quantifying the probability that a microlensing event of timescale $t_E$ is detected by the OGLE data . . . . .	127
5.5	Comparison of the 5-years OGLE data with the model predictions from stellar components . . . . .	128
5.6	Posterior distribution of the $f_{\text{PBH}}$ parameter (the PBH mass fraction to DM) assuming “null hypothesis” that there is no PBH microlensing in the OGLE data . . . . .	131
5.7	The 95% C.L. upper bound on the PBH mass fraction to dark matter, derived assuming the null hypothesis that there is no PBH microlensing event in the 5-year OGLE data . . . . .	132
5.8	The 95% CL allowed region of PBH abundance, obtained by assuming that 6 ultrashort-timescale microlensing events in the OGLE data are due to PBHs	133
5.9	The best-fit PBH model in each of the 4 shortest timescale bins, which shows a good agreement with the distribution of 6 ultrashort-timescale OGLE events	134
5.10	The contribution of PBHs at each distance to the total event rate of timescale $t_E = 0.2$ days . . . . .	135
A.1	Light curve of a flaring star possibly in M31 . . . . .	146
A.2	Light curve of a nova candidate . . . . .	146
A.3	Light curves of flare events (either in 2014 or 2017) . . . . .	148
A.4	Light curves of flare events . . . . .	149
A.5	Light curves of binary-star candidates (part I) . . . . .	151
A.6	Light curves of binary-star candidates (part II) . . . . .	152
A.7	Light curves of binary-star candidates (part III) . . . . .	153
A.8	Light curves of eclipsing binary candidates (part I) . . . . .	155
A.9	Light curves of eclipsing binary candidates (part II) . . . . .	156

# List of Tables

1.1	Matter density $\Omega_M$ . . . . .	15
3.1	Definitions of Statistics . . . . .	74
3.2	Selection Criteria . . . . .	74
4.1	Selection Criteria for 2017 data . . . . .	99
4.2	Summary of archival data of M31 by HSC- <i>r</i> . . . . .	101
5.1	Summary of the Galactic models . . . . .	117
5.2	The mass spectrum for each of astrophysical objects: brown dwarfs, main-sequence stars, and stellar remnants in the standard Galactic bulge and disk models. . . . .	118
A.1	Coordinates of flare events . . . . .	150
A.2	Coordinates of binary-star systems . . . . .	154
A.3	Coordinates of eclipse binary systems . . . . .	156

# Acknowledgements

This work would not be possible without the help of my collaborators. First of all, I would like to express my gratitude to my supervisor, Professor Hiroaki Aihara, for his great support. He supported my research both mentally and financially, and also gave me lots of helpful advices about my presentations and manuscripts. I owe special thanks to Masahiro Takada, for helpful suggestions, discussion and huge supports during all the years. He taught me from the basics of gravitational lensing and astrophysics, and suggested the research projects which were all interesting to me. His comments on the manuscripts were also very helpful. I also appreciate a lot to Naoki Yasuda, for helpful discussion and suggestions about the data analysis. His suggestions on data analysis were indispensable for my thesis projects. I especially owe a lot to him about his continuous efforts of maintaining computing resources at IPMU. Special thank also goes to Takahiro Sumi, for giving me advice about the basics of gravitational microlensing effect. His comments about the data analysis and OGLE data were very helpful. I also express many thanks to Surhud More and Anupreeta More, for helpful suggestions and discussion during my graduate study. I really appreciate their help to interpret the outcomes of Chapter 4.

I would like to express further thanks to my collaborators: I am grateful to Robert Lupton, for the improvement of pipeline, Toshiki Kurita and Sunao Sugiyama, for the estimation of wave effect, Masamune Oguri and Masashi Chiba, for helpful discussion regarding the M31 projects (Chapter 3 & 4). I also owe thanks to Chiaki Kobayashi and Masaomi Tanaka, for discussion about interpretation of the properties of variable stars. Many thanks also go to Yoshiaki Ono, Song Huang and Ryoma Murata, for kindly providing me instructions for running the Synpipe. Their suggestions were very helpful for estimating the properties of the HSC data. I am also grateful to my collaborators regarding OGLE project (Chapter 5), Shuichiro Yokoyama and Shogo Masaki, for suggestions and discussion about the analysis. Their continuous supports help me a lot to go with this project.

## *Acknowledgements*

---

Besides the contents of my research projects, I am grateful to supports by many people who provided a comfortable research environment. In particular, I am grateful to Masashi Yokoyama, Yoshiyuki Onuki, Denis Epifanov and Kuniko Kono, who helped me a lot to spend fruitful time at laboratory. Also very warm thanks go to the encouragements from all the staffs, researchers and friends at Aihara-Yokoyama lab and IPMU. Without their supports I could not enjoy my student life at graduate school. I would also like to appreciate my thesis refereeing committee, Tadayuki Takahashi, Yasushi Suto, Noriko Yamasaki, Junichi Tanaka, and Tomonori Totani, for their helpful comments and suggestions.

I would like to conclude this section by thanking my family. I did not expect the things would be not easy for these five years, and I apologize for having not being much of a help. Still I really appreciate all the kind supports they provided me, and wish them to keep in good shape in years to come.

# Chapter 1

## Introduction

The current standard model of cosmology, in which the universe is dominated by cold dark matter (CDM) – the so-called  $\Lambda$ CDM model, has been remarkably successful in reproducing various observations of the large-scale distribution of galaxies in space. This model assumes a flat spatial geometry, and is based on the cosmological principle that the Universe is homogeneous and isotropic. One important suggestion of this model is that the mass-energy density of the Universe is composed by three distinct components: normal matter (baryons), dark matter and dark energy. The normal matter we now know accounts for only about 4% of the total density of the universe, and the rest of around 96% of the Universe is “dark”.

Dark energy is unknown energy component which drives the acceleration of expansion of the Universe. The expansion of the Universe was first reported by Hubble in 1929. In the article “A relation between distance and radial velocity among extra-galactic nebulae”, Hubble showed that galaxies recede from us in all directions and more distant ones recede more rapidly in proportion to their distance. This discovery does not support the picture of the static Universe model, and the Einstein’s cosmological constant becomes unnecessary. However, the existence of cosmological constant has been preferred in order to explain the structure formation scenario and/or to solve the age problem of the universe. Then in the end of 1990’s, the existence of cosmological constant was firmly confirmed by the analysis of distance type-Ia supernova. Currently, combination of recent observations shows that cosmic expansion has been speeding up over the last 5 billion years. This acceleration suggests that the other 70% of the universe is composed of a “dark” energy whose properties we only dimly grasp but that must have a negative pressure to make cosmic expansion speed up over time. However, the property of dark energy is still big mystery, and requires further evidence both from observational and theoretical studies.

The nature of dark matter also remains one of the largest unsolved astrophysical mys-

teries. The evidence of dark matter was first discovered by Fritz Zwicky in the 1930's. He investigated the peculiar motions of galaxies in a cluster of galaxies and found that visible matter cannot provide enough gravity to hold these galaxies in the cluster. Since then, the existence of dark matter has nearly been established by observations of the rotational speeds of galaxies and gravitational lensing. Currently, the property we know or require is that dark matter interact with ordinary matter only via its gravitational interaction. Recent analysis of cosmological observation and numerical simulations suggest that dark matter plays a dominant role in the structure formation theory, and supports the picture that the Universe is hierarchically formed. The  $\Lambda$ CDM model suggests that approximately 84% of the matter in the Universe is constituted by this “dark” matter.

Many candidates of non-baryonic matter have been discussed, and those beyond the standard model are generally categorized as the hot dark matter (HDM) or the cold dark matter (CDM). The hot dark matter, such as a massive neutrino, is a particle with significant thermal speeds, and hence behaves as relativistic collisionless gas. Cosmological simulations suggest that fluctuations smaller than the horizon scale will disappear in the Universe with hot dark matter, and thus can hardly form clumpy structures as we observe today. Therefore the hot dark matter scenario is ruled out in the modern cosmology.

On the other hand, cold dark matter (CDM) is a type of dark matter which is free from collisionless damping. In the picture of  $\Lambda$ CDM model, small structures are created first from gravitational instability of initial perturbations. As the cold dark matter does not reduce perturbation during structure formation compared to the hot dark matter, small structures gather gravitationally, and merged many times to form larger structures. This kind of structure formation mechanism is called “bottom-up” structure formation. The  $\Lambda$ CDM model, assuming the existence of cold dark matter and dark energy, is quite successful to describe the observed structures in the universe, and thus becomes the cosmological standard model.

Although a viable candidate of dark matter is unknown, hypothetical elementary particle, the so-called weakly interacting massive particle (WIMP), might exist beyond the standard model of particle physics. However, it has not yet been found by any terrestrial experiments such as those going on at the Large Hadron Collider (LHC). Alternative models of dark matter have been also proposed; Massive Astrophysical Compact Halo Objects (MACHOs), axions, sterile neutrinos, and plenty of particle models ranging from simple scalar fields to complex particle models with an entire “dark” sector of interactions. Therefore, revealing the nature and properties of dark matter with astronomical dataset is one of the most important problems in modern cosmology and particle physics.

In this chapter we will introduce the cosmological properties of dark matter. We will first review the role of dark matter in the cosmological structure formation and evolution (Section 1.1). Then we will provide an overview of the current astrophysical properties of dark matter (Section 1.2). In particular, we will focus on the feasible candidate of dark matter from compact object origins (Section 1.3), and describe the objective of this thesis (Section 1.4).

## 1.1 The origins of cosmological structure

In this section we explore the cosmological components in the Universe, and look into the basic procedures of cosmic structure formation. We refer to Dodelson (2003) for more detail.

### 1.1.1 The standard cosmological model

In the view of modern cosmology, the matter distribution in the universe is homogeneous and isotropic. This assumption is called as cosmological principle. Within the framework of cosmological principle, the evolution of the Universe is governed by the Friedmann and the Einstein equations.

#### (1) Friedmann equation

We start with the spacial properties of the universe assuming the cosmological principle. In four space-time dimensions, the dynamics of the universe is described by the **Friedmann-Lemaître-Robertson-Walker** (FLRW) metric (Friedmann 1922, 1924; Lemaître 1931; Robertson 1935; Walker 1936):

$$ds^2 = -c^2 dt^2 + a^2(t) \left\{ \frac{dr^2}{1 - Kr^2} + r^2(d\theta^2 + \sin^2\theta d\phi^2) \right\}, \quad (1.1)$$

where  $K$  is spatial curvature, and  $a(t)$  is scale factor. Scale factor is an indicator of cosmological distance, and closely related to another conventional description of the distance; the redshift. The redshift is a distance estimator described by the observed wavelength  $\lambda_0$  and the original wavelength  $\lambda_s$  as  $z = (\lambda_0 - \lambda_s)/\lambda_s$ . The connection between the redshift and scale factor is given by  $a = 1/(1 + z)$ , where the current scale factor is defined as  $a_0 = 1$  (for  $z = 0$ ).

In the FLRW metric, if photons emitted from a source at redshift  $z$  are observed by an observer at the coordinate origin, they propagate along the geodesic specified by

$ds^2 = 0$  with  $d\theta = d\phi = 0$ . Then we can introduce the distance to  $\chi(z)$  as comoving distance:

$$\int_0^{\chi(z)} \frac{dr}{\sqrt{1 - Kr^2}} = \int_{t(z)}^{t_0} \frac{cdt}{a(t)}, \quad (1.2)$$

where  $t(z)$  denotes the time when the light is emitted, and  $t_0$  is the present time. With this definition of comoving distance, the radial distance  $r$  is given as follows:

$$r(\chi) = \begin{cases} \sinh(\sqrt{K}\chi)/\sqrt{K} & K > 0, \\ \chi & K = 0, \\ \sinh(\sqrt{-K}\chi)/\sqrt{-K} & K < 0. \end{cases} \quad (1.3)$$

This suggests that the spatial curvature represents the shape of the universe;  $K > 0$  is open,  $K = 0$  is flat, and  $K < 0$  is closed universe, respectively.

Another set of equations that are essential for the dynamics description is the **Einstein equation**. Under the FLRW metric, the Einstein equation describes how the universe expands as a function of time, and how the expansion rate is related to the matter-energy contents;

$$G_{\mu\nu} = R_{\mu\nu} - \left(\frac{1}{2}R - \Lambda\right)g_{\mu\nu} = \frac{8\pi G}{c^4}T_{\mu\nu}, \quad (1.4)$$

where  $\Lambda$  is cosmological constant. Here we assume the perfect fluid approximation under with the FLRW metric. Then the energy-momentum tensor in the right hand side of Eq. (1.4) is given by:

$$T_{\mu\nu} = (\rho + p)u_\mu u_\nu + pg_{\mu\nu}, \quad (1.5)$$

where  $u^\mu$  stands for the velocity components,  $\rho$  for the density, and  $p$  for the pressure of the universe, respectively. With Eq. (1.1) and Eq. (1.5), we can derive the time-time component and the space-space component as:

$$\left(\frac{\dot{a}}{a}\right)^2 + \frac{c^2 K}{a^2} = \frac{8\pi G}{3c^2}\rho + \frac{c^2 \Lambda}{3}, \quad (1.6)$$

$$\frac{\ddot{a}}{a} = -\frac{4\pi G}{3c^2}(\rho + 3p) + \frac{c^2 \Lambda}{3}, \quad (1.7)$$

where the dot notation denotes the time derivative, and  $\rho$  and  $p$  denote the total energy

density and pressure, respectively. We also introduce the equation of state

$$p = w\rho, \quad (1.8)$$

where the  $w$  parameter takes specific values for different components;  $w = 1/3$  for relativistic component, whereas  $w = 0$  for non-relativistic particles such as dark matter. Then the combination of Eq. (1.6), Eq. (1.7), and Eq. (1.8) give the time evolution of energy density components;

$$\rho \propto \exp\left(-3 \int \frac{da'}{a'}(1 + w(a'))\right). \quad (1.9)$$

This equation gives  $\rho_m \propto a^{-3}$  and  $\rho_\gamma \propto a^{-4}$ , for matter and radiation components, respectively. If we assume that the fluid corresponds to cosmological constant, the energy density of the fluid is obtained by inserting  $w_{\text{DE}} = p_\Lambda/\rho_\Lambda = -1$  as  $\rho_\Lambda = c^4\Lambda/8\pi G$ . Hence the energy density  $\rho_\Lambda$  does not evolve with time, which is the same property as the dark energy.

More generally, the density evolution of the universe is often characterized by cosmological parameters as in the following:

$$H \equiv \dot{a}/a \quad : \text{Hubble parameter}, \quad (1.10)$$

$$\Omega \equiv \rho/\rho_{\text{cr}} \equiv 8\pi G\rho/3H^2 \quad : \text{density parameter}, \quad (1.11)$$

$$\Omega_K \equiv c^2K/a^2H^2 \quad : \text{curvature parameter}, \quad (1.12)$$

$$\Omega_\Lambda \equiv c^2\Lambda/3H^2 \quad : \text{dimensionless cosmological constant}, \quad (1.13)$$

where  $\rho_{\text{cr}}$  is the critical density of the Universe. With these quantities the evolution of scale factor in Eq. (1.6) is determined as:

$$H^2(a) = H_0^2 \left[ \frac{\Omega_{m0}}{a^3} + \frac{\Omega_{\gamma0}}{a^4} - \frac{\Omega_{K0}}{a^2} + \Omega_{\Lambda0} \exp\left\{-3 \int \frac{da'}{a'}(1 + w_{\text{DE}}(a'))\right\} \right], \quad (1.14)$$

where the parameters with index 0 in the right hand side represent current density contents. The  $H(a)$  in the Eq. (1.14) is called the **Hubble rate**, which represents how rapidly the scale factor changes.

## (2) The observational review of cosmological component

As described in Eq. (1.14), the density evolution in the FLRW metric universe can be quantitatively characterized by the density components of the universe. In modern

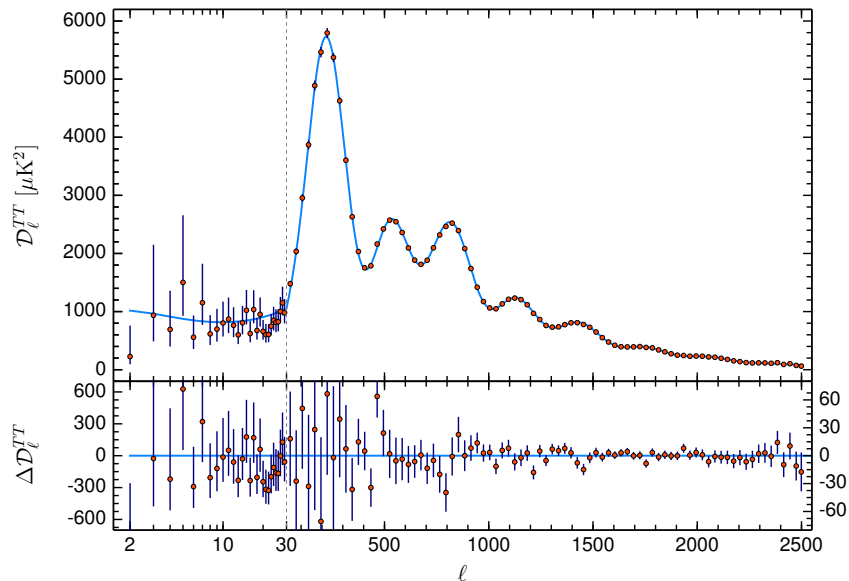


Figure 1.1: Planck 2018 temperature power spectrum, where  $D_l = l(l+1)C_l/2\pi$ . The base- $\Lambda$ CDM theoretical spectrum best fit to the Planck TT, TE, EE + lowE + lensing likelihoods is plotted in light blue in the upper panel. Residuals with respect to this model are shown in the lower panel. The error bars show  $\pm 1\sigma$  diagonal uncertainties, including cosmic variance (approximated as Gaussian) and not including uncertainties in the foreground model at  $l \geq 30$ . This figure is reproduced from Fig. 1 of Planck Collaboration et al. (2018).

cosmology, observations to constraint the density components have played important roles to probe the evolution of the universe. In the following we briefly summarize some key observational properties that support the  $\Lambda$ CDM model.

#### a) **Baryonic component**

Baryonic component has began to be formed a few minutes after Big Bang. At the beginning, particles were in very hot plasma and stayed in equilibrium. When the timescale of expansion became shorter than the nuclear interaction timescale, the particles started to experience “freeze out” phase, and chemical elements have been begun to settle. Thus we can study the baryonic component by comparing the primordial abundance of the light elements from simulation and observation. In particular, the measurement of primordial deuterium abundance pins down the baryon fraction  $\Omega_b$  extremely accurately. For example, Cooke et al. (2018) provides  $D/H = 2.527 \pm 0.030 \times 10^{-5}$ , corresponding to  $\Omega_b h^2 = 0.0222 \pm 0.0005$ .

#### b) **Flatness**

One of the most fundamental parameters in the Friedmann equation is the cur-

vature of the universe. This is a key parameter to explain whether the universe is finite or infinite. One possible solution to this flatness problem is to study the accelerating phase in the early universe. The cosmic microwave background (CMB) radiation is a useful tracer for this because it offers the universe when photons last scattered off electrons at  $z \sim 1100$ . Observations with microwave experiments have indicated that the temperature spectrum of CMB is isotropic, corresponding to blackbody spectrum around  $T = 2.7255 \pm 0.0006\text{K}$  (Fixsen 2009). Also, the temperature fluctuation pattern of CMB is characterized by the angular power spectrum  $C_l$  defined as:

$$\frac{\Delta T}{T} = \sum_{lm} a_{lm} Y_l^m, \quad (1.15)$$

$$C_l \equiv \langle |a_{lm}^2| \rangle, \quad (1.16)$$

where  $Y_l^m$  is spherical harmonics, and  $C_l$  is the ensemble average of the coefficient of the multipole expansion of the temperature fluctuations. Since the angular diameter distance to the last scattering surface of CMB strongly depends on the curvature of the universe, the angular scale of peaks in angular power spectrums of CMB is an excellent indicator of the curvature of the universe. As shown in Fig. 1.1, the first peak of CMB power spectrum locates at  $l \sim 200$ , which corresponds to  $1^\circ$  scale, indicating that the universe is almost flat,  $\Omega_M + \Omega_\Lambda \sim 1$ .

c) **Matter component**

As discussed above, the peak position of the first peak in the CMB power spectrum strongly constrains the curvature property of the Universe. On the other hand, the peak height of first peak gives another constraint on the cosmic energy components; the increase in matter component results as a larger gravitational potential, which suppress all the peaks. Similarly, an increase in baryon density means that the internal mass of the system becomes larger, which suppresses the second peak with respect to the first and third peaks. The measurement of peaks by Planck satellite indicates small density boost around the peak of order  $10^{-5}$ , which provides the ratio of baryonic component to the matter component as  $\Omega_b/\Omega_m = 0.158 \pm 0.004$ . Therefore, the matter component of the universe is  $\Omega_M \sim 0.3$ , suggesting that most of the matter component in the Universe should be non-baryonic (Spergel et al. 2003).

d) **Acceleration**

The cosmic expansion history has been investigated by distance indicators. One of the most popular indicators is Type-Ia supernova, which has constant peak

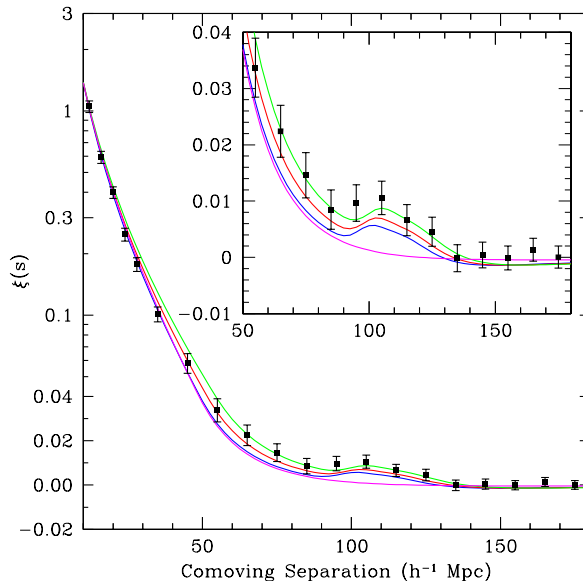


Figure 1.2: The large-scale redshift-space correlation function of the SDSS LRG sample. The inset shows an expanded view with a linear vertical axis. The models are  $\Omega_M h^2 = 0.12$  (top, green), 0.13 (red), and 0.14 (bottom with peak, blue), all with  $\Omega_b h^2 = 0.024$  and  $n = 0.98$  and with a mild non-linear prescription folded in. The magenta line shows a pure CDM model ( $\Omega_M h^2 = 0.105$ ), which lacks the acoustic peak. The bump at  $100h^{-1}$  Mpc scale is statistically significant. This figure is reproduced from the left panel Fig. 2 of Eisenstein et al. (2005).

luminosity in absolute magnitude. Hence we can derive a relation between the luminosity and the distance, which is useful to test whether the universe is decelerating or accelerating. The first clear evidence of acceleration was reported by the measurement of distant supernovae reported in 1990's, which strongly supports the existence of cosmological constant (Riess et al. 1998; Perlmutter et al. 1999).

Another popular distance indicator is baryon acoustic oscillation (BAO). BAO is the characteristic structure from photons emitted at the last scattering surface. Originally the Universe was hot plasma, and the radiation pressure from the CMB prevents the baryons from clustering. Since dark matter only interacts gravitationally, the radiation pressure behaves as relativistic sound waves, which propagate until the Universe becomes neutral around  $z \sim 1000$ . The imprint of these sound waves can be detected by the analysis of CMB anisotropy data in the harmonic space (Hinshaw et al. 2003). Another imprint is also obtained by measuring the clustering of galaxies. The feature was first detected by Sloan Digital Sky Survey (SDSS), suggesting a small excess in number of pairs of galaxies

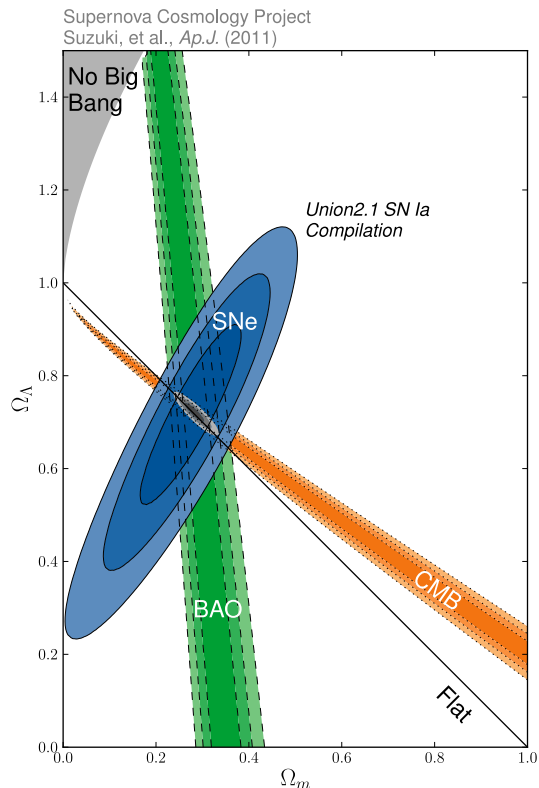


Figure 1.3: 68.3%, 95.4%, and 99.7% confidence regions of the  $(\Omega_M, \Omega_\Lambda)$  plane for the  $\Lambda$ CDM model. Measurements derived from Type-Ia SNe by Union2.1 (Suzuki et al. 2012), combined with the constraints from BAO by SDSS DR7 and 2dFGRS data (Percival et al. 2010), and CMB by 7-year WMAP data (Komatsu et al. 2011). The SN Ia confidence region only including statistical errors. This figure is reproduced from the left panel Fig. 5 of (Suzuki et al. 2012).

separated by around  $100h^{-1}\text{Mpc}$ , as shown in Fig. 1.2 (Eisenstein et al. 2005). Since the characteristic scale of acoustic oscillation is determined by the sound horizon at last scattering surface, combination of BAO measurements among different redshifts can behave as a distance indicator. Current measurements of BAO strongly favor a flat universe, indicating the presence of the cosmological constant (Hinshaw et al. 2013; Anderson et al. 2014).

The combination of these multiple indicators have strongly constrained the density components in the Universe. In particular, the combined results of Type-Ia supernovae, CMB and BAO measurements have placed strongly limits on the abundance of cosmic density components. Fig. 1.3 shows the recent constraints on the density parameters, indicating that the universe is better described with  $\Omega_M \sim 0.3$  and  $\Omega_\Lambda \sim 0.7$ . Note that we can also derive the densities of radiation components composed of photons and neutrinos from the CMB temperature. For example, the CMB temperature from FIRAS experiment corresponds to

$\Omega_\gamma h^2 = 2.47 \times 10^{-5}$  (O'Meara et al. 2001). Under the assumption of the three massless species of neutrinos, current radiation densities can be calculated from the standard thermal history as  $\Omega_\nu h^2 = 6 \times \frac{g(\nu)}{g(\gamma)} \left( \frac{T(\nu)}{T(\gamma)} \right)^4 \Omega_\gamma h^2 \sim 1.7 \times 10^{-5}$ , where we put the neutrino temperature  $T(\nu) = 1.95\text{K}$ .

## 1.1.2 Structure formation

The universe with FLRW metric describes the properties of isotropic and homogeneous expansion. On the other hand, current universe contains various structures such as galaxies, clusters of galaxies, super clusters, filaments and voids, whose formation need other scenario of structure evolution. These structures are now believed to arise from gravitational amplification of tiny seed density fluctuations as observed in the CMB anisotropies. In this section we describe the fluctuation evolution in the  $\Lambda\text{CDM}$  universe.

### (1) Density evolution in Linear perturbation theory

Here we consider the mass fluctuations at scale larger than a few Mpc, where the amplitude  $\delta$  can be approximated as  $\delta \ll 1$ . This approximation is called as ‘‘linear’’ fluctuations, where the Newtonian approximation plays a role. Then the matter density of fluid  $\rho$  satisfies the following fluid equations and the Poisson equation:

$$\frac{\partial \rho}{\partial t} + \vec{\nabla} \cdot (\rho \vec{u}) = 0 \quad : \text{Continuity equation,} \quad (1.17)$$

$$\Delta \phi = 4\pi G \rho \quad : \text{Poisson equation,} \quad (1.18)$$

$$\frac{\partial \rho}{\partial t} + (\vec{u} \cdot \vec{\nabla}) \rho = -\frac{1}{\rho} \vec{\nabla} p - \vec{\nabla} \phi \quad : \text{Euler equation} \quad (1.19)$$

where  $\phi$  is the gravitational potential. We can rewrite these quantities using the FLRW metric:  $\vec{x} = \vec{r}/a(t)$ ,  $\vec{v} = a(t)\dot{\vec{x}}$ ,  $\Phi = \phi(\vec{x}, t) + \frac{1}{2}a(t)\ddot{a}(t)x^2$ . Also we can characterize fluctuation  $\delta$  by taking  $\bar{\rho}$  as homogeneous part

$$\delta(\vec{x}, t) = \frac{\rho(\vec{x}, t) - \bar{\rho}}{\bar{\rho}}, \quad (1.20)$$

then Eqs. (1.17)(1.18) and (1.19) can be converted to:

$$\frac{\partial \delta}{\partial t} + \frac{1}{a} \vec{\nabla} \cdot \vec{v} = 0 \quad , \quad (1.21)$$

$$\Delta \Phi = 4\pi G \bar{\rho} \delta a^2 \quad , \quad (1.22)$$

$$\frac{\partial \vec{v}}{\partial t} + \frac{\dot{a}}{a} \vec{v} = -\frac{c_s^2}{a} \vec{\nabla} \delta - \frac{1}{a} \vec{\nabla} \Phi \quad , \quad (1.23)$$

where  $c_s^2$  is the sound velocity defined as  $c_s^2 = \sqrt{\partial p / \partial \rho}$ . Now we apply linear approximation and neglect terms larger than second order to get;

$$\ddot{\delta} + 2\frac{\dot{a}}{a}\dot{\delta} - \left( \frac{c_s^2 k^2}{a^2} \Delta \delta + 4\pi G \bar{\rho} \delta \right) = 0. \quad (1.24)$$

This equation can be solve by applying the Fourier decomposition of  $\delta$ ;

$$\ddot{\delta}_k + 2\frac{\dot{a}}{a}\dot{\delta}_k + \left( \frac{c_s^2 k^2}{a^2} - 4\pi G \bar{\rho} \right) \delta_k = 0. \quad (1.25)$$

This equation indicates that  $\delta_k$  can have the growing solution if the wavelength  $\lambda$  is longer than some critical value  $\lambda_J$ :

$$\lambda = \frac{2\pi a}{k} > \lambda_J \equiv c_s \sqrt{\frac{\pi}{G \bar{\rho}}}, \quad (1.26)$$

where  $\lambda_J$  is called as the Jeans length. Therefore the pressure gradient balances the gravitational infall, and the fluctuations oscillate when their wavelength is smaller than the Jeans length.

Next we focus on the matter-dominated universe with  $p = 0$ . Then the evolution of the density fluctuation can be described as:

$$\ddot{\delta} + 2\frac{\dot{a}}{a}\dot{\delta} - 4\pi G \bar{\rho} \delta = 0. \quad (1.27)$$

The solution is composed by growing mode  $D_1(t)$  and decaying mode  $D_2(t)$  as follows:

$$\delta(t) = C_1 D_1(t) + C_2 D_2(t). \quad (1.28)$$

Now we look into the properties of density evolution for the  $\Lambda$ CDM universe. For simplicity we neglect the radiation density  $\Omega_{\gamma 0}$ , curvature  $K$ , and assume  $w_{\text{DE}} = -1$ . Then the Hubble parameter  $H$  is given by:

$$H(a) = H_0 \sqrt{\Omega_{\text{m}0} a^{-3} + \Omega_{\Lambda 0}}. \quad (1.29)$$

Since  $H(a)$  is a specific solution of Eq. (1.27), the linear growth of matter density is

obtained by assuming  $D(a) = H(a)f(a)$ :

$$D_1(a) = H(a) \int_0^a \frac{da'}{(a'H(a'))^3}, \quad (1.30)$$

$$D_2(a) = H(a). \quad (1.31)$$

## (2) Density evolution for cosmic structures : non-linear regime

In the following we focus on the density evolution for  $\delta \gg 1$  case, where the effect of the non-linear terms overcomes the Hubble expansion in the evolution of over density. Even though the evolution of non-linear growth is difficult to describe analytically, the simplified model, the **spherical collapse model**, allows us to analytically solve the evolution of nonlinear density perturbations.

Here we summarize the characteristic dynamics for the spherical collapse model. For simplicity, we consider a positively curved matter-dominated universe, where the Friedmann equations have the parametric form

$$r = A(1 - \cos \theta), \quad (1.32)$$

$$t = B(\theta - \sin \theta), \quad (1.33)$$

where the parameters  $A$  and  $B$  are for the matter dominated universe:  $A = \Omega_{m0}/[2(\Omega_{m0} - 1)]$ ,  $B = \Omega_{m0}/[2H_0(\Omega_{m0} - 1)^{3/2}]$ . This solution gives the same evolutionary picture for the shell at radius  $r$  with the inner mass  $M$ , with the equation of motion :  $d^2r/dt^2 = -GM/r^2$ . These models characterize the shell behavior: the shell first expands from  $\theta = 0$  to  $\theta = \pi$ , then contracts from  $\theta = \pi$  to form singularity at  $\theta = 2\pi$ . These two phases correspond to turn around phase and virialization in structure formation.

### ◇ turn around

The solution of Eq. (1.32) and Eq. (1.33) shows that the spherical region reaches the maximum radius at  $\theta = \pi$ , where the radius  $r_{\max} = 2A$ , and  $t_{\max} = \pi B$ . Then the density of spherical region at the turn around phase is characterized as:

$$\frac{\rho}{\rho_0} = \frac{\Omega_{m0}\rho_{c0}/r_{\max}^3}{\rho_{c0}/a^3} = \frac{9\pi^2}{16} \sim 5.55, \quad (1.34)$$

$$\delta = \frac{3(6\pi)^{2/3}}{20} \sim 1.06, \quad (1.35)$$

where  $a = (\frac{3}{2}H_0t)^{2/3}$ . Therefore the characteristic overdensity does not depend on the shell mass  $M$ .

◇ **virialization**

Eq. (1.32) and Eq. (1.33) indicate that the mass density collapse to singularity at  $\theta = 2\pi$ . In reality, however, the mass distribution reach virtualized first and the singularity is never formed. The potential energy satisfies  $E_k = -E_p(r_{\max}/2)/2$ , where  $E_p(r_{\max}) = -3GM^2/5r_{\max}$  at  $r_{\max}$  and  $E_p(r_{\max}/2) = -6GM^2/5r_{\max}$  at  $r = r_{\max}/2$ . Thus the contraction of each shell forms objects with a finite size of  $r_{\text{vir}} = r_{\max}/2$ , and  $t_{\text{vir}}$  can be characterized as  $t_{\text{vir}} = 2r_{\max}$  (or the case of  $\theta = 3\pi/2$  as  $t_{\text{vir}} = (\frac{3}{2} + \frac{1}{\pi})t_{\max} \sim 1.81t_{\max}$ ). Hence the typical overdensity follows;

$$\frac{\rho}{\rho_0} = \nabla_{\text{vir}} = \frac{9\pi^2}{16} \times 8 \times \left(\frac{t_{\text{vir}}}{t_{\max}}\right)^2 \sim 178, \quad (1.36)$$

$$\delta = \frac{3}{20} \left(6\pi \frac{t_{\text{vir}}}{t_{\max}}\right)^{2/3} \sim 1.69. \quad (1.37)$$

(3) **Dark matter halos**

In the hierarchical structure formation, small-scale structure so-called halos constitutes a large fraction of dark matter. Cosmic structure formation theory suggests that matter was accreted along filaments, and halos underwent tidal disruption and mergers. There exists some properties of halo structures beyond predictions from the spherical collapse model: concentrated mass distribution in the central region and the slope of mass density profile. One prediction is that dark matter halos tend to approach an equilibrium halo shape known as the **Navarro-Frenk-White** (1997; hereafter NFW) profile. This universal halo structure has a spherically-averaged radial density that goes as

$$\rho_{\text{NFW}}(r) = \frac{\rho_c}{(r/r_s)(1+r/r_s)^2}, \quad (1.38)$$

where  $r_s$  is the scale radius and  $\rho_c$  is the central density parameter. The parameter  $\rho_c$  is specified by imposing that the mass enclosed within a sphere of a given overdensity  $\Delta$  is equal to the halo mass  $M_\Delta$ ,

$$\rho_c = \frac{\Delta \rho_{\text{cr}}(z) c_\Delta^3}{3m_{\text{NFW}}(c_\Delta)} = \frac{M_\Delta}{4\pi r_s^3 m_{\text{NFW}}(c_\Delta)}, \quad (1.39)$$

where  $m_{\text{NFW}}(c_\Delta) \equiv \int_0^{c_\Delta} dx x/(1+x)^2 = \ln(1+c_\Delta) - c_\Delta/(1+c_\Delta)$ ,  $c_\Delta \equiv r_\Delta/r_s$ , a concentration parameter, and  $\Delta(z)$  is a nonlinear overdensity introduced to define the interior mass for each halo. The NFW profile predicts a monotonically steepened profile with increasing radius, with logarithmic slopes shallower than an isothermal sphere interior to the characteristic “scale” radius  $r < r_s$ , but steeper at larger radius,

approaching to  $r^{-3}$  at the virial radius,  $r \rightarrow r_{\text{vir}}$ .

Note that one sometimes adopts corrections in addition to this simple inner density profile of halos. For example, one need to take into account the surrounding mass distribution, especially at larger radius around  $R \simeq 10\text{Mpc}/h$  where the mass distribution can be suffered from that of neighboring galaxies. One can include this effect as two-halo term, by taking advantage of the two-point correlation function between the clusters and the surrounding mass distribution (Miyatake et al. 2015). For more precise modeling, one can also consider the effect from stellar mass contribution and miss-centering effect (Takada & Jain 2002; Oguri & Hamana 2011).

Observations of halo kinematics have further complicated the view of halo profiles, with rotation curves providing evidence that many halos have far flatter central densities than those seen in simulations. This problem is known as the core-cusp problem, and remains as one of the unsolved problem in the small-scale cosmology (de Blok et al. 2001; Gentile et al. 2004; Oh et al. 2011).

## 1.2 Relics of cold dark matter

Since the first discovery of dark matter by Fritz Zwicky, the existence of dark matter have been tested by many astrophysical observations. In this section we first review the observational properties of cold dark matter (Section 1.2.1), and then look into the possible relics when dark matter behaves as particle (Section 1.2.2) or compact objects (Section 1.2.3).

### 1.2.1 Observational evidences of cold dark matter

In the following we would briefly explain astrophysical properties of dark matter which have been revealed by observations.

- **Non-baryonic**

As discussed in Section 1.1.1, the current matter density of the Universe is observationally constrained to  $\Omega_{\text{M}} \sim 0.3$ , while the baryonic component in the universe is constrained to  $\Omega_b \sim 0.02$ . This evidence suggests that we cannot explain the whole matter component just by known matter, which strongly supports the existence of non-baryonic matter.

The abundance of dark matter density have been tested by multiple indicators. For example, CMB power spectrum offers a strong constraint on matter density, as discussed

Table 1.1: Matter density  $\Omega_M$ 

Observations	Matter density	References
Planck PR2 <sub>++</sub> 2015	$0.3098 \pm 0.0062$	Planck Collaboration et al. (2015)
SNIa 2014	$0.295 \pm 0.034$	Betoule et al. (2014)
BOSS weak lensing 2014	$0.310 \pm 0.020$	More et al. (2015)
Planck SZ+BAO+BBN 2013	$0.29 \pm 0.02$	Addison et al. (2013)
WMAP9 <sub>++</sub> 2013	$0.2865 \pm 0.0096$	Hinshaw et al. (2013)

in Section 1.1.1. Another good test is performed by measurements of baryon acoustic oscillation. Besides the constraint on  $\Omega_\Lambda$  obtained from the angular location of BAO peak in the galaxy clustering, the amplitude of BAO peak places tight constraint on the matter content of the Universe, providing  $\Omega_M = 0.273 \pm 0.025$  (Eisenstein et al. 2005). Current constraints from notable observations are summarized in the Table 1.1.

- **Massive**

The puzzling property of dark matter is that it interacts with ordinary matter only via its gravity. This makes it difficult to reveal the nature of dark matter, since we cannot probe them through electromagnetic signals. One unique tool to probe the nature of dark matter is the gravitational lensing effect. General relativity predicts that light rays are bent around massive bodies, which causes the source bodies to be distorted, brightened, or sometimes creates multiple images in the sky. The strength of the lensing effect is that it does not related to the nature of the particles in the region, but only related to its total mass. Hence we can construct a mass map by studying the distortion patterns of sources provided by the lens distribution.

- **Collisionless**

The famous detection of collisionless property of dark matter is reported by the observations of the Bullet Cluster (Clowe et al. 2006). The Bullet Cluster is the result of merging of two clusters, in which the gas has collided, stripped, and slowed. The properties of these two gas clumps have been investigated by X-ray observation with Chandra, which shows significant deviations from the cluster mass contours probed by the gravitational lensing effect, as shown in Fig. 1.4. This deviation suggests that the two clumps made of gas components got slowed down after the collision due to their friction, while the dark matter components within these clusters have passed through without frictions. Hence we expect that the matter component within these clusters is collisionless, which results in the difference of mass maps between the luminous gas component and dark matter.

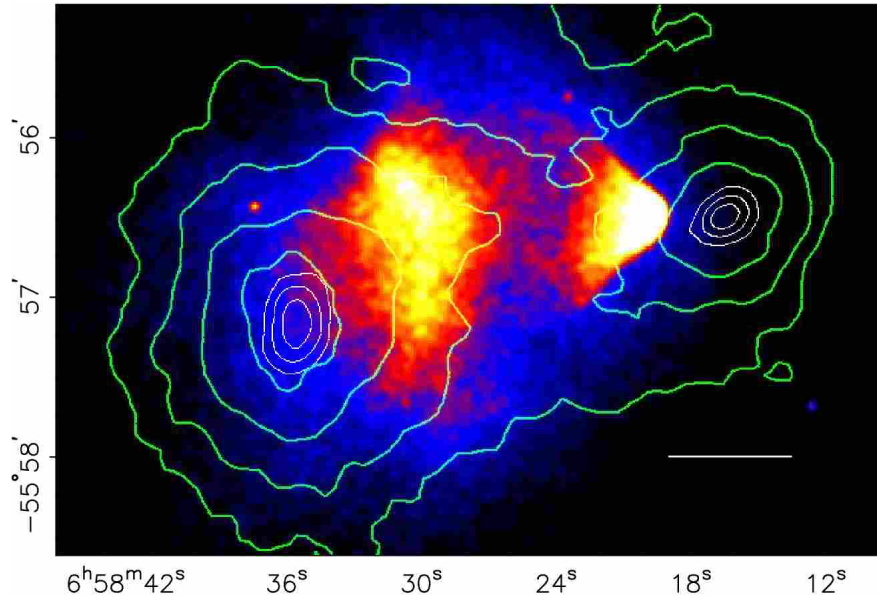


Figure 1.4: 500 ks Chandra image of the Bullet Cluster (1E0657-558), with the white bar indicating 200kpc at the distance of the cluster. The green contours are the weak lensing  $\kappa$  reconstruction, and the white contours show the errors on the positions of the  $\kappa$  peaks, corresponding to 68.3%, 95.5%, and 99.7% confidence levels. This figure is reproduced from the left panel Fig. 1 of Clowe et al. (2006).

- **Cold**

Many candidates of non-baryonic matter have been discussed, and those beyond the standard model are generally categorized as the hot dark matter (HDM) or the cold dark matter (CDM). The hot dark matter, such as massive neutrino, is a particle which has significant thermal speeds, and thus behaves as relativistic collisionless gas. This means that particles do not fall into the initial overdensities, and suppress the formation of small-scale structures as we observe today. Since this scenario does not support the observational properties of large scale structures, the hot dark matter scenario is ruled out in the modern cosmology.

On the other hand, the velocity of cold dark matter is proposed as non-relativistic at the time of decoupling, and can form galactic structures. In the picture of  $\Lambda$ CDM model, small structures are created first from gravitational instability of initial perturbations. As the cold dark matter does not reduce perturbation during structure formation compared to the hot dark matter, small structures gather gravitationally, and merged many times to form larger structures. This kind of structure formation mechanism is called bottom-up structure formation, and now becomes the standard view of modern

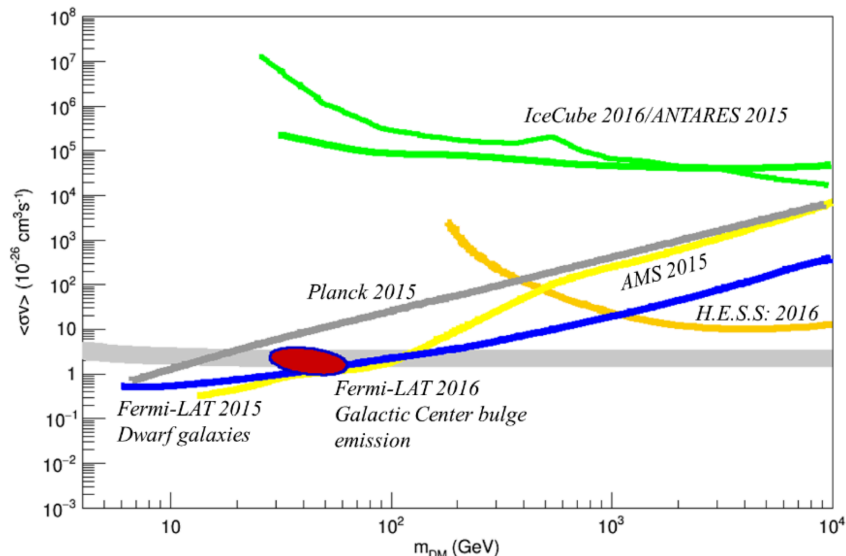


Figure 1.5: The current constraints on the annihilation cross-section versus WIMP mass from the highlighted observations. The constraints are for the annihilation to b-quark pairs. Whereas indirect methods exploring gamma-ray photons and cosmic rays from satellite measurements compete well up to hundreds of GeVs, at higher energies Air Cherenkov Telescopes appear to be driving the present limits. The thermal relic cross-section is indicated by the light grey band. Note that different assumptions for the DM distributions affect these limits quantitatively, but do not change the situation qualitatively. This figure is reproduced from Fig. 3 of Conrad & Reimer (2017).

cosmology.

## 1.2.2 WIMPs as dark matter

Dark matter could be a particle with a finite decay lifetime. In this case we require a relatively stable particle with a lifetime longer than the age of the Universe. The most plausible candidate for dark matter particles are weakly interacting massive particles (WIMPs). After inflation, all the particles were in close contact with the rest of the cosmic plasma at high temperatures. However, as the temperature dropped below their mass scale, the particles experienced a phase so-called freeze-out, where they became unable to annihilate and maintain the abundance in equilibrium. Here we summarize the relic density of dark matter as particles such as WIMPs.

In the generic WIMP scenario, two heavy particles  $W$  can annihilate producing two light (essentially massless) particles (here note as  $l$ ). The light particles are assumed to be very tightly coupled to the cosmic plasma, so they are in complete equilibrium with  $n_l = n_l^{\text{eq}}$ .

Then we use the Boltzmann equation to solve the abundance of dark matter particle  $n_W$ ;

$$a^{-3} \frac{d(n_W a^3)}{dt} = \langle \sigma v \rangle \{ (n_W^{\text{eq}})^2 - n_W^2 \}, \quad (1.40)$$

where  $\sigma v$  is the annihilation cross section times the relative velocity averaged with the velocity distribution function. This equation indicates the balance between the annihilation and creation of particles under the expansion of the Universe. Here we rewrite this equation with  $Y \equiv n_W/T^3$  and  $Y_{\text{eq}} \equiv n_W^{\text{eq}}/T^3$ ;

$$\frac{dY}{dt} = T^3 \langle \sigma v \rangle \{ (Y_{\text{eq}}^2)^2 - Y^2 \}, \quad (1.41)$$

where  $T$  is the temperature of thermal equilibrium. We also introduce the following the mass of the dark matter particle  $m$  and introduce  $x \equiv m/T$ . In this case,  $Y \simeq Y_{\text{eq}}$  at  $x \ll 1$ , and  $Y_{\text{eq}}$  is exponentially suppressed at large  $x$ , Then we can obtain the following equation during radiation dominated universe;

$$\frac{dY}{dx} = -\frac{\lambda}{x^2} \{ (Y_{\text{eq}}^2)^2 - Y^2 \}, \quad (1.42)$$

where  $\lambda = m^3 \langle \sigma v \rangle / H(m)$ . Here we can make use of our understanding of the freeze-out process to get an analytic expression for the final freeze-out abundance  $Y_\infty \equiv Y(x = \infty)$ . Since  $Y$  will be much larger than  $Y_{\text{eq}}$  well after freeze-out, dark matter particles will not be able to annihilate fast enough to maintain equilibrium at late time  $x \rightarrow \infty$  Then the analytic approximation of  $Y_\infty$  at the late times to get

$$Y_\infty = -\frac{x_f}{\lambda}, \quad (1.43)$$

where  $x_f$  is the epoch of freeze-out, and  $x_f \sim 10$  for dark matter particles.

After the freeze-out, the number density of dark matter particles simply falls off as  $a^{-3}$ . So its energy density today is equal to  $m(a_1/a_0)^3$  times its number density, where  $a_1$  corresponds to a time sufficiently late that  $Y$  has reached its asymptotic value  $Y_\infty$ . As the number density at that time is  $Y_\infty T_1^3$ ,

$$\rho_W = m Y_\infty T_0^3 \left( \frac{a_1 T_1}{a_0 T_0} \right) \equiv \frac{m Y_\infty T_0^3}{30}. \quad (1.44)$$

Then the fraction of critical density today contributed by dark matter particle W would be

$$\Omega_W = \frac{x_f}{\lambda} \frac{mT_0^3}{30\rho_{\text{cr}}} = \frac{H(m)x_fT_0^3}{30m^2\langle\sigma v\rangle\rho_{\text{cr}}}, \quad (1.45)$$

where  $\rho \equiv g_* \frac{\pi^2}{30} T^4$  is the energy density in the radiational era, and  $g_*$  is the effective numbers of relativistic degrees of freedom. By normalizing  $g_*(m)$  and  $x_f$  with their nominal values at the temperatures of interest for dark matter production,

$$\Omega_W = \left[ \frac{4\pi^3 G g_*(m)}{45} \right] \frac{x_f T_0^3}{30\langle\sigma v\rangle\rho_{\text{cr}}} \quad (1.46)$$

$$= 0.3h^{-2} \left( \frac{x_f}{10} \right) \left( \frac{g_*(m)}{100} \right)^{1/2} \frac{10^{-37} \text{cm}^2}{\langle\sigma v\rangle}. \quad (1.47)$$

This indicates that roughly cross sections of order  $10^{-40}$  are needed to get the dark matter abundance observed today. Such small cross sections emerge naturally in extensions of the Standard Model of particle physics, such as supersymmetry models. Even with these small cross sections, the interaction with WIMPs may have implications on astrophysical scales, and imprint upon the properties of luminous matter. For example, self-annihilation of WIMPs can result in the emission of standard model particles such as gamma rays, neutrinos, or electrons/positrons. Several indirect dark matter searches are performed based on this strategy, and current constraints are given in the Fig. 1.5. Also, direct search by accelerator experiments have been intensively going on, and may also be tested in the near future.

### 1.2.3 Dark matter as astrophysical compact objects

As discussed in the previous section, particle dark matter such as WIMPs are one of the feasible candidates of dark matter. However, none of particle candidates have been detected today either by the direct or indirect experiments. On the other hand, there exists another form of dark matter candidate as compact object in the Galactic halo. Here we briefly review feasible candidates of dark matter as compact objects.

- **Massive compact halo objects (MACHOs)**

One of the well-known type of compact dark matter is called as massive compact halo object (MACHO). MACHOs are generally composed by stellar remnants such as brown dwarfs, white dwarfs, neutron stars, and stellar black holes. Previous microlensing surveys towards Large Magellanic Cloud conclude that MACHOs can contribute up to

20% of the mass of Galactic halo (Alcock et al. 2000).

- **Primordial black holes (PBHs)**

One alternative candidate for non-baryonic dark matter is MACHO consisted of primordial black hole (PBH). PBHs have been proposed to be formed by primordial perturbation at inflation epoch (Hawking 1974). Since they were created before the Big Bang Nucleosynthesis (BBN), they are not counted for the baryon budget afterwards. Hence there is no limit on the amount of PBHs created before BBN, and it is possible for them to constitute the whole dark matter in the Universe.

- **Ultracompact minihalos (UCMHs)**

Ultracompact minihalos (UCMHs) have been proposed as a form of high density dark matter structure. UCMHs are proposed to be produced by large-amplitude overdensities ( $\delta \sim 10^{-3}$ ) in the early universe, and collapsed shortly after matter-radiation equality. Because of the formation in this early epoch, UCMHs form by almost pure radial infall; this formation scenario then lead to a steeper density profile ( $\rho \propto r^{-9/4}$ ) compared to that of the NFW halo profile ( $\rho \propto r^{-1}$ ) (Bringmann & Weniger 2012). These extremely dense cores are expected to exhibit large amounts of dark matter annihilation, even when a small fraction of dark matter is contained within UCMHs. They can release significant amount of energy via annihilation, which potentially affects the history of structure formation in the Universe .

## 1.3 Primordial black hole as dark matter

In this section we focus on primordial black hole as dark matter candidate, and look into the basic properties and possibility of detection. We first briefly review the theoretical properties of primordial black holes, and give a brief history to put constraints on the abundance of primordial black holes. We refer to Carr et al. (2016) and Sasaki et al. (2018) for more detail.

### 1.3.1 Formation mechanism

Until now, several different mechanisms have been proposed to form PBHs, for example from cosmic string loops (Hawking 1989; Polnarev & Zembowicz 1991; Garriga & Vilenkin 1993), vacuums bubble collisions (Garriga et al. 2016; Deng & Vilenkin 2017), and domain walls (Garriga et al. 2016; Deng et al. 2017). The most frequently studied PBH formation scenario is a gravitational collapse of the overdense region in the early Universe.

In the context of PBH formation, we generally consider a density perturbation that is initially super-horizon. The perturbation is small in the super-horizon limit, and thus can be treated as a linear perturbation. As the universe evolves and the horizon grows, the perturbation grows and quickly becomes non-linear. Once the perturbation reenters the horizon, it will typically either quickly collapse or dissipate. In this situation, if the density contrast is very close to critical, a highly overdense region would gravitationally collapse to form a black hole, directly.

In the following we briefly review the formation condition of the PBHs from the collapse of large density perturbations. Here we consider a locally perturbed region that would eventually collapse to a black hole. As discussed in the Section 1.1.1, the background spacetime can be well-described by the spatially-flat FLRW metric. Since an overdensed region to become black hole will be very rare in the space, it can be approximated as a spherically symmetric regions of positive curvature. Hence we can assume the following metric;

$$ds^2 = -c^2 dt^2 + a^2(t) \left\{ \frac{dr^2}{1 - Kr^2} + r^2(d\theta^2 + \sin^2\theta d\phi^2) \right\}, \quad (1.48)$$

where the time-time component of the Einstein equation can be described as:

$$H^2 + \frac{c^2 K(r)}{a^2} = \frac{8\pi G}{3c^2} \rho. \quad (1.49)$$

This equation is equivalent to the Friedmann equation with a small inhomogeneity induced by the curvature term. One could regard this as the Hamiltonian constraint on the comoving hypersurface on which the expansion rate is spatially homogeneous and isotropic. Then we can define the density contrast on the comoving hypersurface by

$$\Delta = \frac{\rho - \bar{\rho}}{\bar{\rho}} = \frac{3c^4 K}{8\pi G \bar{\rho} a^2} = \frac{c^2 K}{H^2 a^2}. \quad (1.50)$$

Here we assume  $\Delta = 1$  corresponds to the time of black hole formation  $t_c$ , because the universe stops expanding under the condition. Since a perturbation cannot collapse when it is smaller than the Jeans length, we can put a condition by  $c_s^2 k^2 / a^2 = H^2$  or  $c^2 k^2 / a^2 = 3H^2$  where  $c_s^2 = c^2/3$  holds at the radiation-dominated era;

$$1 = \Delta(t_c) = \frac{\rho - \bar{\rho}}{\bar{\rho}} = \frac{3c^4 K}{8\pi G \bar{\rho} a^2} = \frac{c^2 K}{H^2 a^2}, \quad (1.51)$$

$$\therefore c^2 K = c_s^2 k^2. \quad (1.52)$$

Hence the condition for the black hole formation can be describe as;

$$\Delta(t_k) = \frac{c^2 K}{H^2(t_k) a^2(t_k)} = \frac{c_s^2 k^2}{H^2(t_k) a^2(t_k)} \geq \Delta_c = \frac{1}{3}, \quad (1.53)$$

where  $t_k$  is the time at which  $ck/a = H$ . This tells that the PBH formation occurs when the density perturbation becomes comparable to  $1/3$ .

### 1.3.2 Theoretical properties

In the following we look into main properties of primordial black holes predicted by their formation theory.

- **Mass**

As discussed in the previous subsection, PBHs could have been produced in the early universe due to various mechanisms. For all of these, the increased cosmological energy density at early times plays a major role (Hawking 1971; Carr & Hawking 1974). This then yield a rough connection between the PBH mass and the horizon mass at formation time:

$$M_{\text{PBH}} \sim \frac{c^3 t}{G} \sim 10^{15} \left( \frac{t}{10^{-23} \text{sec}} \right) \text{g}. \quad (1.54)$$

Hence PBHs could span an enormous mass range: those formed at the Planck time ( $10^{-43} \text{sec}$ ) would have the Planck mass ( $10^{-5} \text{g}$ ), whereas those formed at  $1 \text{sec}$  would be as large as  $10^5 M_\odot$ , comparable to the mass of the black holes thought to reside in galactic nuclei. Note that the situation is quite different for the black holes forming at the present epoch; for example, black holes formed in the final stages of stellar evolution can never be smaller than around  $1 M_\odot$ .

- **Evaporation**

Primordial back holes give out thermal radiation known as Hawking radiation, and will eventually evaporate. Hawking (1971) predicts that lighter black holes emit more radiation, and thus evaporate faster. The mass threshold of PBHs which have evaporated by the cosmic age  $t_0$  is given by

$$M_c \simeq \left( \frac{3\hbar c^4 \alpha_0}{G^2} t_0 \right)^{\frac{1}{3}} \sim 10^{15} \text{g} \left( \frac{\alpha_0}{4 \times 10^{-4}} \right)^{\frac{1}{3}} \left( \frac{t_0}{13.8 \text{Gyr}} \right)^{\frac{1}{3}}, \quad (1.55)$$

where  $\alpha_0$  is the numerical coefficient that depends on which particle species can be emitted at a significant rate (Page 1976). This indicates that PBHs lighter than  $\simeq$

$10^{15}$  g do not exist in the present universe, and more massive PBHs will persist until today. Nevertheless, their abundance can be constrained by looking for the effects of radiation from their evaporation. For instance, PBHs in the mass range  $10^9$ - $10^{13}$ g change abundance of light elements produced by the Big Bang nucleosynthesis due to high energy particles emitted by the evaporating PBHs (Miyama & Sato 1978). Also, comparison between the observed light elements and the theoretical prediction tightly constrains the abundance of such PBHs (Carr et al. 2010).

- **Abundance**

In order to investigate the abundance of formed PBHs, it is useful look into the mass fraction of PBHs at the formation time. Assuming PBHs which form at a redshift  $z$  or time  $t$ , the mass fraction of PBHs at formation time  $\beta$  can be described as;

$$\beta = \frac{\rho_{\text{PBH}}}{\rho_{\text{tot}}} = \left(\frac{H_0}{H_{\text{form}}}\right)^2 \left(\frac{a_{\text{form}}}{a_0}\right)^{-3} \Omega_{\text{CDM}} f_{\text{PBH}}, \quad (1.56)$$

where  $f_{\text{PBH}}$  is a fraction of PBHs against the total dark matter component, and  $\Omega_{\text{CDM}}$  is a density parameter of the matter component at present, here noted “0”. If the PBHs have a monochromatic mass function, we can determine this relationship more precisely for the standard  $\Lambda$ CDM model by Carr et al. (2010) and Carr (1975);

$$\beta = \frac{MN_{\text{PBH}}(t_i)}{\rho_{\text{tot}}(t_i)} \sim 3.7 \times 10^{-9} \gamma^{-1/2} \left(\frac{g_{*,\text{form}}}{10.75}\right)^{1/4} \left(\frac{M_{\text{PBH}}}{M_{\odot}}\right)^{1/2} f_{\text{PBH}}, \quad (1.57)$$

where  $\gamma$  is a numerical factor which depends on the details of gravitational collapse, and  $g_{*,\text{form}}$  is the number of relativistic degrees of freedom at PBH formation. We also applied the relation  $M_{\text{PBH}} = \gamma M_{\text{horizon}} \simeq \gamma(1/2G)H_{\text{form}}^{-1}$ , as given in Carr et al. (2010). Thus, for each mass of PBHs, the observational constraint on PBH fraction  $f_{\text{PBH}}$  can be interpreted as that on mass fraction at formation time  $\beta$ .

### 1.3.3 Possible observational imprints

As discussed in the previous subsection, observational constraints on the abundance of PBHs can be crucial when testing any early universe models which predict the PBH formation. In the following we review the possible observational imprints on the abundance of primordial black holes.

- **Gravitational lensing**

Gravitational lensing is a powerful tool to probe primordial black holes. One strong

point of the lensing signals is that they are based only on the gravitational physics; thus lensing is free from uncertainties which exist in the other effects resulting from electromagnetic interactions. Many studies to search lensing signals by PBHs has been based on gravitational microlensing technique. If PBHs exists in the current Universe, we can probe them through magnification effect on the background objects such as stars. Following the first proposal by Paczynski (1986), many constraints on PBH abundance have been obtained by targeting at dense stellar fields such as in the Galactic center and the Large Magellanic Cloud. Various possibilities of microlensing events have also been investigated, ranging from distant quasars, radio sources to intra-cluster stars.

- **Dynamical effects**

To a certain degree, PBHs can affect any astrophysical system by their gravitational interactions. By appropriately evaluating the impact of PBHs on the astrophysical systems, it is possible to put upper limit on the PBH fraction.

One example comes from disruption of astrophysical objects by PBHs. Once the PBH lies inside the object such as white dwarfs, it quickly accretes the nuclear matter and destroys the object. Thus, such object must not be exposed to frequent encounters with the PBHs, from which we can constrain the PBH abundance by studying the observational abundance of the astrophysical objects today. The possible constraints on PBHs have been investigated for various astrophysical objects such as white dwarfs, neutron stars, halo binaries, globular clusters.

Dynamical effects of PBHs can also have imprints on the properties of the Galactic structure. If the Galactic halo is entirely or partially composed of massive PBHs, some of them must be in the region near the Galactic center. Such PBHs receive strong dynamical friction from the stars and the dark matter in the form of lighter PBHs or elementary particles, lose their kinetic energy and spiral in to the center. Hence an upper limit on the mass in the Galactic center can be translated into the fraction of PBHs in the Galactic halo. We can also constrain the PBH abundance by studying the observed velocity of the Galactic disk, which can be increased by the passing of PBHs.

- **Radiation from accreting matter**

Accretion of gas onto the PBHs can have some impact on the constraint of the PBH abundance. Although we require some assumptions or observational empirical rules for the calculation, we can derive the PBH constraint based on the two different processes;

the accretion effects that arise in the very early Universe, and the electromagnetic waves from the accreted matter onto the PBHs.

The former effect induces the CMB spectral distortions since photons produced by the accreting PBHs are not completely thermalized. Photons generated in the redshift  $5 \times 10^4 < z < 2 \times 10^6$  yields the  $\mu$ -distortion, where photons became in the kinetic equilibrium state and thus produced the non-vanishing chemical potential. We can put upper limit in the corresponding redshift where the photon-number changing process became efficient to make the distribution Planckian, while lower limit is obtained from the period where the kinetic equilibrium is no longer maintained. Another distortion is caused by photons generated in the redshift  $200 < z < 5 \times 10^4$ , where the baryonic gas decouples from the CMB and induce the Compton- $y$  distortion at the corresponding temperature. Note that both the  $\mu$  and  $y$ -distortions from these accretions onto the PBHs have too small amplitudes to be relevant to present and future observations (Ali-Haïmoud & Kamionkowski 2017).

On the other hand, the accreted matter to the PBHs after CMB decoupling could have a profound effect on the thermal history of the Universe (Ricotti et al. 2008). The Bondi-type accretion of surrounding gas onto PBHs and its associated emission of radiation are proposed to modify the standard ionization history. Two main mechanisms of ionization discussed here are achieved by either the collisional ionization or the photoionization. The increase of the ionization fraction associated with these mechanisms can enhance the CMB optical depth, which results in the damping of the small scale CMB fluctuations, and the enhancement of the polarization power on large angular scales. The accretion can also shift the redshift of the last scattering, which changes the phase of the acoustic oscillations in the CMB spectrum.

- **Growth of large scale structure**

Sufficiently large PBHs could have important consequences for large-scale structure formation. Assuming that PBHs were randomly distributed in space in the early Universe, they generate primordial density perturbations by their Poisson fluctuations on scales larger than the mean distance of PBHs. Since the Poisson fluctuations in the number of PBHs can enhance the dark matter perturbations on small scales, statistical properties of optical depth in the baryons are also expected to encode those inhomogeneity. The possible impact on the Ly $\alpha$  forest observations was investigated in Afshordi et al. (2003), which allows us to probe matter perturbations on small scales down to  $\sim$ Mpc, where the minimum scale is determined by the thermal broadening of the spectra of the Ly $\alpha$  forest.

- **Gravitational wave**

The thing which recently kicked off the recent interest in the primordial black hole study is the detection of gravitational wave by LIGO experiment. LIGO has detected gravitational waves from mergers of  $\sim 10M_{\odot}$  black holes, and so far reported five merger events for them. Thus it is important to reveal their properties to see if those mergers are caused by black holes with primordial origin. Gravitational-wave observations provide a novel tool to probe PBHs independently of the electromagnetic observations, irrespective of whether the observed mergers of BH binaries are attributed to PBHs or not. The formation theory of PBH binary indicates that  $30M_{\odot}$ - $30M_{\odot}$  PBH binaries, which are formed in the radiation dominated era, merge with frequency consistent with the one estimated by the LIGO observations if  $f_{\text{PBH}} \sim 10^{-3}$  (Nakamura et al. 1997).

The dynamical effects of PBH collisions on astronomical objects have also been a subject of long-standing interest for gravitational-wave observatories in space. For example, eLISA has potential to detect the dynamical effects of PBHs in the mass range  $10^{14}$ - $10^{20}$ g directly, by measuring the gravitational impulse induced by them when passing nearby (Adams & Bloom 2004; Seto & Cooray 2004).

### 1.3.4 Brief history of observational constraints

Since the proposal of primordial black holes by Hawking (1971), there has been many attempts to prove the abundance of primordial black holes, both theoretically and experimentally. Although some constraints, especially those from star formation scenario and globular cluster abundance, include some ambiguity because of their multiple assumptions on models, we can almost close the entire mass window, except for a unexplored mass window of  $M_{\text{PBH}} = [10^{-14}, 10^{-9}] M_{\odot}$ . In this section we overview the major efforts that contribute to the current constraints on the abundance of primordial black holes.

- **Hawking radiation**

As proposed in Hawking (1974), PBHs emit radiation at a rate inversely proportional to their mass. This Hawking radiation causes PBHs to evaporate, and light candidates in mass range of  $m_{\text{BH}} < 5 \times 10^{14}$ g cannot exist as a candidate of dark matter today (Page & Hawking 1976). Also, PBHs slightly heavier than this mass limit are expected to emit  $\gamma$ -ray around 100MeV. Thus the observation of extra galactic  $\gamma$ -ray background can constrain the cosmic density of PBH. Current constraint is achieved from the Energetic Gamma Ray Experiment Telescope (EGRET) as  $\Omega_{\text{PBH}} \leq 10^{-9}$  for  $m_{\text{BH}} = 10^{15}$ g (Sreekumar et al. 1998; Carr et al. 2010). In summary, PBH of  $m_{\text{BH}} \leq 10^{16}$ g

cannot constitute dark matter more than 1%, and that of  $m_{\text{BH}} \geq 7 \times 10^{16} \text{g}$  disappears due to Hawking radiation.

- **CMB (WMAP3, FIRAS)**

The early energy injection by PBHs may produce observable distortions of the CMB spectrum (Battistelli et al. 2000) and may also affect CMB anisotropies (Ricotti et al. 2008). For example, cosmological parameter estimates from CMB observations are affected because models with PBHs allow for larger values of the Thomson scattering optical depth, whose correlation with other parameters may not be correctly taken into account when PBHs are ignored. This may modify the cosmic recombination history, and hence lead to  $\mu$  and  $y$ -distortions. The constraint displayed in Fig. 1.6 is given by WMAP3 and FIRAS experiments (Ali-Haïmoud & Kamionkowski 2017; Ricotti et al. 2008)

- **Caustic crossing**

Given the drastic change of lensing properties near the critical curve, it has been argued that caustic crossing events in giant arcs of clusters may serve as a powerful probe of a range of dark matter scenarios such as PBHs and scalar field dark matter. Recently discovery of a fast transient event MACS J1149 Lensed Star 1 (LS1) provoked a constraint on PBH abundance by taking advantage of this method (Oguri et al. 2018). This event is interpreted as a highly magnified image of an single star in the vicinity of critical curves of massive galaxy clusters. In this caustic crossing event, stars that are closer to the critical curve can have higher magnifications. The magnification saturates when the distance to the caustic becomes comparable to the size of the source in the source plane. However, the high fraction of compact dark matter leads to significant saturation at the position of MACS J1149 LS1, which effectively reduces the macro model magnification at that position. The LS1 caustic crossing event team discuss the constraint on the compact dark matter, by assuming that the MACS J1149 LS1 is produced by an intra-cluster light star. By analyzing peak magnitude and source radius of the event, they put constraint as in Fig. 1.6.

- **Microlensing (MACHO, EROS, Kepler)**

Two representative microlensing projects which have put constraint on the mass fraction of PBHs are the EROS + MACHO collaboration and the Kepler mission (Alcock et al. 1998; Tisserand et al. 2007; Griest et al. 2014). They put constraint on the abundance of PBHs from the null detection of microlensing events of PBHs, in the same way as our observation adopts. The strongest constraint comes from the MACHO project,

where they search for microlensing events with timescale longer than a few days in the Large Magellanic Cloud. The mission of Kepler satellite, on the other hand, targets at events with a-few-hour timescale in the Cygnus-Lyra region which have sensitivity to PBH DM in the mass range of  $10^{-9}M_{\odot}$  to  $10^{-7}M_{\odot}$ . The Kepler mission has large advantages on precise photometry and longer time-allocation, and current constraint is obtained by 2 year observation.

- **Femtolensing**

Femtolensing is a type of gravitational lensing effect caused by PBHs, named after the very small separation of lens images. As Schwarzschild radius of PBHs are as large as the wavelength of photons, one needs to consider radiative electromagnetic properties in femtolensing regime, where interference patterns are expected to show up in the energy power spectrum of the lensed object. Therefore the abundance of PBHs can be constrained by the event rate of femtolensing effect, in the same way as we adopt for microlensing study. The current constraint described in Fig. 1.6 is derived from the search of femtolensing by compact objects, sensitive to PBH of  $m_{\text{BH}} \geq 10^{19} - 10^{20}\text{g}$  by combing the Fermi satellite GRB data and redshift data (Barnacka et al. 2012).

Following shows constraints under discussion which require some uncertain assumptions;

- **Star formation**

During their star-formation epoch, dark matter is trapped by stars due to the adiabatic contraction. If PBHs exist as kind of dark matter, they should be also trapped by compact stars such as white dwarf or neutron stars. As the matter accretion rate to PBH is expected to be very fast, compact stars including PBHs are in fate be destroyed (Kouvaris & Tinyakov 2011a; Kouvaris 2012; Kouvaris & Tinyakov 2011b). Therefore the capture process of PBH needs to be very small for the star remnant compacts, stars after the phase of white dwarf, to be observed up to data. The constraint of PBH abundance here is derived from the observation of globular clusters, where the density of dark matter is relatively high and have small velocity. By considering the scenario of destruction, the amount of PBH with typical mass is constrained by the dark matter distribution during the formation epoch of globular cluster; represented by the current number of compact stars. This constraint is sensitive to PBHs in mass range of  $10^{16}\text{g} \leq m_{\text{BH}} \leq 3 \times 10^{22}\text{g}$  (Capela et al. 2013b).

- **Neutron stars in globular cluster**

One can also apply the star formation scenario for the current abundance of dark matter

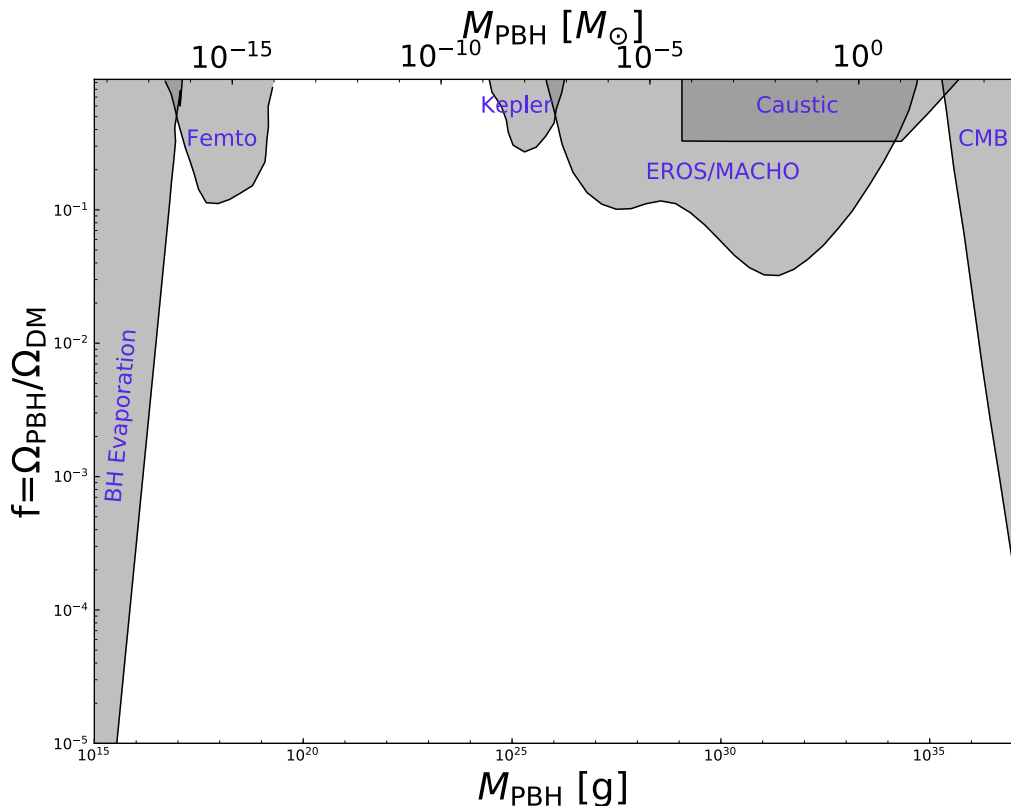


Figure 1.6: The 95% C.L. upper bound on the PBH mass fraction to DM from previous observational constraints (gray shaded regions): extragalactic  $\gamma$ -rays from PBH evaporation (Carr et al. 2010), femtolensing of  $\gamma$ -ray burst (“Femto”) (Barnacka et al. 2012), microlensing search of stars from the satellite 2-years Kepler data (“Kepler”) (Griest et al. 2014), MACHO/EROS/OGLE microlensing of stars (“EROS/MACHO”) (Tisserand et al. 2007), microlensing by caustic crossing event (“Caustic”) (Oguri et al. 2018), and the accretion effects on the CMB observables (“CMB”) (Ali-Haïmoud & Kamionkowski 2017), updated from the earlier estimate (Ricotti et al. 2008).

in globular clusters. The current amount of PBHs in compact objects is expected to be small enough to avoid the capture process. Strong constraint can be achieved from the dense core of globular clusters by comparing the direct capture mechanism of neutron stars with the corresponding numerical simulation. Fig. 1.6 shows constraint from Capela et al. (2013a), sensitive to PBH mass range of  $3 \times 10^{18} \text{g} \leq m_{\text{BH}} \leq 10^{24} \text{g}$ . The dark matter density derived from the model indicates that the abundance of PBH in this mass range is less than 5%.

## 1.4 Objective of this thesis

This thesis presents microlensing study to search for dark matter candidate called primordial black hole (PBH). Primordial black holes (PBHs) have long been suggested as a viable candidate for the elusive dark matter (DM). The abundance of such PBHs has been constrained using a number of astrophysical observations, except for a hitherto unexplored mass window of  $M_{\text{PBH}} = [10^{-14}, 10^{-9}]M_{\odot}$ .

We especially focus on two possible observational cases, where all the dark matter in the Galactic halo are composed by either (I) in the range  $[10^{-11}, 10^{-6}]M_{\odot}$  or (II) Earth-mass ( $10^{-6}M_{\odot}$ ) scale black holes. In the part (I) of my thesis, we investigated microlensing events in the disk region of Andromeda Galaxy (M31). There exists unexplored mass window for PBHs with  $M_{\text{PBH}} = [10^{-16}, 10^{-9}]M_{\odot}$ , which can occupy the entire dark matter halo of our Galaxy. In order to explore this mass window by microlensing observation, we require frequent photometry of many stars with cadence shorter than 10 minutes. Here we propose microlensing search by taking advantage of many stars in M31. We performed one-night observations in 2014 and 2017, and took images every two minutes with the Subaru Hyper Suprime-Cam (HSC). We developed an image difference technique to detect time-variable objects, and performed microlensing analysis of these data to set the stringent upper limit on the abundance of PBHs, targeting at the sub-lunar mass scale.

In the part (II) of this thesis we consider microlensing events with longer duration than Part (I). We constrained the abundance of primordial black holes (PBH) using 2622 microlensing events obtained from 5-years observations of stars in the Galactic bulge by the Optical Gravitational Lensing Experiment (OGLE). The majority of microlensing events display a single or at least continuous population that has a peak around the light curve timescale  $t_{\text{E}} \simeq 20$  days and a wide distribution over the range  $t_{\text{E}} \simeq [1, 300]$  days, while the data also indicates a second population of 6 ultrashort-timescale events in  $t_{\text{E}} \simeq [0.1, 0.3]$  days, which are advocated to be due to free-floating planets. We confirmed that the main population of OGLE events can be well modeled by microlensing due to brown dwarfs, main sequence stars and stellar remnants (white dwarfs and neutron stars) in the standard Galactic bulge and disk models for their spatial and velocity distributions. Using the dark matter (DM) model for the Milky Way (MW) halo relative to the Galactic bulge/disk models, we obtained the tightest upper bound on the PBH abundance in the mass range  $M_{\text{PBH}} \simeq [10^{-6}, 10^{-3}]M_{\odot}$  (Earth-Jupiter mass range), *if* we employ “null hypothesis” that the OGLE data does not contain any PBH microlensing event. More interestingly, we also showed that Earth-mass PBHs can well reproduce the 6 ultrashort-timescale events, without the need of free-floating

planets, if the mass fraction of PBH to DM is at a per cent level.

The rest of this thesis is organized as follows: In Chapter 2 we briefly review the property of gravitational lensing. Chapter 3 and Chapter 4 describes the part (I) of this thesis. In Chapter 3 we describe the details of our microlensing study of M31 with HSC, based on one night data taken in 2014. In Chapter 4, we discuss the time-variability of one remaining microlensing candidate detected in Chapter 3, and also update the PBH constraint by analyzing the new microlensing observation of M31 performed in 2017 with HSC. In Chapter 5 we describe the implications regarding the part (II) study, and give the summary in Chapter 6.

# Chapter 2

## Gravitational lensing

In the picture of modern observational cosmology, the evolution of overdensities in the initial cosmic density field leads to the formation of cosmic structures such as galaxy clusters. Recent development of observational techniques have enabled us to unveil the unique characteristics around these massive structures; among them noted are distortion and magnification effects of objects lying behind them. These features are caused by distorted light path in the foreground gravitational field, originally predicted by general relativity, and called as gravitational lensing effect. In the following we describe the basic properties of gravitational lensing, and give brief summary of observational characteristics.

### 2.1 Theory

General relativity describes the distortion of light path in the gravitational field. In the following we describe the behavior of light path.

#### 2.1.1 Light path in the unperturbed metric

In this section we describe the deflection angle in the spherically symmetric gravitational field, following the method of Futamase (1995). Since the general relativity predicts the light path as Schwarzschild metric, we consider the following geodesic equation without perturbation:

$$ds^2 = 0 \iff 2K \equiv \left(1 - \frac{2m}{r}\right) \dot{t}^2 - \left(1 - \frac{2m}{r}\right)^{-1} \dot{r}^2 - r^2 \dot{\theta}^2 - r^2 \sin^2 \theta \dot{\phi}^2 = 0, \quad (2.1)$$

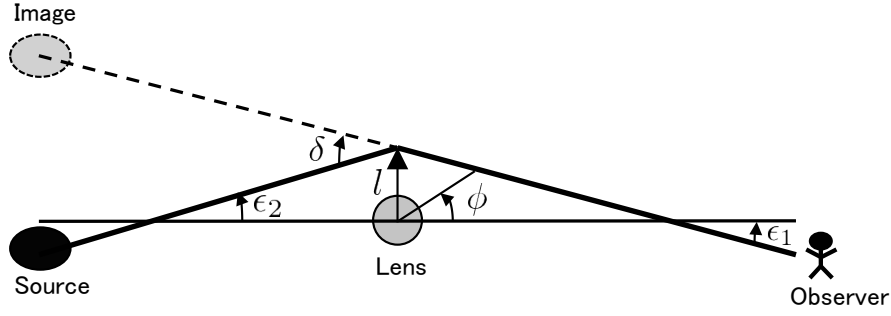


Figure 2.1: A simple schematic representation of gravitational lensing effect describing the deflection of light path around massive object.

where  $\cdot$  is the differential derivative with affine parameter  $s$ . We adopt the variational calculus using the Euler-Lagrange equation:

$$\frac{\partial K}{\partial x^\alpha} - \frac{d}{ds} \left( \frac{\partial K}{\partial \dot{x}^\alpha} \right) = 0, \quad (2.2)$$

where the four variable  $x^0 = t(x)$ ,  $x^1 = r(s)$ ,  $x^2 = \theta(s)$ ,  $x^3 = \phi(s)$ . Combining  $\alpha = 0, 2, 3$  cases with Eq. (2.1):

$$\alpha = 0: \quad \frac{d}{ds} \left( \left( 1 - \frac{2m}{r} \right) \dot{t} \right) = 0, \quad (2.3)$$

$$\alpha = 2: \quad \frac{d}{ds} (r^2 \dot{\theta}) - r^2 \sin \theta \cos \theta \dot{\phi}^2 = 0, \quad (2.4)$$

$$\alpha = 3: \quad \frac{d}{ds} (r^2 \sin^2 \theta \dot{\phi}) = 0. \quad (2.5)$$

Here we consider the motion in the  $\theta = \pi/2$  plane. If  $\dot{\theta} = 0$  holds in this plane, the motion is within this plane because  $\ddot{\theta} = 0$ , and higher-order derivative also becomes zero from Eq. (2.4). Integrating Eq. (2.5) makes preservation of angular momentum equation,

$$r^2 \dot{\phi} = h, \quad (2.6)$$

where  $h$  is constant. Similarly integrating Eq. (2.3) makes:

$$\left( 1 - \frac{2m}{r} \right) \dot{t} = k, \quad (2.7)$$

where  $k$  is constant. Putting this equation into Eq. (2.1) becomes:

$$\left(1 - \frac{2m}{r}\right)^{-1} k^2 - \left(1 - \frac{2m}{r}\right)^{-1} \dot{r}^2 - r^2 \dot{\phi}^2 = 0. \quad (2.8)$$

Also  $r$  in Eq. (2.6) can be transform by  $u = 1/r$  as:

$$\dot{r} = \frac{d}{ds} \left( \frac{1}{u} \right) = -\frac{1}{u^2} \dot{u} = -\frac{1}{u^2} \frac{du}{d\phi} \dot{\phi} = -h \frac{du}{d\phi}. \quad (2.9)$$

Putting Eq. (2.6) and Eq. (2.8) into Eq. (2.9) becomes

$$\left( \frac{du}{d\phi} \right)^2 + u^2 = \frac{k^2}{h^2} + 2mu^3. \quad (2.10)$$

Then differentiating this equation with  $\phi$  describes a light path projected to a  $t = \text{const.}$  plane,

$$\frac{d^2u}{d\phi^2} + u = 3mu^2. \quad (2.11)$$

Since  $m = 0$  holds in the limit of the special relativity theory, the general solution can be described as:

$$u = \frac{1}{l} \sin(\phi - \phi_0). \quad (2.12)$$

This solution has the same form with Newtonian prediction, which expresses the straight line from  $\phi_0$  to  $\phi_0 + \pi$  where  $l = \text{const.}$  Thus the light path in the Schwarzschild metric can be considered as the perturbed form of the special case. Then the solution of Eq. (2.11) can be written as

$$u = u_0 + 3mu_1, \quad (2.13)$$

where  $u_0$  is Eq. (2.12) in the limit that  $mu$  is small enough, and  $\phi_0 = 0$ . Putting Eq. (2.13) into Eq. (2.11) and neglecting terms with order higher than  $O(mu)$  becomes

$$\frac{d^2u_1}{d\phi^2} + u_1 = u_0^2 = \frac{\sin^2\phi}{l^2}. \quad (2.14)$$

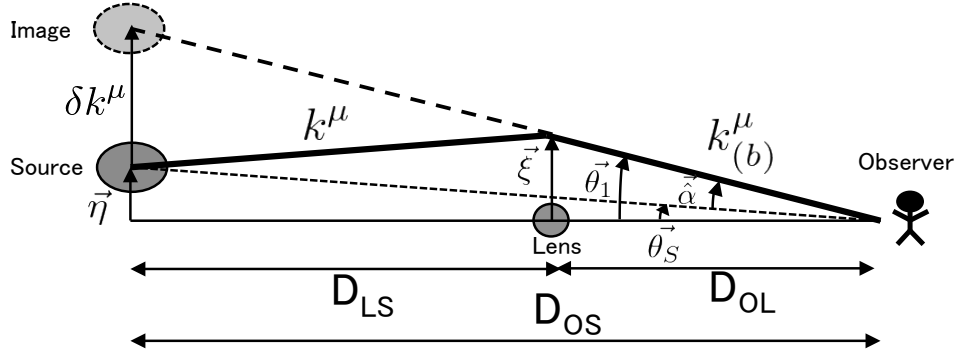


Figure 2.2: Gravitational lensing scheme. The bold line describes the light path from the source object (left) to the observer (right), bent around the gravitational field of the lens (middle).

Therefore, general solution of Eq. (2.11) is:

$$u = \frac{\sin\phi}{l} + \frac{m(1 + C\cos\phi + \cos^2\phi)}{l^2}, \quad (2.15)$$

where we assume  $m/l$  is small.

Next we look into deflection angle  $\delta$  in spherically symmetric gravitational field. Considering the case of  $r \rightarrow \text{inf}$ , where  $u \rightarrow 0$  and the right side of Eq. (2.15) becomes zero. Then we denote the values of asymptote angle  $\phi$  as  $-\epsilon_1$  and  $\pi + \epsilon_2$ , as shown in the Fig. 2.1. In the limit of  $\epsilon_1, \epsilon_2 \rightarrow 0$ , Eq. (2.15) gets to;

$$\begin{aligned} -\frac{\epsilon_1}{l} + \frac{m(2+C)}{l^2} &= 0, \\ -\frac{\epsilon_2}{l} + \frac{m(2+C)}{l^2} &= 0, \\ \therefore \delta = \epsilon_1 + \epsilon_2 &= \frac{4m}{l}. \end{aligned} \quad (2.16)$$

If we explicitly write the gravitational constant  $G$  and light velocity  $c$ , the deflection angle can be written as:

$$\delta = \frac{4Gm}{c^2 l}. \quad (2.17)$$

## 2.1.2 Light path in the perturbed metric

### (1) Lens equation

Here we consider a case where gravitational potential  $\Phi$  is small. In this case, the

metric of inhomogeneously expanding universe can be described as:

$$ds^2 = - \left(1 + \frac{2\Phi}{c^2}\right) c^2 dt^2 + a^2(t) \left(1 - \frac{2\Phi}{c^2}\right) [d\chi^2 + r^2(\chi)d\theta^2], \quad (2.18)$$

where  $d\chi = dr^2/1 - Kr^2$ , and  $d\theta^2 \simeq (d\theta^1)^2 + (d\theta^2)^2$  for distant galaxies. Considering a light path at  $x^i = (\theta^1, \theta^2, \chi)$ , then the derivative of affine parameter can be described as:

$$\frac{d}{d\lambda} = \frac{d\chi}{dx^0} \frac{dx^0}{d\lambda} \frac{d}{d\chi} = -\frac{P^0}{a} \frac{d}{d\chi}, \quad (2.19)$$

where  $P^0 = dx^0/d\lambda$ . Thus perturbed part of geodesic equation  $dk^\mu/d\lambda + \Gamma_{\alpha\beta}^\mu k^\alpha k^\beta = 0$  for  $k^\mu = k_{(b)}^\mu + \delta k^\mu$  can be reduced to the first order of  $\theta^1, \theta^2$  and  $\Phi/c^2$  in Taylor expansion (e.g. Schneider et al. (1992)):

$$\frac{d^2(r\theta^i)}{d\chi^2} + Kr\theta^i = -\frac{2}{c^2} \frac{\partial\Phi}{\partial(r\theta^i)}. \quad (2.20)$$

Therefore the solution is described as:

$$\theta_S^i = \theta^i - \hat{\alpha}^i, \quad (2.21)$$

$$\hat{\alpha}^i = \frac{2}{c^2} \int_0^\chi d\chi' \partial_i \Phi(\chi') \frac{r(\chi - \chi')}{r(\chi)}, \quad (2.22)$$

where  $\theta_S^i$  represents the position of the source image without lensing effect as in Fig. 2.2, and  $\chi$  is the position of the source. This is a general expression of the lens equation, and  $\hat{\alpha}$  is the deflection angle. In the following we adopt some approximation to describe the basic properties.

#### ◇ Thin lens approximation

Here we adopt so-called thin-lens approximation; the case where the light deflects within a sufficient small region compared to the distance between the source and the observer. In this approximation the deflection angle  $\hat{\alpha}$  can be described as:

$$\begin{aligned} \hat{\alpha}^i &\simeq \frac{2}{c^2} \frac{r(\chi - \chi')}{r(\chi)} \int_0^\chi d\chi' \partial_i \Phi(\chi') \\ &\simeq -\frac{2G}{c^2} \frac{r(\chi - \chi')}{r(\chi)} \int_{-\infty}^\infty dz \partial_i \int d\xi' dz' \frac{\rho(\vec{x})}{\sqrt{|\vec{\xi} - \vec{\xi}'|^2 + |z - z'|^2}} \\ &\simeq \frac{4G}{c^2} \frac{r(\chi - \chi')}{r(\chi)} \int d^2\xi' \frac{\vec{\xi} - \vec{\xi}'}{|\vec{\xi} - \vec{\xi}'|^2} \Sigma(\vec{\xi}'), \end{aligned} \quad (2.23)$$

where we rewrite the gravitational potential as:

$$\Phi(\vec{x}) = -G\bar{\rho} \int d^3x' \frac{\vec{x} - \vec{x}'}{|\vec{x} - \vec{x}'|^2} \delta(\vec{x}), \quad (2.24)$$

and the surface mass density as  $\Sigma(\vec{\xi}) = \int_{-\infty}^{\infty} dz \rho(\vec{x})$ . In this description we assume  $\rho(\vec{x}) \gg \bar{\rho}$ , and  $\chi$  and  $\chi'$  are the position of the source and lens respectively. Then according to Fig. 2.2, we can substitute the angular diameter distance  $D_A$  for  $r(\chi)$  and  $\vec{\xi} = D_{\text{OL}}\vec{\theta}$ . Hence,  $\vec{\alpha}$  can be described as:

$$\begin{aligned} \vec{\alpha} &= \frac{4G D_{\text{OL}} D_{\text{LS}}}{c^2 D_{\text{OS}}} \int d^2\theta' \frac{\vec{\theta} - \vec{\theta}'}{|\vec{\theta} - \vec{\theta}'|^2} \Sigma(D_{\text{OL}}\vec{\theta}) \\ &= \frac{1}{\pi} \int d^2\theta' \frac{\vec{\theta} - \vec{\theta}'}{|\vec{\theta} - \vec{\theta}'|^2} \hat{\kappa}(D_{\text{OL}}\vec{\theta}) \Sigma(D_{\text{OL}}\vec{\theta}). \end{aligned} \quad (2.25)$$

In the second equality we conventionally adopt the following description of the critical surface mass density  $\Sigma_{\text{cr}}$  and the dimensionless surface mass density  $\hat{\kappa}(D_{\text{OL}}\vec{\theta})$ :

$$\Sigma_{\text{cr}} = \frac{c^2}{4\pi G} \frac{D_{\text{OS}}}{D_{\text{OL}} D_{\text{LS}}}, \quad (2.26)$$

$$\hat{\kappa}(D_{\text{OL}}\vec{\theta}) = \frac{\Sigma(D_{\text{OL}}\vec{\theta})}{\Sigma_{\text{cr}}}. \quad (2.27)$$

Furthermore we transfer the lens equation into dimensionless form. The lens equation can be described with quantities featured in Fig. 2.2:

$$\frac{D_{\text{OL}}}{D_{\text{OS}}}\vec{\eta} = \vec{\xi} - D_{\text{OL}}\vec{\alpha}(\vec{\xi}/D_{\text{OL}}). \quad (2.28)$$

Also we define the characteristic length  $\xi_0$ ,  $\eta_0 = \xi_0 D_{\text{OS}}/D_{\text{OL}}$  in the source plane. In this case the dimensionless lens equation can be converted with the dimensionless vector  $\vec{x} = \vec{\xi}/\xi_0$ ,  $\vec{y} = \vec{\eta}/\eta_0$  as:

$$\vec{y} = \vec{x} - \vec{\alpha}(\vec{x}), \quad (2.29)$$

$$\vec{\alpha}(\vec{x}) = \frac{1}{\pi} \int d^2x' \kappa(\vec{x}') \frac{\vec{x} - \vec{x}'}{|\vec{x} - \vec{x}'|^2}, \quad (2.30)$$

$$\kappa(\vec{x}) \equiv \hat{\kappa}(\vec{\xi}) = \frac{\Sigma(\xi_0\vec{x})}{\Sigma_{\text{cr}}} = \frac{1}{\Sigma_{\text{cr}}} \int_{-\infty}^{\infty} \rho(\vec{r}) dz. \quad (2.31)$$

◇ **Axially symmetric lens**

Here we focus on the case where lens are axially symmetric, and derive the expressions of basic lensing formulae. As for the axially symmetric mass distribution, we can rewrite  $\kappa(\vec{x}) = \kappa(x)$ , where  $|\vec{x}| = x$ . In this situation, the lens potential of the general form is described as:

$$\Phi(\vec{x}) \equiv \frac{1}{\pi} \int d^2x' \kappa(\vec{x}') \ln|\vec{x} - \vec{x}'|, \quad (2.32)$$

where the scaled deflection angle  $\alpha(x)$  is calculated using Eq. (1.20) as:

$$\vec{\alpha}(\vec{x}) = \vec{\nabla}\Phi(x) = 2\frac{\vec{x}}{x} \int_0^x dx' x' \kappa(x') \equiv \alpha(x) \frac{\vec{x}}{x}. \quad (2.33)$$

Then the integral form of Eq. (2.32) is described using (4.22) and (4.14) of Gradshcheyn & Ryzhik (1994):

$$\begin{aligned} \Phi(\vec{x}) &= \frac{1}{\pi} \int dx' \int d\phi x' \kappa(x') \ln \sqrt{x^2 + x'^2 - 2xx' \cos\phi} \\ &= 2\ln x \int_0^x dx' x' \kappa(x') + 2 \int_x^{\text{inf}} dx' x' \kappa(x') \ln x' \\ &= 2 \int_0^x dx' x' \kappa(x') \ln \left( \frac{x}{x'} \right) + \text{const.} \end{aligned} \quad (2.34)$$

Therefore the lens equation is reduced to a scalar equation under the condition of  $\vec{\alpha} \propto \vec{x}$ :

$$y = x - \alpha(x) = x - \frac{d}{dx}\Phi(x), \quad (2.35)$$

and also the Laplacian of  $\Psi$  in Eq. (2.32) can be reduced as:

$$\Delta\Phi(\vec{x}) = 2\kappa(\vec{x}). \quad (2.36)$$

## (2) Magnification, convergence and shear

In the following we discuss the basic properties of gravitational lensing: magnification and distortion. Using Eq. (2.36), the distortion of source image can be represented by the following Jacobian matrix:

$$A_{ij} = \frac{\partial\theta_S^i}{\partial\theta^j} \equiv \begin{pmatrix} 1 - \kappa - \gamma_1 & -\gamma_2 \\ -\gamma_2 & 1 - \kappa + \gamma_1 \end{pmatrix} = \begin{pmatrix} 1 - \kappa & 0 \\ 0 & 1 - \kappa \end{pmatrix} + \begin{pmatrix} -\gamma_1 & -\gamma_2 \\ -\gamma_2 & +\gamma_1 \end{pmatrix}, \quad (2.37)$$

where  $\kappa$  is convergence and  $\gamma$  is shear;  $\gamma_1 = \frac{1}{2}(\Phi_{,11} - \Phi_{,22})$ , and  $\gamma_2 = \Phi_{,12}$ . The former component in the right hand side of Eq. (2.37) contributes to magnification effect of the size of a source image, and the latter one is for anisotropic-stretching effect of the image. The distortion can also be reduced with Eq. (2.23) as following:

$$A_{ij} = \delta_{ij} - \Phi_{,ij}, \quad (2.38)$$

$$\Phi = \frac{2}{c^2} \int_0^\chi d\chi' g(\chi, \chi') \partial_i \partial_j \Phi(\chi'), \quad (2.39)$$

where  $g(\chi, \chi') = r(\chi - \chi')r(\chi')/r(\chi)$ , and we consider up to the second order. Note that the magnification of the image brightness can be described as:

$$\mu = |\mu(\vec{x})| = \left| \frac{1}{\det A(\vec{x})} \right|. \quad (2.40)$$

As Eq. (2.38) indicates that  $2\kappa = \Phi_{,11} + \Phi_{,22}$  holds,  $\kappa$  can be described as the integral of matter density perturbation along the line of sight, combined with Eqs. (2.37) and (2.38) as:

$$\kappa = \frac{1}{c^2} \int_0^\chi d\chi' g(\chi, \chi') [\Delta - \partial_\chi^2] \Phi \quad (2.41)$$

$$\begin{aligned} &= \frac{3}{2} \left( \frac{H_0}{c} \right)^2 \Omega_{m0} \int_0^\chi d\chi' g(\chi, \chi') \frac{\delta}{a} - \frac{1}{c^2} \int_0^\chi d\chi' g(\chi, \chi') \partial_\chi^2 \Phi \\ &\simeq \frac{3}{2} \left( \frac{H_0}{c} \right)^2 \Omega_{m0} \int_0^\chi d\chi' g(\chi, \chi') \frac{\delta}{a}, \end{aligned} \quad (2.42)$$

where we neglect the second derivative of gravitational potential, and combined the following Poisson equation:  $\Delta \Phi = \frac{3}{2} H_0^2 \Omega_{m0} \delta / a$ .

On the other hand, convergence and shear in Fourier space are given by:

$$\tilde{\gamma}(\vec{k}) = \tilde{\gamma}_1(\vec{k}) + i\tilde{\gamma}_2(\vec{k}) \quad (2.43)$$

$$\tilde{\kappa}(\vec{k}) = \tilde{\gamma}_1(\vec{k}) \cos 2\phi_{\vec{k}} + \tilde{\gamma}_2(\vec{k}) \sin 2\phi_{\vec{k}} \quad (2.44)$$

$$\therefore \tilde{\gamma}(\vec{k}) = \frac{k_1^2 + k_2^2 + ik_1 k_2}{k^2} \tilde{\kappa}(\vec{k}), \quad (2.45)$$

where  $\vec{k} = (k_1, k_2) = k(\cos \phi_{\vec{k}}, \sin \phi_{\vec{k}})$ . Therefore the inverse transform of Eq. (2.43) is given as (Seitz & Schneider 1996):

$$\kappa(\vec{k}) = -\frac{1}{\pi} \int d^2\theta' \text{Re}[D^*(\vec{\theta} - \vec{\theta}') \gamma(\vec{k})], \quad (2.46)$$

where  $D(z) = (z_1^2 - z_2^2 + 2iz_1z_2)/z^4$ .

Also Eq. (2.38) in polar coordinate provides the following relations:

$$\kappa = \frac{1}{2} \left( \Phi_{\theta\theta} + \frac{1}{\theta} \Phi_{\theta} + \frac{1}{\theta^2} \Phi_{\phi\phi} \right), \quad (2.47)$$

$$\gamma_+ = \tilde{\gamma}_1(\vec{k}) \cos 2\phi_{\vec{k}} + \tilde{\gamma}_2(\vec{k}) \sin 2\phi_{\vec{k}}, \quad (2.48)$$

$$\gamma_{\times} = \frac{k_1^2 + k_2^2 + ik_1k_2}{k^2} \tilde{\kappa}(\vec{k}), \quad (2.49)$$

where  $(\theta_1, \theta_2) = (\theta \cos \phi, \theta \sin \phi)$ , taking origin at the center of gravitational source. Furthermore  $\gamma_+$  and  $\gamma_{\times}$  are tangential shear and cross component of shear defined as:

$$\gamma_+ = -\gamma_1 \cos 2\phi - \gamma_2 \sin 2\phi, \quad (2.50)$$

$$\gamma_{\times} = \gamma_1 \sin 2\phi - \gamma_2 \cos 2\phi. \quad (2.51)$$

The averaged description of these quantities in the range of  $[\theta, \theta + d\theta]$  is:

$$\langle \kappa \rangle(\theta) = \frac{1}{2} \left( \langle \Phi_{\theta\theta} \rangle + \frac{1}{\theta} \langle \Phi_{\theta} \rangle \right), \quad (2.52)$$

$$\langle \gamma_+ \rangle(\theta) = -\frac{1}{2} \left( \langle \Phi_{\theta\theta} \rangle - \frac{1}{\theta} \langle \Phi_{\theta} \rangle \right), \quad (2.53)$$

$$\langle \gamma_{\times} \rangle(\theta) = 0. \quad (2.54)$$

The property of Eq. (2.54),  $\langle \gamma_{\times} \rangle$  is often adopted as the indicator of systematic uncertainty in the observation. Therefore the averaged tangential component is given by:

$$\langle \gamma_+ \rangle(\theta) = -\langle \kappa \rangle(\theta) + \bar{\kappa}(\theta), \quad (2.55)$$

where  $\bar{\kappa}(\theta)$  is the circle average of convergence given by:

$$\bar{\kappa}(\theta) = \frac{1}{\pi\theta^2} \int_0^{\theta} 2\pi d\theta' \theta' \langle \kappa \rangle(\theta') = \frac{1}{\theta^2} \int_0^{\theta} 2\pi d\theta' \partial_{\theta'} (\theta' \Phi_{\theta'}) = \frac{1}{\theta} \langle \Phi_{\theta} \rangle. \quad (2.56)$$

### (3) Lensing distortion effect

In the following we describe the relation between the shear quantity and observables. As discussed in previous section, the distortion of source image is given by Eq. (2.37). However,  $\kappa$  cannot be measured directly without the knowledge about the original size of the image. What we can only measure is the reduced shear, which is given by taking

a factor of  $(1 - \kappa)$  out front of Eq. (2.37):

$$g(\vec{\theta}) = \frac{\gamma(\vec{\theta})}{1 - \kappa(\vec{\theta})}. \quad (2.57)$$

The ellipticity of galaxies affected by gravitational lensing effect has major axis  $a = 1/(1 - \kappa - |\gamma|)$ , and minor axis  $b = 1/(1 - \kappa + |\gamma|)$ . Thus by utilizing ellipticity of galaxies we can reconstruct the shear information.

In order to characterize the system in detail, here we define ellipticity as:

$$\epsilon = \frac{a - b}{a + b}. \quad (2.58)$$

The definition of ellipticity can be related to the shear quantity by considering the second order surface brightness moments of a galaxies image (see Bartelmann & Schneider 2001). Suppose that the observed surface brightness of galaxies  $I(\theta)$ , the center of the image  $\bar{\theta}$  is given for all angular separations as:

$$\bar{\theta} \equiv \frac{\int d^2\theta w[I(\theta)]\vec{\theta}}{\int d^2\theta w[I(\theta)]}, \quad (2.59)$$

where  $w[I(\theta)]$  is weight function. Then the tensor component of the second moment of surface brightness can be described as:

$$Q_{ij} = \frac{\int d^2\theta w[I(\theta)](\theta_i - \bar{\theta}_i)(\theta_j - \bar{\theta}_j)}{\int d^2\theta w[I(\theta)]}, \quad (2.60)$$

where  $Q_{11} = Q_{22}$  and  $Q_{12} = Q_{21} = 0$  for a circular image. Also by the definition of  $Q_{ij}$ , we can describe the original ellipticity of galaxy as (Schneider 1996):

$$\epsilon = \epsilon_1 + i\epsilon_2 = \frac{Q_{11} - Q_{22} + 2iQ_{12}}{Q_{11} + Q_{22} + 2(1(Q_{11})Q_{22} - Q_{12}^2)^{1/2}}, \quad (2.61)$$

where  $\epsilon_1 = \epsilon_2 = 0$  for a circular image. Under these conditions we can calculate the original ellipticity of galaxy as:

$$\epsilon^{\text{int}} = \begin{cases} \frac{\epsilon - g}{1 - g^*\epsilon} & (\text{for } |g| \leq 1), \\ \frac{1 - g\epsilon^*}{\epsilon^* - g^*} & (\text{for } |g| > 1), \end{cases} \quad (2.62)$$

where  $\epsilon \sim \epsilon^{\text{int}} + g$ . Note that the signal from shear is usually overwhelmed by large

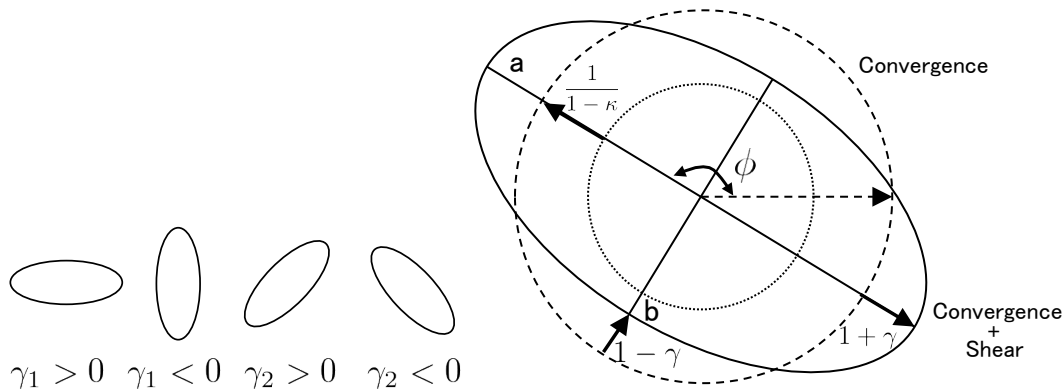


Figure 2.3: Right figure describes ellipticity of a galaxy with gravitational lensing effect. The innermost circle is the original ellipticity of galaxy, the elongated one is affected by right shear and convergence, and the dashed circle represents the case only with convergence signal. Left figures describes the elongated patterns for different shear properties.

uncertainty from the measurement of ellipticity of galaxy. Therefore the statistical analysis of ellipticity plays a key role. As there is no reason for preferred orientation of galactic shear, the average intrinsic ellipticity would be canceled if we stack the ellipticities from multiple galaxies. Hence  $\langle g \rangle + 0 = \langle \epsilon \rangle$ , and we can construct the estimator for the shear as:

$$\gamma \sim g \sim \langle g \rangle = \langle \epsilon \rangle. \quad (2.63)$$

This stacking method is valid for the small sky survey where the gravitational field can be taken as uniform.

## 2.2 Observational characteristics

The main characteristics of gravitational lensing is distortion and magnification. These properties provide useful information to probe various cosmic properties. Here we briefly summarize the characteristic schemes in lensing observations following a conventional classification.

- Strong lensing

When the foreground object is as massive as clusters of galaxies, multiple images of a background object show up in the sky. This phenomenon is first observed for quasar system (Walsh et al. 1979). Since the distortion patterns and the number of images differ in every system, it has played a great role to probe the mass distribution around multiple lensing systems. One unique point of strong lensing is that different images

have different timing of maximum magnification. Hence the analysis of single lensing system is strong enough to provide precise measurements of Hubble constant.

- Weak lensing

In the system of strong gravitational field around the clusters of galaxies, the image of background galaxies are distorted in the coherent patterns. By statistical analysis of multiple lensing signals, one can extract an averaged shear property even for weakly lensed field. If enough statistics can be achieved, we can reconstruct the mass distribution in Mpc scales. Nowadays, multiple surveys have been performed to reveal various properties of large scale structures, including tests of cosmological parameters.

- Microlensing

One important feature of gravitational lensing is magnification of the surface brightness of background objects. In the case where two lensed images are too close to be separated, one can detect only this magnification effect. This lensing scheme is called microlensing, and various searches have been proposed to probe dark object such as exoplanets.

## 2.3 Microlensing basics

In this section we describe the general properties of microlensing system. We first look into the basic observational scheme where the lens radius is smaller than the background source objects, and then give two exceptional cases where the lens size is comparable to source size, or where the Schwarzschild radius is smaller than the observational wavelength.

### 2.3.1 Point source approximation

In the following we look into the lensing system in the point source approximation, as illustrated in Fig. 2.4. We denote, by  $\beta$ , the angle between the lens and the source object on the sky, and  $\alpha$  as the angular separation between the source and the image. We also define the following distances;  $r_0$  as the distance between the lens and the image in the lens plane,  $r$  between the lens and the image,  $D_S$  as the distance between the observer and the source, and  $x$  as the distance to the lens normalized by  $D_S$ . Then  $\beta$  and  $\alpha$  can be described as:  $\beta = r_0/xD_S$ , and  $\alpha = r/xD_S$ . As discussed in Section 2.1.1, the bending angle for a point mass lens is given as

$$\delta = \frac{4Gm}{c^2l}. \quad (2.64)$$

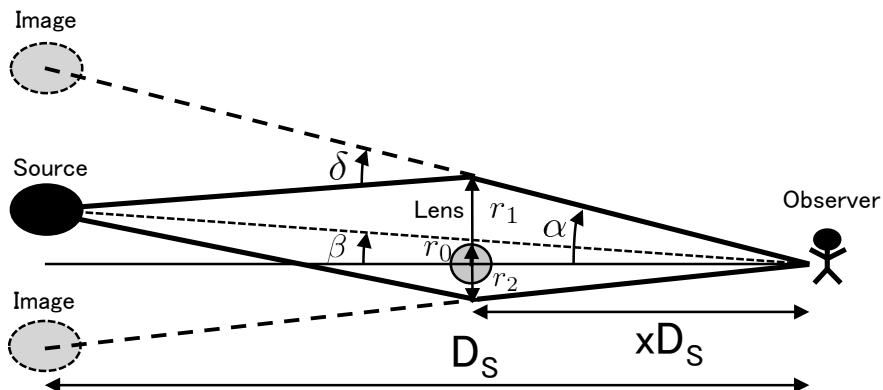


Figure 2.4: An illustration of gravitational lensing system. The light ray emitted from a source is bent by the gravitational field of a lens, and the source can be observed by multiple images due to the lensing. For a system where a star in M31 is a source object and a PBH of  $10^{-7}M_{\odot}$  in either halo region of MW or M31 is a lensing object, the two images due to lensing are not resolved even by the Subaru data, because the angular separation between the two images is about  $10^7$  arcseconds compared to  $O(0.1'')$ , a typical angular resolution of the HSC/Subaru data.

Here we call the object which makes foreground gravitational field as “lens”, and “source” for the background object (eg.  $m$  in Eqs. (2.64) denotes the lens mass as in Eq. (2.17), and  $l$  is the minimum distance between the light pass and the lens). Then the lens equation in this system can be described as:

$$D_S \beta + D_S (1-x) \delta = D_S \alpha. \quad (2.65)$$

Putting  $\alpha, \beta, \delta$  in this equation:

$$r^2 - r_0 r - R_E^2 = 0 \quad (2.66)$$

where  $R_E$  is Einstein radius defined as:

$$R_E^2 = \frac{4GM D}{c^2}, \quad D \equiv D_S x(1-x). \quad (2.67)$$

Note that Einstein radius is the size of so-called Einstein ring, which appears only when the observer, lens, and source are perfectly aligned in the line of sight and the lens has a axially symmetric mass distribution. Thus the following solutions of the lens equation represent positions of the two images:

$$r_{1,2} = \frac{r_0 \pm \sqrt{r_0^2 + 4R_E^2}}{2}. \quad (2.68)$$

Since lensing does not change the surface brightness of a source object, the lensing magnification is given by the change of the apparent angular extent of the source object due to lensing:

$$A_{1,2} = \left| \frac{r_{1,2} dr_{1,2}}{r_0 dr_0} \right| = \left| \frac{r_{1,2}^4}{r_{1,2}^4 - R_E^4} \right|. \quad (2.69)$$

Hence the total magnification of the lensed image is given by

$$A = A_1 + A_2 = \frac{u^2 + 2}{u\sqrt{u^2 + 4}}, \quad u \equiv \frac{r_0}{R_E}. \quad (2.70)$$

Next we describe time variation of the flux during a microlensing event. The magnification of source image varies with time as the lens object moves in front of the source object. Here we define  $v$  as the relative velocity component of the lens object perpendicular to the line of sight, and  $d$  as the closest distance of lens to the line of sight. The closest distance to the lens image can also be characterized by the impact parameter, defined as  $u_{\min} = d/R_E$ . Here we define a typical time scale of the magnification time variation as

$$t_0 = \frac{R_E}{v}. \quad (2.71)$$

With this parameter, the time variation of lens flux can be characterized as:

$$(v(t - t_{\max}))^2 + d^2 = r_0^2, \quad (2.72)$$

where  $t_{\max}$  is the time when the lens and the source are in the closest separation on the sky. By combining Eqs. (2.70) and (2.72), we obtain

$$u^2 = \frac{r_0^2}{R_E^2} = \frac{(t - t_{\max})^2}{t_0^2} + u_{\min}^2. \quad (2.73)$$

Hence the flux magnification of microlensing event is given by a function of time as:

$$A(t) = \frac{y^2 + u_{\min}^2 + 2}{\sqrt{y^2 + u_{\min}^2} \sqrt{y^2 + u_{\min}^2 + 4}}, \quad y = \frac{t - t_{\max}}{t_0}, \quad (2.74)$$

which implies that magnification gets larger when impact parameter  $u_{\min}$  is smaller. Note that lensing magnification is independent from the original luminosity of the source and the observational wavelength.

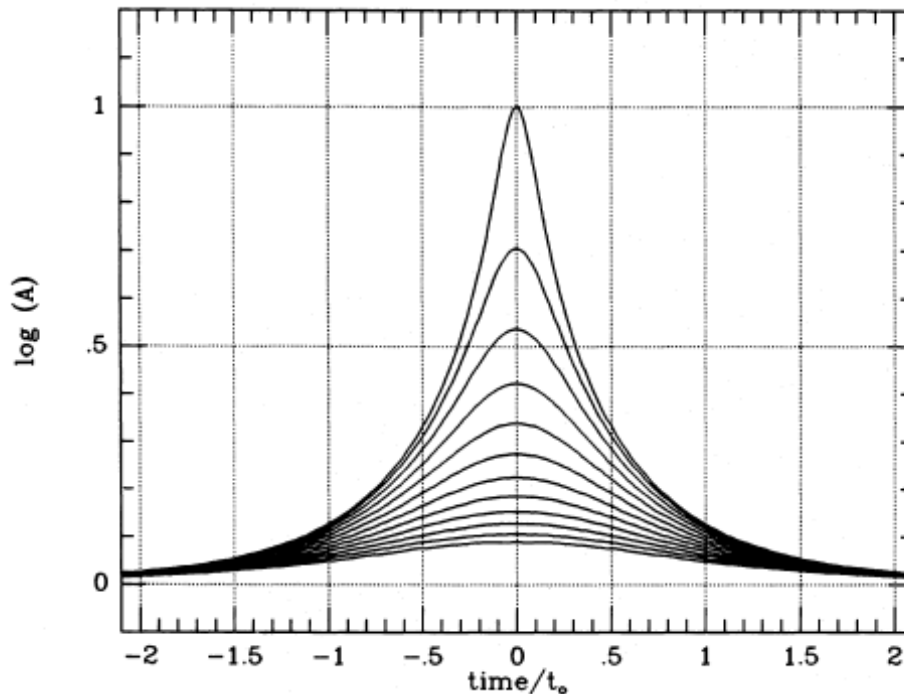


Figure 2.5: Simulated light curves for microlensing events, taken from Fig. 2 of Paczyński (1986). Each light curve stands for different impact parameter  $u_{\min}$  at 0.1, 0.2, ..., 1.1, 1.2, and light curve with larger magnification amplitude corresponds to smaller  $u_{\min}$  parameter.

The standard timescale of microlensing event as in Eq. (2.71) is given by:

$$t_0 \simeq 1.8 \text{hours} \left( \frac{M}{10^{-7} M_{\odot}} \right)^{\frac{1}{2}} \left( \frac{x D_S}{100 \text{kpc}} \right)^{\frac{1}{2}} \left( \frac{200 \text{km/sec}}{v} \right), \quad (2.75)$$

where we assumed PBH with  $10^{-7} M_{\odot}$  is located at  $D_L = 100 \text{kpc}$ , and the perpendicular velocity of the lens is around  $V_{\text{halo}} = 200 \text{km/sec}$ .

### 2.3.2 Finite source size effect

The point source approximation case discussed in *Section 2.3.1* is only valid when the source size is smaller than the Einstein radius of the lens. In the following, we briefly review the magnification of an extended source caused by a point mass lens. We refer to Witt & Mao (1994) and Cieplak & Griest (2013) for more detail.

If the source is extended one can obtain the lensed flux and the total amplification by integrating  $A(u)$  as in Eq. (2.74) over the source area, weighted by the surface-brightness profile of the source. Then the amplification for the extended source can be derived by the

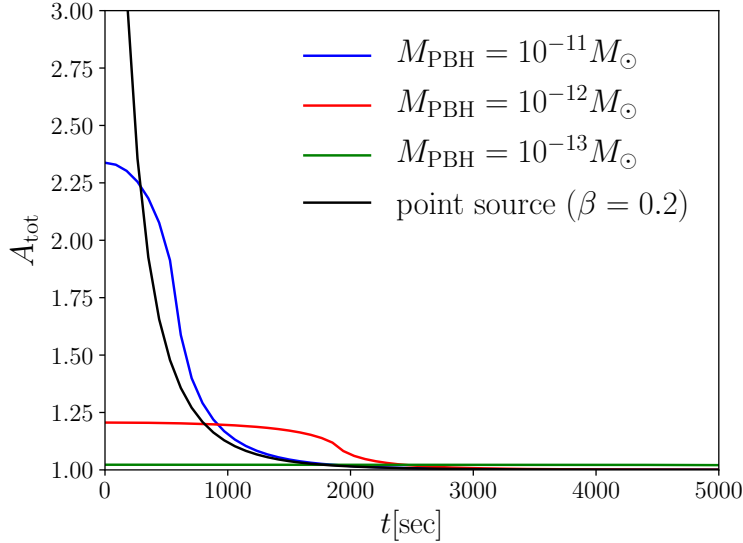


Figure 2.6: Effect of finite source size effect on microlensing light curves. We assume observation of microlensing events toward Andromeda galaxy ( $D_S = 770$  kpc) with lens position at  $D_L = 100$  kpc and the impact parameter is  $\beta = 0.2$ . We assume light curves have timescale  $t_{\text{FWHM}} = 360$  sec for cases with point source approximation.

convolution of the point source, which averages the magnification of the point source

$$A^{\text{finite}}(t) = \frac{1}{\pi U^2} \int_{\vec{y} \in \text{source}} d^2y A^{\text{point}}(y), \quad (2.76)$$

where  $U$  is the finite source parameter

$$U = \frac{R_S/d_S}{R_E/d_L} = 5.8 \left( \frac{M}{10^{-10} M_\odot} \right)^{-1} \left( \frac{d_L}{d_S} \right)^{1/2} \left( 1 - \frac{d_L}{d_S} \right)^{-1/2}. \quad (2.77)$$

Fig. 2.6 shows the example of light curves considering finite source size effect. There is larger deviation around the peak magnification for lens with smaller mass. The above discussion indicates that the amplification gets smaller when  $U$  is larger. The finite source size parameter  $U$  depends both on the distance of the source and the mass of the lens object;  $U$  gets larger when the lens locates closer to the source object, or when the mass of the lens is smaller.

### 2.3.3 Wave effect

#### Review of Basic Formalism

For special cases of microlensing observations, where the Schwarzschild radius of the lens is comparable to the observational wave length, we need to take into account the effect of wave optics. In the following we review the basic formalism of wave optics under thin lens approximation. We refer to Nakamura (1998) and Matsunaga & Yamamoto (2006) for more detail.

Here we start from a case in Fig. 2.2. Here the background space-time can be described with the following metric:

$$ds^2 = g_{\mu\nu}dx^\mu dx^\nu = -(1 + 2U(\vec{r})) dt^2 + (1 - 2U(\vec{r})) d\vec{r}^2, \quad (2.78)$$

where  $U(\vec{r})$  is the Newtonian gravitational potential with the condition  $U(\vec{r}) \ll 1$ . On the Newtonian background space-time, we consider the wave propagation of the scalar field  $\Phi$ , as described in Eq. (2.18). The propagation of electro-magnetic wave can be well described by the scalar wave equation, which is given by

$$\partial_\mu(\sqrt{-g}g^{\mu\nu}\partial_\nu\Phi) = 0. \quad (2.79)$$

This equation is written as

$$(\Delta^2 + \omega^2)\Phi = 4\omega^2U(\vec{r})\Phi \quad (2.80)$$

on the space-time with the line element in Eq. (2.78), where we assume the monochromatic wave with the angular frequency  $\omega$ . By assuming spherically symmetric potential under the thin lens approximation, the amplification factor  $F = \Phi/\Phi_0$ , where  $\Phi_0$  is the wave amplitude in the absence of gravitational potential  $U = 0$ , is given by

$$F(\omega, \vec{\eta}) = \frac{d_S}{d_L d_{LS}} \frac{\omega}{2\pi i} \int_{-\infty}^{\infty} d^2\xi \exp[i\omega\hat{\phi}(\vec{\xi}, \vec{\eta})], \quad (2.81)$$

where  $\hat{\phi}(\vec{\xi}, \vec{\eta})$  is the time delay function given by

$$\hat{\phi}(\vec{\xi}, \vec{\eta}) = \frac{d_L d_S}{2d_{LS}} \left( \frac{\vec{\xi}}{d_L} - \frac{\vec{\eta}}{d_S} \right)^2 - \hat{\psi}(\vec{\xi}) \quad (2.82)$$

where  $d_L$  is the distance between the lens and the source,  $d_S$  is the distance between the source and the observer, and  $d_{LS}$  is the distance between the lens and the source, respectively.

Note that we omit a term  $\hat{\phi}_m(\vec{\eta})$  in the right hand side because the inclusion of this term does not alter our argument. The two dimensional gravitational deflection potential is defined by

$$\hat{\psi}(\vec{\xi}) = 2 \int_{-\infty}^{\infty} dz U(\vec{\eta}, z). \quad (2.83)$$

Note that  $|F| = 1$  in the absence of the lens potential  $U = 0$ .

It is useful to rewrite the amplification factor  $F$  in terms of dimensionless quantities:  $\vec{x} = \vec{\xi}/\xi_0$ ,  $\vec{y} = \vec{\eta}d_L/\xi_0d_S$ ,  $w = \omega d_S \xi_0^2/d_L d_{LS}$ , and  $\psi = \hat{\psi}d_L d_{LS}/\xi_0^2 d_S$ , where  $\xi_0$  is the normalization constant of the length in the lens plane, for which we adopt  $\xi_0 = \theta_E d_L$ .  $\theta_E$  is the Einstein angle derived as the solution of the lens equation with  $\theta_S = 0$  in Eq. (2.23). We also introduce the dimensionless time delay function by

$$T(\vec{x}, \vec{y}) = \frac{d_L d_{LS}}{d_S \xi_0^2} \hat{\phi}(\vec{\xi}, \vec{\eta}) = \frac{1}{2} |\vec{x} - \vec{y}|^2 - \psi(\vec{x}). \quad (2.84)$$

Then, the amplification factor is written as

$$F(w, \vec{y}) = \frac{w}{2\pi i} \int_{-\infty}^{\infty} d^2x \exp[iwT(\vec{x}, \vec{y})]. \quad (2.85)$$

Hence, the effect of the wave optics is characterized by the dimensionless parameter  $w$ . In the case of the spherically symmetric lens model, the gravitational deflection potential  $\psi(\vec{x})$  depends only on  $x = |\vec{x}|$ . Then, the amplification factor is reduced to the relatively simple formula

$$F(w, y) = -iwe^{\frac{i}{2}wy^2} \int_0^{\infty} dx x J_0(wxy) \exp \left[ iw \left( \frac{1}{2}x^2 - \psi(x) \right) \right], \quad (2.86)$$

where  $J_0(z)$  is the Bessel function of the zeroth order and  $y = |\vec{y}|$ .

### Geometrical optics approximation

Next we consider the limit of the short wave length in the wave optics ( $w \gg 1$ ), which reproduces the conventional geometrical optics in the gravitational lensing. In the limit of the geometrical optics, the diffraction integral Eq. (2.85) is evaluated around the stationary points of the time delay function  $T(\vec{x}, \vec{y})$ . The stationary points are determined by the solution of the lens equation as in Eq. (2.23). Then the time delay function  $T(\vec{x}, \vec{y})$  is expressed around the  $j$ -th image position  $\vec{x}_j$  as

$$T(\vec{x}, \vec{y}) = T(\vec{x}_j, \vec{y}) + \frac{1}{2} \sum_{a,b=1,2} \partial_a \partial_b T(\vec{x}_j, \vec{y}) X_a X_b + O(X^3), \quad (2.87)$$

where  $\vec{X} = \vec{x} - \vec{x}_j$ . Inserting Eq. (2.87) into Eq. (2.85), we obtain the amplification factor in geometrical optics limit

$$F_{\text{geo}}(w, \vec{y}) = \sum_j |\mu(\vec{x}_j)|^{1/2} \exp \left[ iwT(\vec{x}_j, \vec{y}) - i\frac{n_j}{2}\pi \right], \quad (2.88)$$

where the magnification of the  $j$ -th image is  $\mu(\vec{x}_j) = 1/\det(\partial\vec{y}/\partial\vec{x})$  and  $n_j = 0, 1, 2$  when  $\vec{x}_j$  is a minimum, saddle, maximum point of  $T(\vec{x}, \vec{y})$ , respectively.

### Point mass lens

Now we consider a simple case of the point mass lens model, in which we write  $\rho(\vec{x}, z) = M\delta^{(2)}(\vec{\xi})\delta^{(1)}(z)$ , where  $M$  is the mass of the lens object. Then, the surface mass density is  $\Sigma(\vec{x}) = M\delta^{(2)}(\vec{\xi}) = M\delta^{(2)}(xi_0x)$ . Using mathematical formula, the expression of the amplification factor Eq. (2.86) yields

$$F = e^{\frac{i}{2}w(y^2 + \log(w/2))} e^{\frac{\pi}{4}w} \Gamma \left( 1 - \frac{i}{2}w \right) {}_1F_1 \left( 1 - \frac{i}{2}w, 1; -\frac{i}{2}wy^2 \right), \quad (2.89)$$

where  ${}_1F_1(a, c, z)$  is the confluent hypergeometric function. In this model we have the dimensionless parameter  $w$ , which characterizes the wave optics,

$$w = 2\pi \frac{2r_s}{\lambda} = 8\pi GMf = 6.2 \left( \frac{M}{10^{-10}M_\odot} \right). \quad (2.90)$$

Note that  $w$  has the meaning of the ratio of the Schwarzschild radius to the wavelength of the propagating wave. Then we define the magnification by  $\mu(w, y) \equiv |F(w, y)|^2$  as

$$\mu(w, y) = \frac{\pi w}{1 - e^{-\pi w}} \left| {}_1F_1 \left( 1 - \frac{i}{2}w, 1; -\frac{i}{2}wy^2 \right) \right|^2, \quad (2.91)$$

where we give the expression from Eq. (2.86). The maximum magnification is achieved when  $y = 0$ , which provides the configuration of the Einstein ring,

$$\mu_{\text{max}} = \frac{\pi w}{1 - e^{-\pi w}}. \quad (2.92)$$

We next consider the approximation based on the geometrical optics. The point mass lens model has the two images in the geometrical optics. Namely, the lens equation as in Eq. (2.23) has the two solution (the minimum and the saddle points of the time delay

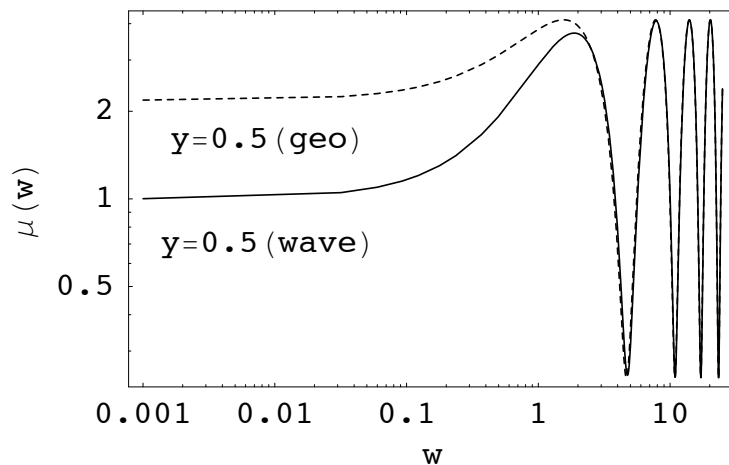


Figure 2.7: Effect of wave optics on microlensing effect. This figure is reproduced from Fig. 3 of Matsunaga & Yamamoto (2006).

function). Then, Eq. (2.88) yields

$$F_{\text{geo}}(w, \vec{y}) = |\mu_+|^{1/2} \exp \left[ iw \left( \frac{1}{2}(p_+ - y)^2 - \log |p_+| \right) \right] - i|\mu_-|^{1/2} \exp \left[ iw \left( \frac{1}{2}(p_- - y)^2 - \log |p_-| \right) \right], \quad (2.93)$$

where the magnification of each image is  $\mu_{\pm} = 1/2 \pm (y^2 + 2)/(2y\sqrt{y^2 + 4})$  and  $p = (1/2)(y \pm \sqrt{y^2 + 4})$ . Then, the corresponding magnification is

$$\mu_{\text{geo}}(w, y) = \frac{y^2 + 2}{y\sqrt{y^2 + 4}} + \frac{2}{y\sqrt{y^2 + 4}} \sin \left[ w \left( \frac{1}{2}y\sqrt{y^2 + 4} + \log \left| \frac{\sqrt{y^2 + 4} + y}{\sqrt{y^2 + 4} - y} \right| \right) \right]. \quad (2.94)$$

Fig. 2.7 shows the magnification from Eq. (2.89) and Eq. (2.93), as a function of the parameter  $w$  with the source position fixed  $y = 0.5$ . For  $w \geq 1$ , the oscillation feature appears due to the interference in the wave effect between the double images. Both the curves agree, and the geometrical optics is a very good approximation. For  $w \leq 1$ , however, the two curves are not in good agreement because the geometrical optics approximation is not suitable.

Note that the case for the extended source can be described as in the following:

$$\bar{\mu}(w, a_S, r_S) = \frac{\int_{-\infty}^{\infty} W(\vec{y}) \mu(w, y) d^2 y}{\int_{-\infty}^{\infty} W(\vec{y}) d^2 y}, \quad (2.95)$$

where we assume the distribution of the source intensity. For example, in the case of the Gaussian distribution we can assume

$$W(\vec{y}) = \exp\left(-\frac{|\vec{y} - \vec{Y}|^2}{2a_S^2}\right), \quad (2.96)$$

where  $\vec{Y}$  ( $|\vec{Y}| = r_S$ ) specifies the dimensionless source position, and  $a_S$  is the dimensionless source size.

# Chapter 3

## Microlensing constraints on primordial black holes with the Subaru/HSC Andromeda observation

The nature of dark matter (DM) remains one of the most important problems in physics. Previous studies have suggested that DM is non-baryonic, non-relativistic, and interacts with ordinary matter only via gravity (Davis et al. 1985; Clowe et al. 2006; Dodelson & Liguori 2003). Currently, unknown stable particle(s) beyond the Standard Model of Particle Physics, such as Weakly Interacting Massive Particles (WIMPs), are considered to be viable candidates (Jungman et al. 1996). However such particles have so far evaded detection in either elastic scattering experiments, indirect experiments or collider experiments (Klasen et al. 2015). Primordial black holes (PBH), which can be formed during the early universe, are also viable candidates for the elusive DM (Zel'dovich & Novikov 1967; Hawking 1971; Carr & Hawking 1974). In this chapter we describe our efforts on search of PBHs via microlensing events with Subaru Hyper Suprime-Cam.

### 3.1 Introduction

The abundance of PBHs of different mass scales is already constrained by various observations except for a mass window of  $M_{\text{PBH}} \simeq [10^{19}, 10^{24}] \text{g}$  or equivalently  $[10^{-14}, 10^{-9}] M_{\odot}$  (Carr et al. 2016). The existing constraints based on the capture of neutron stars and white dwarfs (Capela et al. 2013b) in this mass regime are based on uncertain assumptions about the presence of DM in a globular cluster (Lane et al. 2009). Thus it is of critical importance to further explore observational constraints on the PBH abundance for this mass window.

Gravitational microlensing is a powerful method to probe DM in the Milky Way (MW) (Paczynski 1986; Griest et al. 1991). Microlensing causes a time-varying magnification of a background star when a lensing object crosses the line-of-sight to the star at close proximity. The microlensing experiments, MACHO (Alcock et al. 2000) and EROS (Tisserand et al. 2007), have previously monitored large number of stars in the Large Magellanic Cloud (LMC) with roughly a 24 hour cadence. They have ruled out massive compact halo objects (MACHOs) such as brown dwarfs with mass scales  $[10^{-7}, 10]M_{\odot}$  as DM candidates. We also note that, if PBHs at  $\sim 10M_{\odot}$  mass scale, which are the possible source of LIGO gravitational wave detections, make a significant fraction of DM, by more than  $\sim 1\%$ , the merger rates of the resulting binaries could be larger than the LIGO event rate (Sasaki et al. 2016; Ali-Haïmoud et al. 2017). Microlensing searches on time scales of 15 or 30 minutes have also been carried out using the public 2-year Kepler data to constrain the abundance of  $10^{-8}M_{\odot}$  PBHs (Griest et al. 2014).

With the aim of constraining the abundance of PBH on even smaller mass scales, we carried out a dense cadence observation of the Andromeda galaxy (M31), with the Subaru Hyper Suprime-Cam (HSC). We search for microlensing event(s) of M31 stars by intervening PBHs in both the halo regions of MW and M31. M31 is the MW’s largest neighboring spiral galaxy, at a distance of 770 kpc (the distance modulus  $\mu \simeq 24.4$  mag). Even a single night of HSC/Subaru yields an ideal dataset to search for the PBH microlensing events because of the following reasons. First, the 1.5 degree diameter field-of-view of HSC (Miyazaki et al. 2018) allows us to cover the entire region of M31 (the bulge, disk and halo regions) with a single pointing. Secondly, the 8.2m large aperture of Subaru Telescope and its superb image quality (typically  $0.6''$ ) (Aihara et al. 2017) allow us to detect fluxes from M31 stars down to  $m_r \simeq 26$  even with a short exposure of 90 sec. These two facts allow us to simultaneously monitor a sufficiently large number of stars in M31. Thirdly, the 90 sec exposure and a short camera readout of  $\sim 35$  sec enable us to take data at an unprecedented cadence of 2 min. Thus, we can search for microlensing events with PBH mass scales smaller than those probed by Griest et al. (2014). Finally, the huge volume between M31 and the Earth, leads to a large optical depth of PBH microlensing to each star in M31, which allows us to put meaningful constraints on the PBH DM scenario.

The analysis of M31 time domain data presents a formidable challenge, as it is a dense stellar field. We are in the pixel lensing regime, where we need to detect the microlensing of a single unresolved star among many stars that contribute photons to each CCD pixel (Crotts 1992; Baillon et al. 1993; Gould 1996). All of the previous work on M31 microlensing (e.g., see Calchi Novati (2010)) has been carried out using smaller aperture telescopes, which can

only be sensitive to microlensing of relatively bright stars such as red giants with event rates of a few tens (Aurière et al. 2001). In addition the image quality of HSC corresponds to a significant step ahead with typical seeing size  $\sim 0.6''$ . In order to search for pixel lensing, we used the image subtraction technique described in Alard & Lupton (Alard & Lupton 1998). This technique has been integrated into the standard HSC data reduction pipeline, `hscPipe` (Bosch et al. 2017). The pipeline subtracts a reference image (constructed from the 10 epochs with the best seeing data) from a target image for M31 taken at a different epoch, and catalogs variable star candidates that are identified in the difference image.

The structure of this chapter is as follows. In Section 3.2, after a brief review of the microlensing phenomena, we first derive an event rate for microlensing due to the intervening PBHs for a single star in M31, by employing a halo model for the MW and M31. In Section 3.3 we describe the details of our data analysis including the image subtraction technique, and define the master catalog of variable star candidates. In Section 3.4 we describe the selection criteria for microlensing events from the catalog of variable star candidates. In Section 3.5, we use the result to derive an experimental upper bound on the abundance of PBHs as a function of PBH mass. We then discuss how different assumptions in our analysis affect the upper bound in Section 3.6.

## 3.2 Event rate of PBH microlensing for M31 stars

In this section we estimate event rates of PBH microlensing for a star in M31. We extend the formulation in previous studies (Griest et al. 1991; Alcock et al. 1996; Kerins et al. 2001; Riffeser et al. 2006) to microlensing cases due to PBHs in the halo regions of MW and M31 for a source star in M31.

### 3.2.1 Microlensing basics for M31 observation

If a star in M31<sup>1</sup> and a foreground PBH are almost perfectly aligned along the line-of-sight to an observer, the star is multiply imaged due to strong gravitational lensing. In case these multiple images are unresolved, the flux from the star appears magnified. When the source star and the lensing PBH are separated by an angle  $\beta$  on the sky, the total lensing magnification, i.e. the sum of the magnification of the two images, is

$$A = A_1 + A_2 = \frac{u^2 + 2}{u\sqrt{u^2 + 4}}, \quad (3.1)$$

---

<sup>1</sup>Throughout this paper we assume that a source star is in M31, not in the MW halo region, because of the higher number density on the sky.

where  $u \equiv (d \times \beta)/R_E$ , and  $d$  is the distance to a lensing PBH. The Einstein radius  $R_E$  is defined as

$$R_E^2 = \frac{4GM_{\text{PBH}}D}{c^2}, \quad (3.2)$$

where  $M_{\text{PBH}}$  is the PBH mass.  $D$  is the lensing weighted distance,  $D \equiv d(1 - d/d_s)$ , where  $d_s$  is the distance to a source star in M31, and  $d$  is the distance to the PBH. By plugging typical values of the parameters, we can find the typical Einstein radius:

$$\theta_E \equiv \frac{R_E}{d} \simeq 3 \times 10^{-8} \text{ arcsec} \left( \frac{M_{\text{PBH}}}{10^{-8}M_\odot} \right)^{1/2} \left( \frac{d}{100 \text{ kpc}} \right)^{-1/2} \quad (3.3)$$

where we assumed  $d_s = 770$  kpc for distance to a star in M31 and we assumed  $D \sim d$  for simplicity, and employed  $M_{\text{PBH}} = 10^{-8}M_\odot$  as a working example for the sake of comparison with Griest et al. (2014). In the following analysis we will consider a wide range of PBH mass scales. The PBH lensing phenomena we search for are in the microlensing regime; we cannot resolve two lensed images with angular resolution of an optical telescope, and we can measure only the total magnification. A size of a star in M31 is viewed as

$$\theta_s \simeq \frac{R_s}{d_s} \simeq 5.8 \times 10^{-9} \text{ arcsec}, \quad (3.4)$$

if the source star has a similar size to the solar radius ( $R_\odot \simeq 6.96 \times 10^{10}$  cm). Comparing with Eq. (3.3) we find that the Einstein radius becomes smaller than the source size if PBH mass  $M_{\text{PBH}} \lesssim 10^{-10}M_\odot$  corresponding to  $M_{\text{PBH}} \lesssim 10^{23}$  g. We will later discuss such lighter PBHs, where we will take into account the effect of finite source size on the microlensing (Witt & Mao 1994; Cieplak & Griest 2013; Griest et al. 2014).

Since the PBH and the source star move relative to each other on the sky, the lensing magnification varies with time, allowing us to identify the star as a variable source in a difference image from the cadence observation. The microlensing light curve has a characteristic timescale that is needed for a lensing PBH to move across the Einstein radius:

$$t_E \equiv \frac{R_E}{v}, \quad (3.5)$$

where  $v$  is the relative velocity. Assuming fiducial values for these parameters, we can estimate the typical timescale as

$$t_E \simeq 34 \text{ min} \left( \frac{M_{\text{PBH}}}{10^{-8}M_\odot} \right)^{1/2} \left( \frac{d}{100 \text{ kpc}} \right)^{1/2} \left( \frac{v}{200 \text{ km/s}} \right)^{-1}, \quad (3.6)$$

where we assumed  $v = 200$  km/s for the typical relative velocity. Thus the microlensing light curve is expected to vary over several tens of minutes, and should be well sampled by our HSC observation. It should also be noted that a PBH closer to the Earth gives a longer timescale light curve for a fixed velocity. Since we can safely assume that the relative velocity stays constant during the Einstein radius crossing, the light curve should have a symmetric shape around the peak, which we will use to eliminate fake candidates.

### 3.2.2 Microlensing event rate

Here we estimate expected microlensing event rates from PBHs assuming that they consist of a significant fraction of DM in the MW and M31 halo regions.

We first need to assume a model for the spatial distribution of DM (therefore PBHs) between M31 and us (the Earth). Here we simply assume that the DM distribution in each halo region of MW or M31 follows the NFW profile (Navarro et al. 1997):

$$\rho_{\text{NFW}}(r) = \frac{\rho_c}{(r/r_s)(1+r/r_s)^2}, \quad (3.7)$$

where  $r$  is the radius from the MW center or the M31 center,  $r_s$  is the scale radius and  $\rho_c$  is the central density parameter. In this paper we adopt the halo model in Klypin et al. (2002):  $M_{\text{vir}} = 10^{12} M_{\odot}$ ,  $\rho_c = 4.88 \times 10^6 M_{\odot}/\text{kpc}^3$ , and  $r_s = 21.5$  kpc for MW, taken from Table 2 in the paper, while  $M_{\text{vir}} = 1.6 \times 10^{12} M_{\odot}$ ,  $\rho_c = 4.96 \times 10^6 M_{\odot}/\text{kpc}^3$ , and  $r_s = 25$  kpc for M31, taken from Table 3. Thus we assume a slightly larger DM content for the M31 halo than the MW halo. Dark matter profiles with these parameters have been shown to fairly well reproduce the observed rotation curves for MW and M31, respectively. There might be an extra DM contribution in the intervening space between MW and M31, e.g. due to a filamentary structure bridging MW and M31. However, we do not consider such an unknown contribution.

Consider a PBH at a distance  $d$  (kpc) from the Earth and in the angular direction to M31,  $(l, b) = (121.2^\circ, -21.6^\circ)$  in the Galactic coordinate system. Assuming that the Earth is placed at distance  $R_{\oplus} = 8.5$  kpc from the MW center, we can express the separation to the PBH from the MW center,  $r_{\text{MW-PBH}}$ , in terms of the distance from the Earth,  $d$ , as

$$r_{\text{MW-PBH}}(d) = \sqrt{R_{\oplus}^2 - 2R_{\oplus}d \cos(l) \cos(b) + d^2}. \quad (3.8)$$

If we ignore the angular extent of M31 on the sky (which is restricted to 1.5 degree in diameter for our study), the distance to the PBH from the M31 center,  $r_{\text{M31-PBH}}$ , is approximately

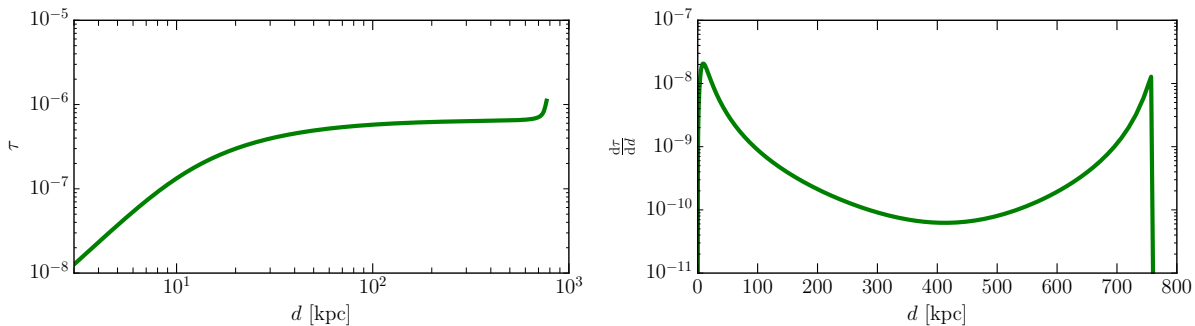


Figure 3.1: *Left*: The optical depth of PBH microlensing effect on a single star in M31 as a function of the distance to PBH,  $d$ , which can be obtained by integrating the integrand in Eq. (3.10) over  $[0, d]$ , rather than  $[0, d_s]$ . The optical depth is independent of PBH mass, and we assumed NFW parameters to model the DM distribution in each of the MW and M31 halo regions, where we determined the NFW parameters so as to reproduce their rotation curves (see text for details). *Right*: Similar plot, but the fractional contribution of PBHs at the distance,  $d$ , to the optical depth. Note that  $d$  in the  $x$ -axis is in linear scale. The area under this curve up to  $d$  gives the optical depth to  $d$  in the left plot.

given by,

$$r_{\text{M31-PBH}}(d) \simeq d_s - d, \quad (3.9)$$

where we approximated the distance to a source star in M31 to be the same as the distance to the center of M31,  $D_{\text{M31}} \simeq d_s$ , which we assume to be equal to  $d_s = 770$  kpc throughout this paper.

By using Eqs. (3.7)-(3.9), we can compute the DM density, contributed from both the MW and M31 halos, as a function of the distance to PBH,  $d$ .

Assuming that PBHs make up the DM content by a fraction,  $\Omega_{\text{PBH}}/\Omega_{\text{DM}}$ , we can compute the optical depth  $\tau$  for the microlensing of PBHs with mass  $M_{\text{PBH}}$  for a *single* star in M31. The optical depth is defined as the probability for a source star to be inside the Einstein radius of a foreground PBH on the sky or equivalently the probability for the magnification of source flux to be greater than that at the Einstein radius,  $A \geq 1.34$  (Paczynski 1986):

$$\tau = \frac{\Omega_{\text{PBH}}}{\Omega_{\text{DM}}} \int_0^{d_s} dd \frac{\rho_{\text{DM}}(d)}{M_{\text{PBH}}} \pi R_E^2(d, M_{\text{PBH}}). \quad (3.10)$$

Here the mass density field of DM is given by the sum of NFW profiles for the MW and M31 halos:  $\rho_{\text{DM}}(d) = \rho_{\text{NFW,MW}}(d) + \rho_{\text{NFW,M31}}(d)$ . Note that, because of  $R_E^2 \propto M_{\text{PBH}}$ , the optical depth is independent of PBH mass.

In Fig. 3.1, we show the optical depth of PBH microlensing for a single star in M31, calculated using the above equation. Here we have assumed that all the DM in the halo

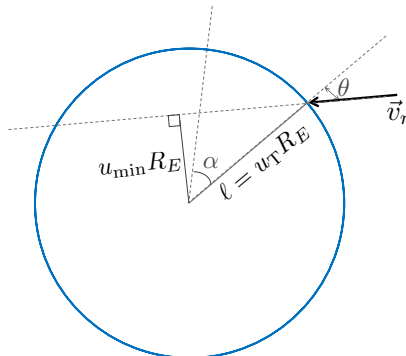


Figure 3.2: A schematic illustration of configurations of a lensing PBH and a source star in M31 in the lens plane, following Fig. 4 of Griest et al. (1991). The orbit of a lensing PBH, around a source star in M31 (placed at the origin in this figure), is parameterized as in the figure, which is used to derive the microlensing event rate (see text for details).

regions of MW and M31 is composed of PBHs, i.e.,  $\Omega_{\text{PBH}}/\Omega_{\text{DM}} = 1$ . The optical depth for microlensing,  $\tau \sim 10^{-6}$ , is larger compared to that to LMC or a star cluster in MW ( $\tau \sim 10^{-7}$ ) by an order of magnitude, due to the enormous volume and large mass content between the Earth and M31. The PBHs in each of the MW and M31 halos result in a roughly equal contribution to the optical depth to an M31 star. Although there is an uncertainty in the DM density in the inner region of MW or M31 (at radii  $\lesssim 10$  kpc) due to poorly-understood baryonic effects, the contribution is not large.

Next we estimate the rate for microlensing events with a given timescale for its light curve. First we model the velocity distribution of DM in the halo regions. We simply assume an isotropic Maxwellian velocity distribution for DM particles (e.g., Jungman et al. (1996)):

$$f(\mathbf{v}; r) d^3\mathbf{v} = \frac{1}{\pi^{3/2} v_c(r)^3} \exp\left[-\frac{|\mathbf{v}|^2}{v_c(r)^2}\right] d^3\mathbf{v} \quad (3.11)$$

where  $v_c(r)$  is the velocity dispersion at radius  $r$  from the MW or M31 center. For  $v_c(r)$ , we assume that it is given as

$$v_c(r) = \sqrt{\frac{GM_{\text{NFW}}(< r)}{r}}, \quad (3.12)$$

where  $M_{\text{NFW}}(< r)$  is the interior mass within radius  $r$  from the halo center, defined as  $M_{\text{NFW}}(< r) = 4\pi\rho_s r_s^3 [\ln(1+c) - c/(1+c)]$ , where  $c = r/r_s$  for each of the MW and M31 halos.

We start from the geometry and variables shown in Fig. 4 of Griest et al. (1991) and their Eq. (10) (see Fig. 3.2), which gives the rate  $d\Gamma$  of PBHs entering a volume element

along the line-of-sight where they can cause microlensing for a single star in M31:

$$d\Gamma = \frac{\Omega_{\text{PBH}}}{\Omega_{\text{DM}}} \frac{\rho_{\text{DM}}(d)}{M_{\text{PBH}}} \frac{u_{\text{T}} R_{\text{E}}}{\pi v_{\text{c}}^2} \exp\left[-\frac{v_{\text{r}}^2}{v_{\text{c}}^2}\right] v_{\text{r}}^2 \cos\theta \, dv_{\text{r}} \, d\theta \, dd \, d\alpha. \quad (3.13)$$

Here  $n_{\text{PBH}}(d) = \rho_{\text{DM}}(d)/M_{\text{PBH}}$  is the number density of PBHs at the distance  $d$  from the Earth,  $v_{\text{r}}$  is the velocity of the PBH in the lens plane,  $\theta$  is the angle at which the PBH enters the volume element, and  $\alpha$  is an angle with respect to an arbitrary direction in the lens plane, as shown in Fig. 3.2. Microlensing events are identified if they have a given threshold magnification  $A_{\text{T}}$  at peak. This threshold magnification defines a threshold impact parameter with respect to the Einstein radius of a PBH,  $u_{\text{T}} = R_{\text{T}}/R_{\text{E}}$ . Compared to Griest et al. (1991), we have further ignored motions of source stars for simplicity, i.e.  $v_{\text{t}} = 0$ . The parameters vary in the range of  $\theta \in [-\pi/2, \pi/2]$ ,  $\alpha \in [0, 2\pi]$ ,  $v_{\text{r}} = [0, \infty)$ .

The time scale for the microlensing event described by the above geometry is given by  $\hat{t} = 2R_{\text{E}} \cos\theta \, u_{\text{T}}/v_{\text{r}}$ . Thus the differential rate of microlensing events, occurring per unit time scale  $\hat{t}$ , is given by

$$\begin{aligned} \frac{d\Gamma}{d\hat{t}} &= \frac{\Omega_{\text{PBH}}}{\Omega_{\text{DM}}} \int_0^{d_{\text{s}}} dd \int_0^{\infty} dv_{\text{r}} \int_{-\pi/2}^{\pi/2} d\theta \int_0^{2\pi} d\alpha \frac{\rho_{\text{DM}}(d)}{M_{\text{PBH}}} \\ &\quad \times \frac{u_{\text{T}} R_{\text{E}}}{\pi v_{\text{c}}^2} \exp\left[-\frac{v_{\text{r}}^2}{v_{\text{c}}^2}\right] v_{\text{r}}^2 \cos\theta \, \delta_{\text{D}}\left(\hat{t} - \frac{2R_{\text{E}} u_{\text{T}} \cos\theta}{v_{\text{r}}}\right). \end{aligned} \quad (3.14)$$

Using the Dirac-delta function identity,

$$\delta_{\text{D}}\left(\hat{t} - \frac{2R_{\text{E}} u_{\text{T}} \cos\theta}{v_{\text{r}}}\right) = \delta_{\text{D}}\left(v_{\text{r}} - \frac{2R_{\text{E}} u_{\text{T}} \cos\theta}{\hat{t}}\right) \frac{v_{\text{r}}^2}{2R_{\text{E}} u_{\text{T}} \cos\theta}, \quad (3.15)$$

and integrating over  $\alpha$  and  $v_{\text{r}}$ , we obtain

$$\frac{d\Gamma}{d\hat{t}} = \frac{\Omega_{\text{PBH}}}{\Omega_{\text{DM}}} \int_0^{d_{\text{s}}} dd \int_{-\pi/2}^{\pi/2} d\theta \frac{\rho_{\text{DM}}(d)}{M_{\text{PBH}} v_{\text{c}}^2} v_{\text{r}}^4 \exp\left[-\frac{v_{\text{r}}^2}{v_{\text{c}}^2}\right], \quad (3.16)$$

with  $v_{\text{r}} = 2R_{\text{E}} u_{\text{T}} \cos\theta/\hat{t}$ . One can rewrite this equation by changing variable  $\theta$  to the minimum impact  $u_{\text{min}} = u_{\text{T}} \sin\theta$ , such that,  $d\theta = du_{\text{min}}/\sqrt{u_{\text{T}}^2 - u_{\text{min}}^2}$ . This results in

$$\frac{d\Gamma}{d\hat{t}} = 2 \frac{\Omega_{\text{PBH}}}{\Omega_{\text{DM}}} \int_0^{d_{\text{s}}} dd \int_0^{u_{\text{T}}} \frac{du_{\text{min}}}{\sqrt{u_{\text{T}}^2 - u_{\text{min}}^2}} \frac{\rho_{\text{DM}}(d)}{M_{\text{PBH}} v_{\text{c}}^2} v_{\text{r}}^4 \exp\left[-\frac{v_{\text{r}}^2}{v_{\text{c}}^2}\right], \quad (3.17)$$

where  $v_{\text{r}} = 2R_{\text{E}} \sqrt{u_{\text{T}}^2 - u_{\text{min}}^2}/\hat{t}$ . To compute the event rate due to PBHs in both the halo regions of MW and M31, we sum the contributions,  $d\Gamma = d\Gamma_{\text{MW}} + d\Gamma_{\text{M31}}$ . As we described

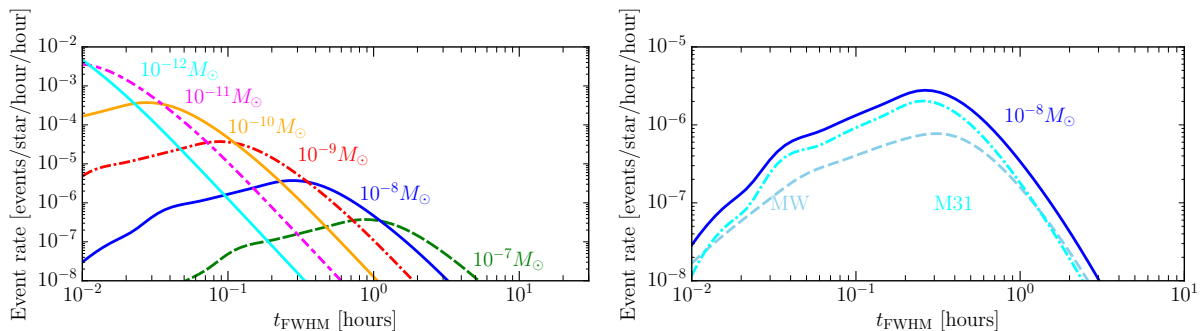


Figure 3.3: The differential event rate of PBH microlensing for a single M31 star (Eq. (3.17)); the rate per unit observation time (hour), per a single source star in M31, and per unit timescale of the microlensing light curve (hour) for PBHs of a given mass scale. Here we assumed that all the DM in the MW and M31 halo regions is made of PBHs;  $\Omega_{\text{PBH}}/\Omega_{\text{DM}} = 1$ . The  $x$ -axis is the full-width-half-maximum (FWHM) timescale of microlensing light curve. The lighter or heavier PBH has a shorter or longer timescale of microlensing light curve. The right panel shows the relative contribution to the microlensing event rate due to PBHs in either MW or M31 halo region, for the case of  $M_{\text{PBH}} = 10^{-8} M_{\odot}$ .

above, we can express the centric radius of each halo,  $r$ , entering into  $v_c(r)$ , in terms of the distance to the lensing PBH,  $d$ ;  $r = r(d)$ . Unless explicitly stated, we will employ  $u_T = 1$  as our default choice.

Fig. 3.3 shows the expected event rate for the PBH microlensing, computed using Eq. (3.17). Here we show the event rate as a function of the full-width-half-maximum (FWHM) timescale of the light curve, which matches our search of microlensing events from the real HSC data. If a PBH is in the mass range  $M = [10^{-12}, 10^{-7}] M_{\odot} \simeq 2 \times [10^{21}, 10^{26}]$  g, it causes the microlensing event that has a typical timescale in the range of  $[10^{-1}, 1]$  hour. The lighter or heavier PBHs tend to cause a shorter or longer timescale event. The event rate is quite high up to  $10^{-4}$  for a microlensing timescale with  $[0.1, 1]$  hours. That is, if we take about 10 hours observation and observe  $10^8$  stars at once for each exposure, we expect many events up to  $10^4$  events (because  $10^{-4} \times 10$  [hour]  $\times 0.1$  [hour]  $\times 10^8$  [stars]  $\simeq 10^4$ ), assuming that such PBHs constitute a majority of DM in the intervening space bridging MW and M31. The right figure shows that the PBHs in the M31 halo region give a slightly larger contribution to the event rate, because we assumed a larger halo mass for M31 than that of MW. Thus the high-cadence HSC observation of M31 is suitable for searching for microlensing events of PBHs.

### 3.2.3 Light Curve characterization in pixel lensing regime

As we described above, the timescale for the PBH and M31 star microlensing system is typically several tens of minutes for a PBH with  $10^{-8} M_{\odot}$ . However, there is an observational challenge. Since the M31 region is such a dense star field, fluxes from multiple stars are overlapped in each CCD pixel (0.17'' pixel scale for HSC/Subaru). In other words individual stars are not resolved even with the Subaru angular resolution (about 0.6'' for the seeing size). Hence we cannot identify which individual star in M31 is strongly lensed by a PBH, even if it occurs. Such a microlensing of unresolved stars falls in the ‘‘pixel microlensing’’ regime (Gould (1996), also see Calchi Novati (2010) for a review).

To identify microlensing events in the pixel microlensing regime requires elaborate data reduction techniques. In this chapter, we use the image subtraction or image difference technique first described in Alard & Lupton (1998). The image difference technique allows us to search for variable objects including candidate stars that undergo microlensing by PBHs. In brief, starting with the time sequenced  $N_{\text{exp}}$  images of M31, the analysis proceeds as follows. (i) We generate a reference image by co-adding some of the best-seeing images in order to gain a higher signal-to-noise. Next we subtract this reference image from each of the  $N_{\text{exp}}$  images after carefully matching their point spread functions (PSFs) as described in Alard & Lupton (1998). (ii) We search for candidate variable objects that show up in the difference image. In reality, if the image subtraction is imperfect, the difference image would contain many fake candidates, as we will discuss further. (iii) Once secure variable objects are detected, we determine the position (RA and DEC) of each variable object in the difference image. We perform PSF photometry for each variable candidate using the PSF center to be at the position of the candidate in the difference image. By repeating the PSF photometry in each difference image of the  $N_{\text{exp}}$  images, we can measure the light curve of the candidate as a function of the observation time.

The light curve of a microlensing event obtained using the PSF flux in the difference image at time  $t$ , obtained as described above, can be expressed as

$$\Delta F(t) = F_0 [A(t) - A(t_{\text{ref}})], \quad (3.18)$$

where  $\Delta F(t)$  is the differential flux of the star at time  $t$  relative to the reference image,  $F_0$  is the intrinsic flux,  $A(t)$  is the lensing magnification at  $t$  and  $A(t_{\text{ref}})$  is the magnification at the time of the reference image,  $t_{\text{ref}}$ . In the above equation,  $\Delta F(t)$  is a direct observable, and others ( $F_0, A(t), A(t_{\text{ref}})$ ) are parameters that have to be modeled.

As can be seen from Eq. (3.1), the light curve for the microlensing of a point source by

a point mass can be characterized by two parameters. The first parameter is the maximum amplification  $A_0 = A(u_{\min})$  when the lensing PBH is closest to a source star on the sky, where  $u_{\min}$  is the impact parameter relative to the Einstein radius  $R_E$  ( $u_{\min}$  is dimension-less). The second one is the timescale of the light curve, which depends on the Einstein radius as well as the transverse velocity of the PBH moving across the sky. For the timescale parameter we use the FWHM timescale of the microlensing light curve,  $t_{\text{FWHM}}$ , instead of  $t_E$ , defined as

$$A\left(\frac{t_{\text{FWHM}}}{2}\right) - 1 \equiv \frac{A_0 - 1}{2}. \quad (3.19)$$

Thus the light curve of microlensing can be fully modeled by the three parameters,  $F_0$ ,  $u_{\min}$  and  $t_{\text{FWHM}}$ . In the following we will use the three parameters when performing a fitting of the microlensing model to the observed light curve of microlensing candidate in the image difference. Note that the use of  $t_{\text{FWHM}}$ , instead of  $t_E$ , gives slightly less degenerate constraints on the parameters (Gondolo 1999).

## 3.3 Data Analysis and Object Selection

### 3.3.1 Observations

The HSC camera is a wide-field imaging camera attached at the prime focus of Subaru telescope. This camera consists of 116 CCD chips; 104 for science, 4 for auto-guide, and 8 for auto-focus, and each CCD has 2k x 4k pixels, with a pixel scale of 0.17'' (Miyazaki et al. (2015), see also Niikura et al. (2016) for more details). The 1.5 degree diameter FoV of HSC enables us to cover the entire region of M31, from the inner bulge to the outer disk and halo regions with a single pointing. Moreover, the 8.2m large aperture of Subaru Telescope and its superb angular resolution (typically 0.6'' seeing owing to the low humidity of the summit of 4200 m Maunakea)(Aihara et al. 2017) allow us to detect fluxes from M31 stars down to  $m_r \simeq 26$  depth even with a short exposure of 90 sec. This allows us to monitor a sufficiently large number of stars in M31 simultaneously. The pointing is centered at the coordinates of the M31 central region: (RA, dec) = (00h 42m 44.420s, +41d 16m 10.1s). We do not perform any dithering between different exposures in order to compare stars in the same CCD chip, which makes the image difference somewhat easier. However, in reality the HSC/Subaru system has some subtle inaccuracies in its auto-guidance and/or pointing system. This results in variations in the pointings of different exposures, typical variations range from few to a few tens of pixels.

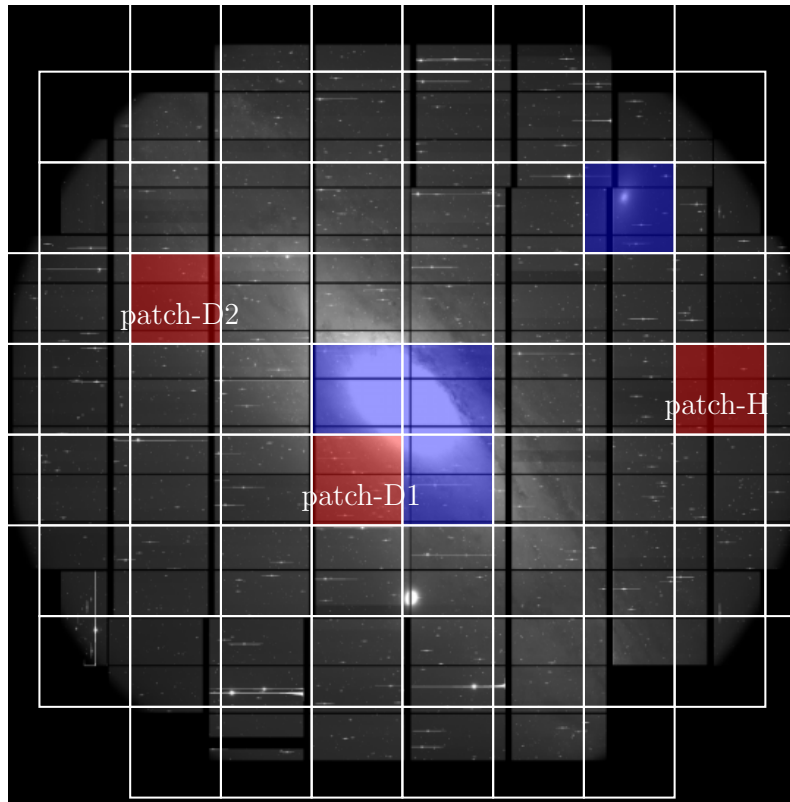


Figure 3.4: The background image of M31 shows configuration of 104 CCD chips of the Subaru/HSC camera. The white-color grids are the HSC “patch” regions. The patches labeled as “patch-D1”, “patch-D2” and “patch-H” are taken from representative regions of the disk region closer to the central bulge, the outer disk region and the halo region, respectively, which are often used to show example results of our data processing in the main text. The dark-blue regions are the patches we exclude from our data analysis due to too dense star fields, where fluxes from stars are saturated and the data are not properly analyzed.

Fig. 3.4 shows the configuration of the 104 CCD chips relative to the image of M31 on the sky. The white-color boxes denote locations of HSC “patches”, which are convenient tessellations of the HSC FoV. The image subtraction and the search of microlensing events will be done on a patch-by-patch basis. The patches labeled “patch-D1”, “patch-D2” and “patch-H” denote the regions that represent inner and outer disk regions (-D1 and -D2) and a halo (-H) region, respectively. These representative regions will be used to show how the results vary in the different regions.

Our observations were conducted on November 23, 2014 which was a dark night, a day

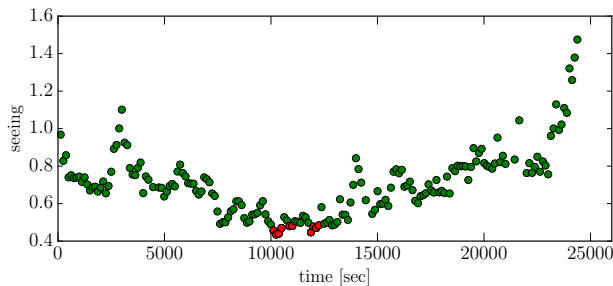


Figure 3.5: The PSF FWHM (seeing size) of each exposure (90 sec exposure each) as a function of time  $t$  [sec] from the start of our observation. We took the images of M31 region every 2 min (90 sec exposure plus about 35 sec for readout), and have 188 exposures in total. The red points show the 10 best-seeing images ( $\sim 0.45''$ ) from which the reference image, used for the image difference, was constructed.

after the new moon. In total, we acquired 194 exposures of M31 with the HSC  $r$ -band filter<sup>2</sup>, for the period of about 7 hours, until the elevation of M31 fell below about 30 degrees. We carried out the observations with a cadence of 2 minutes, which allows us to densely sample the light curve for each variable object. The total exposure time was 90 seconds on source and about 35 seconds were spent for readout on average. The weather was excellent for most of our observation as can be seen from Fig. 3.5, which shows how the seeing FWHM changed with time from the start of our observation. The seeing size was better than  $0.7''$  for most of the observation period, with a best seeing FWHM of about  $0.4''$  at  $t \sim 10,000$  sec (2.8 hours). However, the seeing got worse than  $1''$  towards the end of our observation. We exclude 6 exposures which had seeing FWHM worse than  $1.2''$  and use the remaining 188 exposures for our science analysis.

We also use the  $g$ - and  $r$ -band data, which were taken during the commissioning run on June 16 and 17 in 2013, respectively, in order to obtain color information of stars as well as to test a variability of candidates at different epochs. The  $g$ -band data consist of  $5 \times 120$  sec exposures and  $5 \times 30$  sec exposures in total, while the  $r$ -band data consists of  $10 \times 120$  sec exposures.

### 3.3.2 Data reduction and Sample selection

#### Standard data processing

We performed basic standard data reduction with the dedicated software package for HSC, `hscPipe` (version 3.8.6; also see Bosch et al. (2017)), which is being developed based on

<sup>2</sup>See <http://www.naoj.org/Projects/HSC/forobservers.html> for the HSC filter system

the Large Synoptic Survey Telescope software package (Ivezic et al. 2008; Axelrod et al. 2010; Jurić et al. 2015)<sup>3</sup>. This pipeline performs a number of common tasks such as bias subtraction, flat fielding with dome flats, coadding, astrometric and photometric calibrations, as well as source detection and measurements.

After these basic data processing steps, we subtract the background contamination from light diffusion of atmosphere and/or unknown scattered light. However the background subtraction is quite challenging for the M31 region, because there is no blank region and every CCD chip is to some extent contaminated by unresolved, diffuse stellar light. To tackle this problem, we first divide each CCD chip into different meshes (the default subdivision is done into 64 meshes in each CCD chip). We then employ a higher-order polynomial fitting to estimate a smooth background over different meshes. We employed a 10-th order polynomial fitting for the CCD chips around the bulge region, which are particularly dense star regions. For other CCD chips, we use a 6-th order polynomial fitting scheme. However, we found residual systematic effects in the background subtraction, so we will further use additional correction for photometry of the difference image, as we will discuss later.

For our study, accurate PSF measurements and accurate astrometric solutions are crucial, because those allow for an accurate subtraction of different images. The pipeline first identifies brightest star objects ( $S/N \gtrsim 50$ ) to characterize the PSF and do an initial astrometric and photometric calibration. From this initial bright object catalog, we select star candidates in the size and magnitude plane for PSF estimation (see Bosch et al. (2017) for details). The selected stars are fed into the PSFEx package (Bertin 2011) to determine the PSF as a function of positions in each CCD chip. The functional form of the PSF model is the native pixel basis and we use a second-order polynomial per CCD chip for interpolation. For the determination of the astrometry, we used a 30 sec calibration image that we took at the beginning of our observation, where bright stars are less saturated. We obtain an astrometry solution after every 11 images, 30 sec calibration frame plus 10 time-consecutive science exposures, by matching the catalog of stars to the Pan-STARRS1 system Schlafly et al. (2012); Tonry et al. (2012); Magnier et al. (2013). The HSC pipeline provides us with a useful feature, the so-called “hscMap”, which defines a conversion of the celestial sphere to the flat coordinate system, “hscMap coordinate”, based on a tessellation of the sky. In Fig. 3.4 the white-color regions denote the hscMap “patch” regions. We perform image difference separately on each patch. Due to too many saturated stars in the bulge region and M101, we exclude the patches, marked by dark blue color, from the following analysis.

---

<sup>3</sup>Also see <http://www.astro.princeton.edu/~rhl/photo-lite.pdf> for details of the algorithm used in the pipeline.

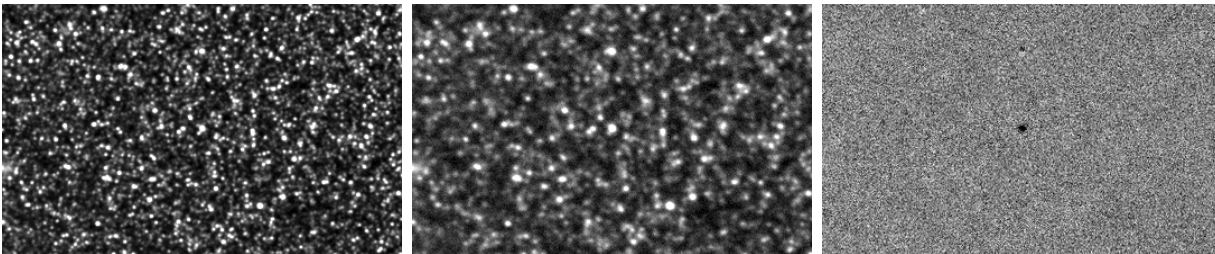


Figure 3.6: An example of the image subtraction technique we use for the analysis in this chapter. The left-panel image is the reference image which was constructed by co-adding the 10 best-seeing data, with typical seeing of  $0.45''$ . The size of the image is  $222 \times 356$  pixels (corresponding to about  $0.63$  sq. arcmin), which is taken from the disk region in M31. The middle panel is the target image (coadded image of 3 exposures) whose seeing size is  $0.8''$ . The right panel shows the difference image, showing that the pipeline properly subtracts the two images even for such a dense star region and a variable star candidate shows up at the center. In this case, the candidate object appears as a negative flux in the difference image, because the object has a fainter flux in the target image than in the reference image.

### Image subtraction and Object detection

In order to find variable objects, we employ the difference image technique developed in Alard & Lupton (1998) and Alard (2000), which is integrated into the HSC pipeline. To do this, we first generated the “reference” image by co-adding 10 best-seeing images among the 188 exposure images, where the 10 images are not time-consecutive (most of the 10 images are from images around about 3 hours from the beginning of the observation, as shown in Fig. 3.5). We use the mean of the 10 images as the observation time of the reference image,  $t_{\text{ref}}$ , which is needed to model the microlensing light curve (Eq. (3.18)).

In order to make a master catalog of variable object candidates, we constructed 63 target images by co-adding 3 time-consecutive images from the original 188 exposure images. A typical limiting magnitude is about 26 mag ( $5\sigma$  for point sources), and even better for images where seeing is good (see below). When subtracting the reference image from each target image, the Alard & Lupton algorithm uses a space-varying convolution kernel to match the PSFs of two images. The optimal convolution kernel is derived by minimizing the difference between convolved PSFs of two images. A variable object, which has a flux change between the two images, shows up in the difference image.

Fig. 3.6 shows the result of the image subtraction performed by the pipeline. Even for a dense star region in M31, the pipeline properly subtracts the reference from the target image, by matching the PSFs and astrometry. A point source which undergoes a change in its flux shows up in the difference image, as seen in the right panel. In this case, the candidate appears as a black-color point source meaning a negative flux, because it has a

fainter flux in the target image than in the reference image.

We detect objects in the difference image each of which is defined from a local minimum or maximum in the difference image, where we used  $5\sigma$  for the PSF magnitude as detection threshold. The pipeline also measures the center of each object and the size and ellipticity from the second moments. In this process we discarded objects that have ill-defined center, a saturated pixel(s) in the difference and/or original image or if the objects are placed at a position within 50 pixels from the CCD edge.

### PSF photometry and master catalog of variable star candidates

For each variable star candidate, we obtain PSF photometry in the difference image to quantify the change of flux. We allow negative PSF fluxes for candidates that have fainter flux in the target image than in the reference image. Since the photon counts in each CCD pixel is generally contaminated by multiple stars in most of the M31 regions, we often find a residual coherent background (large-scale modulated background) in each difference image, due to imperfect background subtraction in the original image. To avoid contamination from such a residual background, we first measure the spatially constant background from the median of counts in  $41 \times 41$  pixels around each object in the postage-stamp image, and then subtract this background from the image. Then we perform the PSF-photometry counts in ADU units taking the PSF center to be at the candidate center. Hereafter we sometimes refer to PSF magnitude in the difference image as “PSF counts”. The pipeline also estimates noise in each pixel assuming the background limit (Poisson noise), and gives an estimation of the noise for the PSF photometry (see equations 14 and 15 in Mandelbaum et al. (2013) for the similar definition). However, the noise estimation involves a non-trivial propagation of Poisson noise in the image difference procedures, so we will use another estimate for the PSF photometry error in each patch, as described below.

In the following we focus on the PSF photometry counts in ADU units in the difference image, rather than the magnitude, because it is the direct observable. However, we will also need to infer the magnitude of each candidate; for example, to estimate the luminosity function of source stars in each magnitude bin or to plot the light curve of variable star candidates in units of the magnitude. In this case we estimate the magnitude of an object in the  $i$ -th target image,  $m_i$ , based on

$$m_i = -2.5 \log \left( \frac{C_{\text{diff},i} + C_{\text{ref}}}{F_{0,i}} \right), \quad (3.20)$$

where  $C_{\text{diff},i}$  is the PSF flux for the object in the difference image of the  $i$ -th target image,

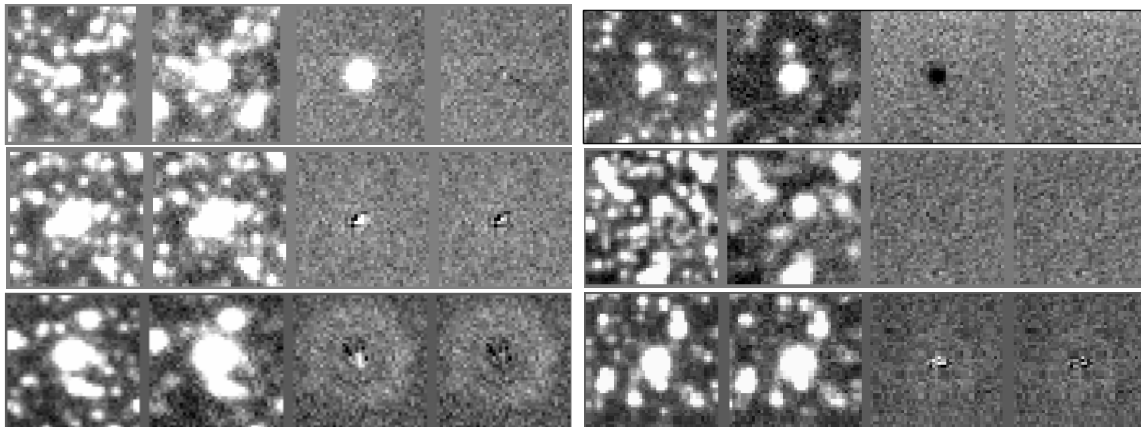


Figure 3.7: Examples of detected objects in the difference image, which pass or do not pass the selection criteria to define a master catalog of variable star candidates (see text for details). Each panel shows 4 postage-stamp images: the leftmost image is the reference image (the coadded image of 10 best-seeing exposures), the 2nd left is the target image (the coadded image of 3 time-consecutive exposures), the 3rd image is the difference image between the reference and target images, and the rightmost image is the residual image after subtracting the best-fit PSF image from the difference image at the object position. The two objects in top row are successful candidates that passed all the selection criteria: the left-panel object has a brighter flux in the target image than in the reference image, while the right-panel object has a fainter flux (therefore appear as a black-color image with negative flux). The lower-row objects are removed from the catalog after the selection criteria. The objects in the middle row are excluded because the object is either smaller or larger than the PSF size. The left object in the bottom row is excluded because it has a too large ellipticity than PSF. The right object is excluded because of too large residual image.

$C_{\text{ref}}$  is the PSF flux of the reference image at the object position, and  $F_{0,i}$  is the zero-point flux in the  $i$ -th image. Note that the counts of the reference image  $C_{\text{ref}}$  can be contaminated by fluxes from neighboring stars, so the above magnitude might not be accurate.

From the initial catalog constructed from the  $5\sigma$  candidates from the 63 coadded images, we prune it down to a *master* catalog of “secure” variable star candidates by applying the following criteria:

- *PSF magnitude threshold* – A candidate should have a PSF magnitude, with a detection significance of  $5\sigma$  or higher (including a negative flux), in any of the 63 difference images.
- *Minimum size* – The size of the candidate should be greater than 0.75 times the PSF size of each difference image.
- *Maximum size* – The size of the candidate should be smaller than 1.25 times the PSF size.

- *Roundness* – The candidate should have a round shape. We require our candidates to have an axis ratio greater than 0.75, as the PSF does not show extreme axis ratios.
- *PSF shape* – We impose that the shape of an object should be consistent with the PSF shape. The residual image, obtained by subtracting a scaled PSF model from the candidate image in the difference image, should be within  $3\sigma$  for the cumulative deviation over pixels inside the PSF aperture.

Fig. 3.7 shows examples of objects that pass or fail the above criteria. Note that the above conditions are broad enough in order for us not to miss a real candidate of microlensing if it exists. We make a master catalog of variable star candidates from objects that pass all the above conditions as well as are detected in the image difference at least twice in the 63 difference images at the same position within 2 pixels. These criteria result in 15,571 candidates of variable objects, which is our master catalog of variable star candidates.

### Light curve measurement

Once each candidate is identified, we measure the PSF counts in each of the 63 difference images. This allows us to measure the light curve with a 6 min resolution, as a function of time from the beginning to the end of our 7 hour long observations. In order to restore the highest time resolution of our data, we then used each of 188 exposures and measured the PSF counts in each of the 188 difference image that was made by subtracting the reference image (the coadded image of 10 best-seeing exposures) from every single exposure. Here we used the same position of candidate as used in the 63 images. In this way we measure the light curve of the object with 2 min time resolution.

Fig. 3.8 shows the light curves for examples of real variable stars. Note that we converted the PSF counts of each candidate in the difference image to the magnitude based on Eq. (3.20). However, the magnitude might be contaminated by fluxes from blended stars surrounding the candidate star. This demonstrates our ability to properly sample the light curves with high time resolution. Thus the figure shows that the difference image technique works well and can identify variable star candidates as well as measure their light curves.

Fig. 3.9 shows the distribution of secure variable star candidates detected in our analysis over the HSC field-of-view, for candidates with magnitudes  $m_r \leq 24$  and 25 mag in the left and right panel, respectively. To estimate the magnitude of each candidate, we used the PSF magnitude of the candidate in the reference image. Based on the shape of the light curve for each candidate, we visually classified the candidates in different types of variable stars; i) stellar flares, ii) eclipsing or contact binary systems, iii) asteroids (moving

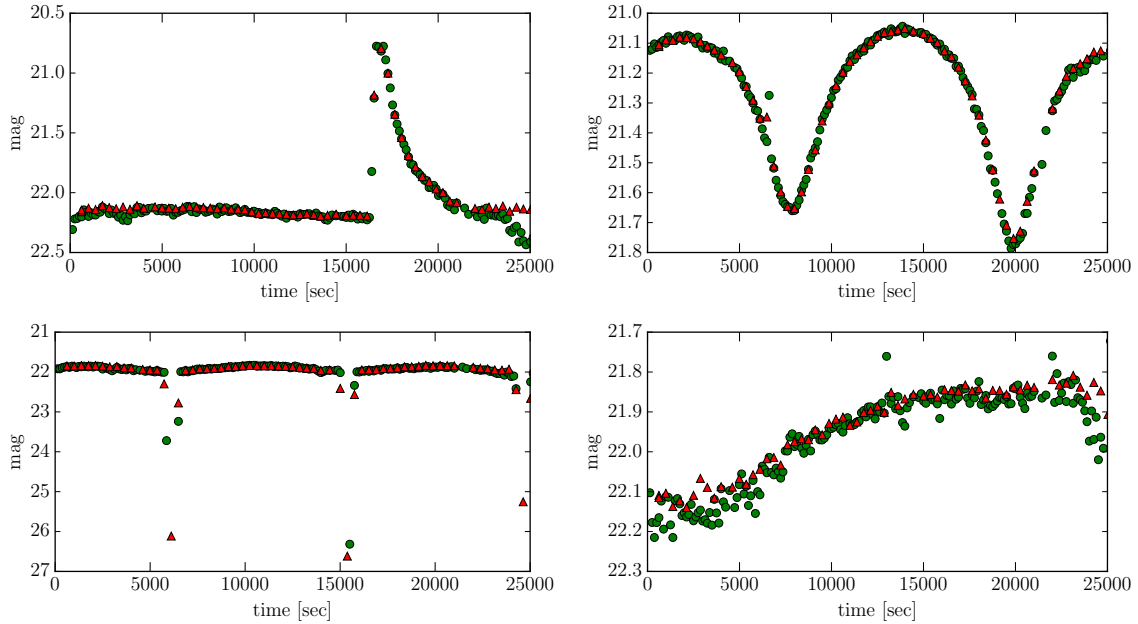


Figure 3.8: Examples of light curves for real variable stars identified in our method. The green-circle data points show the light curve sampled by our original data of 2 min sampling rate, while the red-triangle points are the light curve measured from the coadded data of 3 time-consecutive exposures (therefore 6 min cadence) (see text for details). *Upper left:* candidate stellar flare. When converting the magnitude from the counts in the difference image at each observation time, we used Eq. (3.20). Note that the estimated magnitude might be contaminated by fluxes of neighboring stars in the reference image. *Upper right:* candidate contact binary stars. *Lower left:* the eclipse binary system, which is probably a system of white dwarf and brown dwarf, because one star (white dwarf) has a total eclipse over about 10 min duration, and then the eclipse has about 3 hours period. *Lower right:* candidate variable star, which has a longer period than our observation duration (7 hours).

object), iv) Cepheid variables if the candidates appear to have a longer period than our observation duration (7 hours), and v) “fakes”. Here fakes are those candidates which show time variability only when the seeing conditions are as good as  $\lesssim 0.6''$ . Since such good-seeing data is deeper as found from Figs. 3.5 and 3.10, we seem to find RR-Lyrae type variables whose apparent magnitudes would be around  $r \sim 25$  mag. When the seeing gets worse, these stars cannot be reliably seen in the difference image. Since RR-Lyrae stars should exist in the M31 region, we think the “fake” stars are good candidates for RR-Lyrae stars. The figure shows that our analysis successfully enables to find variable stars across the disk and halo regions. The total number of candidates are 1,334 and 2,740 for  $m_r \leq 24$  and 25 mag, respectively.

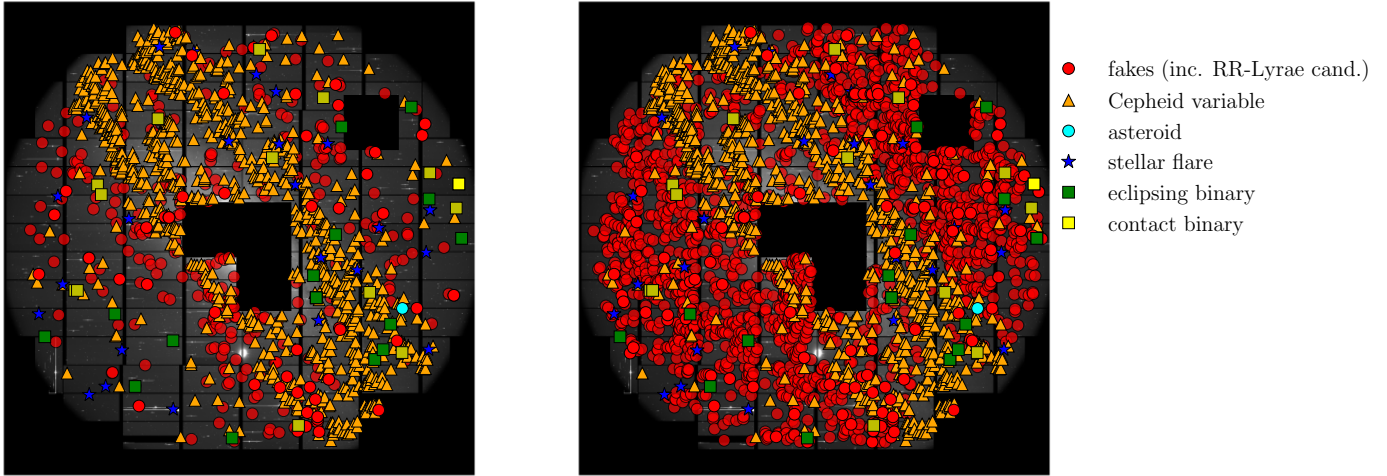


Figure 3.9: Distribution of secure variable star candidates, detected from our analysis using the image difference technique. The different symbols denote different types of candidates classified based on the shapes of their light curves. Here we exclude other non-secure candidates that are CCD artifacts and fake events near to the CCD edge or bright stars. The left panel shows the distribution for the candidates with magnitudes  $m_r \leq 24$  mag, while the right panel shows the candidates at  $m_r \leq 25$  mag. The number of candidates are 1,334 and 2,740, respectively.

### 3.4 Statistics and Selection Criteria

Given the catalog of variable star candidates each of which has its measured light curve, we now search for secure candidates of PBH microlensing. In this section we describe our selection criteria to discriminate the microlensing event from other variables.

#### 3.4.1 Photometric errors of the light curve measurement

Our primary tool to search for variable objects in the dense star regions of M31 is the use of the image difference technique, as we have shown. To robustly search for secure candidates of PBH microlensing that have the expected light curve shapes, it is crucial to properly estimate the photometry error in the light curve measurement. However, accurate photometry for dense star regions in M31 is challenging. To overcome this difficulty, we use the following approach to obtain a conservative estimate of the error. The pipeline performs image subtraction on each patch basis (as denoted by white-color square regions in Fig. 3.4). For a given difference image, we randomly select 1,000 points in each patch region, and then perform PSF photometry at each random point in the same manner as that for the variable

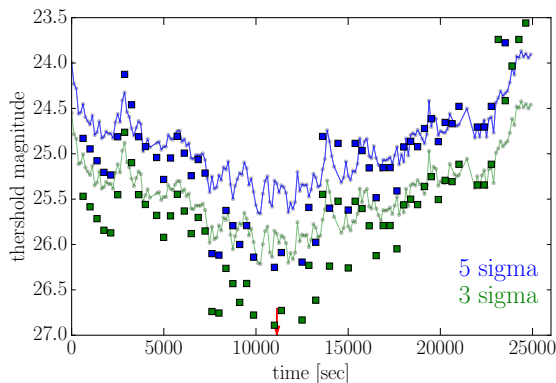


Figure 3.10: The photometric error used for the light curve measurement in the difference image; we randomly select 1,000 points in the difference image of a given patch (here shown for the patch-D2 in Fig. 3.4), measure the PSF photometry at each random point, and then estimate the variance of the PSF photometries (see text for details). The square symbols show the 3- or 5-sigma photometric errors estimated from the variance when using the difference images constructed from the coadded images of 3 exposures, as a function of observation time. The circle symbols, connected by the line, are the results for each exposure. Although we use the photometric error in the ADU counts for a fitting of the microlensing model to the light curve, we here convert the counts to the magnitude for illustrative convenience.

star candidates. In selecting random points, we avoided regions corresponding to bad CCD pixels or near the CCD chip edges. We then estimate the variance from those 1,000 PSF magnitudes, repeat the variance estimation in the difference image for every observation time, and use the variance as a  $1\sigma$  photometry error in the light curve measurement at the observation time. The photometric error estimated in this way would include a contamination from various effects such as a large-scale residual background due to an imperfect background subtraction. We find that the photometric error is larger than the error estimated from the pipeline at the candidate position, which is locally estimated by propagating the Poisson noise of the counts through the image subtraction processes.

Fig. 3.10 shows the photometric error on the light curve measurement in the difference image, estimated based on the above method. The shape of the photometric error appears to correlate with the seeing conditions in Fig. 3.5. The figure shows that most of our data reaches a depth of 26 mag or so thanks to the 8.2m large aperture of Subaru.

### 3.4.2 Microlensing model fit to the light curve data

Here we describe our selection procedure for PBH microlensing events from the candidates. The unique part of our study is the high cadence for the light curve of each candidate,

Table 3.1: Definitions of Statistics

Statistic	Definition
$\Delta C(t_i)$	PSF-photometry counts of a candidate in the $i$ -th difference image at the observation time $t_i$ ; the time sequence of $\Delta C(t_i)$ forms the light curve of each candidate (188 data points, sampled by every 2 min).
$\Delta C_{\text{coadd}}(t_i)$	PSF-photometry counts of a candidate in the $i$ -th difference image of 3 coadded images at $t_i$ (63 data points, sampled by every 6 min)
$\sigma_i$	$1\sigma$ error of PSF-photometry in the $i$ -th difference image (see text for details)
$\sigma_{\text{coadd},i}$	$1\sigma$ error in the $i$ -th difference image of 3 coadded images at $t_i$
bump	sequence of 3 or more time-consecutive data points with $\Delta C_i \geq 5\sigma_i$ in the light curve
bump <sub>len</sub>	length (number) of time-consecutive data points with $\Delta C_i \geq 5\sigma_i$
mlchi2.dof	$\chi^2$ of the light curve fit to microlensing model divided by the degrees of freedom
mlchi2in.dof	$\chi^2$ of the microlensing fit for data points with $t_i$ satisfying $t_0 - t_{\text{FWHM}}^{\text{obs}} \leq t_i \leq t_0 + t_{\text{FWHM}}^{\text{obs}}$
asymmetry $a_{\text{asy}}$	$(1/N_{\text{asy}}) \sum_{t_i} [\Delta C(t_0 - \Delta t_i) - \Delta C(t_0 + \Delta t_i)] / [\Delta C - \Delta C_{\text{min}}]$ (see text for details)
seeing_corr	correlation between the light curve shape and the seeing variation (see text for details)

Table 3.2: Selection Criteria

Selection Criterion	Purpose	No. of remained candidates
$\Delta C_{\text{coadd},i} \geq 5\sigma_{\text{coadd},i}$	initial definition of candidates	15,571
bump <sub>len</sub> $\geq 3$	select candidates with a significant peak(s) in the light curve	11,703
mlchi2dof $< 3.5$	select candidates whose light curve is reasonably well fit by the microlensing	227
$a_{\text{asy}} < 0.17$	remove candidates that have an asymmetric light curve such as star flares	146
significant peak	select candidates that show a clear peak in its light curve (see text for details)	66
visual inspection	visually check each candidate (its light curve and images)	1
seeing_corr	remove candidates whose light curve is correlated with time variation of seeing	1

sampled by every 2 min over about 7 hours. However the monitoring of each light curve is limited by a duration of 7 hours. If a microlensing event has a longer time duration than 7 hours, we can not identify such a candidate. We use the statistics in Table 3.1 to quantify the characteristics of each light curve. Our selection procedure for the candidates are summarized in Table 3.2. We will describe each of the selection steps in detail.

As we described, we start with the master catalog of variable star candidates, which contains 15,571 candidates, to search for microlensing events. Our level 1 requirement is that a candidate event should have a “bump” in its light curve, defined as 3 time-consecutive flux changes each of which has a signal-to-noise ratio greater than  $5\sigma$  in the difference image;  $\Delta C_i \geq 5\sigma_i$ , where the subscript  $i$  denotes the  $i$ -th difference image (at the observation time  $t_i$ ). This criteria leaves us with 11,703 candidates over all the patches.

Next we fit the observed light curves of each candidate with a model describing the expected microlensing light curve. As we described in Section 3.2.3, the light curve of a

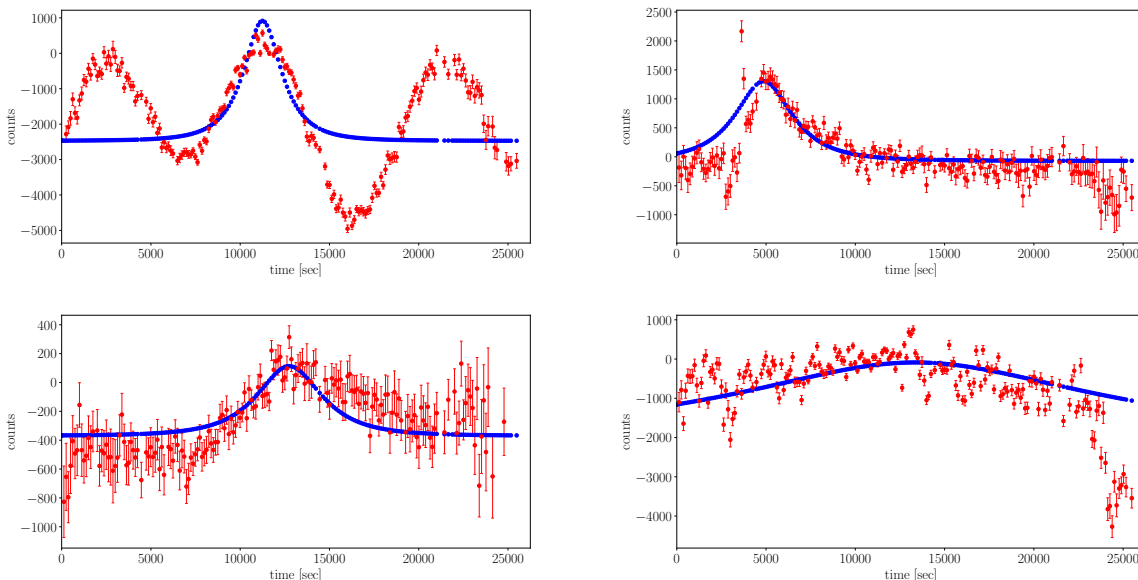


Figure 3.11: Example of the light curves of candidates that are rejected by our selection criteria for a microlensing event. The red points in each panel shows the PSF photometry at each observation time and consist of 188 data points to form the light curve sampled by every 2 min in the difference images. The errorbar around each data point is the  $\pm 1\sigma$  photometry error that is estimated from the PSF photometries of 1,000 random points as shown Fig. 3.10. The blue data points are the light curve for the best-fit microlensing model. The upper-left panel shows an example of the candidates that is rejected due to a bad  $\chi^2_{\min}$  for the fitting to the microlensing light curve. The upper-right panel shows an example of the candidates that is rejected by the asymmetric shape of the light curve around the peak. The lower two panels show examples of the candidates that do not show a prominent peak feature as expected for a microlensing event.

microlensing in the difference image is given as

$$\Delta C(t_i) = C_0 [A(t_i) - A(t_{\text{ref}})], \quad (3.21)$$

where  $C_0$  is the PSF-photometry counts of an unlensed image in the difference image, corresponding to  $F_0$  in Eq. (3.18), and  $A(t_i)$  and  $A(t_{\text{ref}})$  are lensing magnifications at the observation time  $t_i$  and the time of the reference image  $t_{\text{ref}}$ . As described in Section 3.2.3, the light curve in the difference image is characterized by 3 parameters:  $(u_{\min}, t_{\text{FWHM}}, C_0)$ , where  $u_{\min}$  is the impact parameter of closest approach between PBH and a source star in units of the Einstein radius, and  $t_{\text{FWHM}}$  is the FWHM timescale of the light curve.

We identify the time of maximum magnification in the light curve and denote it by  $t_0$ . For the model fitting, we employ the following range for the model parameters:

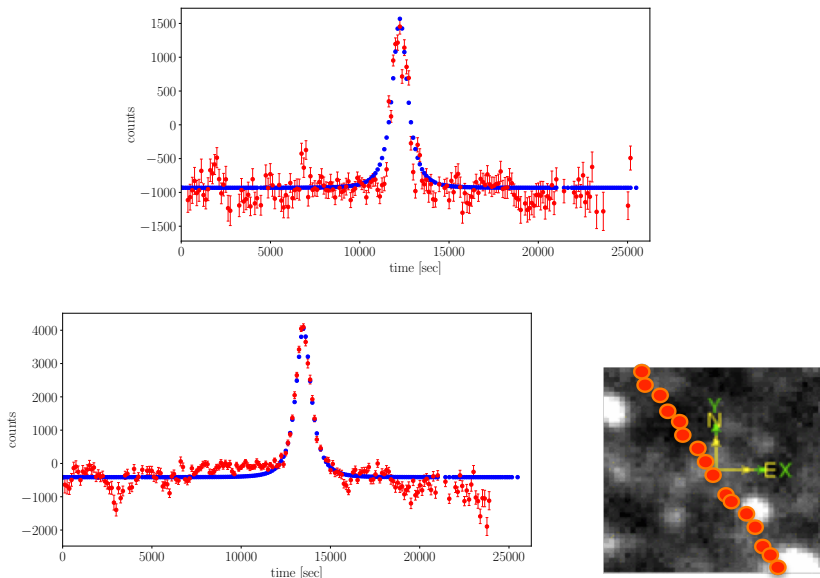


Figure 3.12: The upper panel shows an example of light curves for fake events that are caused by a spike-like image around a bright star. The light curve appears to look like a microlensing event, but it is found to be near a bright star. The lower panel shows the light curve for an asteroid that also shows a microlensing-like light curve. If the PSF photometry is made at the fixed position (the center in the lower-right image), the measured light curve looks like a microlensing event. The red points in the image denotes the asteroid trajectory. From our analysis of M31 observation, we identified one asteroid.

- $0.01 \leq u_{\min} < 1$ , which determines the maximum magnification,  $A_{\max} \equiv A(u_{\min})$  (see Eq. (3.1)). Thus we assume the range of maximum magnification to be  $1.34 \leq A_{\max} \lesssim 100$ .
- $0.01 \leq t_{\text{FWHM}}/[\text{sec}] < 25,000$ . Here the lower limit is much shorter than the sampling rate of light curve (2 min), but we include such a short time-scale light curve for safety (see below). The upper limit corresponds to the longest duration of our observation ( $\sim 7$  hours).
- Once the parameters,  $u_{\min}$  and  $t_{\text{FWHM}}$ , are specified, the intrinsic flux can be estimated as  $C_0 = \Delta C_{\max}^{\text{obs}}/[A_{\max} - A(t_{\text{ref}})]$ , where  $\Delta C_{\max}^{\text{obs}}$  is the counts of the light curve peak in the difference image. In practice, the flux measurement is affected by measurement noise as well as the sampling resolution of light curve, so we allow the intrinsic flux to vary in the range of  $0.5 \times \Delta C_{\max}^{\text{obs}}/(A_{\max} - 1) \leq C_0 \leq 1.5 \times \Delta C_{\max}^{\text{obs}}/(A_{\max} - 1)$ .

The above ranges of parameters are broad enough in order for us not to miss a real candidate of microlensing. For each candidate, we perform a standard  $\chi^2$  fit by comparing the model

microlensing light curve to the observed light curve:

$$\chi^2 = \sum_{i=1}^{188} \frac{[\Delta C^{\text{obs}}(t_i) - \Delta C^{\text{model}}(t_i; C_0, t_{\text{FWHM}}, u_{\text{min}})]^2}{\sigma_i^2}, \quad (3.22)$$

where  $\Delta C^{\text{model}}(t_i)$  is the model light curve for microlensing, given by Eq. (3.21), and  $\sigma_i$  is the rms noise of PSF photometry in the  $i$ -th difference image, estimated from the 1,000 random points as described above.

We compute the reduced  $\chi^2$  by dividing the minimum  $\chi^2$  by the degrees of freedom (188-3=185). We discard candidates that have `mlchi2_dof` > 3.5. This criterion is reasonably conservative (the P-value is  $\sim 10^{-5}$ ). We further impose the condition that the best-fit  $t_{\text{FWHM}} < 14,400$  sec (4 hours), in order to remove candidates whose light curve has a longer time variation than what we can robustly determine. This selection removes most of Cepheid-type variables. This selection leaves 227 candidates. The upper-left panel of Fig. 3.11 shows an example of candidates that are removed by the condition `mlchi2_dof` < 3.5 (i.e. `mlchi2_dof` > 3.5 for this candidate). This is likely to be a binary star system.

Microlensing predicts a symmetric light curve with respect to the maximum-magnification time  $t_0$  ( $A_{\text{max}}$ ); the light curve at  $t_i = |t_0 \pm \Delta t|$  should have a similar flux as the lensing PBH should have a nearly constant velocity within the Einstein radius. Following Griest et al. (2014), we define a metric to quantify the asymmetric shape of the light curve,

$$a_{\text{asy}} = \frac{1}{N_{\text{asy}}} \sum_{t_i \in |t_0 \pm t_{\text{FWHM}}^{\text{obs}}|} \frac{|\Delta C(t_0 - \Delta t_i) - \Delta C(t_0 + \Delta t_i)|}{\overline{\Delta C} - \Delta C_{\text{min}}}. \quad (3.23)$$

Here  $t_{\text{FWHM}}^{\text{obs}}$  is the timescale that the observed light curve declines to half of its maximum value. For this purpose, we take the longer of the timescales from either side of the two half-flux points from the maximum peak. If the expected half-flux data point is outside the observation window of light curve, we take the other side of the light curve to estimate  $t_{\text{FWHM}}^{\text{obs}}$ . The summation runs over the data points satisfying  $t_i \leq |t_0 \pm t_{\text{FWHM}}^{\text{obs}}|$ , 2 times the FWHM timescale around the light curve peak. Note that, if the summation range is outside the observation window, we take the range  $|t_0 \pm (t_0 - t_{\text{start}})|$  or  $|t_0 \pm (t_{\text{end}} - t_0)|$ , where  $t_{\text{start}}$  or  $t_{\text{end}}$  is the start or end time of the light curve.  $N_{\text{asy}}$  is the number of data points in the above summation,  $\overline{\Delta C}$  is the average of the data points taken in the summation, and  $\Delta C_{\text{min}}$  is the minimum value of the counts.

By imposing the condition  $a_{\text{asy}} < 0.17$ , we eliminate candidates that have an asymmetric light curve, and we have confirmed that this condition eliminates most of the star flare events

from the data base. This condition also eliminates some of the variable stars that are likely to be Cepheids. After this cut the number of candidates is reduced to 146. The upper-right panel of Fig. 3.11 shows an example of the candidates that are removed by the condition  $a_{\text{asy}} < 0.17$ .

In addition we discard candidates, if the observed light curve does not have any significant peak; e.g., we discard candidates if  $\text{mlchi2in\_dof} > 3.5$  (see Table 3.1 for the definition) or if the time of the light-curve peak is not well determined. The lower panels of Fig. 3.11 show two examples of such rejected candidates, which do not show a clear bump feature in the light curve as expected for microlensing. This selection cut still leaves us with 66 candidates.

Finally we perform a visual inspection of each of the remaining candidates. We found various fake events that are not removed by the above automated criteria. Most of the fake events are caused by an imperfect image subtraction; in most cases the difference image has significant residuals near the edges of CCD chips and around bright stars. In particular, bright stars cause a spiky residual image in the difference image, that results in fake candidates that have microlensing-like light curve if measured at a fixed position. We found 44 fake events caused by such spike-like images around bright stars. There are 20 fake events around the CCD edges. The upper panel of Fig. 3.12 shows an example of spike-like fakes. We were also able to identify 1 fake event caused by a moving object, an asteroid. If the light curve is measured at the fixed position which the asteroid is passing, it results in a light curve which mimics microlensing, as shown in the lower panel of Fig. 3.12.

Thus our visual inspection leads us to conclude that 65 events among 66 remaining candidates are fake and we end up with one candidate event which passes all our cuts and visual checks. The candidate position is  $(\text{RA}, \text{dec}) = (00\text{h } 45\text{m } 33.413\text{s}, +41\text{d } 07\text{m } 53.03\text{s})$ .

Fig. 3.13 shows the images and the light curve for this candidate of microlensing event. Although the light curve looks noisy, it is consistent with the microlensing prediction. The magnitude inferred from the reference image implies that the candidate has a magnitude of  $r \sim 24.5$  mag. The obvious question to consider is whether this candidate is real. Unfortunately, the candidate is placed outside the survey regions of the Panchromatic Hubble Andromeda Treasury (PHAT) catalog in Williams et al. (2014) (also see Dalcanton et al. (2012))<sup>4</sup>, so the HST image is not available. It is unclear if there are any variable stars that could produce the observed light curve, with a single bump. To test the hypothesis that the candidate is a variable star, we looked into another  $r$ -band data that was taken in the commissioning run in 2013, totally different epoch from our observing night. However, the seeing condition of the  $r$ -band is not good (about  $1.2''$ ), so it is difficult to conclude whether

---

<sup>4</sup><https://archive.stsci.edu/prepds/phat/>

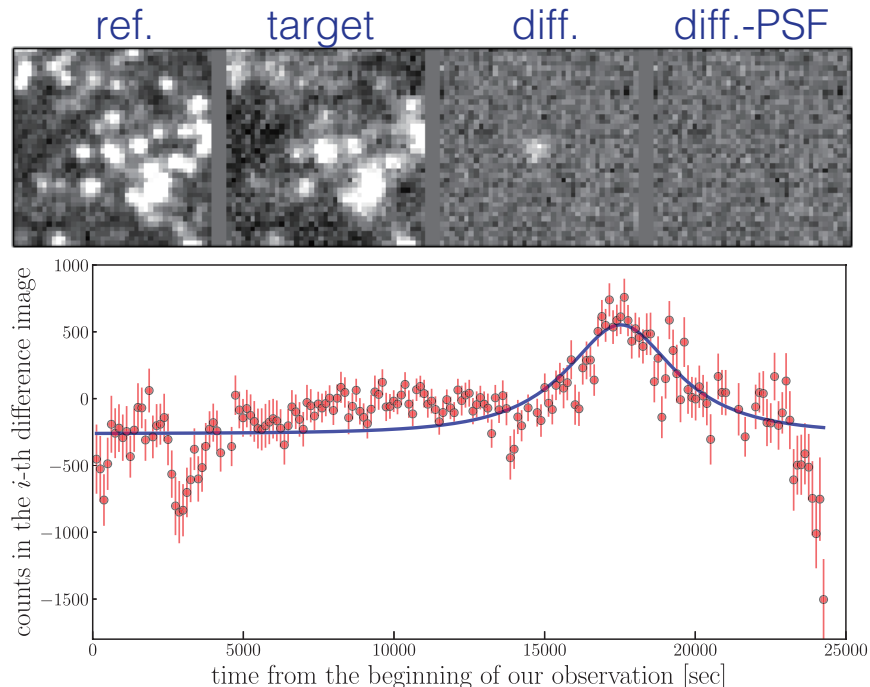


Figure 3.13: One remaining candidate that passed all the selection criteria of microlensing event. The images in the upper plot show the postage-stamped images around the candidate as in Fig. 3.7: the reference image, the target image, the difference image and the residual image after subtracting the best-fit PSF image, respectively. The lower panel shows that the best-fit microlensing model gives a fairly good fitting to the measured light curve.

the star pops out of the noise in the difference images. Similarly we looked into the  $g$ -band images taken in the HSC commissioning run. However, due to the short duration of the data itself ( $\sim 15$  min), it is difficult to judge whether this candidate has a time variability between the  $g$  images. Hence we cannot draw any convincing conclusion on the nature of this candidate (we will discuss the additional test of this candidate in Section 4.3). In what follows, we derive an upper bound on the abundance of PBHs as a constituent of DM for both cases where we include or exclude this remaining candidate.

### 3.5 Results: Upper bound on the abundance of PBH contribution to dark matter

In this section we describe how we use the results of our PBH microlensing search to derive an upper limit on the abundance of PBHs assuming PBHs consist of some fraction of DM in the MW and M31 halos. In order to do this, we need three ingredients – (1) the event rates of microlensing as we estimated in Section 3.2.2, (2) a detection efficiency for PBH

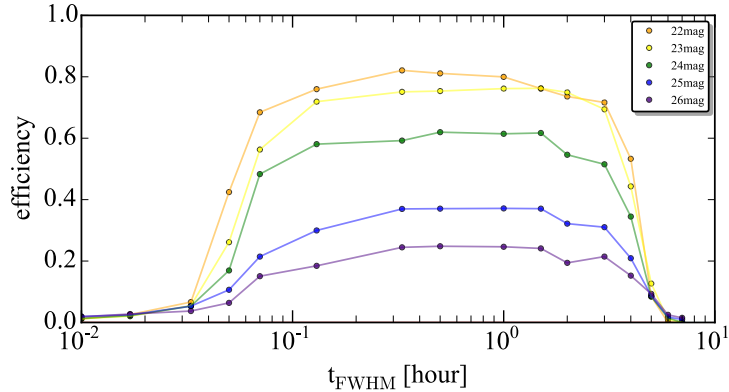


Figure 3.14: The detection efficiency estimated from light curve simulations taking into account the PSF photometry error in each of 188 target images we used for the analysis (see text for details). Here we generated Monte Carlo simulations of microlensing events randomly varying the three parameters: the impact parameter (or maximum lensing magnification), the FWHM timescale of microlensing light curve ( $x$ -axis), and the observation time of the microlensing magnification peak, for source stars of a fixed magnitude as indicated by legend. The detection efficiency for each source magnitude is estimated from 1,000 realizations.

microlensing events, which quantifies the likelihood of whether a microlensing event, even if it occurs during our observation duration, will pass all our selection cuts, and (3) the number of source stars in M31. In this section we describe how to estimate the latter two ingredients and then derive the upper bound result.

### 3.5.1 Efficiency Calculation: Monte Carlo simulation

The detection efficiency of PBH microlensing events depends upon the unlensed flux of the star in M31,  $F_0$ , and quantifies the fraction of microlensing events with a given impact parameter ( $u_{\min}$ ) and time scale ( $t_{\text{FWHM}}$ ) that can be detected given our selection cuts.

To estimate the efficiency we carry out simulations of microlensing light curves. We vary the model parameters to generate a large number of realizations of the simulated microlensing light curves. First we randomly select the time of maximum magnification ( $t_{\max}$ ) from the observation window, the impact parameter  $u_{\min} \in [0, 1]$  and the FWHM timescale  $t_{\text{FWHM}}$  in the range of  $0.01 \leq t_{\text{FWHM}}/[\text{sec}] \leq 25,000$  to simulate the input light curve in the difference image for a given intrinsic flux of a source star,  $F_0$  (more precisely, the intrinsic counts  $C_0$  in the difference image). Then, we add random Gaussian noise to the light curve at each of the observation epochs  $t_i$ , estimated from the  $i$ -th difference image in a given patch (Section 3.4.1). For each intrinsic flux, we generate 10,000 simulated light curves in each patch region.

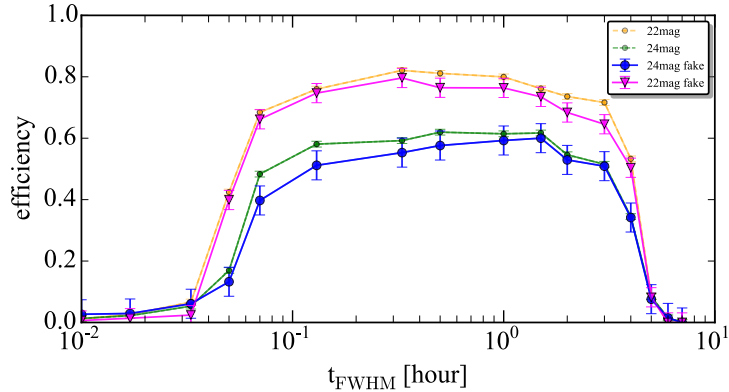


Figure 3.15: A justification of the detection efficiency estimation, based on the different method using the fake image simulations. We injected fake microlensing star images in individual exposures of the real HSC data (patch-D2 in Fig. 3.4), re-ran the whole data processing, and assessed whether the fake images pass all the selection criteria for a microlensing event. The small circles show the results from light curve simulations (the same as shown in Fig. 3.14), and the large symbols show the results from the fake image simulations, for the intrinsic magnitudes of 22 and 24 mag, respectively.

For each simulated light curve, we applied all of our selection cuts (see Section 3.4 and Tables 3.1 and 3.2) to assess whether the simulated event passes all the criteria. Fig. 3.14 shows the estimated efficiency for a given intrinsic flux of a star as a function of the timescale ( $t_{\text{FWHM}}$ ) of the simulated light curve, in the patch-D2 of Fig. 3.4. Our results indicate that our pipeline can recover about 70–60% of microlensing events for stars with intrinsic magnitude  $m_r = 23$ –24 mag, if the timescale is in the range  $t_{\text{FWHM}} \simeq [0.1, 3]$  hours. For fainter stars with  $m_r = 25$ –26 mag, the efficiency is reduced to about 30–20%. A microlensing event for a bright star is easier to detect, if it occurs, because even a slight magnification is enough to identify it in the difference image. On the other hand, a fainter star needs more significant magnification to be detected. If the microlensing timescale is in the range of  $4 \text{ min} \lesssim t_{\text{FWHM}} \lesssim 3 \text{ hours}$ , the event can be detected by our observation (2 min sampling rate and 7 hours observation). We interpolated the results for different intrinsic fluxes to estimate the detection efficiency for an arbitrary intrinsic flux. We repeated the simulations using the photometry errors to estimate the efficiency for each patch.

We also performed an independent estimation of the detection efficiency. We used fake image simulations where we injected fake microlensing star events into individual HSC images using the software GalSim in Ref. Rowe et al. (2015) (also see Huang et al. (2017)), and then re-ran the whole data reduction procedure including image subtraction to measure the light curve. We then assessed whether the fake microlensing event can be detected by our selection criteria. Fig. 3.15 compares the detection efficiency estimated using the fake image

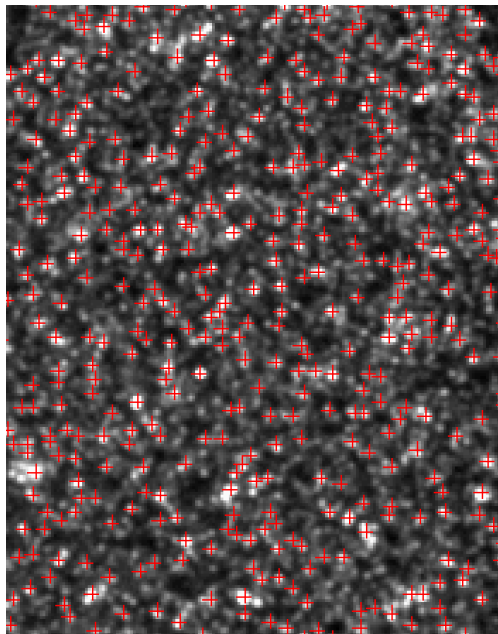


Figure 3.16: An example image of the distribution of peaks (cross symbols) identified in a small region of the reference image (the coadded image of 10 best-seeing exposures), which has a size of about  $38'' \times 30''$  area and is taken from the patch-D2 region. We measure the PSF photometry of each peak, and then use the number of peaks as an estimation of the number of source stars in each magnitude bin.

simulations with the results of the simulated light curves (Fig. 3.14) in the patch-D2. The figure clearly shows that the two results fairly well agree with each other. The fake image simulations are computationally expensive. With the results in Fig. 3.15, we conclude that our estimation of the detection efficiency using the simulated light curves are fairly accurate.

### 3.5.2 Estimation of star counts in M31

The expected number of microlensing events depends on the number of source stars in M31. However, since individual stars are not resolved in the M31 field, it is not straightforward to estimate the number of source stars from the HSC data. This is the largest uncertainty in our results, so we will discuss how the results change for different estimations of the source star counts. As a conservative estimate for the number of source stars, we use the number of “detected peaks” in the reference image of M31 data, which has the best image quality (coadding the 10 best-seeing exposures) and is used for the image subtraction. Fig. 3.16 shows the distribution of peaks identified from the reference image in an example region (with a size  $226 \times 178$  pixels corresponding to about  $38'' \times 30''$ ), taken from the patch-D2 region. The figure clearly shows that only relatively bright stars, or prominent peaks,

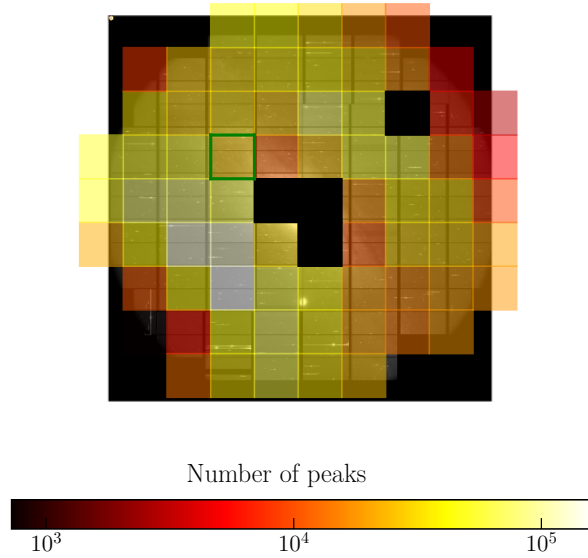


Figure 3.17: The color scale denotes the total number of detected peaks in each patch region for the HSC data. Note that the black-color patches are excluded from our analysis due to too crowded regions. The number of the peaks in a disk region tends to be smaller than that in a outer, halo region, because stars in a disk region are more crowded and only relatively brighter stars or more prominent peaks are identified.

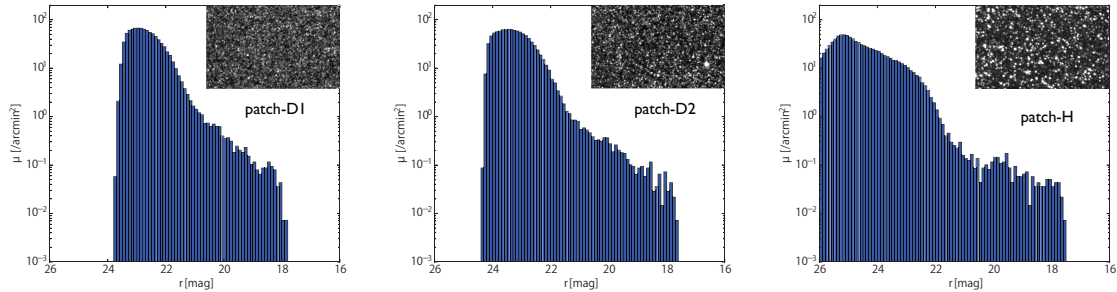


Figure 3.18: The peaks counts of HSC data in different regions of M31; two disk regions denoted as patch-D1 and patch-D2 and the halo region denoted as patch-H in Fig. 3.4. The HSC data can find a more number of fainter peaks in the halo regions because individual stars are more resolved and less crowded.

are identified, but a number of faint stars or even bright stars in a crowded (or blended) region will be missed. Thus this estimate of the source star counts is extremely conservative. Nevertheless this is one of the most secure way to obtain source counts, so we will use these counts in each patch region.

The color scale in Fig. 3.17 shows the total number of peaks in each patch region. It can be seen that a relatively larger number of the peaks are identified in the outer halo region of

M31, because each star can be resolved without confusion. On the other hand, there are less number of resolved peaks in the patches corresponding to the disk region due to crowding. The total number of peaks identified over all the patch regions is about 6.4 million. Fig. 3.18 shows the surface density of peaks identified in HSC in the disk and halo regions of M31 for the three patches marked in Fig. 3.4. To estimate the magnitudes for the surface density, we performed PSF photometry of each peak using its location as the PSF center. The figure confirms that more number of peaks are identified in the halo region.

As another justification for the estimation of the source star counts, we compare the number counts of peaks in the HSC image with the luminosity function of stars in the HST PHAT catalog in Ref. Williams et al. (2014) (also see Dalcanton et al. (2012)), where individual stars are more resolved thanks to the high angular resolution of the ACS/HST data. Since the PHAT HST data was taken with F475W and F814W filters, we need to make color transformation of the HST photometry to infer the HSC  $r$ -band magnitude. For this purpose, we first select 100 relatively bright stars in the PHAT catalog. Then we match the HST stars with the HSC peaks by their RA and dec positions, and compare the magnitudes in the HST and HSC photometries. In order to derive the color transformation, we estimated a quadratic relation between the HST and HSC magnitudes for the matched stars in a two-dimensional space of  $(m_r^{\text{HSC}} - m_{\text{F475W}})$  and  $(m_{\text{F475W}} - m_{\text{F814W}})$ :

$$m_r^{\text{HSC}} = m_{\text{F475W}} - 0.0815 - 0.385(m_{\text{F475W}} - m_{\text{F814W}}) - 0.024(m_{\text{F475W}} - m_{\text{F814W}})^2. \quad (3.24)$$

We then applied this color transformation to all the PHAT stars. Although the above one-to-one color transformation is not perfect for different types of stars, we do not think that the uncertainty largely affects our main results as we will discuss below.

Fig. 3.19 compares the surface density of stars in the HST PHAT catalog with that of the HSC peaks, as a function of magnitudes, in the overlapping regions between our M31 data and HST PHAT. These regions correspond to “bricks07” and “bricks11”. The figure clearly shows that the HSC peak counts fairly well reproduces the HST results down to  $r \sim 23$  mag. Since the HSC photometry of each peak should be contaminated by fluxes of neighboring stars, we would expect a systematic error in the PSF photometry, which causes a horizontal shift in the surface density of peaks (the HSC photometry is expected to over-estimate the magnitude). Even with this contamination, the agreement looks promising. However, it is clear that the HSC peak counts clearly misses the fainter stars, which can be potential source stars for PBH microlensing. The surface density of HST stars in different regions look similar.

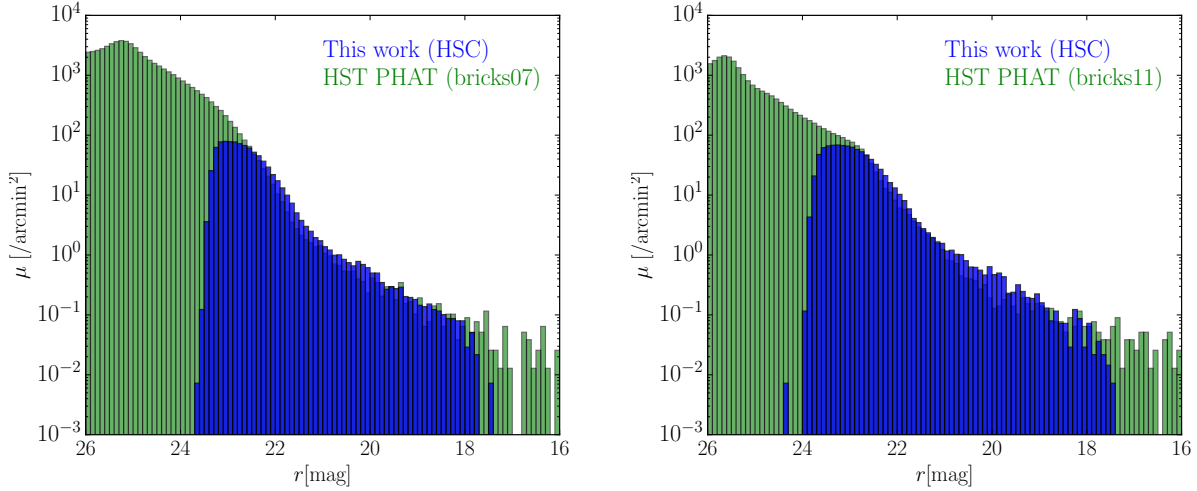


Figure 3.19: The green histogram shows the luminosity function of M31 stars in the HST PHAT catalog, while the blue histogram shows that of the peaks in the HSC image. We converted the magnitudes of HST stars to the HSC  $r$ -band magnitudes using Eq. (3.24). The comparison is done using the PHAT catalog in the two regions of “bricks07” (or B7) and “bricks11” (B11) in Fig. 1 of Dalcanton et al. (2012), which are contained in the patch right next to or one-upper to the patch-D2 in the HSC data (see Fig. 3.4). These regions are in a disk region of M31. The luminosity function of HSC peaks fairly well reproduces the HST result down to  $r \sim 23$  mag, but clearly misses fainter stars. The PHAT luminosity functions in the two regions appear to be in a similar shape.

The data overlap between HSC and PHAT covers the disk region only partially. Nevertheless, as an optimistic estimate of our star counts, we infer the underlying luminosity function of stars in the disk region from the HST PHAT catalog based on the number counts of HSC peaks at  $m_r = 23$  mag in each patch of the disk regions, assuming that the luminosity function of HST stars is universal in the disk regions. For the halo regions, we use the HSC peak counts. In this optimistic estimate of source stars, we find about  $8.7 \times 10^7$  stars down to  $m_r = 26$  mag over the entire region of M31, which is a factor of 14 more number of stars than that of HSC peaks. However, the source stars extrapolated from the HST data are faint, and will suffer from lower detection efficiency. Therefore, the final constraints do not improve a lot from these improved star counts.

One might worry about a possible contamination of dust extinction to the number counts of source stars. However our estimation of the source star counts is based on the HSC photometry that is already affected by dust extinction. Hence, we do not think that dust extinction largely affects the following results.

### 3.5.3 Expected number of PBH microlensing events

Now we use the results of our microlensing search to constrain the abundance of PBHs in the halo regions of MW and M31. The expected number of PBH microlensing events in our HSC data is given by

$$N_{\text{exp}}\left(M_{\text{PBH}}, \frac{\Omega_{\text{PBH}}}{\Omega_{\text{DM}}}\right) = \frac{\Omega_{\text{PBH}}}{\Omega_{\text{DM}}} \int_0^{t_{\text{obs}}} \frac{dt_{\text{FWHM}}}{t_{\text{FWHM}}} \int dm_r \frac{dN_{\text{event}}}{d \ln t_{\text{FWHM}}} \frac{dN_s}{dm_r} \epsilon(t_{\text{FWHM}}, m_r), \quad (3.25)$$

where  $dN_{\text{exp}}/dt_{\text{FWHM}}$  is the differential event rate for a single star (Fig. 3.3) per logarithmic timescale,  $dN/dm_r$  is the luminosity function of source stars in the  $r$ -band magnitude range  $[m_r, m_r + dm_r]$ , and  $\epsilon(m_{\text{FWHM}}, m_r)$  is the detection efficiency quantifying a probability that a microlensing event for a star with magnitude  $m_r$  and the light curve timescale  $t_{\text{FWHM}}$  is detected by our selection procedures. The number counts  $dN/dm_r$  and the detection efficiency  $\epsilon(m_{\text{FWHM}}, m_r)$  are estimated in each patch of the HSC data, so we sum the expected number of microlensing events over all the patches to estimate the expected number of total events. The event rate depends on the mass fraction of PBHs to the total DM mass in the halo regions,  $\Omega_{\text{PBH}}/\Omega_{\text{DM}}$ . Note that we have assumed a parametric model for the total matter content of the MW and M31 halos constrained by their respective rotation curves (see the explanation for Fig. 3.3). The PBH DM mass fraction does not depend on the cosmological matter parameter,  $\Omega_{\text{m}0}$ , that is relevant for the cosmic expansion.

We use the following procedure to estimate  $dN_s/dm_r$  and  $\epsilon$  in Eq. (3.25). Since individual stars are not resolved in the HSC data, especially in the disk region of M31, it is not straightforward to estimate the number of source stars from the HSC data alone. This constitutes a significant uncertainty in our results. To overcome this difficulty, we use the HST PHAT star catalog (e.g. Fig. 3.19). For the overlapping regions with the HST PHAT survey, we used the PHAT star counts down to  $m_r \sim 26$ . For the non-overlapping regions in the M31 disk, we infer the luminosity function by extrapolating the number counts of HSC peaks at  $m_r = 23$  down to  $m_r = 26$  based on the PHAT luminosity function of stars at a similar distance from the M31 center. For our default analysis, we used about  $8.7 \times 10^7$  stars down to  $m_r = 26$  mag over the entire region of M31, which is a factor 14 more number of stars than that of HSC peaks. The large number of source stars in the M31 region can be compared with those in previous studies, e.g., Griest et al. (2014) used  $\sim 1.5 \times 10^5$  source stars for the microlensing search in Kepler data.

For an estimation of the detection efficiency  $\epsilon(t_{\text{FWHM}}, m_r)$  in Eq. (3.25), we carry out Monte Carlo simulations of microlensing light curves adopting random combinations of the model parameters (the impact parameter,  $t_{\text{FWHM}}$ , and the intrinsic flux) and adding the

statistical noise based on the photometry errors in each HSC-patch region (e.g. Fig 3.14). These simulations allow us to estimate the fraction of simulated light curves that can be recovered by our selection procedures. Our results indicate that our pipeline can recover about 70–60% of microlensing events for stars with intrinsic magnitude  $m_r = 23$ –24 mag, if the timescale is in the range  $t_{\text{FWHM}} \simeq [0.1, 3]$  hours. For fainter stars with  $m_r = 25$ –26 mag, the efficiency is reduced to about 30–20%.

### 3.5.4 Experimental limits on the abundance of PBHs

Next we combine the estimates of  $dN_{\text{event}}/d \ln t_{\text{FWHM}}$ ,  $dN_s/dm_r$  and  $\epsilon(t_{\text{FWHM}}, m_r)$  in Eq. (3.25) to constrain the abundance of PBHs. Assuming the number of microlensing events follow a Poisson distribution, the probability to observe a given number of such events,  $N_{\text{obs}}$ , is given by  $P(k = N_{\text{obs}} | N_{\text{exp}}) = \left[ (N_{\text{exp}})^k / k! \right] \exp[-N_{\text{exp}}]$ . Hence 95% C.L. interval is estimated as  $P(k = 0) + P(k = 1) \geq 0.05$ , leading to  $N_{\text{exp}} \leq 4.74$  assuming that the candidate in Fig. 3.13 is real. Fig. 5.7 shows our result in comparison with other observational constraints on the abundance of PBHs on different mass scales. In the results, we took into account the effect of finite source star size (Witt & Mao 1994) as well as the effect of wave optics on the microlensing cross section (Gould 1992; Nakamura 1998). The finite-source size effect modifies our constraints on mass scales,  $M_{\text{PBH}} \lesssim 10^{-7} M_{\odot}$  where the Einstein radii of the PBHs become comparable to or smaller than the size of the source stars. We caution that we may have underestimated the impact somewhat as we have assumed a solar radius for all stars in M31, while some of the stars would likely be giants. The wave effect arises from the fact that the Schwarzschild radii of light PBHs with  $M \lesssim 10^{-11} M_{\odot}$  become comparable to the wavelength of HSC  $r$ -band filter (centered around 600 nm). In this regime, the wave nature of light becomes important and can further lower the maximum magnification of the microlensing light curve. This results in a lower event rate for a given detection threshold. These effects need to be further studied and carefully accounted for. Nevertheless the figure shows that a single night of HSC data on M31 results in a tight upper bound on the mass fraction of PBHs to DM,  $\Omega_{\text{PBH}}/\Omega_{\text{DM}}$ . The origin of the constraint can be easily understood. Given that we monitor about  $10^8$  stars, we expected to observe about 1,000 microlensing events if PBHs of a single mass scale  $M_{\text{PBH}} \sim 10^{-9} M_{\odot}$  make up all DM in the MW and M31 halo regions (see Fig. 3.3), and yet we could identify only a single event. In other words, only a small mass fraction of PBHs such as  $\Omega_{\text{PBH}}/\Omega_{\text{DM}} \simeq 0.001$  is allowed in order to reconcile the PBH DM scenario with our M31 data. Our results constrain PBHs in an open window of PBH masses,  $M_{\text{PBHs}} \simeq [10^{-11}, 10^{-9}] M_{\odot}$ , as well as give tighter constraints than the previous works in the range of  $M_{\text{PBH}} \simeq [10^{-9}, 10^{-6}] M_{\odot}$ . In particular, our constraint is tighter than

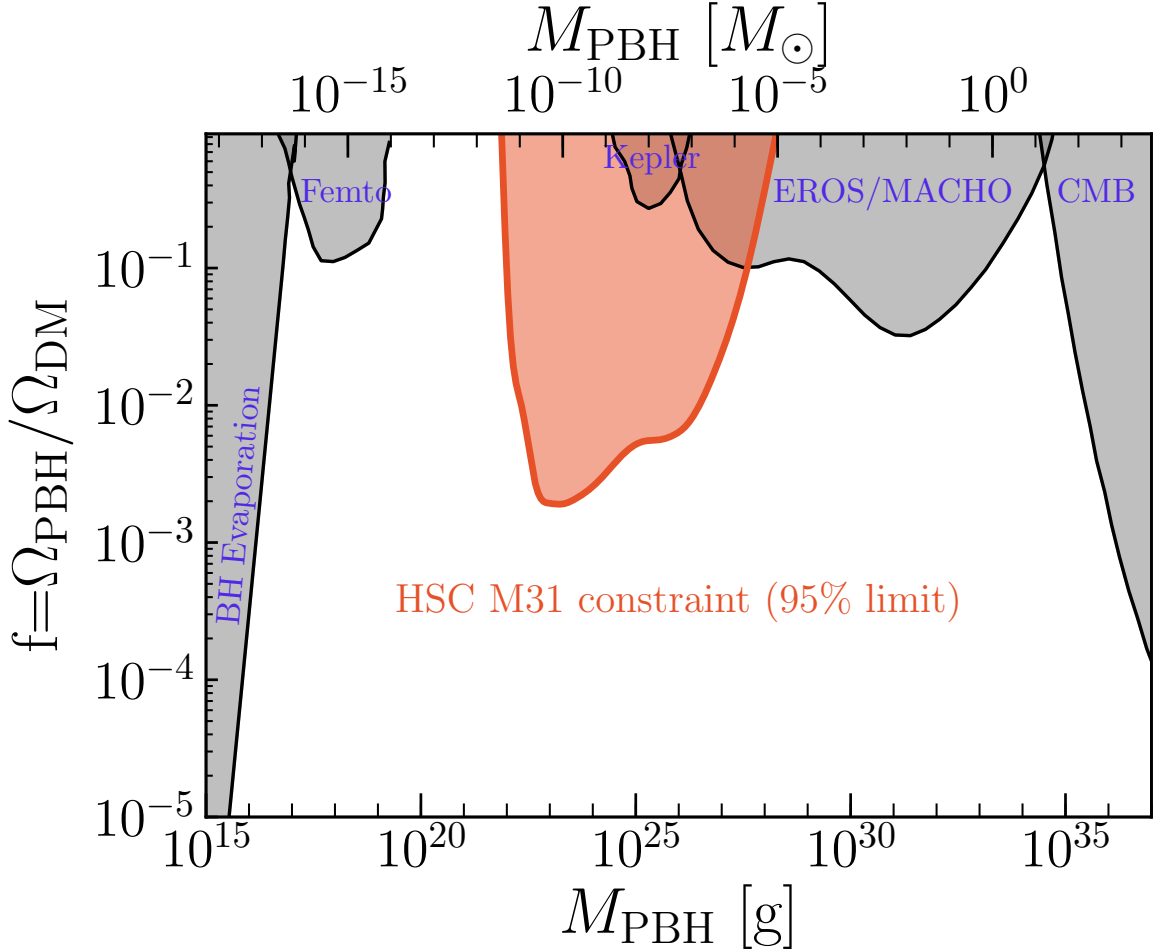


Figure 3.20: The red-color shaded region show the 95% C.L. upper bound on the PBH mass fraction to DM in the halo regions of MW and M31, derived from our microlensing search of M31 stars based on the “one-night” HSC/Subaru data. To derive this constraint, we took into account the effect of finite source size, assuming that all source stars in M31 have a solar radius, as well as the effect of wave optics in the HSC  $r$ -band filter on the microlensing event (see text for details). The effects weaken the upper bounds at  $M \lesssim 10^{-7} M_{\odot}$ , and give no constraint on PBH at  $M \lesssim 10^{-11} M_{\odot}$ . Our constraint can be compared with other observational constraints as shown by the gray shaded regions: extragalactic  $\gamma$ -rays from PBH evaporation (Carr et al. 2010), femtolensing of  $\gamma$ -ray burst (“Femto”) (Barnacka et al. 2012), microlensing search of stars from the satellite 2-years Kepler data (“Kepler”) (Griest et al. 2014), MACHO/EROS/OGLE microlensing of stars (“EROS/MACHO”) (Tisserand et al. 2007), and the accretion effects on the CMB observables (“CMB”) (Ali-Haïmoud & Kamionkowski 2017), updated from the earlier estimate (Ricotti et al. 2008).

the constraint from the 2-year Kepler data that had monitored an open cluster containing  $10^5$  stars, with about 15 or 30 min cadence over 2 years (Griest et al. 2014).

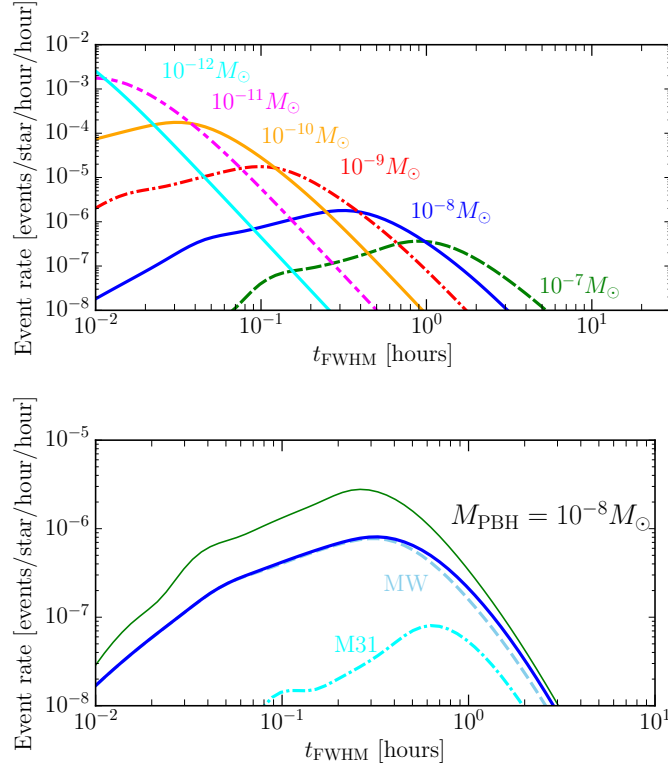


Figure 3.21: The event rate of PBH microlensing for a single star in M31 when taking into account the effect of finite source size. Given the fact that the HSC data (down to  $r \simeq 26$  mag) is sufficiently deep to reach main-sequence stars in M31, rather than red-giant branch stars, we assume a solar radius for source star size. The finite source size effect lowers the event rate compared to Fig. 3.3. The lower panel shows the relative contribution of PBHs in the MW or M31 halo region to the event rate for PBHs with  $M_{\text{PBH}} = 10^{-8} M_{\odot}$ . The upper thin solid curve is the result for a point source, the same as in the right panel of Fig. 3.3. The microlensing events in M31 are mainly from nearby PBHs to a source star at distance within a few tens of kpc (see Fig. 3.1), so the finite source size effect is more significant for such PBHs due to their relatively small Einstein radii.

## 3.6 Discussion

Although our results for the upper bounds in Fig. 5.7 are promising, we employed several assumptions. In this section, we discuss the impacts of our assumptions.

One uncertainty in our bounds comes from the number counts of source stars in M31, which is a result of blending of stars in the HSC data due to overcrowding, especially in the disk regions of M31. If we use the number of HSC peaks for the counts of source stars,  $6.4 \times 10^6$  instead of  $8.7 \times 10^7$ , the counts extrapolated from the HST luminosity function, the upper bounds in Fig. 5.7 are weakened by a factor of 10. Nevertheless the upper bounds are quite tight, and very meaningful. However, we again stress that the use of HSC peak counts

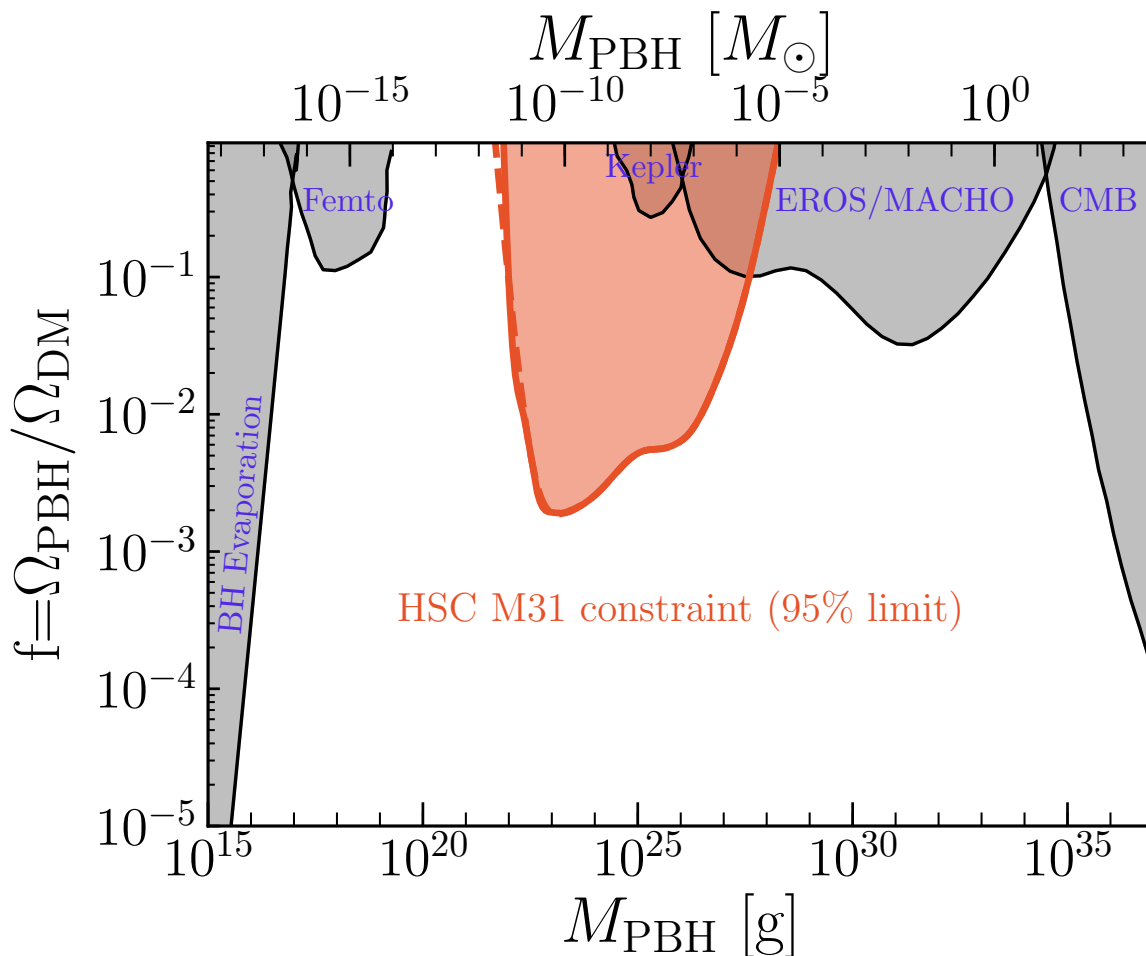


Figure 3.22: The solid curve shows the 95% C.L. upper bound when taking into account the effects of finite source size on the event rate of microlensing, assuming a solar radius for stars in M31. For comparison, the dashed curve shows the results without considering the wave effect.

is extremely conservative, so we believe that our fiducial method using the HST-extrapolated counts of source stars is reasonable.

Another uncertainty in our analysis is the effect of finite source size. As can be found by comparing Eqs. (3.3) and (3.4), the angular size of the source star can be greater than the Einstein radius if PBHs are close to M31 or if PBHs are in the small mass range such of  $M_{\text{PBH}} \lesssim 10^{-10} M_{\odot}$  (assuming solar radius for the star), all of which result in a smaller Einstein radius. Compared to the distance modulus for M31 is  $\mu \simeq 24.4$  mag, our HSC depth is deep enough ( $r \simeq 26$  mag) to reach main sequence stars whose absolute magnitudes  $M_r \simeq 1.5$  mag. According to Figs. 23 and 24 in Dalcanton et al. (2012), most such faint stars at  $r \sim 25$ –26 mag would be either main sequence stars (probably A or F-type stars) or

subgiant stars. In either case such stars have radii similar to the Sun within a factor of 2 or so <sup>5</sup>(North et al. 2007). The shallower data such as the work by de Jong et al. (2006) probes the microlensing events only for much brighter stars such as red giant branch (RGB) stars. RGB stars have much greater radius than that of main sequence stars, where the finite source size effect is more significant. Here we employ a solar radius ( $R_{\odot} \simeq 6.96 \times 10^{10}$  cm) for all source stars for simplicity, assuming that the upper bound is mainly from the microlensing for main sequence stars, rather than for RGB stars (Dalcanton et al. 2012). We followed Witt & Mao (1994) to re-estimate the event rates of PBHs microlensing taking into account the finite source size effect. Fig. 3.21 shows that the finite source size effect lowers the event rate, compared to Fig. 3.3. In particular the effect is greater for PBHs of smaller mass scales and in the M31 halo region.

The dashed curve in Fig. 3.22 shows the upper bounds when ignoring the finite source size effect (i.e. assuming a point source for M31 stars), for both cases of the HST PHAT-extrapolated counts of source stars. As expected, the finite source size effect significantly weakens the upper bounds for PBHs of smaller mass scales. Nevertheless, our results give the tightest, observational upper bounds in the mass range,  $M_{\text{PBH}} \simeq [10^{-11}, 10^{-6}]M_{\odot}$ , a range spanning 5 orders of magnitude. Since the Schwarzschild radii for light PBHs with  $M \lesssim 10^{-10}M_{\odot}$  become comparable with or smaller than the wavelength of the HSC  $r$ -band filter, the wave effect lowers the maximum magnification of the microlensing light curve (Nakamura 1998; Takahashi & Nakamura et al. 2003). These finite source size and wave effects need to be further carefully studied, and this is our future work.

In our study above, we only considered a case where PBHs have a monochromatic mass spectrum. On the other hand, theory for PBH formation, via the nature of primordial fluctuations or the nonlinear collapse mechanism, predicts that PBHs generally have a mass spectrum, rather than the monochromatic spectrum. To compare models with non-monochromatic spectrum, our observed number of events should be compared to the events predicted using Eq. (3.25) further integrated over the PBH mass spectrum, i.e.,

$$N_{\text{exp}} \left( \frac{\Omega_{\text{PBH}}}{\Omega_{\text{DM}}} \right) = \frac{\Omega_{\text{PBH}}}{\Omega_{\text{DM}}} \int dM_{\text{PBH}} \int_0^{t_{\text{obs}}} \frac{dt_{\text{FWHM}}}{t_{\text{FWHM}}} \int dm_r \frac{dN_{\text{event}}}{d \ln t_{\text{FWHM}}} \frac{dN_s}{dm_r} \epsilon(t_{\text{FWHM}}, m_r) P(M_{\text{PBH}}), \quad (3.26)$$

where  $P(M_{\text{PBH}})$  is a mass spectrum of PBHs, normalized so as to satisfy  $\int_0^{\infty} dM_{\text{PBH}} P(M_{\text{PBH}}) = 1$ . Then one can use our constraints to constrain the overall PBH mass fraction to DM,  $\Omega_{\text{PBH}}/\Omega_{\text{DM}}$ , following the method in Carr et al. (2016); Green (2016); Inomata et al. (2017); Carr et al. (2017)).

<sup>5</sup><http://cas.sdss.org/dr4/en/proj/advanced/hr/radius1.asp>

# Chapter 4

## Reobserving Andromeda for Microlensing: Improved constraints on PBH abundance

In the previous chapter, we presented the result of microlensing search with the Subaru/HSC by a one-night observation of M31. We developed image difference technique for the Subaru/HSC data, and succeeded to put the tightest upper limit on PBH abundance at sublunar mass scale. We also found one remaining candidate for which it is difficult to rule out the PBH microlensing hypothesis. If it is a real microlensing event, it is a discovery suggesting that PBHs constitute some fraction of DM. In this chapter, we analyze the archival data of M31 taken with the Subaru/HSC, and discuss the possible implication about the remaining candidate as well as the improved constraint on PBH abundance.

### 4.1 Introduction

Gravitational microlensing has been used as a powerful method to probe dark matter (DM) in the Milky Way (MW) (Paczynski 1986; Griest et al. 1991). With the aim of constraining the abundance of PBHs, we previously carried out microlensing experiment with the Subaru Hyper Suprime-Cam (HSC) by monitoring large number of stars in the Andromeda galaxy (M31) with roughly a 2 minute cadence (see Chapter 3 for the detail). We searched for microlensing event(s) of M31 stars by intervening PBHs in both the halo regions of MW and M31. The huge volume between M31 and the Earth, leads to a large optical depth of PBH microlensing to each star in M31, which allows us to put meaningful constraints on the PBH DM scenario. Even a single night of HSC/Subaru yielded an ideal dataset to search

for the PBH microlensing events because of the deep and wide field of view of HSC and the good seeing condition. Among the 15,571 transient candidates we found one remaining candidate for which it is difficult to rule out the PBH microlensing hypothesis. If it is a real microlensing event, it is a discovery suggesting that PBHs constitute to some fraction of DM. Alternatively the one remaining candidate could be a microlensing by a free-floating planet in the halo region (e.g. Sumi et al. (2011)), rather than a PBH. This could also be another important discovery, especially for the halo regions.

Here we carried out another one-night HSC observation of M31 in the  $r$ -band on the night of September 19, 2017. We took the same observational strategy as we did in previous 2014 observation, and acquired 224 exposures for M31 with a cadence of 2 minutes during 7.5 hours within single night. One main purpose of this study is to reveal the nature of the one remaining microlensing candidate from previous observation in 2014. The remaining candidate is very faint about 24.5 magnitude in  $r$ -band, and it was difficult to confirm the nature of this event from the archival data by other telescopes. Our new observation with the Subaru/HSC is expected to probe a signature of time variability of this candidate owing to the deep field of view, if it is a variable star. Another goal of this new observation is to search for new microlensing events due to PBHs, as well as to improve the constraint on their abundance. Even though it is hard to probe PBHs with mass lighter than  $10^{-10}M_{\odot}$  by HSC due to the wave optics, it is still meaningful to look the tighter abundance of PBHs with any mass scale, because it should lead to constrain some formation scenario of the universe. Moreover, the dataset from new observation also enables us to classify various types of transient objects. These transients could include supernova, nova, RR-Lyrae variable stars, free-floating planets, some signatures in common-envelope binary system of massive stars, and so on. By combining the new data with those from the previous observation of M31 with Subaru/HSC including SMOKA archive <sup>1</sup>, we are expected to find various kinds of transient candidates. This dataset will bring a legacy value for future cadence observation over coming years; if we have repeated observation of one hour every time and a few runs every month over several months/years, we can constrain various kinds of variable stars over different timescales.

The structure of this chapter is as follows. In Section 4.2 we describe the details of our data analysis, and define the master catalog of variable star candidates for 2017 observation. In Section 4.3 we describe the selection criteria for microlensing events from the 2017 catalog of variable star candidates. Based on this analysis, we first discuss the time-variability of one remaining microlensing candidate detected from 2014 observation in Section 4.4. In

---

<sup>1</sup><https://smoka.nao.ac.jp/index.ja.jsp>

Section 4.5, we then use the result to derive an experimental upper bound on the abundance of PBHs as a function of PBH mass, by combining previous constraint derived from 2014 data. Finally we present our conclusions and summary in Section 4.6.

## 4.2 Data analysis and Object Selection for 2017 observation

### 4.2.1 Observation

Here we describe the detail of our new microlensing observation in 2017. Basically we took the same observational strategy as previous microlensing observation of M31 in 2014. The pointing is centered at the coordinates of the M31 central region: (RA, dec) = (00h 42m 44.420s, +41d 16m 10.1s), which enables us to cover the entire disk region of M31 with a single pointing. We do not perform any dithering between different exposures in order to compare stars in the same CCD chip, which makes the image difference somewhat easier.

Our observations were conducted on September 19, 2017 which was a dark night, a day before the new moon. We carried out the observations with a cadence of 2 minutes which allows us to densely sample the light curve for each variable object. The total exposure time was 90 seconds on source and about 35 seconds were spent for readout on average. In total, we acquired 224 exposures of M31 with the HSC  $r2$ -band filter<sup>2</sup>, for the period of about 7.5 hours, until the elevation of M31 fell below about 30 degrees. The  $r2$ -band filter have been procured to replace  $r$ -band filter, which was improved to have uniformity in the transmission curve (Kawanomoto et al. 2018). The weather was stable, but the seeing size change drastically during the observation as can be seen from Fig. 4.1, which shows how the seeing FWHM changed with time from the start of our observation. The seeing size ranged from about 0.5'' to 1.8'', and got worse than 1.2'' towards the beginning and end of our observation.

### 4.2.2 Data reduction and Sample selection

In the following we describe the summary of data reduction and sample selection for observation in 2017. We basically follow the same procedure as we applied for 2014 data, and more details of each procedure are discussed in Section 3.3.2.

---

<sup>2</sup>See <http://www.naoj.org/Projects/HSC/forobservers.html> for the detail of the HSC filter system.

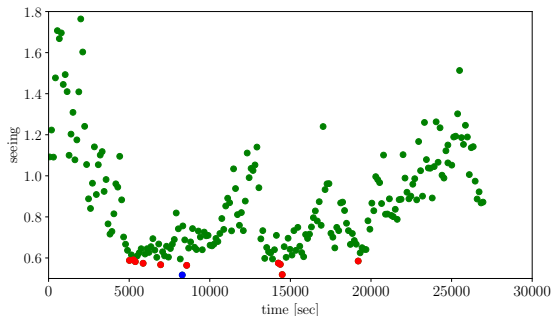


Figure 4.1: The PSF FWHM (seeing size) of each exposure (90 sec exposure each) as a function of time  $t$  [sec] from the start of our 2017 observation. We took the images of M31 region every 2 min (90 sec exposure plus about 35 sec for readout), and have 224 exposures in total. The red points show the 10 best-seeing images ( $\sim 0.5''$ ) from which the reference image, used for the image difference, was constructed. The blue point corresponds to a 5 sec exposure image taken only once during 2017 observation.

### Standard data processing

We performed basic standard data reduction with the dedicated software package for HSC, `hscPipe` (version 4.0.5; also see Bosch et al. (2017)), which is being developed based on the Large Synoptic Survey Telescope software package (Ivezic et al. 2008; Axelrod et al. 2010; Jurić et al. 2015)<sup>3</sup>. We followed the data processing steps as we performed for 2014 data, including basic data reduction, careful background subtraction and the determination of the astrometry. One difference from previous data reduction is that we removed two dead CCDs for our new analysis. Due to too many saturated stars in the bulge region and M101, we also exclude the patches marked by dark square regions in Fig. 4.2, from the following analysis.

### Image subtraction and Object detection

In order to find variable objects, we employ the difference image technique developed in Alard & Lupton (1998), which is integrated into the HSC pipeline. Following strategy of previous data analysis, we first generated the “reference” image by co-adding 10 best-seeing images among the 224 exposure images, where the 10 images are not time-consecutive, displayed as red points in Fig. 4.1.

In order to make a master catalog of variable object candidates, we constructed 75 target images by co-adding 3 time-consecutive images from the original 224 exposure images. Then we subtract the reference image from each target image, resulting 75 difference images.

<sup>3</sup>Also see <http://www.astro.princeton.edu/~rhl/photo-lite.pdf> for details of the algorithm used in the pipeline.

## PSF photometry and master catalog of variable star candidates

From the initial catalog constructed from the  $5\sigma$  candidates from the 75 coadded-difference images, we prune it down to a *master* catalog of “secure” variable star candidates by applying the following criteria, as we adopted for 2014 data: first we select those with a significance of  $5\sigma$  or higher (including a negative flux) (“*PSF magnitude threshold*”), and then put threshold which allows candidates greater than 0.75 times (“*Minimum size*”), or smaller than 1.25 times the PSF size (“*Maximum size*”) in each difference image. Finally we select candidates which have consistent “*PSF shape*” within  $3\sigma$  for the cumulative deviation over pixels inside the PSF aperture.

Fig. 4.2 shows the distribution of secure variable star candidates with magnitudes  $m_r \leq 25$  from the 2017 observation. We make a master catalog of variable star candidates from objects which pass all the above conditions for each image difference, and select only those which are detected at least twice among the 75 difference images, allowing a variance of position within 2 pixels for every candidate. These criteria result in 8,461 candidates of variable objects, which is our master catalog of variable star candidates for 2017 observation. The number of transient candidates is around half compared to 2014 observation. One reason is that we have worse seeing condition than 2014 observation, which decrease the number of faint transient candidates. Another cause considered is the lower reflectivity of the primary mirror at Subaru telescope, due to the postpone of mirror coating; the reflectivity of the primary mirror gets around 15% decrease compared to 2014 observation <sup>4</sup>.

## Light curve measurement

Once each candidate is identified, we measure the PSF counts as a function of time from the beginning to the end of our 7.5 hour long observations. In order to restore the highest time resolution of our data, we used each of 224 exposures and measured the PSF counts in each of the 224 difference image that was made by subtracting the reference image (the coadded image of 10 best-seeing exposures) from every single exposure. In this way we measure the light curve of the object with 2 min time resolution.

---

<sup>4</sup>see <https://www.subarutelescope.org/Observing/Telescope/Parameters/Reflectivity/> for the detail

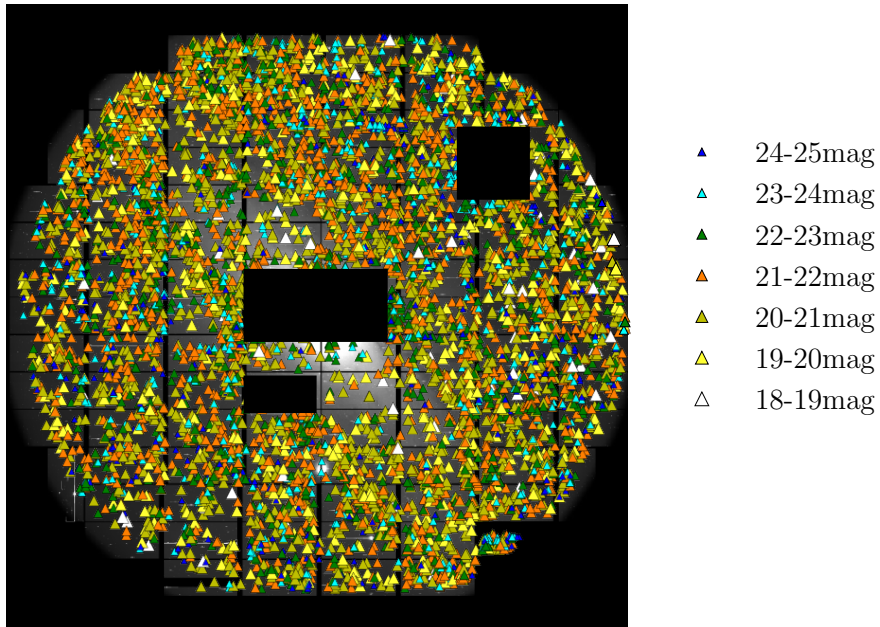


Figure 4.2: Distribution of secure variable star candidates, detected from our analysis using the image difference technique. The different symbols denote the PSF magnitude of candidate in the reference image. We only show candidates which satisfies  $18 \leq m_r \leq 25$  mag. The total number of transient candidates detected for 2017 data are 8,461.

## 4.3 Statistics and Selection Criteria for 2017 observation

In this section we describe our selection criteria for 2017 data to discriminate the microlensing event from other variables.

### 4.3.1 Photometric errors of the light curve measurement

Given the catalog of variable star candidates each of which has its measured light curve, we now search for secure candidates of PBH microlensing. To robustly search for secure candidates of PBH microlensing that have the expected light curve shapes, it is crucial to properly estimate the photometry error in the light curve measurement. As we performed in previous 2014 observation (Section 3.4.1), we use the following approach to obtain a conservative estimate of the error. For a given difference image, we randomly select 1,000 points in each patch region, and then perform PSF photometry at each random point in the same manner as that for the variable star candidates. In selecting random points, we avoided

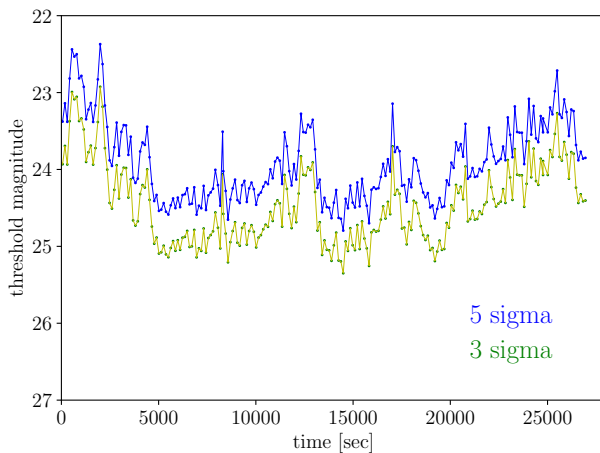


Figure 4.3: The photometric error used for the light curve measurement in the difference image; we randomly select 1,000 points in the difference image of a given patch (here shown for the patch-D2 in Fig. 3.4), measure the PSF photometry at each random point, and then estimate the variance of the PSF photometries (see text for details). The square symbols show the 3- or 5-sigma photometric errors estimated from the variance when using the difference images constructed from the coadded images of 3 exposures, as a function of observation time. The circle symbols, connected by the line, are the results for each exposure. Although we use the photometric error in the ADU counts for a fitting of the microlensing model to the light curve, we here convert the counts to the magnitude for illustrative convenience.

regions corresponding to bad CCD pixels or near the CCD chip edges. We then estimate the variance from those 1,000 PSF magnitudes, repeat the variance estimation in the difference image for every observation time, and use the variance as a  $1\sigma$  photometry error in the light curve measurement at the observation time.

Fig. 4.3 shows the photometric error on the light curve measurement in the difference images for 2017 data, estimated based on the above method. The shape of the photometric error appears to correlate with the seeing conditions in Fig. 4.1. Similar to the analysis of 2014 observation, we find that the photometric error is larger than the error estimated from the pipeline at the candidate position, which is locally estimated by propagating the Poisson noise of the counts through the image subtraction processes. The figure also shows that most of our data reaches a depth of 25 mag or so, which is around one magnitude shallower than 2014 observation. This result is consistent with the smaller number of variable candidates as we discussed in Fig. 4.2.

### 4.3.2 Microlensing model fit to the light curve data

Table 4.1: Selection Criteria for 2017 data

Selection Criterion	Purpose	No. of remained candidates
$\Delta C_{\text{coadd},i} \geq 5\sigma_{\text{coadd},i}$	initial definition of candidates	8,461
$\text{bump} \geq 3$	select candidates with a significant peak(s) in the light curve	1,465
$\text{mlchi2dof} < 3.5$	select candidates whose light curve is reasonably well fit by the microlensing	161
$a_{\text{asy}} < 0.17$	remove candidates that have an asymmetric light curve such as star flares	133
significant peak	select candidates that show a clear peak in its light curve (see text for details)	58
visual inspection	visually check each candidate (its light curve and images)	0
seeing_corr	remove candidates whose light curve is correlated with time variation of seeing	0

Here we describe our selection procedure for PBH microlensing events from the candidates for 2017 observation. We basically followed the same the statistics as we adopted for 2014 data analysis to quantify the characteristics of each light curve. Our selection procedure for the candidates are summarized in Table 4.1. We will briefly describe each of the selection steps in the following.

We start with the master catalog of variable star candidates, which contains 8,461 candidates. Our level 1 requirement to search for microlensing events is that a candidate event should have a ‘‘bump’’ composed by more than 3 time-consecutive flux changes which satisfies  $\Delta C_i \geq 5\sigma_i$ , where the subscript  $i$  denotes the  $i$ -th difference image (at the observation time  $t_i$ ). This criteria strongly reduce the number of secure candidates for 2017 observation because of the higher noise threshold as in Fig 4.3, and only leaves us with 1,465 candidates over all the patches.

Next we fit the observed light curves of each candidate with a model describing the expected microlensing light curve. As described in Section 3.2.3, the microlensing light curve in the difference image is characterized by 3 parameters:  $(u_{\min}, t_{\text{FWHM}}, C_0)$ , where  $u_{\min}$  is the impact parameter, and  $t_{\text{FWHM}}$  is the FWHM timescale of the light curve. For the model fitting of 2017 data, we employ the following range for the model parameters:  $0.01 \leq u_{\min} < 1$ ,  $0.01 \leq t_{\text{FWHM}}/[\text{sec}] < 27,000$ , and  $0.5 \times \Delta C_{\text{max}}^{\text{obs}}/(A_{\text{max}} - 1) \leq C_0 \leq 1.5 \times \Delta C_{\text{max}}^{\text{obs}}/(A_{\text{max}} - 1)$ , where  $\Delta C(t_i) = C_0 [A(t_i) - A(t_{\text{ref}})]$  is the light curve of a microlensing in the difference image,  $C_0 = \Delta C_{\text{max}}^{\text{obs}}/[A_{\text{max}} - A(t_{\text{ref}})]$  is the intrinsic flux, and  $\Delta C_{\text{max}}^{\text{obs}}$  is the counts of the light curve peak in the difference image. For each candidate, we perform a standard  $\chi^2$  fit by comparing the model microlensing light curve to the observed light curve:

$$\chi^2 = \sum_{i=1}^{224} \frac{[\Delta C^{\text{obs}}(t_i) - \Delta C^{\text{model}}(t_i; C_0, t_{\text{FWHM}}, u_{\min})]^2}{\sigma_i^2}, \quad (4.1)$$

where  $\sigma_i$  is the rms noise of PSF photometry in the  $i$ -th difference image, estimated from the 1,000 random points as described in Section 4.3.1. We then compute the reduced  $\chi^2$  by dividing the minimum  $\chi^2$  by the degrees of freedom (224-3=221). We discard candidates that have `mlchi2_dof`  $> 3.5$ . We further impose the condition that the best-fit  $t_{\text{FWHM}} < 14,400$  sec (4 hours), in order to remove candidates whose light curve has a longer time variation than what we can robustly determine. This selection leaves 161 candidates.

We also utilize the shape of bump for the selection. Microlensing predicts a symmetric light curve with respect to the maximum-magnification time  $t_0$  ( $A_{\text{max}}$ ); the light curve at  $t_i = |t_0 \pm \Delta t|$  should have a similar flux as the lensing PBH should have a nearly constant velocity within the Einstein radius. By imposing the same condition  $a_{\text{asy}} < 0.17$  as we applied for 2014 observation by following Eq. (3.23) in Chapter 3, we eliminate candidates that have an asymmetric light curve, including Cepheids and flaring stars for our observation. After this cut the number of candidates is reduced to 133.

In addition we discard candidates, if the observed light curve does not have any significant peak; e.g., we discard candidates if `mlchi2in_dof`  $> 3.5$  (see Table 3.1 for the definition) or if the time of the light-curve peak is not well determined. This selection cut still leaves us with 58 candidates.

Finally we perform a visual inspection of each of the remaining candidates. Most of the fake events are expect to be caused by an imperfect image subtraction; in most cases the difference image has significant residuals near the edges of CCD chips or spike-like structure around bright stars. We found 57 fake events caused by such spike-like images around bright stars. We have no contamination from fake events around the CCD edges, but identify 1 fake event caused by a moving object, an asteroid.

Thus our visual inspection leads us to conclude that all the remaining candidates are fake, and we end up with no secure candidate event which passes all our cuts and visual checks.

## 4.4 Result 1: Time-variability of one microlensing candidate

Although we have no secure microlensing candidate from 2017 observation, we were left with one microlensing candidate from 2014 observation as shown in the top left panel of Fig. 3.13 in Chapter 3. The candidate position is (RA, dec) = (00h 45m 33.413s, +41d 07m 53.03s), and the magnitude inferred from the reference image implies that the candidate has a magnitude of  $r \sim 24.5$  mag in 2014. Unfortunately, the candidate is placed outside the survey regions

Table 4.2: Summary of archival data of M31 by HSC-*r*

Date	Filter	Exposure time [sec]	Field	No. of exposures
June 17, 2013	HSC- <i>r</i>	120	M31*	10
November 23, 2014	HSC- <i>r</i>	90	M31	194
November 18, 2015	HSC- <i>r</i>	300	M31N	34
November 18, 2015	HSC- <i>r</i>	300	M31S	31
September 19, 2017	HSC- <i>r2</i>	90	M31	224

of the Panchromatic Hubble Andromeda Treasury (PHAT) catalog in Williams et al. (2014) (also see Dalcanton et al. (2012)), and hence the HST image is not available to test the properties of this candidate.

Here we look into the properties of this remaining candidate by using multi-epoch observations of M31. By combining multiple deep images of M31 by Subaru/HSC, we are expected to test the nature of the candidate more in detail. We first explain the properties of archival data of M31 in Section 4.4.1, and describe the properties of light curves (Section 4.4.2) and its implication about the time-variability (Section 4.4.3).

#### 4.4.1 Archival observation of the M31 with the Subaru/HSC

To test the hypothesis that the candidate is a variable star, we looked into other *r*-band data of the M31 that was taken by Subaru/HSC <sup>5</sup>. Other than a commissioning run in 2013 as discussed in Section 3.4, we have access to only one observation run in 2015. The observation was carried out in November 18, 2015. They targeted at two regions named M31N and M31S, each of which has some overlap with the target field of view of our 2014 observation. The total exposure time was basically 300 seconds on source and about 35 seconds were spent for readout on average. In total, they acquired 34 exposures of M31N and 31 exposures of M31S with the HSC *r*-band filter, for the period of about 5.8 hours in total with four-pointing dithering.

Table 4.2 summarizes the archival observation of M31-disk region with HSC. Since the observation in 2013 has worse seeing condition (about 1.2'') compared to other observations, we did not include them for the following time-variability test of one remaining microlensing candidate.

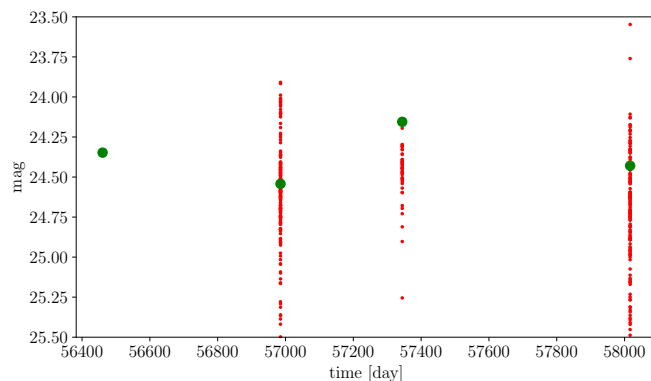


Figure 4.4: Light curves of one remaining microlensing candidate detected during the observation in 2014. Green points show the flux measurement at the target coordinate using reference images constructed by every observational epoch in 2013, 2014, 2015 and 2017 time sequentially. Red data points show the flux measurements of the candidate using difference images for every visit.

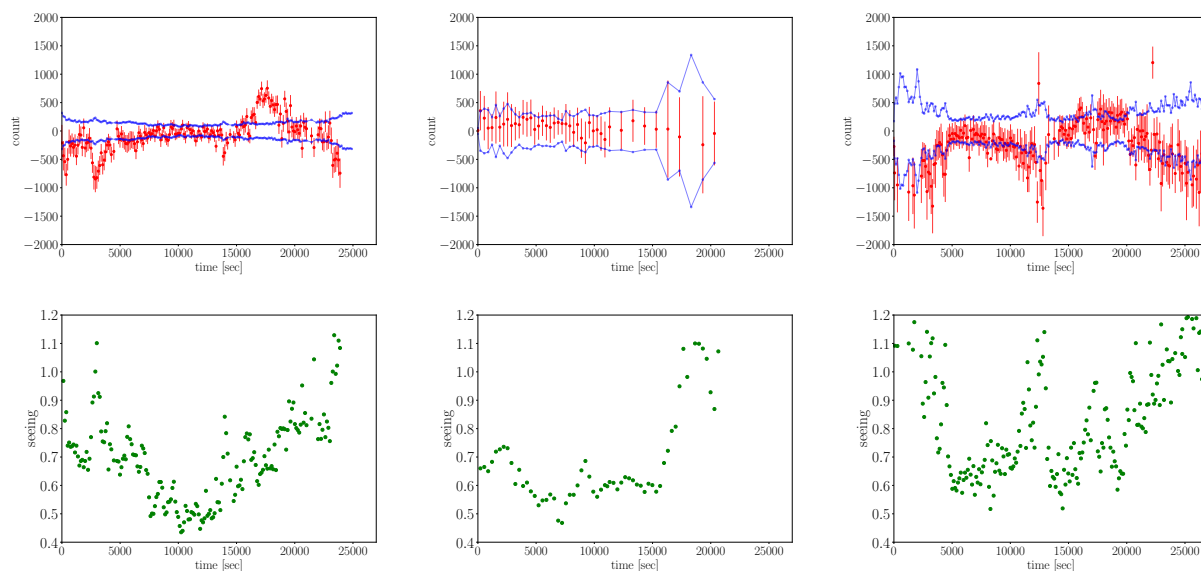


Figure 4.5: *Upper panel:* Light curves of our target showing the microlensing event. Left panel shows the microlensing event in 2014, and middle and right panels indicate photometry of the same position from 2015 and 2015 observations, respectively. Red data points show the flux measurements from difference images for every visit. Two thin blue curves are the  $1\sigma$  noise level in difference images. In order to compare with the other observations, the light curve in the middle panel are multiplied by  $90[\text{sec}]/300[\text{sec}]$ . *Bottom panel:* The PSF FWHM (seeing size) of each exposure as a function of time  $t$  [sec] for each observational epoch. Here we only plot the points where the seeing is smaller than  $1.2''$ .

### 4.4.2 Light curves of one remaining candidate from archival data

Fig. 4.4 shows the magnitude of the remaining candidate from the photometry of reference images at different observational epoch. The reference images are constructed by co-adding the 10 best-seeing images among the images taken during the every observational epoch. The deep photometry on the reference image enables us to probe the year-scale change of flux of the remaining candidate expect for the observation in 2013, This figure indicates than the remaining candidate does not show significant change of flux among the difference observational epoch.

Fig. 4.5 shows the light curve of the one remaining microlensing candidate. Here we use the same reference image which is constructed by co-adding the 10 best-seeing images during the observation in 2014; hence all the light curves are measured in the difference images, which are produced by the combination of reference image of 2014 observation and the target images in each observational epoch. The noise of light curves are measured by evaluating the variance of 1,000 random points for each difference image, in the same way as we estimated in Section 4.3.1. In order to perform a secure test for the very faint candidate, we only look into the images which have better seeing condition than  $1.2''$ . The light curve in the middle panel are multiplied by  $90[\text{sec}]/300[\text{sec}]$ , in order to compare with the other observations. Our result indicates that the light curve from 2015 observation has no significant time-variability, and all the photometry values reside within the  $1\sigma$  noise level. On the other hand, the light curve from 2017 observation presents relatively larger variance of photometry compared to the 2015 observation. However, the change of flux in the light curve is strongly correlated with the change of the seeing. Since the change of flux is less than  $5\sigma$  significance, we conclude that the candidate does not show significant time-variability during 2017 observation.

### 4.4.3 Test of time-variability

As discussed in Section 4.4.2, we could not detect significant time-variability of flux for the one remaining microlensing candidate detected from our microlensing observation in 2014. We expect that we should be able to observe its brightest phase repeatedly if our target is a variable star. On the other hand, if this was indeed a microlensing event, it should be a one-off occurrence at the observed location. A non-detection from the additional observations should be able to rule out some of the periods expected for known variable stars, and establish the nature of this event as microlensing, which can lead to detections of more such microlensing

---

<sup>5</sup>All the archival data are downloaded from the SMOKA archive

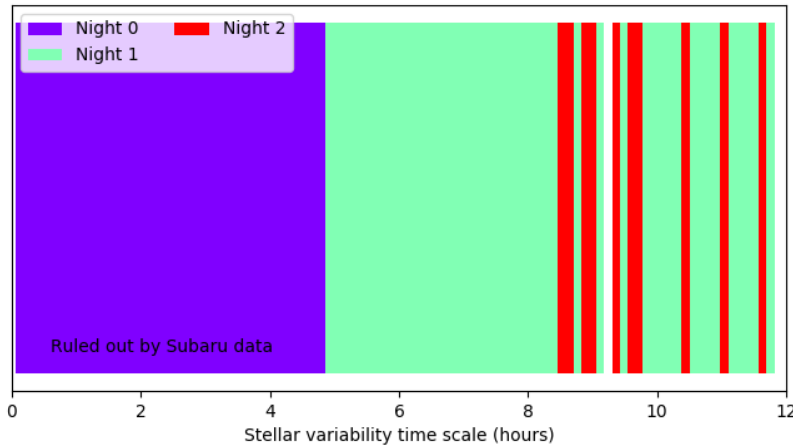


Figure 4.6: Fraction of region to be ruled out for a period up to 12 hours. Night 0 is our previous microlensing event in 2014 observation and nights 1,2 correspond to the observations in 2015 and 2017, respectively. Variability timescales of up to 5hours are ruled out by our HSC observation in 2014. If we take into account the observation of our target in 2015 which has no significant time-variability for 5 hours, we can rule out 87.9% of the time-scales between 5-12hours. Similarly, we can rule out the 98% of the time-scales between 5-12hours by assuming that we have no significant time variability during 2017 observation.

events (expected number  $\sim 10^4$  for given the optical depth of our observation).

Here we performed a test to estimate the excluded range of time-variability from our follow-up observations. Since variable stars with period longer than 7 hours (e.g. Cepheids) are expected to be detected from the previous 7-hour observations, we only focus on the time-variability within 12 hours, where we can expect variable star candidates such as  $\delta$ -Scuti, RR-Lyrae, and binary-star systems. The methodology of our test is as follows. First we assume that an event could be defined as peak-to-peak distance or time. By assuming that the new observations happen between time  $t_1$  and  $t_2$ , we calculate how many events should occur from  $dt_1 = t_1 - t_0$  and  $dt_2 = t_2 - t_0$ , where  $t_0$  corresponds to the remaining microlensing candidate event. If an object has time period  $T$ , we will either see a new event (i.e.  $\geq 1$  event) between  $dt_2 - dt_1$  or we won't (i.e 0 event). If we don't see any event, we rule out the time period  $T$ . Then we repeat this test for various values of  $T$  and different combinations of observations with  $(t_1, t_2)$ .

Fig. 4.6 shows the excluded region of time-variability of the microlensing candidate from the combination of observations in 2014, 2015, and 2017. The night 0,1,2 corresponds to the HSC observations of 2014, 2015, and 2017, respectively. We rule out variability timescales of up to 5 hours by the single observation in 2014. The other time-space regions can be also

widely excluded by taking into account the other two-night observations. Our test indicates that we can rule out 87.9% of the time-scales between 5-12hours by taking advantage of observations in 2014 and 2015. Similarly, we can rule out the 98% of the time-scales between 5-12hours by assuming that we detect no significant time variability during three-night observations in 2015 and 2017.

## 4.5 Result 2: Tighter Upper bound on the abundance of PBHs

From the analysis of our microlensing search, we were left with one microlensing candidate. In this section we estimate the expected number of microlensing effect by the taking advantage of observations in 2014 and 2017.

### 4.5.1 Efficiency Calculation: Monte Carlo simulation of observation in 2017

In the following, we will estimate the detection efficiency of PBH microlensing events for our 2017 observation, in the same way as we did for 2014 observation in Section 3.5.1. To estimate the efficiency we carry out simulations of microlensing light curves by imitating the microlensing observation in 2017. First we randomly select the time of maximum magnification ( $t_{\max}$ ) from the observation window, the impact parameter  $u_{\min} \in [0, 1]$  and the FWHM timescale  $t_{\text{FWHM}}$  in the range of  $0.01 \leq t_{\text{FWHM}}/[\text{sec}] \leq 27,000$  to simulate the input light curve in the difference image for a given intrinsic flux of a source star,  $F_0$ . Then, we add random Gaussian noise which was estimated in Section 4.3.1, to the light curve at each of the observation epochs  $t_i$ . For each intrinsic flux, we generate 1,000 simulated light curves in each patch region, and applied all of our selection cuts (see Section 4.3 and Tables 4.1) to assess whether the simulated event passes all the criteria.

Fig. 4.7 shows the estimated efficiency for a given intrinsic flux of a star as a function of the timescale ( $t_{\text{FWHM}}$ ) of the simulated light curve, in the patch-D2 of Fig. 3.4 of Chapter 3. We found the same trend as seen in previous observation (Section 3.5.1), indicating that a microlensing event for a bright star is easier to detect, because even a slight magnification is enough to identify it in the difference image. However, the detection efficiency becomes around half compared to the case of 2014 observation as in Fig. 3.14. One reason considered is that we place higher threshold as in Fig. 4.3, which drastically reduces the number of secure transient candidates for the 2017 observation as discussed in Section 4.3. This high

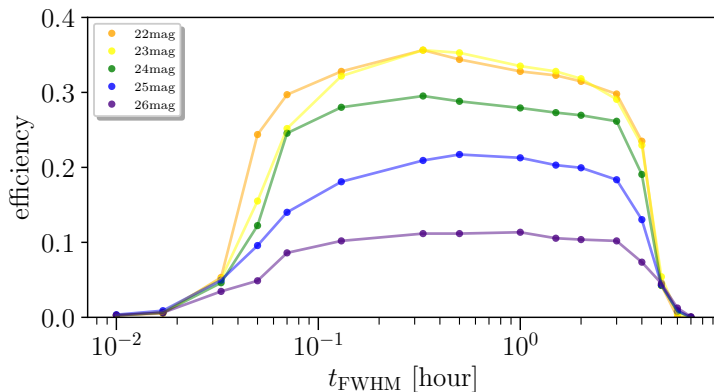


Figure 4.7: The detection efficiency estimated from light curve simulations taking into account the PSF photometry error in each of 224 target images we used for the analysis (see Fig. 3.14 for the detail). Here we generated Monte Carlo simulations of microlensing events randomly for 2017 observation data. The detection efficiency for each source magnitude is estimated from 1,000 realizations.

threshold also reduces the effective number of our simulated microlensing events, and thus leads to lower detection efficiency as shown in Fig. 4.7.

### 4.5.2 Expected number of PBH microlensing events

Now we use the results of our microlensing search to constrain the abundance of PBHs from combined observations in 2014 and 2017. The expected number of PBH microlensing events in our 2-year HSC data is given by

$$N_{\text{exp}} \left( M_{\text{PBH}}, \frac{\Omega_{\text{PBH}}}{\Omega_{\text{DM}}} \right) = \frac{\Omega_{\text{PBH}}}{\Omega_{\text{DM}}} \left[ \int_0^{t_{\text{obs}}^{2014}} \frac{dt_{\text{FWHM}}}{t_{\text{FWHM}}} \int dm_r \frac{dN_{\text{event}}}{d \ln t_{\text{FWHM}}} \frac{dN_s}{dm_r} \epsilon(t_{\text{FWHM}}, m_r) |_{2014} + \int_0^{t_{\text{obs}}^{2017}} \frac{dt_{\text{FWHM}}}{t_{\text{FWHM}}} \int dm_r \frac{dN_{\text{event}}}{d \ln t_{\text{FWHM}}} \frac{dN_s}{dm_r} \epsilon(t_{\text{FWHM}}, m_r) |_{2017} \right], \quad (4.2)$$

where  $\Omega_{\text{PBH}}/\Omega_{\text{DM}}$  is the mass fraction of PBHs to the total DM mass in the halo regions,  $dN_{\text{exp}}/dt_{\text{FWHM}}$  is the differential event rate for a single star (Fig. 3.3) per logarithmic timescale,  $dN/dm_r$  is the luminosity function of source stars in the  $r$ -band magnitude range  $[m_r, m_r + dm_r]$ , and  $\epsilon(m_{\text{FWHM}}, m_r)$  is the detection efficiency quantifying a probability that a microlensing event for a star with magnitude  $m_r$  and the light curve timescale  $t_{\text{FWHM}}$  is detected by our selection procedures. Note that we calculated the expected number of PBH microlensing events separately for observations in 2014 and 2017, as in Eq. (4.2). The only difference between the estimation of two observations is the values of detection efficiency as

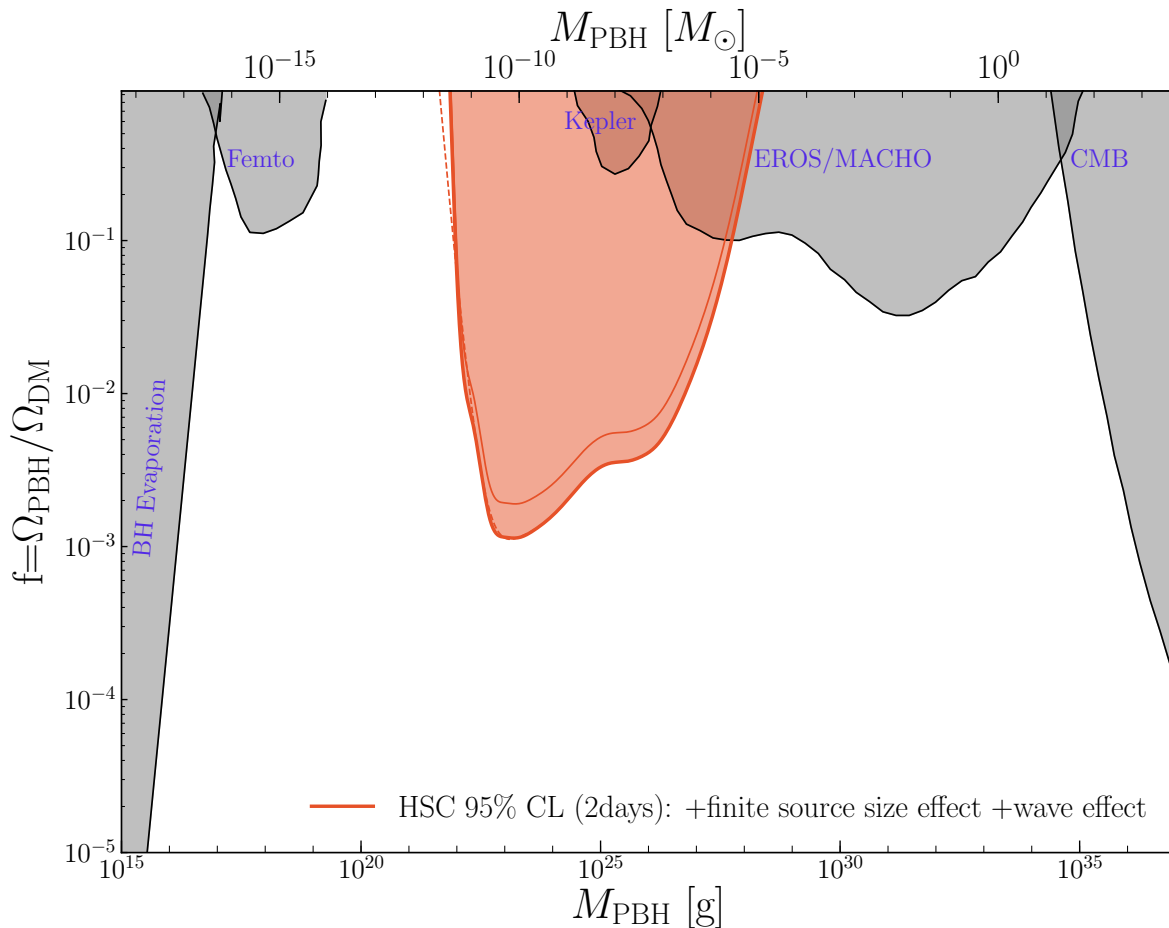


Figure 4.8: The red-color shaded region show the 95% C.L. upper bound on the PBH mass fraction to DM in the halo regions of MW and M31, derived from our microlensing search of M31 stars based on the “two-night” HSC/Subaru data. The inner solid line shows the previous constraint derived from the one-night observation in 2014. The dashed curve shows the results without considering the wave effect.

in Fig. 3.14 and Fig. 4.7, and we adopt the same event rate models (Fig. 3.3) and the same estimate of number counts of source stars in M31 (see Section 3.5.2 for the detail).

### 4.5.3 Experimental limits on the abundance of PBHs from two-night observations

Here we combine the estimates of  $dN_{\text{event}}/d \ln t_{\text{FWHM}}$ ,  $dN_s/dm_r$  and  $\epsilon(t_{\text{FWHM}}, m_r)$  in Eq. (4.2) to constrain the abundance of PBHs. Assuming the number of microlensing events follow a Poisson distribution, the probability to observe a given number of such events,  $N_{\text{obs}}$ , is given by  $P(k = N_{\text{obs}} | N_{\text{exp}}) = \left[ (N_{\text{exp}})^k / k! \right] \exp[-N_{\text{exp}}]$ . Hence 95% C.L. interval is estimated as

$P(k = 0) + P(k = 1) \geq 0.05$ , leading to  $N_{\text{exp}} \leq 4.74$  assuming that the candidate in Fig. 3.13 is real, as we verified in Section 4.4.2. Fig. 4.8 shows our updated result in comparison with other observational constraints on the abundance of PBHs on different mass scales. As a result, our new result provides around 1.5 times stringent constraint compared to the previous constraint by observation in 2014. We cannot go twice as deep as the previous constraint because of the lower detection efficiency from new observation in 2017. Note that we cannot explore constraints on PBHs with  $M \lesssim 10^{-11} M_{\odot}$  from new Subaru observation, because the effect of finite source star size (Witt & Mao 1994) as well as the effect of wave optics on the microlensing cross section (Gould 1992; Nakamura 1998) significantly reduce the event rate for those PBHs.

## 4.6 Discussion and future prospects

In Chapter 3 and Chapter 4, we have used the unprecedented dense-cadence data of M31, taken with the HSC/Subaru, in order to search for microlensing effects of PBHs on M31 stars. The combination of the wide field-of-view and the 8.2m aperture of HSC/Subaru is ideal for our study. With this unique HSC data set, we expect up to  $10^3$  PBH microlensing events of M31 stars, if PBHs constitute a majority of DM in the MW and M31 halo regions. To search for the pixel lensing event by PBH, i.e. the microlensing of unresolved stars, we used the image subtraction technique in Alard & Lupton (1998), and successfully managed to find many candidate variable stars such as stellar flares, eclipsing binaries, and Cepheid variables. After careful selection criteria including the microlensing fitting to the measured light curve, we concluded that most candidates are not microlensing events, but found one remaining candidate for which it is unlikely to be a periodic variable star (see Fig. 4.5). If this is a real event, it is a discovery, unveiling some contribution of PBHs to DM. Alternatively the remaining candidate could also be a result of microlensing by a free-floating planet in the halo region, rather than a PBH (Sumi et al. 2011) (again recall that the short timescale of the light curve requires a planetary mass scale, rather than stellar mass scale. Also note that Earth-mass object at 100 kpc is more likely to cause microlensing rather than occultation, because the Einstein radius is larger than the size of this object itself, and the size larger than the angular size of the source). This could also be another important discovery, especially for the halo regions, and is worth exploring.

We derived the tightest upper bounds on the abundance of PBHs as a candidate for DM in the MW and M31 halo regions in the range of  $M_{\text{PBH}} \simeq [10^{-11}, 10^{-5}] M_{\odot}$ . Some inflation-inspired model predicts that PBHs span over a wide range of mass scales possibly extending

to mass scales of a few  $10M_{\odot}$ , mass scales of the LIGO binary black holes (Kawasaki et al. 2016,b; Inomata et al. 2017). If binary black holes for gravitational wave sources originate from PBHs, a wide mass spectrum of PBHs is required, because a scenario with  $\Omega_{\text{PBH}}/\Omega_{\text{DM}} = 1$ , for mass scales around  $10 M_{\odot}$ , is already ruled out by observations such as MACHO microlensing and CMB constraints. Our results give a strong constraint on such a wide-mass-spectrum model; a model with  $\Omega_{\text{PBH}}/\Omega_{\text{DM}} \gtrsim 10^{-2}-10^{-3}$  is not allowed for mass scales of  $M_{\text{PBH}} \simeq [10^{-11}, 10^{-9}]M_{\odot}$ .

Although our results for the upper bounds in Fig. 4.8 are promising, we employed several assumptions. As discussed in Section 3.6, one uncertainty in our bounds comes from the number counts of source stars in M31. If we use the number of HSC peaks for the counts of source stars, the upper bounds in Fig. 4.8 are weakened by a factor of 10. However, the use of HSC peak counts is extremely conservative, so we believe that our fiducial method using the HST-extrapolated counts of source stars is reasonable. We also have another uncertainty from the effect of finite source size in the small mass range such of  $M_{\text{PBH}} \lesssim 10^{-10}M_{\odot}$ . Here we employ a solar radius for all source stars for simplicity. However, the upper bound also has contribution from RGB stars, which can lowers the microlensing event rate. We believe that our assumption is reasonable because main contribution to the total microlensing event comes from faint stars at  $r \sim 25-26$  mag.

There is still some scope to improve our results. First of all, if we have more HSC nights, we can tighten the bound; e.g., if additional 10 clear nights are provided, we can tighten the upper bound by a factor of 10. Also, we could extend our constraints to heavier mass scales, if M31 can be monitored over a longer timescale from months to years. For example, if we have repeated observations of M31 every few months over 10 years, say 10 minutes observation for each observation run, we should be able to improve the constraints at heavier mass scales. Since M31 is the most suitable target in the northern hemisphere for HSC, this is a valuable opportunity, waiting to be explored.

# Chapter 5

## Earth-mass black holes? – Constraints on primordial black holes with 5-years OGLE microlensing events

In this chapter, we give the upper bound on the PBH abundance and a possible implication of Earth-mass PBHs using microlensing events obtained from 5-years observations of stars in the Galactic bulge by the Optical Gravitational Lensing Experiment (OGLE).

### 5.1 Introduction

Microlensing is the most robust, powerful tool among various methods to probe a compact, macroscopic dark matter (DM) in the Milky Way (MW) halo region (Paczynski 1986; Griest et al. 1991), because lensing is a gravitational effect and can directly probe mass (gravity strength) of a lensing object irrespective of whether a lensing object is visible or not. The Optical Gravitational Lensing Experiment (OGLE<sup>1</sup>) collaboration (Udalski et al. 1994, 2015) has been making invaluable long-term efforts, more than a decade, to make monitoring observations of million stars in the Galactic bulge fields. The OGLE team has been finding more than two thousands of microlensing events and obtained various constraints on exoplanetary systems, brown dwarfs, low-mass stars as well as presented even an indication of free-floating planets in inter-stellar space (Mróz et al. 2017) (also see Sumi et al. 2003, 2011, for the similar constraints from the MOA microlensing experiments).

In this chapter we use the 5-years OGLE data containing 2622 microlensing events in Mróz et al. (2017) to constrain the PBH abundance. Interestingly the OGLE data indi-

---

<sup>1</sup><http://ogle.astrouw.edu.pl>

cates 6 ultrashort-timescale microlensing events that have their light curve timescales of  $t_E \simeq [0.1, 0.3]$  days (also see Mróz et al. 2018, for the new candidates), which is a distinct population from the majority of OGLE events. The ultrashort-timescale events indicate Earth-mass “unbounded” (wide-orbit or free-floating) planets (Sumi et al. 2011; Mróz et al. 2017). However, the origin of such free-floating planets is poorly understood because it involves complicated physics of star formation, planetary system formation and interaction of planetary system with other stars/planets. Hence we pay a particular attention to a possibility of whether PBHs can give an alternative explanation of the ultrashort-timescale events. For this purpose, we first study the standard Galactic bulge and disk models to estimate event rates of microlensing events due to astrophysical objects including brown dwarfs, main sequence stars and stellar remnants (white dwarfs, neutron stars and astrophysical black holes) following the pioneer work in Han & Gould (1995) (also see Han & Gould 1996). After comparing the model predictions of astrophysical objects with the OGLE data including the calibration factor that takes into account observational effects, we use the OGLE data to constrain the PBH abundance using the standard MW halo model for the spatial and velocity distributions of DM (therefore PBHs). In doing this we employ two working hypotheses. First, we employ “null hypothesis” that there is no PBH microlensing in the OGLE data and then derive an upper bound on the PBH abundance. Second, we employ the assumption that the 6 ultrashort-timescale events are due to PBHs and derive an allowed region of PBHs in the mass and abundance parameter space. To obtain the results, we properly use the likelihood function of OGLE events assuming the Poisson uncertainty in the counts of microlensing events.

The structure of this chapter is as follows. In Section 5.2, we give equations relevant for the event rate calculations. In Section 5.3 we review the standard models for the Galactic disk and bulge describing the spatial and velocity distributions for brown dwarfs, stars and stellar remnants as the constitutions, and also describe the MW halo model for the distributions of DM, i.e. PBH in our study. In Section 5.4, we give the main results of this chapter, after reviewing the OGLE data; the upper bound on the PBH abundance and a possible implication of Earth-mass PBHs. We will then give conclusion and discussion in Section 5.5.

## 5.2 Microlensing for bulge stars

### 5.2.1 Microlensing optical depth and event rate for a star in the Galactic bulge

#### Definition of microlensing optical depth and event rate

Here we define the optical depth and event rate of microlensing for a single star in the Galactic bulge region. The optical depth is defined as the probability for a source star to be inside the Einstein radius of a foreground lensing object on the sky at a certain moment. This corresponds to the probability for the lensing magnification to be greater than  $A \geq 1.34$ . The total optical depth due to lensing objects in the bulge and disk regions as well as due to PBHs in the MW halo region is formally expressed as

$$\tau \equiv \tau_b + \tau_d + \tau_{\text{PBH}}. \quad (5.1)$$

Hereafter we employ abbreviations: “b” for “bulge” and “d” for “disk”, respectively, and we ignore a multiple lensing case for a single star (this is a good approximation given the low optical depth as we show below). For a lensing object in the bulge and disk regions, we consider brown dwarfs and stellar components, where the latter includes main sequence stars and stellar remnants (white dwarfs, neutron stars and astrophysical black holes), as we will explain in detail later.

The differential event rate of microlensing event is defined by the frequency of microlensing event of a given lightcurve timescale (denoted as  $\hat{t}$ ) for a single source star per unit observational time ( $t_{\text{obs}}$ ):

$$\frac{d\Gamma_\alpha}{d\hat{t}} = \frac{d^2\tau_\alpha}{dt_{\text{obs}}d\hat{t}}, \quad (5.2)$$

where the subscript  $\alpha = \text{bulge, disk or PBH}$ , respectively.

#### Coordinate system

It would be useful to explicitly define the coordinate system we employ in the following calculations. For the rectangular coordinate system, denoted as  $(x, y, z)$ , we choose the Galactic center as the coordinate origin. Without loss of generality, we can take the  $x$ -direction to be along the direction connecting the Galactic center and the Earth position (an observer’s position). We assume that the Earth is located at the position,  $(x, y, z)_\oplus =$

(8 kpc, 0, 0), i.e. 8 kpc in distance from the Galactic center. Furthermore, we take the  $y$ -direction to be along the Earth's rotation direction in the Galactic disk plane, and the  $z$ -direction to be in the direction perpendicular to the disk plane.

In this chapter we consider the microlensing datasets obtained from the 5-years OGLE survey (Udalski et al. 2015)<sup>2</sup>. In the Galactic coordinates, the OGLE fields are located in the range of  $-15^\circ \lesssim b \lesssim 15^\circ$  and  $-20^\circ \lesssim l \lesssim 20^\circ$ . Throughout this chapter we simply assume that the OGLE field is in the direction to the field BLG505 with  $(b, l) = (-2^\circ 389, 1^\circ 0879)$ , which has the largest number of background stars among the OGLE fields. We believe that this approximation is valid because our results are based on relative contributions of microlensing due to stellar components in the bulge and disk regions compared to microlensing due to PBHs in the MW halo region.

### Bulge lens

First we consider a microlensing that both lens and source are in the Galactic bulge region. The average optical depth of microlensing due to the  $i$ -th stellar component for a single source star is given by

$$\begin{aligned} \tau_b &\equiv \frac{1}{N_s} \int_{d_{s,\min}}^{d_{s,\max}} dd_s n_s(d_s) \sum_i \int_{d_{s,\min}}^{d_s} dd_1 \frac{\rho_{b,i}(d_1)}{M_i} \pi R_E^2(M_i) \\ &= \frac{4\pi G}{c^2 N_s} \int_{d_{s,\min}}^{d_{s,\max}} dd_s n_s(d_s) \sum_i \int_{d_{s,\min}}^{d_s} dd_1 \rho_{b,i}(d_1) D, \end{aligned} \quad (5.3)$$

where the integration is along the line-of-sight direction (see below),  $D \equiv d_1 d_{ls} / d_s$ , and the index  $i$  stands for the  $i$ -th stellar component as a lensing object for which we will consider brown dwarfs, main sequence stars, white dwarfs, neutron stars and astrophysical black holes (see below).  $N_s$  is the surface number density of source stars defined by a line-of-sight integration of the three-dimensional number density distribution of source stars,  $n_s$ , as

$$N_s \equiv \int_{d_{s,\min}}^{d_{s,\max}} dd_s n_s(d_s). \quad (5.4)$$

The function  $\rho_{b,i}(d_1)$  is the mass density profile for the  $i$ -th stellar component.  $d_{s,\min}$  and  $d_{s,\max}$  are the maximum and minimum distances to the boundary of the bulge region from an observer's position. Throughout this chapter we employ  $d_{s,\min} = 4$  kpc and  $d_{s,\max} = 12$  kpc; that is, we assume that the bulge has a size of 4 kpc around the center ( $d_s = 8$  kpc) in depth

---

<sup>2</sup>The OGLE-IV fields can be found from <http://ogle.astrouw.edu.pl/sky/ogle4-BLG/>.

from an observer. The integration over  $d_s$  or  $d_l$  in Eq. (5.3) is along the line-of-sight direction of an observer towards the source star in the direction  $(y, z)$ . As long as the lens distribution  $\rho_{b,i}$  and the source star distribution are given, the line-of-sight integration is straightforward to perform as we will show later.

Now we consider the event rate of microlensing. To do this, we start from the geometry and variables defined in Fig. 4 of Griest et al. (1991) (also see Figure 7 of Niikura et al. 2017), which defines the differential event rate of a lensing object entering a volume element along the line-of-sight where the lens causes a microlensing with magnification above a certain threshold value:

$$d\Gamma_b = \sum_i \frac{\rho_{b,i}}{M_i} R_E v_\perp^2 \cos \theta dd_1 d\alpha f_{b,i}(\mathbf{v}_\perp, v_\parallel) dv_\perp d\theta dv_\parallel, \quad (5.5)$$

where  $f_{b,i}(\mathbf{v}_\perp, v_\parallel)$  is the velocity distribution of the  $i$ -th stellar component, defined so as to satisfy the normalization condition  $\int d^2\mathbf{v}_\perp \int dv_\parallel f(\mathbf{v}_\perp, v_\parallel) = 1$ ;  $\mathbf{v}_\perp$  is the perpendicular components of relative velocity between an observer, lens and source star (see below), defined as  $\mathbf{v}_\perp = v_\perp(\cos \theta, \sin \theta)$ ;  $\alpha$  is the azimuthal angle in the two-dimensional  $(y, z)$ -plane, defined as  $(y, z) = \sqrt{y^2 + z^2}(\cos \alpha, \sin \alpha)$ ;  $\theta$  is the angle between the line connecting the source and the lens center and the direction of the transverse velocity  $\mathbf{v}_\perp$ . In this chapter we define the microlensing ‘‘event’’ if the lensing magnification is greater than a threshold magnification,  $A > A(R_E) = 1.34$ , which is satisfied if the separation between lens and source is closer than the threshold separation,  $b \leq R_E$ . The parameters vary in the range of  $\theta \in [-\pi/2, \pi/2]$ ,  $\alpha \in [0, 2\pi]$ , and  $v_\perp \in [0, \infty)$ .

We assume that the velocity distribution can be simplified as

$$f_b(\mathbf{v}_\perp, v_\parallel) = f_b(\mathbf{v}_\perp) f_b(v_\parallel). \quad (5.6)$$

As we discussed, for a characteristic timescale of microlensing light curve, we employ a crossing time scale of the Einstein ring, defined as  $t_E = 2R_E \cos \theta / v_\perp$ . This simplification is not critical for the following discussion because we study the PBH microlensing contribution relative to those due to the stellar components in the disk and bulge regions. In this case,

the microlensing event rate due to the  $i$ -th stellar components is given as

$$\begin{aligned} \frac{d\Gamma_b}{dt_E} &= \frac{2\pi}{N_s} \int_{d_{s,\min}}^{d_{s,\max}} dd_s n_s(d_s) \sum_i \int_{d_{s,\min}}^{d_s} dd_1 \frac{\rho_{b,i}(d_1)}{M_i} R_E(d_s, d_1) \\ &\quad \times \int_0^\infty dv_\perp \int_{-\pi/2}^{\pi/2} d\theta v_\perp^2 \cos\theta f_{b,i}(v_\perp, \theta) \\ &\quad \times \delta_D\left(t_E - \frac{2R_E \cos\theta}{v_\perp}\right). \end{aligned} \quad (5.7)$$

Using the Dirac delta function identity

$$\delta_D\left(t_E - \frac{2R_E \cos\theta}{v_\perp}\right) = \delta_D\left(v_\perp - \frac{2R_E \cos\theta}{t_E}\right) \frac{v_\perp^2}{2R_E \cos\theta}, \quad (5.8)$$

the above equation is simplified as

$$\begin{aligned} \frac{d\Gamma_b}{dt_E} &= \frac{\pi}{N_s} \int_{d_{s,\min}}^{d_{s,\max}} dd_s n_s(d_s) \\ &\quad \times \sum_i \int_{d_{s,\min}}^{d_s} dd_1 \frac{\rho_{b,i}(d_1)}{M_i} \int_{-\pi/2}^{\pi/2} d\theta v_\perp^4 f_{b,i}(v_\perp, \theta), \end{aligned} \quad (5.9)$$

where  $v_\perp = 2R_E \cos\theta/t_E$ . With this condition, the tangential velocity  $v_\perp$  depends on integration variables,  $d_s$ ,  $d_1$ , and  $\theta$  via  $R_E = R_E(d_1, d_s)$ .

### Disk lens

Next we consider an event rate for microlensing due to stellar components in the disk region for a single source star in the bulge region. The calculation is very similar to the case for bulge lens in the preceding section. In this case we employ a single source plane approximation for simplicity; that is, we assume that all source stars are at distance of 8 kpc, the Galactic center. Under this assumption, the optical depth is given by

$$\tau_d = \frac{4\pi G}{c^2} \int_0^{\bar{d}_s} dd_1 \sum_i \rho_{d,i}(d_1) D, \quad (5.10)$$

where  $\rho_{d,i}(d_1)$  is the mass density distribution of the  $i$ -th stellar component,  $D = d_1 d_{ls} / \bar{d}_s$ ,  $\bar{d}_s$  is the mean distance to source stars, i.e.  $\bar{d}_s = 8$  kpc, and  $d_{ls} = \bar{d}_s - d_1$ .

Similarly, the event rate is

$$\frac{d\Gamma_d}{dt_E} = \pi \sum_i \int_0^{\bar{d}_s} dd_1 \frac{\rho_{d,i}(d_1)}{M_i} \int_{-\pi/2}^{\pi/2} d\theta v_{\perp}^4 f_{d,i}(v_{\perp}, \theta), \quad (5.11)$$

where  $v_{\perp} = 2R_E \cos \theta / t_E$ ,  $f_{d,i}(\mathbf{v}_{\perp}) = f_{d,i}(v_{\perp}, \theta)$  is the velocity distribution for velocity components perpendicular to the line-of-sight direction for the  $i$ -th stellar component in the disk region.

### PBH lens

Now we consider a scenario that PBHs constitute some mass fraction of DM in the MW halo region. We call ‘‘PBHs in the halo region’’ because PBHs are distributed from the Galactic center through the outer halo region due to the large velocity dispersion. When a lensing PBH happens to pass across a source star in the bulge on the sky, it could cause microlensing effect on the source star. Throughout this chapter we consider a monochromatic mass distribution for PBHs. Similarly to the disk microlensing, the optical depth of microlensing due to PBHs is

$$\tau_{\text{PBH}} = \frac{4\pi G}{c^2} \int_0^{\bar{d}_s} dd_1 \rho_{\text{DM}}(d_1) D, \quad (5.12)$$

where  $\rho_{\text{DM}}(d_1)$  is the dark matter distribution. If PBHs consist only some partial mass fraction of DM in the MW region, denoted as  $f_{\text{PBH}} \equiv \Omega_{\text{PBH}}/\Omega_{\text{DM}}$ , we replace  $\rho_{\text{DM}}$  in the above and following equations with  $f_{\text{PBH}}\rho_{\text{DM}}$ .

Similarly, the event rate of microlensing due to PBHs for a single source star in the bulge is

$$\frac{d\Gamma_{\text{PBH}}}{dt_E} = \pi \int_0^{\bar{d}_s} dd_1 \frac{\rho_{\text{DM}}(d_1)}{M_{\text{PBH}}} \int_{-\pi/2}^{\pi/2} d\theta v_{\perp}^4 f_{\text{DM}}(v_{\perp}, \theta), \quad (5.13)$$

where  $f_{\text{DM}}(\mathbf{v}_{\perp})$  is the velocity distribution of PBHs.

## 5.3 Models of Galactic disk and bulge and Milky Way dark matter

As we described, once we give the density and velocity distributions for stellar components in the MW bulge and disk regions as well as those for PBHs (equivalently DM) in the halo

lens	mass density profile: $\rho [M_{\odot}\text{pc}^{-3}]$	$\tau [10^{-6}]$	velocity profile: $(\mu, \sigma) [\text{km/s}]$
bulge	$1.04 \times 10^6 \left(\frac{s}{0.482 \text{ pc}}\right)^{-1.85}, (s < 938\text{pc})$	1.07	$f_y : \{-220(1 - \alpha), \sqrt{1 + \alpha^2}100\}$
	$3.53 K_0\left(\frac{s}{667 \text{ pc}}\right), (s \geq 938\text{pc})$		$f_z : \{0, \sqrt{1 + \alpha^2}100\}$
disk	$0.06 \times \exp\left[-\left\{\frac{R-8000}{3500} + \frac{z}{325}\right\}\right]$	1.03	$f_y : \left\{220\alpha, \sqrt{(\kappa\delta + 30)^2 + (100\alpha)^2}\right\}$ $f_z : \left\{0, \sqrt{(\lambda\delta + 30)^2 + (100\alpha)^2}\right\}$
PBH	$4.88 \times 10^{-3} f_{\text{PBH}} \frac{1}{(r/r_s)(1+r/r_s)^2}$	$0.18 f_{\text{PBH}}$	$f_y : \left\{-220(1 - \alpha), \sqrt{\sigma_{\text{DM}}^2 + (\alpha 100)^2}\right\}$ $f_z : \left\{0, \sqrt{\sigma_{\text{DM}}^2 + (\alpha 100)^2}\right\}$

Table 5.1: Summary of the Galactic models for the mass and velocity distributions for stellar components and PBHs.  $\alpha$  is the ratio of distances between lens and source,  $\alpha \equiv d_l/d_s$ . We employ the coordinate system as defined in Section 5.2.1, and take the Galactic center as the coordinate origin. The optical depth ( $\tau$ ) is calculated assuming an observation in the direction of  $(b, l) = (-2^\circ 389, 1^\circ 0879)$  which represents the OGLE Galactic bulge fields. For PBH case, we assume that PBHs constitute DM in the MW region by mass fraction,  $f_{\text{PBH}} \equiv \Omega_{\text{PBH}}/\Omega_{\text{DM}}$ , when computing the microlensing optical depth. We assume a Gaussian for the velocity profile, and the quantities,  $\mu$  and  $\sigma$ , denote the mean and dispersion for the Gaussian distribution. For PBH, we employ  $\sigma_{\text{DM}} = 220$  km/s for our fiducial model, which is taken from the rotational velocity of Galactic disk (see text).

region, we can compute the event rates of microlensing for a star in the bulge region. In this subsection, we briefly review the standard model for the MW bulge and disk following Han & Gould (1995). Then we describe our model for the density and velocity distributions for PBHs in the MW region.

### 5.3.1 The mass density distribution

For the mass density distribution of stellar population in the bulge region, we adopt the model in Kent (1992) that describes the following bar-structured model:

$$\begin{aligned} \rho_b(x, y, z) &= \begin{cases} 1.04 \times 10^6 \left(\frac{s}{0.482 \text{ pc}}\right)^{-1.85} M_{\odot}\text{pc}^{-3}, & (s < 938\text{pc}), \\ 3.53 K_0\left(\frac{s}{667 \text{ pc}}\right) M_{\odot}\text{pc}^{-3}, & (s \geq 938\text{pc}), \end{cases} \end{aligned} \quad (5.14)$$

where  $K_0(x)$  is the modified Bessel function,  $s$  is the radius from the Galactic center in the elliptical coordinates, defined as  $s^4 \equiv R^4 + (z/0.61)^4$  with  $R \equiv (x^2 + y^2)^{1/2}$ , and all the coordinate components  $(x, y, z, s, R)$  are in units of pc. As defined in Section 5.2.1, the coordinate origin is the Galactic center. Note that the above profile is continuous at

object	parameters in $dn/dM$	mass range [ $M_{\odot}$ ]	initial mass range [ $M_{\odot}$ ]	$N$
brown dwarf (BD)	Power-law ( $M^{-0.8}$ )	[0.01, 0.08]	$0.01 \leq M \leq 0.08$	0.18
main-sequence star (MS)	Power-law ( $M^{-2}$ )	[0.5, 1.0]	$0.5 \leq M \leq 1.0$	1
	Power-law ( $M^{-1.3}$ )	[0.08, 0.5]	$0.08 \leq M \leq 0.5$	
white dwarf (WD)	Power-law (initially $M^{-2}$ )	[0.34, 2.0]	$1.0 \leq M \leq 8.0$	0.15
neutron star (NS)	Gaussian ( $M_r = 1.33, \sigma_r = 0.12$ )	[0.73, 1.93]	$8.00 \leq M \leq 20.0$	0.013
black hole (BH)	Gaussian ( $M_r = 7.8, \sigma_r = 1.2$ )	[1.8, 13.8]	$20.0 \leq M \leq 100.0$	0.0068

Table 5.2: Summary of the mass spectrum for each of astrophysical objects: brown dwarfs, main-sequence stars, and stellar remnants (white dwarfs, neutron stars, and astrophysical black holes) in the standard Galactic bulge and disk models. We assume the Kroupa initial mass function as shown in Fig. 5.1, and then assume that each massive star with initial masses  $M \geq 1M_{\odot}$ , as denoted in the column “initial mass range”, evolved into each stellar remnant. For white dwarf, we assume the relation between initial and end masses as given by  $M_{\text{WD}} = 0.339 + 0.129M_{\text{init}}$ . The column “ $dn/dM$ ” denotes parameters of the mass spectrum for each object population, while we assume a Gaussian distribution with the mean and width values for the mass spectrum of neutron stars and black holes. The last column “ $N$ ” gives the number of each object population relative to that of main-sequence stars used in the calculation of microlensing event rate.

$s = 938$  pc, and we consider the above profile is for the total contribution of visible objects, i.e. main sequence stars, as we will describe below. Using the Galactic celestial coordinate variables  $(l, b)$ , a star at the distance  $d$  from an observer (the Earth’s position) is at the distance from the Galactic center,  $r$ , given as

$$r(d) = \sqrt{R_{\oplus}^2 - 2R_{\oplus}d \cos l \cos b + r^2}, \quad (5.15)$$

where  $r = \sqrt{x^2 + y^2 + z^2}$ ,  $x = d \cos b \cos l$ ,  $y = d \cos b \sin l$ , and  $z = d \sin b$ . This variable transformation between  $d$  ( $d_l$  or  $d_s$ ) and  $x, y, z$  enters into the above equations such as Eq. (5.9).

For the mass density distribution in the disk region, we employ the model in Bahcall (1986):

$$\rho_d(R, z) = 0.06 \times \exp \left[ - \left\{ \frac{R - 8000}{3500} + \frac{z}{325} \right\} \right] M_{\odot} \text{pc}^{-3}. \quad (5.16)$$

Note that, as we defined,  $R (= \sqrt{x^2 + y^2})$  denotes the radial distance in the cylindrical coordinates and  $z$  is in the direction perpendicular to the Galactic disk (variables are in units of pc). This model assumes that the disk has an exponential distribution with vertical and radial scale lengths of 325 pc and 3500 pc, respectively. Although the mass-to-light ratio of disk stellar population is not well understood, we normalize the above density profile to  $\rho_{d0} = 0.06 M_{\odot} \text{pc}^{-3}$  at the solar neighborhood ( $R = 8000$  pc).

For the spatial distribution of DM (therefore PBHs) between the Galactic center and an observer (the Earth), we assume the Navarro-Frenk-White (NFW) model (Navarro et al. 1997):

$$\rho_{\text{NFW}}(r) = \frac{\rho_c}{(r/r_s)(1+r/r_s)^2}, \quad (5.17)$$

where  $r_s$  is the scale radius and  $\rho_c$  is the central density parameter. For this model we assume spherical symmetry for the DM distribution for simplicity. In this chapter we adopt the halo model in Klypin et al. (2002):  $M_{\text{vir}} = 10^{12} M_{\odot}$ ,  $\rho_c = 4.88 \times 10^6 M_{\odot}/\text{kpc}^3$ , and  $r_s = 21.5 \text{ kpc}$ , taken from Table 2 in the paper. The DM profile with these parameters has been shown to fairly well reproduce the observed rotation curve in the MW. However, there might still be a residual uncertainty in the total mass (mostly DM) of MW within a factor of 2 (Callingham et al. 2018).

Table 5.1 summarizes models of the mass density profiles for stellar components in the bulge and disk regions and for dark matter in the MW halo region. The table also gives the optical depth for a single source star for lenses in the bulge or disk region and for PBHs, respectively. Note that the optical depth does not depend on a lens mass as indicated from Eq. (5.3). The table shows that the optical depth due to PBHs is smaller than that of astrophysical objects in the disk or bulge region, by a factor of 5, reflecting that astrophysical objects are more centrally concentrated due to the dissipation processes.

### The velocity distribution

A timescale of the microlensing light curve (see Eqs. (5.9), (5.11), and (5.13)) is determined by a transverse component of the relative velocity for source-lens-observer system on the sky (Griest et al. 1991; Han & Gould 1995):

$$\begin{aligned} \mathbf{v}_{\perp} &= \mathbf{v}_l - \left( \frac{d_l}{d_s} \mathbf{v}_s + \frac{d_{ls}}{d_s} \mathbf{v}_o \right) \\ &= \mathbf{v}_l - [\alpha \mathbf{v}_s + (1 - \alpha) \mathbf{v}_o], \end{aligned} \quad (5.18)$$

where  $\mathbf{v}_l$ ,  $\mathbf{v}_s$  and  $\mathbf{v}_o$  are the transverse velocities for lens, source star and an observer, respectively, and we have introduced the notation  $\alpha \equiv d_l/d_s$ . As we described in Section 5.2.1, the  $x$ -direction is along the direction from the observer to the Galactic center (i.e. a source star), which is equivalent to the line-of-sight direction, the  $y$ -direction is along the direction of disk rotation, and the  $z$ -direction is perpendicular to the line-of-sight direction. Hence we need to model the mean and distribution of the transverse velocity components,  $\mathbf{v}_{\perp} = (v_y, v_z)$ . Hereafter we often omit the subscript “ $\perp$ ” in  $\mathbf{v}_{\perp}$  for notational simplicity.

**Bulge lens**

First we consider the velocity distribution for the bulge microlensing where both lens and source star are in the bulge region. For the velocity distribution, we assume that the stellar components are supported by an isotropic velocity dispersion, and do not have any rotational velocity component. Under these assumptions, the mean of the transverse velocities is

$$\begin{aligned}\bar{v}_{by} &\equiv \langle v_{ly} - [\alpha v_{sy} - (1 - \alpha)v_{oy}] \rangle = -220(1 - \alpha) \text{ km/s}, \\ \bar{v}_{bz} &= 0\end{aligned}\tag{5.19}$$

where we have assumed that an observer is in the rest frame of the rigid body rotation of Galactic disk, has the rotational velocity of 220 km/s with respect to the Galactic center, and has no mean velocity in the disk height direction.

The velocity dispersion for the  $y$ -component of relative velocity can be computed as

$$\begin{aligned}\sigma_{by}^2 &\equiv \langle (v_y)^2 \rangle - \langle v_y \rangle^2 \\ &= \langle v_{ly}^2 \rangle + \alpha^2 \langle v_{sy}^2 \rangle \\ &= (1 + \alpha^2)(100 \text{ km/s})^2,\end{aligned}\tag{5.20}$$

Here we assumed that the velocity dispersion per component  $\sigma_y = 100$  km/s, and assumed that the source and lens have independent random motions;  $\langle v_{sy}v_{ly} \rangle = 0$ . The velocity dispersion for the velocity  $z$ -component is

$$\sigma_{bz}^2 = (1 + \alpha^2)(100 \text{ km/s})^2.\tag{5.21}$$

Following Han & Gould (1995), we assume that the velocity distribution is given by a Gaussian and that the velocity distribution for the bulge microlensing is given by

$$f_b(\mathbf{v}) = f_b(v_y)f_b(v_z),\tag{5.22}$$

where

$$\begin{aligned}f_b(v_y) &= \frac{1}{\sqrt{2\pi}\sigma_{by}} \exp\left[-\frac{(v_y - \bar{v}_{by})^2}{2\sigma_{by}^2}\right], \\ f_b(v_z) &= \frac{1}{\sqrt{2\pi}\sigma_{bz}} \exp\left[-\frac{v_z^2}{2\sigma_{bz}^2}\right],\end{aligned}\tag{5.23}$$

**Disk lens**

Next we consider the velocity distribution for stellar components in the disk region. We assume that the stellar components have a rigid rotation on average:

$$\begin{aligned}\bar{v}_{dy} &= 220\alpha \text{ km/s} \\ \bar{v}_{dz} &= 0.\end{aligned}\tag{5.24}$$

For the velocity dispersion, we assume the linear disk velocity dispersion model in Table 1 of Han & Gould (1995):

$$\begin{aligned}\sigma_{dy}^2 &= (\kappa\delta + 30)^2 + (100\alpha)^2 \text{ (km/s)}^2 \\ \sigma_{dz}^2 &= (\lambda\delta + 20)^2 + (100\alpha)^2 \text{ (km/s)}^2\end{aligned}\tag{5.25}$$

with

$$\begin{aligned}\kappa &\equiv 5.625 \times 10^{-3} \text{ km/s/pc}, \\ \lambda &\equiv 3.75 \times 10^{-3} \text{ km/s/pc}, \\ \delta &\equiv (8000 - x) \text{ pc},\end{aligned}\tag{5.26}$$

where  $\kappa$  and  $\lambda$  are the velocity dispersion gradient coefficients. Hence the velocity distribution functions are given by the similar equations to Eq. (5.23).

**PBH lens**

Now we consider a microlensing due to PBHs, acting as DM, in the MW halo region. PBHs are tracers of the MW halo that is much more extended than the bulge size ( $\sim 200$  kpc vs. a few kpc in radius). The large extent of DM halo reflects the fact that PBHs have a larger velocity dispersion than that of bulge stars (100 km/s). First we assume that PBHs have isotropic velocity distribution with respect to the halo center for which we assume the Galactic center. Hence the mean relative velocity for a PBH lens is

$$\begin{aligned}\bar{v}_{PBHy} &= -220(1 - \alpha) \text{ km/s}, \\ \bar{v}_{PBHz} &= 0.\end{aligned}\tag{5.27}$$

For a PBH causing microlensing effect on a bulge star, it should be located somewhere between the Galactic center and the Earth, which is a very inner region compared to the

halo size. Such a PBH (more generally dark matter) tends to have a large velocity when passing through the central region of DM halo; DM tends to have a larger velocity at the closest point to the halo center (i.e. the Galactic center), while a bounded DM should stop at an apocenter point of its orbit, which tends to be around the outer boundary of the halo. Hence we assume that PBHs causing the microlensing have a large velocity dispersion whose amplitude is similar to the rotation velocity. To keep generality of our discussion, we introduce a parameter to model the velocity dispersion of DM per one direction,  $\sigma_{\text{DM}}$ :

$$\begin{aligned}\sigma_{\text{PBH}y}^2 &= \sigma_{\text{DM}}^2 + \alpha^2(100)^2 \text{ (km/s)}^2 \\ \sigma_{\text{PBH}z}^2 &= \sigma_{\text{DM}}^2 + \alpha^2(100)^2 \text{ (km/s)}^2,\end{aligned}\tag{5.28}$$

where we have again assumed the isotropic velocity dispersion. For our fiducial model, we assume  $\sigma_{\text{DM}} = 220$  km/s. We checked that a change in  $\sigma_{\text{DM}}$ , say by  $\pm 10\%$ , gives only a small change in the following PBH constraints. Such a large velocity dispersion in the central region within the halo is supported by  $N$ -body simulation studies that simulate MW-scale halos, for example, Figure 2 of Ref. (Vogelsberger et al. 2009).

Table 5.1 gives a summary of the velocity distributions for stellar components in the bulge and disk regions and for PBHs (DM) in the halo region, respectively.

### 5.3.2 Mass spectrum of astrophysical lensing objects

As implied by Eq. (2.75), a timescale of microlensing light curve varies with a lens mass. To make a quantitative modeling of microlensing events as a function of the light curve timescale, we need to take into account the mass distribution of stellar lenses in the bulge and disk regions. Following Mróz et al. (2017) (also see Gould 2000; Sumi et al. 2011), we consider brown dwarfs (BD), main sequence stars (MS), white dwarfs (WD), neutron stars (NS), and astrophysical black holes (BH) as the constituents in the bulge and disk regions.

To do this, we first assume the Kroupa-like broken power-law *initial* mass function (IMF) for the stellar components (Kroupa 2001):

$$\begin{aligned}\frac{dn_s(M)}{d \ln M} &= \begin{cases} A_{\text{BD}} \left(\frac{M}{0.08 M_\odot}\right)^{1-\alpha_{\text{BD}}} & (0.01 \leq M/M_\odot \leq 0.08) \\ A_{\text{MS}} \left(\frac{M}{0.5 M_\odot}\right)^{1-\alpha_{\text{MS1}}} & (0.08 \leq M/M_\odot \leq 0.5) \\ A_{\text{MS}} \left(\frac{M}{0.5 M_\odot}\right)^{1-\alpha_{\text{MS2}}} & (M/M_\odot \geq 0.5) \end{cases},\end{aligned}\tag{5.29}$$

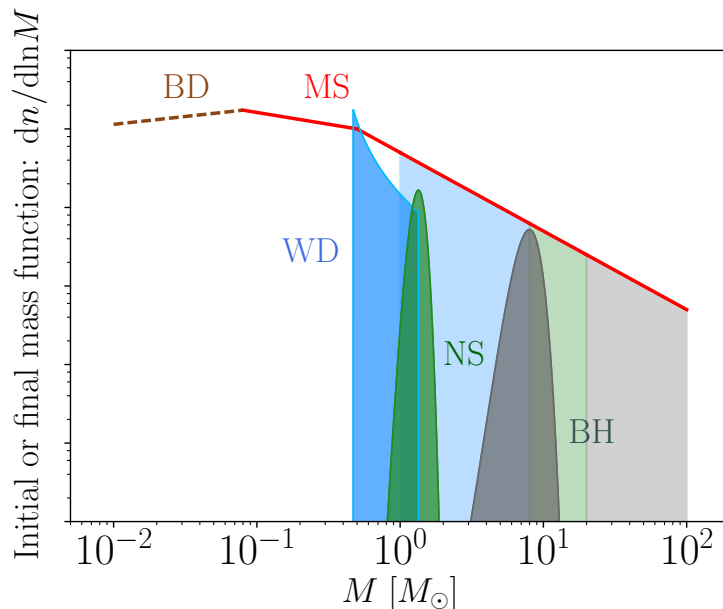


Figure 5.1: Broken power-law curves denote the initial mass function of brown dwarfs (BD) and main-sequence star assuming the Kroupa-like model (see Eq. (5.29)). Note that  $y$  axis is in an arbitrary scale. We assume that each massive star with  $M \geq 1 M_{\odot}$  evolved into stellar remnant until today; white dwarfs (WD) for stars with  $1 \leq M/M_{\odot} \leq 8$  following the initial and end mass relation,  $M_{\text{WD}} = 0.339 + 0.129M_{\text{init}}$ , neutron stars (NS) for  $8 \leq M/M_{\odot} \leq 20$ , and astrophysical black holes (BH) for  $M \geq 20 M_{\odot}$ , respectively. For NSs and BHs, we assume a Gaussian for the end-mass function; we assume the Gaussian with mean and width,  $M_{\text{final}} = 1.33M_{\odot}$  and  $\sigma = 0.12M_{\odot}$  for NSs, while the Gaussian with  $M_{\text{final}} = 7.8M_{\odot}$  and  $\sigma = 1.2M_{\odot}$  for BHs, respectively. The dark-shaded curves are the mass functions for WD, NS and BH, respectively. Because of the number conservation, the area under the curve for each stellar remnant,  $\int d \ln M \, dn/d \ln M$ , is the same as the area of the IMF over the corresponding range of initial main-sequence star masses (the two regions of similar color have the same area). For BDs, we determine the normalization of the mass function so that it matches the OGLE data at short timescales.

for BD, low-mass MS stars ( $0.08 < M/M_{\odot} < 0.5$ ), and high-mass MS stars ( $M \geq 0.5M_{\odot}$ ), respectively;  $A_{\text{BD}}$  and  $A_{\text{MS}}$  are normalization parameters for which we will discuss below, and  $\alpha_{\text{BD}}$ ,  $\alpha_{\text{MS1}}$  and  $\alpha_{\text{MS2}}$  are the power-law index parameters for these components, respectively. Following Mróz et al. (2017) we assume  $\alpha_{\text{BD}} = 0.8$ ,  $\alpha_{\text{MS1}} = 1.3$  and  $\alpha_{\text{MS2}} = 2$ , respectively, where the slope for low-mass stars of  $\lesssim 1 M_{\odot}$  is taken from the study of the Galactic bulge IMF in Ref. (Zoccali et al. 2000). Throughout this chapter we assume the same population composition of stellar components in the disk and bulge regions. The formation of BDs is still poorly understood (see Burrows et al. 2001, for a review). Some fraction of BDs can be found in the planetary disk around a primary main-sequence star. Other population of BDs can form at the center of protoplanetary disk as a primary gravitating object of the system.

Moreover, there might be some population of BDs ejected from the host system due to three-body scattering, which would be observed as “free-floating planets” in the interstellar space. A wide-orbit BD or a free-floating BD causes microlensing event characterized by the BD mass. If a lens system has both primary star and BD in the close orbit, the microlensing event is characterized by the total mass (mainly the host star). Thus, as discussed in Mróz et al. (2017) (Sumi et al. 2011), there is still a lot of discussion for the origin of microlensing events in a short timescale corresponding to BD masses or even shorter (smaller-mass) events. Hence, the amplitude of BD mass function is uncertain, and needs to be further study. In the following results, we will treat the BD normalization parameter  $A_{\text{BD}}$  as a free parameter, and determine it so that the model prediction matches the OGLE data in the corresponding short timescales.

Massive stars with masses  $M_{\text{init}} \geq 1 M_{\odot}$  have a rapid time evolution during the age of MW, and evolved into stellar remnants. Following Mróz et al. (2017), we assume that all stars with initial masses  $1 \leq M/M_{\odot} \leq 8$  evolved into WDs following the empirical initial-final mass relation,  $M_{\text{WD}} = 0.339 + 0.129M_{\text{init}}$ , after the mass loss; stars with  $8 \leq M/M_{\odot} \leq 20$  evolved into NSs for which we assume a Gaussian distribution with peak mass  $M_{\text{final}} = 1.33M_{\odot}$  and width  $\sigma = 0.12M_{\odot}$  for the end masses; stars with  $M \geq 20M_{\odot}$  evolved into astrophysical BHs for which we assume a Gaussian distribution with peak mass  $M = 7.8M_{\odot}$  and width  $\sigma = 1.2M_{\odot}$ . We adopt the number conservation between initial stars and stellar remnants; each massive star evolved into each stellar remnant. Under this assumption, we found the ratio of the number of each stellar remnant relative to that of main sequence stars as

$$\text{MS} : \text{WD} : \text{NS} : \text{BH} = 1 : 0.15 : 0.013 : 0.0068 . \quad (5.30)$$

Throughout this chapter we refer to stars with masses  $0.08 \leq M/M_{\odot} \leq 1$  as “main sequence stars” (MS).

Fig. 5.1 displays the model for the initial or final mass spectrum of BDs, MSs and stellar remnants, which we use in this paper. For the BD mass function, we will determine the normalization parameter so that the model prediction matches the OGLE microlensing events as we show below (we here adopt a normalization that is continuous with the stellar IMF at  $M = 0.08M_{\odot}$ ). The number of each lensing population determines the frequency of microlensing. Then if we focus on the event rates for a particular light curve timescale, the events arise mainly from lensing objects of the corresponding mass scales (Eq. (2.75)). Thus, by studying the event rate as a function of the light curve timescales, one can distinguish contributions from different populations of lensing objects. Table 5.2 also gives the summary of our model for the mass spectrum of BDs, MS stars or stellar remnants.

Furthermore, we assume the binary fraction  $f_{\text{bin}} = 0.4$ ; the fraction of MS stars or stellar remnants are in binary systems. For simplicity we consider equal-mass binary systems: we treat a microlensing of a binary system by that of a lens with mass  $M_{\text{binary}} = 2M$ . We do not consider binary systems that contain two objects of different masses and contain two objects of different populations (e.g., MS-WD system) for simplicity. Consequently we decrease the number of lens systems from the above numbers in Fig. 5.1 by the binary fraction. Including the binary systems give a slightly improved agreement between the model predictions and the OGLE data, but it is not an important assumption for our main results.

To perform a calculation of microlensing event rates, we need to specify the normalization parameter of MS IMF,  $A_{\text{MS}}$  (Eq. (5.29)). Recalling that the mass of Galactic bulge and disk regions is dominated by the total mass of low-mass MS stars, we determine  $A_{\text{MS}}$  by the condition

$$\rho_* = \int_{0.08M_\odot}^{M_\odot} d \ln M M \frac{dn}{d \ln M}. \quad (5.31)$$

Here  $\rho_*$  is the normalization coefficient of mass density profile in the bulge and disk regions as given in Table 5.1. With this normalization,  $A_{\text{MS}}$  has a dimension of [ $\text{pc}^{-3}$ ]. We assume the same composition of stars and stellar remnants everywhere in the disk and bulge regions; that is, we ignore a possible dependence of the composition on a position in the Galactic region. Details of our model are different from the model in Mróz et al. (2017), so we will introduce a fudge normalization parameter later to model a possible uncertainty in the normalization:  $A_{\text{MS}} \rightarrow f_A A_{\text{MS}}$ . However, we find  $f_A \simeq 1$ , implying that our model is sufficiently close to the best-fit model in Mróz et al. (2017) or equivalently that the standard Galactic bulge/disk models are fairly accurate to reproduce the observed timescale (mass) distribution of microlensing events as we will show below.

## 5.4 Results

### 5.4.1 OGLE data

The results shown in this chapter are all based on the microlensing data taken in the OGLE-IV sky survey during the 5 years, 2011–2015 (Udalski et al. 2015; Mróz et al. 2017). The OGLE survey uses the dedicated 1.3m Warsaw Telescope, located at Las Campanas Observatory, Chile. The OGLE survey carried out a long-term monitoring observation of the nine fields towards the Galactic bulge region with a cadence of either 20 min or 60 min, covering 12.6 square degrees in total. After the careful cuts in a selection of microlensing events,

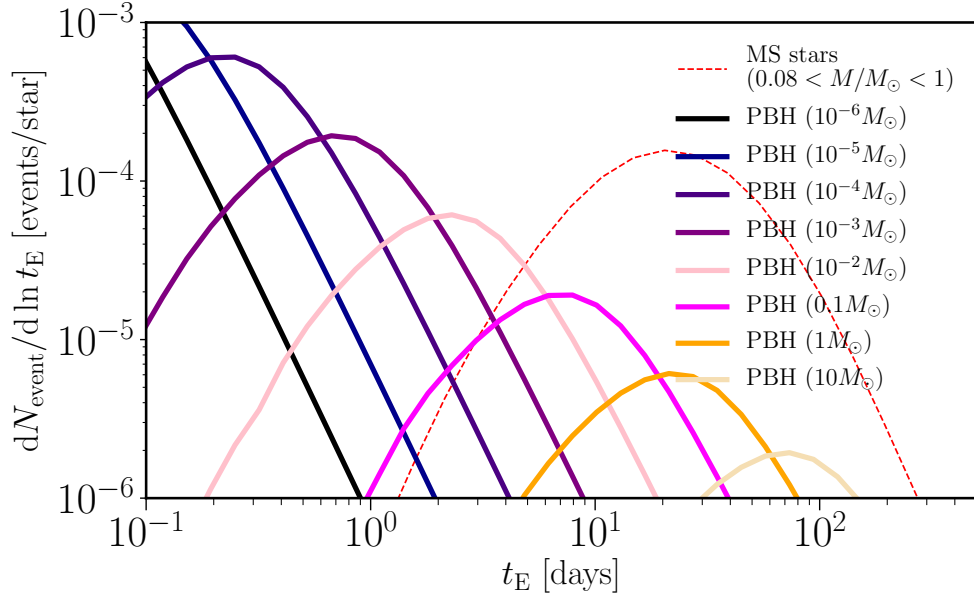


Figure 5.2: The expected differential number of microlensing events per logarithmic interval of the light curve timescale  $t_E$ , for a single star in the Galactic bulge region, assuming the 5-years observation as in the OGLE data. The quantity shown is defined in terms of the event rate described in Section 5.2.1 as  $dN_{\text{exp}}/d \ln t_E \equiv 5 \text{ years} \times t_E \times d\Gamma/dt_E$  (see Eqs. (5.9), (5.11) and (5.13)). Solid curves show the results for PBHs assuming that all DM in the MW region is made of PBHs of a given mass scale denoted by the legend:  $f_{\text{PBH}} = \Omega_{\text{PBH}}/\Omega_{\text{DM}} = 1$ . For comparison, dashed curve shows the result when main-sequence stars with mass in the range  $[0.08, 1]M_\odot$  are lenses, assuming the Galactic model for the star distribution in the bulge and disk regions.

the team created a catalog of 2622 microlensing events for each of which a timescale of the microlensing light curve ( $t_E$ ) is measured. Thus the OGLE datasets are quite rich and allow us to constrain the abundance and mass distribution of each lensing object population. As carefully studied in Mróz et al. (2017), a majority of the OGLE events can be fairly well explained by superposition of microlensing events due to BDs, MS stars, and stellar remnants. Among these contributions, the origin of BDs is not well understood as we discussed (see Burrows et al. 2001, for a review). Thanks to the unique power of microlensing that can probe a gravitational mass of a lensing object regardless of whether it is visible, the OGLE data in timescales less than  $\sim 10$  days can be used to identify a microlensing contribution of BDs. However, the abundance and mass spectrum has not been fully understood yet. In addition to the BD contribution, those papers discussed a possible contribution of unbounded planets (wide-orbit planets or free-floating planets). Mróz et al. (2017) discussed that unbounded Jupiter-mass planets are about 0.05 – 0.25 planets per main sequence star, which is smaller than previously advocated in Ref. Sumi et al. (2011). The large OGLE

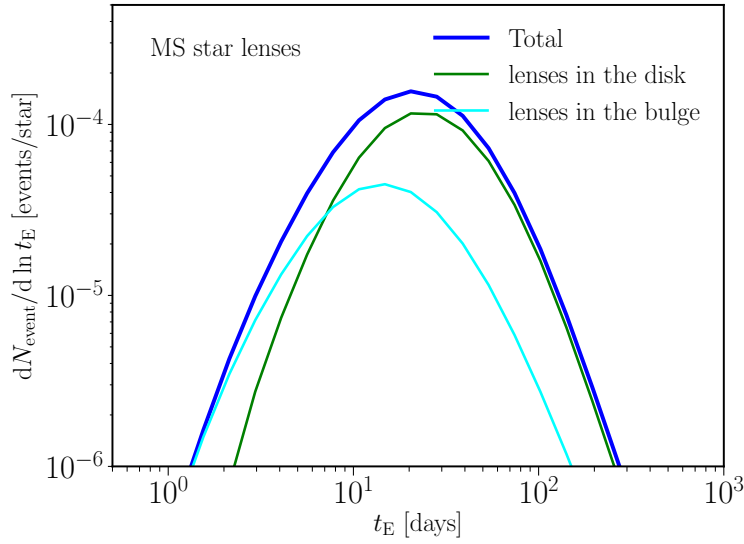


Figure 5.3: Shown is the relative contributions of main-sequence stars in the bulge and disk regions to the total event rates of microlensing in the previous figure.

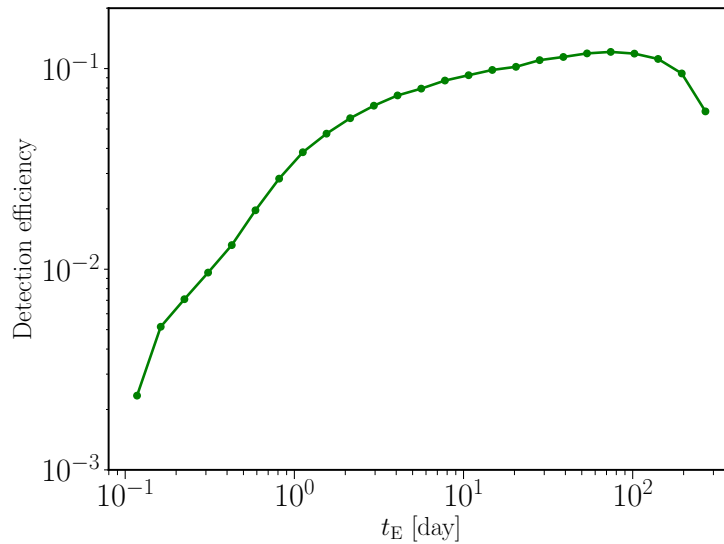


Figure 5.4: The detection efficiency,  $\epsilon(t_E)$ , quantifying the probability that a microlensing event of timescale  $t_E$  is detected by the OGLE data. This represents a typical function that is taken from Extended Data Figure 2 in Mróz et al. (2017).

dataset indicates even shorter timescale events that correspond to unbounded Earth-mass planets. Interestingly, the OGLE data also indicates a "gap" (no microlensing event) at timescales between the BD or unbounded Jupiter-mass microlensing and the Earth-mass planets. Since planetary formation theory would predict a continuous mass spectrum, the gap, if real, seems very challenging to explain. For example, a mechanism preferentially

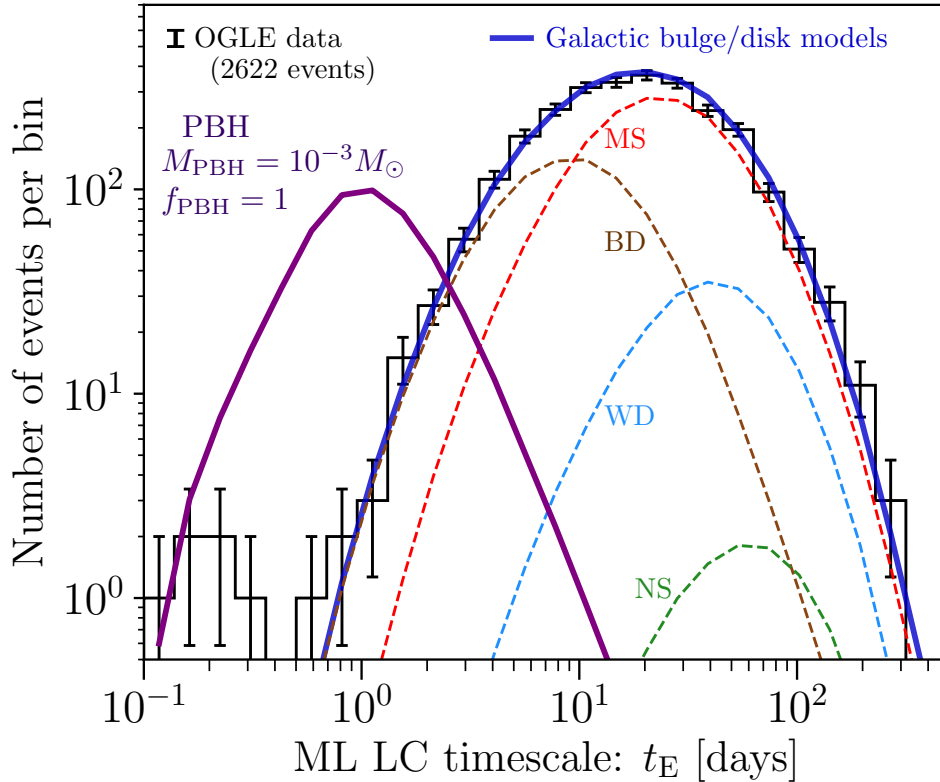


Figure 5.5: Comparison of the 5-years OGLE data with the model predictions. The histogram with errorbars denotes the OGLE data in each logarithmic bin of  $t_E$ , where the errorbar is the  $1\sigma$  Poisson uncertainties on the counts. The bold-blue solid curve shows the best-fit model assuming the stellar components in the bulge and disk regions. Other dashed curves show each contribution of brown dwarfs (BD), main sequence (MS) stars, white dwarfs (WD) and neutron stars (NS) to the total microlensing events, respectively (see Fig. 5.1). The contribution of astrophysical black holes is outside the plotting range. As a demonstration, the purple curve shows the prediction if all DM is PBHs with mass  $M_{\text{PBH}} = 10^{-3} M_{\odot}$  (Jupiter mass scales) for  $f_{\text{PBH}} = 1$ . A sum of the PBH and astrophysical object contributions is too high compared to the OGLE events, and therefore such a PBH scenario is ruled out by the OGLE data.

scattering Earth-mass planets from the planetary system is needed. All these results are very interesting, and worth to further explore. All the datasets we use in this chapter are taken from Extended Data Table in Mróz et al. (2017).

In this chapter, to derive PBH constraints, we employ the following two working hypotheses:

- (1) **Null hypothesis of PBH microlensing:** we assume that all the OGLE microlensing events are due to astrophysical objects, i.e. BDs, stars and remnants, so do not contain

any PBH microlensing event. Then we use all the OGLE events to obtain an upper limit on the abundance of PBHs assuming the monochromatic mass spectrum.

- (2) **PBH hypothesis of the 6 ultrashort-timescale OGLE events**,  $t_E \simeq [0.1, 0.3]$  days. The OGLE data found the 6 ultrashort-timescale microlensing events (Fig. 5.5), which seem a different population from the majority of events in the longer timescales due to BDs, stars and remnants. The timescale implies an Earth-mass lens. Although the origin might be unbounded Earth-mass planets, we here assume that the ultrashort-timescale events are due to PBHs, but other longer timescale events are due to astrophysical objects as in case (1). Under this hypothesis, we derive an allowed region of PBHs in two parameter space of the abundance and mass scale, assuming the monochromatic mass spectrum.

### 5.4.2 Event rate of microlensing

We are now in a position to compute event rates of microlensing by plugging the model ingredients, which we have discussed up to the preceding subsection, into the equations such as Eq. (5.9).

Fig. 5.2 shows the expected differential number of microlensing events per logarithmic interval of the light curve timescale  $t_E$ , for a single source star in the bulge region, assuming the 5-years observation as in the OGLE data. For PBH microlensing, we adopt the model ingredients in Sections 5.3 for the mass density profile and velocity distribution, assuming the monochromatic mass scale. We assumed that all DM is made of PBHs of each mass scale:  $f_{\text{PBH}} = 1$ . If we consider lighter-mass PBHs, the number density of PBHs increases and such PBHs yield a higher frequency of microlensing events with shorter timescales. In particular, for microlensing events with timescales shorter than a few days, PBHs with  $M_{\text{PBH}} \lesssim 10^{-1} M_\odot$  could produce a larger number of microlensing events than MS stars of  $\sim 1 M_\odot$  do, if such PBHs constitute a significant fraction of DM.

In Fig. 5.3 we study relative contributions of MS stars in the bulge and disk regions to the total of MS microlensing events. It can be found that stars in the disk region gives a dominant contribution, while the bulge star contribution is significant for shorter timescale events.

### 5.4.3 Comparison with the 5-years OGLE data

We now compare the model predictions of microlensing events with the 5-years OGLE data. The OGLE data contains 2622 events over the range of light curve timescales,

$t_E = [10^{-1}, 300]$  days (see Extended Data Table 4 in Mróz et al. (2017)). The expected number of microlensing events per a given timescale interval of  $[t_E - \Delta t_E/2, t_E + \Delta t_E/2]$  is computed as

$$N_{\text{exp}}(t_E) = t_{\text{obs}} N_s f_A \int_{t_E - \Delta t_E/2}^{t_E + \Delta t_E/2} d \ln t'_E \frac{d^2 \Gamma}{d \ln t'_E} \epsilon(t'_E), \quad (5.32)$$

where  $t_{\text{obs}}$  is the total observation time,  $N_s$  is the total number of source stars in the OGLE bulge fields, and  $\epsilon(t_E)$  is the “detection efficiency” quantifying the probability that a microlensing event of timescale  $t_E$  is detected by the OGLE data. For the OGLE data,  $t_{\text{obs}} = 5$  years and  $N_s = 4.88 \times 10^7$  (see Extended Data Table 2 in Mróz et al. 2017). We employ the detection efficiency,  $\epsilon(t_E)$ , that is taken from Extended Data Figure 2 in Mróz et al. (2017), which is explicitly shown in Fig. 5.4. We do not include variations of the detection efficiency in the different OGLE fields for simplicity. The coefficient  $f_A$  is a fudge normalization factor that takes into account a possible difference in details of our model calculations and the model of Mróz et al. (2017).

In Fig. 5.5 we compare the model prediction of microlensing event rates with the 5-years OGLE data. First of all, a majority of the OGLE microlensing events has a single peak around the timescale,  $t_E \sim 20$  days, and has a gradual decrease at the shorter and longer timescales than the peak timescale. Thus the OGLE data suggests only a single population of the underlying lensing objects, except for the 6 ultrashort-timescale events,  $t_E = [0.1, 0.3]$  days, which we will discuss later. Interestingly, the model assuming the standard Galactic bulge and disk models (see Section 5.3) can fairly well reproduce event rates for the main population of OGLE microlensing events. Furthermore, by employing the mass distribution of BD, stars and stellar remnants, the model can reproduce the distribution of light curve timescales (see Section 5.3.2). Although we introduced a fudge factor in Eq. (5.32) to model a possible difference between our model and the model in Mróz et al. (2017), we found  $f_A = 0.99$  to have a nice agreement of our model prediction with the OGLE data at timescales greater than the peak timescale. The best-fit  $f_A$  value is close to unity, and reflects the fact that the Galactic bulge and disk model, constructed based on observations and the previous knowledges, is fairly accurate. As we discussed, the origin and nature of unbounded BDs, which cause shorter timescale events, is poorly understood. We found that the model matches the microlensing events at timescales shorter than the peak timescale, if we assume 0.18 BDs per main-sequence star (see Table 5.2). The figure clearly shows that MS stars with  $0.08 \leq M/M_\odot \leq 1$  give a dominant contribution to the OGLE events at timescales,  $t_E \gtrsim 10$  days, while stellar remnants give secondary contributions. BDs

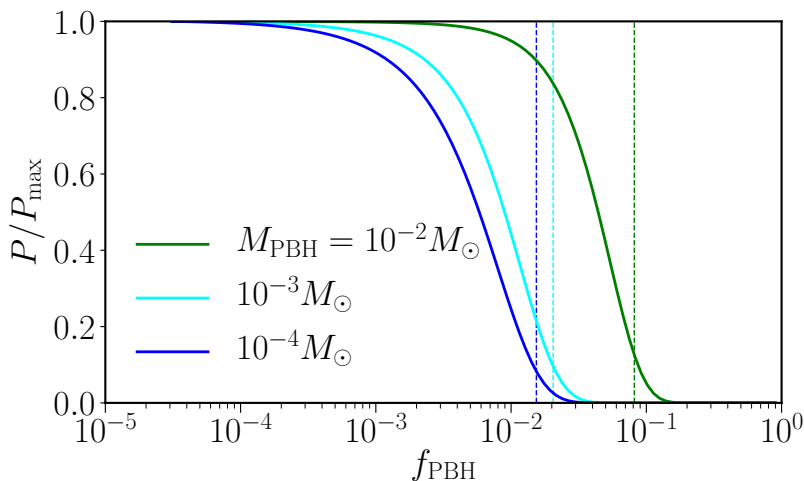


Figure 5.6: Posterior distribution of the  $f_{\text{PBH}}$  parameter (the PBH mass fraction to DM) assuming “null hypothesis” that there is no PBH microlensing in the OGLE data (see text for details). Here we show, as examples, three cases for PBH mass scale;  $M_{\text{PBH}}/M_{\odot} = 10^{-4}$ ,  $10^{-3}$  or  $10^{-2}$ , respectively, which is computed from Eq. (5.35) by comparing the model prediction of PBH microlensing event rates with the OGLE data. The vertical dashed line for each curve denotes 95% CL upper limit on the abundance of PBH for each mass case, which is obtained by computing the integration of the posterior distribution,  $\int_0^{f_{\text{PBH},95\%}} df_{\text{PBH}} P(f_{\text{PBH}}) = 0.95$ .

give a dominant contribution at the shorter timescales. However, the figure shows that, as long as we assume a smooth model for the density and velocity distributions of BDs, the model cannot reproduce the ultrashort-timescale events of  $t_E \sim 0.1$  days. This clearly indicates a distinct, second population of small-mass lensing objects. On the other hand, PBHs do not necessarily follow the similar timescale distribution of microlensing events to that of BD, stars or remnants, because DM has different spatial and velocity distributions from the stellar populations. As an example, Fig. 5.5 shows the result for case that PBHs with mass  $M_{\text{PBH}} = 10^{-3}M_{\odot}$  are DM. A sum of the PBH and stellar population contributions give too many microlensing events compared to the OGLE data. In other words, such a PBH population is not allowed by the OGLE data. Thus we can use the OGLE data to obtain an upper bound on the abundance of PBHs with varying PBH mass scales.

#### 5.4.4 Upper bound on the PBH abundance under null hypothesis

As we showed in the preceding subsection, the Galactic bulge and disk models including the stellar components fairly well reproduce the OGLE data except for the 6 ultrashort-timescale events. In other words, the OGLE data does not necessarily imply the existence of PBH microlensing in the data. As the first working hypothesis (see Section 5.4.1), we here

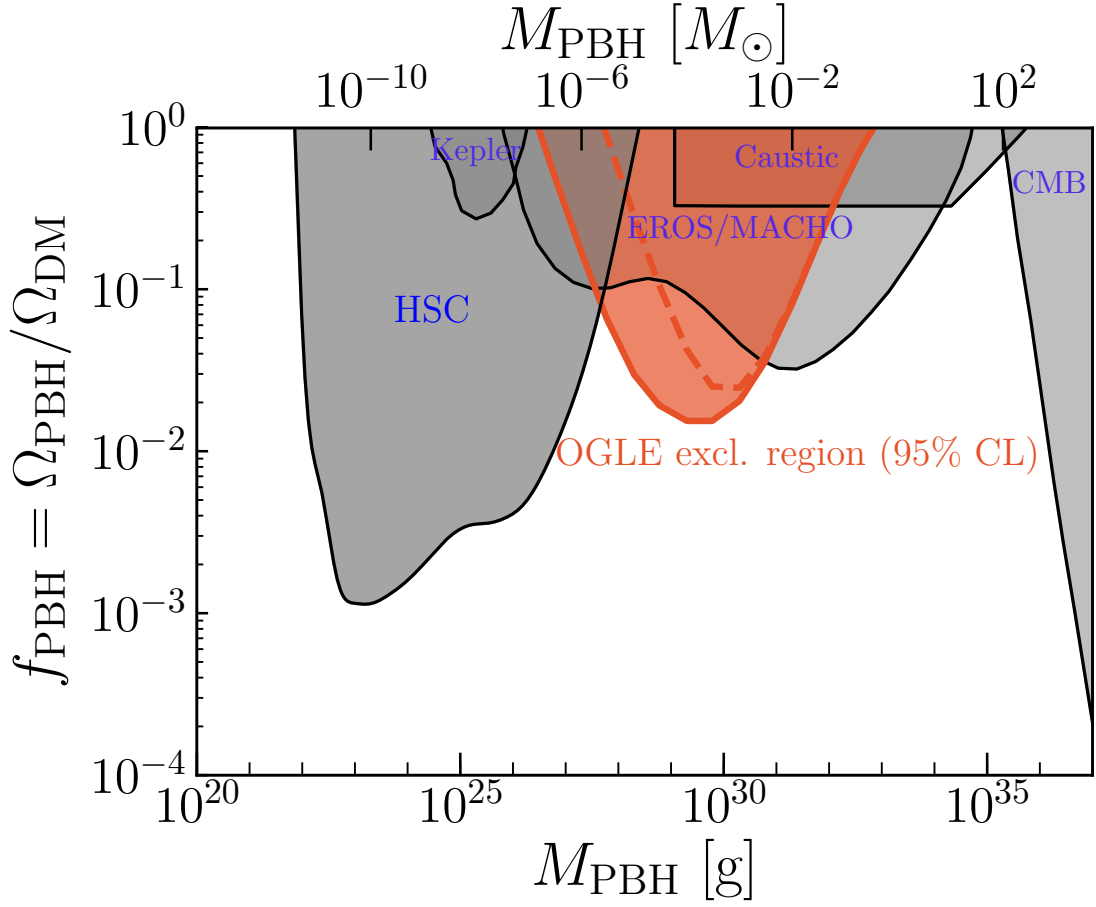


Figure 5.7: Red shaded region corresponds to the 95% C.L. upper bound on the PBH mass fraction to DM, derived assuming the null hypothesis that there is no PBH microlensing event in the 5-year OGLE data (see text for details). Here we assume a monochromatic mass function of PBHs, and we derive the upper bound at each mass scale denoted in the  $x$ -axis. The dashed curve shows the upper bound if the OGLE data in the 4 shortest timescale bins for the ultrashort-timescale events is not used for the null hypothesis. This constraint can be compared with other observational constraints as shown by the gray shaded regions: the microlensing search of stars in the Andromeda galaxy from the one-night Subaru Hyper Suprime-Cam data (“HSC”) (Niikura et al. 2017), the microlensing search from the 2-years Kepler data (“Kepler”) (Griest et al. 2014), the earlier MACHO/EROS/OGLE microlensing search (“EROS/MACHO”) (Tisserand et al. 2007), the microlensing of extremely magnified stars near caustics of a galaxy cluster (“Caustics”) (Oguri et al. 2018) and the accretion effects on the CMB observables (“CMB”) (Ali-Haïmoud & Kamionkowski 2017), which is the result updated from the earlier estimate (Ricotti et al. 2008).

employ “null hypothesis” to obtain an upper limit on the abundance of PBHs. That is, we assume that all the observed OGLE microlensing events, including the 6 ultrashort-timescale events, are due to the stellar components, or equivalently there is no PBH lensing in the

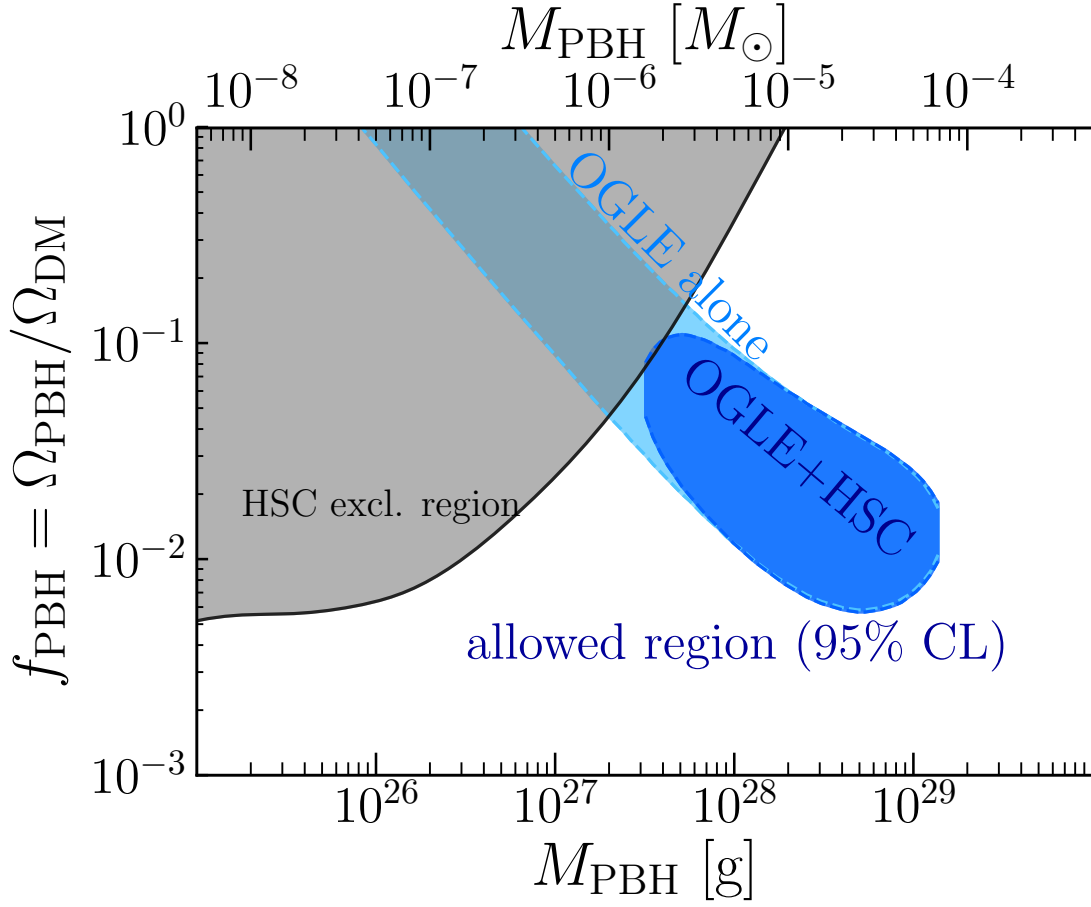


Figure 5.8: Shaded blue region is the 95% CL allowed region of PBH abundance, obtained by assuming that 6 ultrashort-timescale microlensing events in the OGLE data are due to PBHs. Note that we assume a monochromatic mass scale for PBHs as given in the  $x$ -axis. The allowed region is computed from the condition  $P(f_{\text{PBH}}, M_{\text{PBH}})/P_{\text{max}} > 0.046$ , which corresponds to 95% CL if the surface of posterior distribution follows a two-dimensional Gaussian distribution ( $P_{\text{max}}$  is the posterior distribution for the best-fit model). Dark shaded region shows the result when combining the allowed region of the ultrashort-timescale events with the upper bounds from the Subaru constraints and the longer timescale OGLE data.

OGLE data. This would give us a most stringent upper bound on the PBH abundance. If we allow a possible PBH contribution to the OGLE data in addition to the stellar events, it would give us a more relaxed upper bound or could even allow for a detection of PBH. However, this requires a perfect knowledge of the Galactic stellar components, which is not straightforward.

We assume that the OGLE counts of microlensing events at each timescale bin follows the Poisson distribution. This is a good assumption because the same lensing object very unlikely produces multiple lensing events (lensing for multiple source stars) because of smallness of

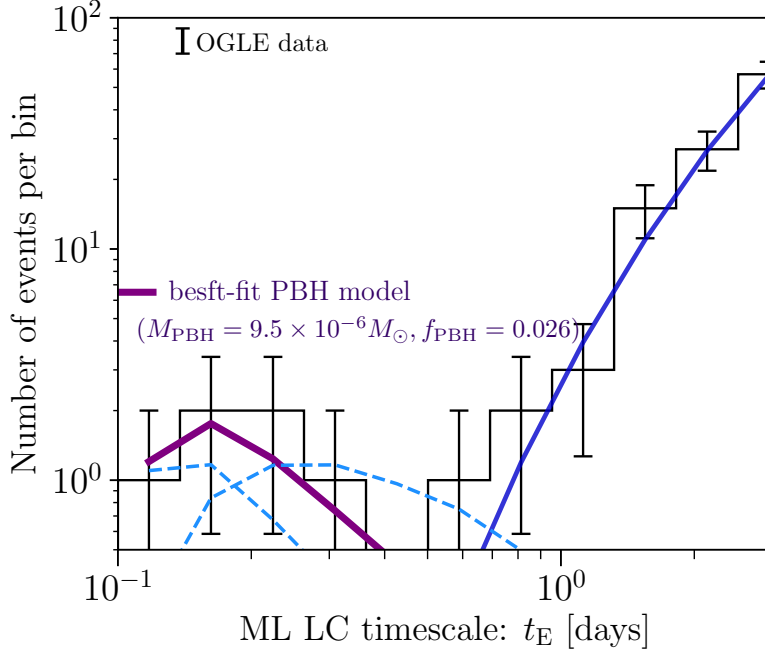


Figure 5.9: Bold purple-solid line shows the best-fit PBH model in each of the 4 shortest timescale bins, which shows a good agreement with the distribution of 6 ultrashort-timescale OGLE events. The best-fit model is characterized by  $M_{\text{PBH}} = 9.5 \times 10^{-6} M_{\odot}$  and  $f_{\text{PBH}} = 0.026$ . For comparison, the two dashed lines show the predictions for two models that are close to the boundary of the allowed region of “OGLE+HSC” in Fig. 5.8;  $(M_{\text{PBH}}, f_{\text{PBH}}) = (1.6 \times 10^{-6}, 0.062)$  or  $(6.9 \times 10^{-5}, 0.014)$ , respectively. These models do not give a good match to the timescale distribution of the ultrashort-timescale events, and also become inconsistent with the upper bounds of the HSC M31 and/or the longer timescale OGLE data.

the lensing optical depth,  $\tau \sim 10^{-6}$  (see Table 5.1). Hence we can safely assume that different microlensing events are independent and uncorrelated with each other. Under these assumptions, we assume that the log likelihood of OGLE microlensing events is given by

$$\ln \mathcal{L}(\mathbf{d}|\mathbf{m}\theta) = \sum_{i=1}^{n_{\text{bin}}} [N_{\text{obs}}(t_{E,i}) \ln \lambda(t_{E,i}) - \lambda(t_{E,i}) - \ln N_{\text{obs}}(t_{E,i})!] \quad (5.33)$$

where  $N_{\text{obs}}(t_{E,i})$  is the observed number of events at the  $i$ -th timescale bin ( $t_{E,i}$ );  $\mathbf{d}$  is the data vector,  $\mathbf{d} \equiv \{N_{\text{obs}}(t_{E,1}), N_{\text{obs}}(t_{E,2}), \dots, N_{\text{obs}}(t_{E,n_{\text{bin}}})\}$  in our case,  $n_{\text{bin}}$  is the number of timescale bins ( $n_{\text{bin}} = 25$  as can be found from Fig. 5.5);  $\mathbf{m}\theta$  is the model vector;  $\lambda(t_{E,i})$  is the expectation number of events at the bin. When we include PBH microlensing contributions,

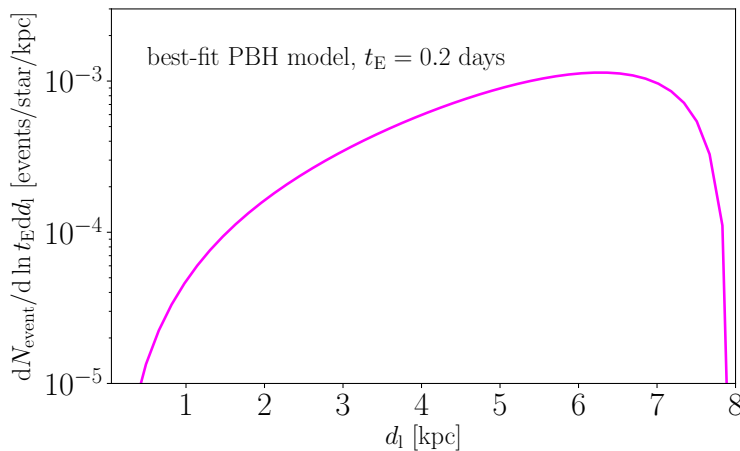


Figure 5.10: The contribution of PBHs at each distance to the total event rate of timescale  $t_E = 0.2$  days. Here we consider the best-fit PBH model ( $M_{\text{PBH}} = 9.5 \times 10^{-6} M_\odot$ ,  $f_{\text{PBH}} = 0.026$ ) to the ultrashort-timescale OGLE events in the previous figure.

we model the expectation number by

$$\lambda(t_{E,i}) = N_{\text{obs}}(t_{E,i}) + N_{\text{exp}}^{\text{PBH}}(t_{E,i}). \quad (5.34)$$

Here  $N_{\text{exp}}^{\text{PBH}}(t_{E,i})$  is the expected number of microlensing events due to PBHs at the  $i$ -th timescale bin, which is computed from Eq. (5.32) once the PBH mass fraction to DM,  $f_{\text{PBH}}$ , is specified for an assumed PBH mass scale ( $M_{\text{PBH}}$ );  $N_{\text{exp}}^{\text{PBH}}(E, i) \propto f_{\text{PBH}}$ . As a conservative approach, we use the observed counts,  $N_{\text{obs}}(t_{E,i})$  for the expectation value of microlensing events due to stellar components. In the following, we assume that the MW DM model for the spatial and velocity distributions for PBH in Sections 5.3, and we treat the PBH mass fraction parameter,  $f_{\text{PBH}}$ , as a free parameter for an assumed PBH mass scale ( $M_{\text{PBH}}$ ). Namely we consider a single model parameter for an assumed PBH mass scale (we will discuss later for a possible extension of this assumption). When  $f_{\text{PBH}} = 0$ , i.e.  $N_{\text{exp}}^{\text{PBH}} = 0$ , the maximum likelihood is realized because of  $N_{\text{exp}}^{\text{PBH}} \geq 0$ . The last term in the above log likelihood is irrelevant for parameter inference, because it is a fixed number irrespectively of model parameter ( $f_{\text{PBH}}$ ).

Given the likelihood function and the PBH model (denoted as  $\mathcal{M}$ ), the posterior distribution of model parameter,  $f_{\text{PBH}}$ , is computed based on the Bayes's theorem as

$$P(f_{\text{PBH}}|\mathbf{d}, \mathcal{M}) = \frac{\mathcal{L}(\mathbf{d}|f_{\text{PBH}})\Pi(f_{\text{PBH}})}{P(\mathbf{d}|\mathcal{M})}, \quad (5.35)$$

where  $\Pi(f_{\text{PBH}})$  is a prior of  $f_{\text{PBH}}$  and  $P(\mathbf{d}|\mathcal{M}) \equiv \mathcal{E}$  is the evidence. In this chapter, we

assume a flat prior,  $f_{\text{PBH}} \leq 1$ ; the total PBH mass in the MW region cannot exceed the DM mass. By computing the above equation with varying the model parameter  $f_{\text{PBH}}$ , we can obtain the posterior distribution for an assumed mass scale of PBH. Fig. 5.6 shows some examples for the posterior distribution for a given PBH mass scale, obtained from the above method.

Fig. 5.7 shows 95% CL upper bound on the PBH abundance at different mass scales. The OGLE data improves the constraints on the abundance for PBHs in the mass range  $M_{\text{PBH}} \simeq [10^{-3}, 10^{-6}]$ . The dashed curve shows the upper bound if we do not include the 6 ultrashort-timescale events in the 4 shortest timescale bins for the null hypothesis. Thus the upper bound at small mass scales is sensitive to the assumption of whether we include the short timescale bins in the analysis. The results can be compared with other constraints such as those from the Subaru Hyper Suprime-Cam (HSC <sup>3</sup>) observation of Andromeda galaxy (M31) (Niikura et al. 2017) and the earlier MACHO/EROS experiments (Alcock et al. 2000; Tisserand et al. 2007). The OGLE bound is stronger than that of MACHO/EROS due to the larger sample of microlensing events. The OGLE constraint is complementary to the Subaru HSC result that uses even denser (2 min) cadence data of M31 to search for microlensing for a larger number of source stars, but from only a single night observation. If we want to extend the constraint to PBHs at larger mass scales, we need to use the microlensing data extending to longer timescales such as year timescales.

#### 5.4.5 A possible detection of Earth-mass scale PBHs from short-timescale OGLE data

Now we employ the second working hypothesis in Section 5.4.1. That is we consider a case that the 6 ultrashort-timescale OGLE events, in  $t_E \simeq [0.1, 0.3]$  days, are due to PBH microlensing. In this case, we assume that the expectation number of microlensing events at each of the first 4 timescale bins (in the ultrashort-timescale bins) is given as

$$\lambda(t_{E,i}) = N_{\text{exp}}^{\text{PBH}}(t_{E,i}) \quad (5.36)$$

for the Poisson distribution of microlensing event counts (Eq. (5.33)). Here we should again note that we assume the monochromatic mass scale for PBHs. We also assume that the OGLE events in the longer timescales, i.e. the majority of OGLE events, are not due to PBHs (i.e no PBH microlensing as in the preceding section).

Fig. 5.8 shows a 95% CL *allowed* region of PBHs in two parameter space of its mass and

---

<sup>3</sup><https://hsc.mtk.nao.ac.jp/ssp/>

abundance. The thin-blue shaded region corresponds to the allowed region obtained from the OGLE data alone, while the thick shaded region is the allowed region when combining the OGLE results with the null hypothesis of PBH lensing for the longer timescale OGLE events ( $t_E \gtrsim 0.5$  days) and the the HSC constraints for M31. The best-fit model, which has a maximum likelihood, is a model with  $M_{\text{PBH}} = 9.5 \times 10^{-6} M_\odot$  and  $f_{\text{PBH}} = 0.026$ . The figure shows that PBHs of Earth-mass scales ( $3 \times 10^{-6} M_\odot$ ) can well reproduce the 6 ultrashort-timescale OGLE events if the abundance is at a per cent level. This allowed region is also consistent with null PBH results in the HSC data and the longer timescale OGLE data (if assuming the monochromatic mass spectrum).

Fig. 5.9 compares the best-fit PBH model with the timescale distribution of OGLE events in the shortest timescales. Interestingly, the width of OGLE timescale distribution is nicely reproduced by the velocity distribution of PBHs in the MW DM model. For comparison, the two dashed curves denote the model predictions for two models that are close to the boundary of 95% C.L. intervals in the allowed region, which are specified by model parameters  $(M_{\text{PBH}}/M_\odot, f_{\text{PBH}}) = (1.6 \times 10^{-6}, 0.062)$  or  $(6.9 \times 10^{-5}, 0.014)$ , respectively. These failed models under- or over-predict the microlensing event rates over the range of lightcurve timescale bins, and also become inconsistent with the upper bounds of the HSC M31 data and the longer timescale OGLE data. This result implies that, if PBHs have a wide mass spectrum extending to larger masses than the best-fit mass, such a model generally fills the gap around  $t_E \simeq 0.4$  days between the ultrashort-timescale events and the main population. Note that PBH models with smaller masses than the best-fit mass generally predict too many microlensing events at even shorter timescales  $t_E \leq 0.1$  days, however, the OGLE data does not have a sensitivity due to the limitation of the cadence data (20 min cadence), and therefore the OGLE data has no sensitivity to events at  $t_E \leq 0.1$  days, which is taken into account by the detection efficiency in Fig. 5.4. The original event rates can have an increasing function at  $t_E \lesssim 0.1$  days. These mass-scale PBHs are well constrained by the HSC results.

As we have shown, the PBH model assuming the MW DM model can give an alternative explanation of the ultrashort-timescale OGLE events. Since there is an uncertainty in the MW DM model, especially the DM distribution around the halo center, one might worry whether such an uncertainty in the PBH distribution around the halo center is sensitive to our results. Fig. 5.10 shows which distant PBHs for the best-fit model contribute the microlensing events at timescale  $t_E = 0.2$  days. Due to lensing efficiency, PBHs over a wide range of distances between the Earth and the Galactic center equally contribute the lensing events. The PBHs near the Galactic center, where the DM distribution is most uncertain,

is not particularly sensitive to the final result. This lens distance dependence is contrary to DM annihilation that is quite sensitive to details of the DM density in the Galactic center.

## 5.5 Discussion and Conclusion

In this chapter we have used the largest sample of microlensing events for stars in the Galactic bulge, obtained from the 5-years OGLE observation, to constrain the abundance of PBH that is a viable candidate of DM in the MW region. The 2622 microlensing data contains rich information on event rates and light curve timescales that correspond to the abundance and mass scale of lensing “compact” objects, because kinematical or velocity structures of lensing objects, even for DM in the MW halo region, are well constrained by various observations; the relative velocity of lens-source-observer determines the crossing time of the lensing Einstein radius, or equivalently the microlensing light curve timescale, once mass of a lensing object is assumed because the mass determines the Einstein radius. Thus we can use the invaluable OGLE data, which covers the wide range of timescales  $t_E \simeq [0.1, 300]$  days, allows us to explore the abundance of unknown “compact” objects over the wide range of mass scales.

To do this, we first revisited the Galactic bulge/disk models to estimate event rates of microlensing due to astrophysical objects such as brown dwarfs, MS stars, and stellar remnants (white dwarfs, neutron stars, and astrophysical black holes), following Mróz et al. (2017). Since the mass of Galactic disk/bulge regions is dominated by low-mass main-sequence (MS) stars around  $M \sim 0.5M_\odot$ , astronomers have a quite good knowledge of the abundance of stars from various observations of star number counts. In addition, stellar remnants are from massive stars, so we can infer their abundances from the initial mass function of low-mass MS stars that is well constrained by various observations. We showed that, even if details of our models would be different from that of Mróz et al. (2017), the standard Galactic bulge/disk models including MS stars and stellar remnants nicely reproduce the OGLE events at timescales  $t_E \gtrsim 20$  days, corresponding to objects with  $M \gtrsim 1M_\odot$ . For the shorter-timescale events, we need to add contributions from brown dwarfs (BD) that are invisible or difficult to directly observe. The origin and nature of BDs ( $0.01 \lesssim M/M_\odot \lesssim 0.08$ ) are not well understood. Some of BDs should form around a primary MS star, while some of BDs would form, as a primary gravitating object, in a protoplanetary disk. The BDs contributing the short timescale microlensing are “unbounded” BDs, because the timescale becomes too long if the host primary star contributes microlensing (because of much larger mass compared to that of BD). Nevertheless, the timescale distribution of OGLE data continuously extends to shorter timescales than the MS peak timescale, and it suggests a population

of BD-mass objects with a continuous abundance to that of MS stars, except for the 6 ultrashort-timescale events in  $t_E \simeq [0.1, 0.3]$  days. We showed that our model can reproduce the entire timescale distribution for the main population of OGLE events if we adjust the abundance of BDs as done in Mróz et al. (2017) (about 0.18 BDs per MS star in our model).

Given a justification of the standard Galactic bulge/disk models, we employ the “null hypothesis”, i.e. no PBH microlensing event in the OGLE data, to obtain the stringent upper bound on the abundance of PBHs in the mass range  $M_{\text{PBH}} \simeq [10^{-6}, 10^{-3}]M_\odot$  (from Earth to Jupiter mass scales), assuming the monochromatic mass spectrum (Fig. 5.7). The upper bounds are tighter than the previous bound from the MACHO/EROS experiments (Tisserand et al. 2007) and the Subaru/HSC microlensing search for M31 (Niikura et al. 2017). This result shows the power of microlensing for exploring the PBH abundance.

Even more interestingly, we showed that the 6 ultrashort-timescale events can be well explained by PBHs of Earth-mass scales if such PBHs constitute about 1% of DM in the MW region (Fig. 5.8). Even if we employ the monochromatic mass spectrum for simplicity, the timescale distribution naturally arises from the velocity distribution of PBHs expected for the DM kinematical structures in the MW region. There is a mechanism in inflation model to produce PBHs in such a narrow mass range or with right abundance (e.g. Inomata et al. 2018). If this is a real PBH microlensing, it would be a big discover. Such a small mass black hole cannot be made by any astrophysical process, so this would also give an evidence of the large primordial perturbations at the corresponding Hubble horizon in the early universe. If we include a possible distribution of PBH masses, the results would be changed. Nevertheless it is rather straightforward to translate our results into a specific PBH model with a given mass spectrum, following the methods developed in Carr et al. (2016) (also see Inomata et al. 2017).

A usual explanation of the ultrashort-timescale OGLE events is due to “unbounded” Earth-like planets, where “unbounded” is needed to have the right microlensing timescale. These unbounded, more exactly wide-orbit or free-floating planets, could be formed by the formation of planetary system or scattering of planetary systems; for example, if a planetary system encounters a massive planet or star, such an Earth-mass planet might be scattered. Even if this happens, why there is a gap around  $t_E \simeq 0.4$  days between the ultrashort-timescale events and the majority of events (i.e. the main population). Of course the gap might be an apparent statistical fluctuation due to the low number statistics, but it would be completely a mystery if this is genuine, because there would be a continuous mass spectrum expected for unbounded planets from Earth (or even smaller-masses) to Jupiter masses. These involve complicated, nonlinear astrophysics in planetary or star formation, so

a further observational study would be a more direct path to resolving the origin and nature of these short timescale events. For example, a more detailed study of lightcurve for each ultrashort-timescale event would be very useful (see Mróz et al. 2018, for such an attempt). This requires a denser cadence data of microlensing search. Such a denser cadence data would be also useful to distinguish genuine microlensing events from other contaminating events such as stellar flare.

To confirm or falsify the PBH hypothesis of short-timescale events against free-floating planets, there is a very promising, robust way. It is a microlensing search for stars in M31 using the Subaru HSC data (or eventually LSST data towards the Magellanic Clouds). The angular direction of M31 is in a high latitude in the Galactic coordinates, i.e. far from the Galactic disk. If the short timescale microlensing events are due to free-floating planets, we should expect a much smaller number of events towards M31, because there is a much less number of stars in the high latitude direction compared to the direction to the Galactic center. On the other hand, if the PBH scenario is true, we should find microlensing events with a frequency predicted by the standard DM model of the MW halo region that is supported by the disk rotation measurements. As shown in Niikura et al. (2017), the Subaru and HSC combination is ideal because its FoV can cover the entire disk region of M31 and the large aperture allows us to use main-sequence stars in M31 for the microlensing search even with short exposure (e.g., 90 sec). We are now carrying out a monitoring observation of M31 with Subaru HSC, and we envision that we can address these important questions in the near future.

# Chapter 6

## Summary and Conclusion

This thesis is based on the results of observational studies to search for dark matter candidate called primordial black hole (PBH). PBHs have long been suggested as a viable candidate of dark matter (DM), because they can span an enormous mass range larger than  $10^{-5}g$ , and can also constitute the whole dark matter in the Universe (see Chapter 1 for more detail). They are also becoming popular targets of gravitational wave experiments, because they can constitute merging black holes theoretically.

The abundance of PBHs has been constrained using a number of astrophysical observations, except for a mass window of  $[10^{-14}, 10^{-9}]M_{\odot}$ . Many studies to search signals by PBHs have been based on gravitational microlensing, which is very powerful to probe compact DM objects such as PBHs (Chapter 2). One strong point of the lensing signal is that it is free from uncertainties which exist in the other probes resulting from electromagnetic interactions. In this thesis, we searched magnification phenomena by microlensing effect with unprecedented dataset, aiming at obtaining new hints about the origin of dark matter.

**Chapter 3** gives a result of microlensing search with the Subaru/HSC by a one-night observation of M31. With the aim of constraining the abundance of PBH on even smaller mass scales, we carried out a dense cadence observation of the Andromeda galaxy (M31), with the Subaru Hyper Suprime-Cam (HSC). The combination of the wide field-of-view and the 8.2m aperture of HSC/Subaru is ideal for microlensing search; we expect up to  $10^3$  PBH microlensing events of M31 stars from one-night observation, if PBHs constitute a majority of DM in the MW and M31 halo regions.

We developed image difference technique for the Subaru/HSC data, and successfully managed to find many candidate variable stars such as stellar flares, eclipsing binaries, and

Cepheid variables. After careful selection criteria including the microlensing fitting to the measured light curve, we concluded that most candidates are not microlensing events, but found one remaining candidate for which it is difficult to rule out the microlensing hypothesis. We derived the stringent upper bounds on the abundance of PBHs as a candidate for DM in the MW and M31 halo regions in the range of  $M_{\text{PBH}} \simeq [10^{-11}, 10^{-6}]M_{\odot}$ , including the previously-unexplored mass window of  $M_{\text{PBH}} = [10^{-11}, 10^{-9}]M_{\odot}$ .

**Chapter 4** uses the archival observations of M31 to update the microlensing study performed in Chapter 3. If the one remaining candidate detected in Chapter 3 is a real microlensing event, it is a discovery, unveiling some contribution of PBHs to DM. Alternatively the remaining candidate could also be a result of microlensing by a free-floating planet in the halo region, rather than a PBH. This could also be another important discovery. Here we performed another dense-candence observation of M31 for 7.5 hours with Subaru/HSC, and study the time-variability of the remaining candidate.

After careful test with the available dataset, we could not detect significant time-variability for the remaining candidate within 12-hour periodicity. Hence we concluded that we cannot rule out the microlensing hypothesis for this candidate, and keep it as a microlensing candidate. We also applied the selection criteria including the microlensing fitting to the new data, and derived tighter upper bounds on the abundance of PBHs as a candidate for DM in the MW and M31 halo regions, which is about 1.5 times more stringent compared to the previous constraint in Chapter 3 for the similar mass range.

**Chapter 5** presents another constraint on PBH abundance by using the outcome of OGLE survey. The OGLE-IV project presents a sample of 2,622 high-quality microlensing events by monitoring the sky towards the Galactic center for 5 years. As presented in Mróz et al. (2017), the timescale distribution of microlensing events can be modeled only with mass functions of stellar components either in Galactic disk or bulge. However, we can expect higher event rate of microlensing events if DM in the Galactic halo are composed by PBHs. For example, we expect up to about  $5 \times 10^2$  additional microlensing events by PBHs by the Galactic bulge observation, if PBHs with  $10^{-3}M_{\odot}$  constitute a majority of DM in the MW halo region.

Motivated by this fact, we first derived an upper bound on the abundance of PBHs, by assuming “null detection” of microlensing events by PBHs from the OGLE-IV data. By taking advantage of Poisson statistics, we improve the upper bound on the PBH abundance in the mass range  $M_{\text{PBH}} = [10^{-5}, 10^{-3}]M_{\odot}$  by a factor of 10 over the previous constraint

by the EROS/MACHO experiments. We also derived another implication from the “detection” of PBHs. In Mróz et al. (2017), they claim a detection of six ultrashort-timescale events (with timescales of less than 0.5 day), which may indicate the existence of Earth- and super-Earth-mass free-floating planets, as predicted by planet-formation theories. However, these six events are not confirmed as planetary objects, and still remains as candidates of dark matter. Hence we performed a likelihood analysis for those short events to study the “allowed” parameter space for the fraction of PBHs to the total dark matter which can realize the observed distribution of these events with  $t_E < 0.5$  day. Our calculation allowed a parameter region for PBHs with mass  $M_{\text{PBH}} \simeq [2 \times 10^{-6}, 4 \times 10^{-5}]$  with a fraction  $f_{\text{PBH}} \simeq [4 \times 10^{-3}, \times 10^{-1}]$  to the total DM in the Galactic halo.

As a future work to improve the constraint on PBH abundance, there are two ways to explore. The first one is to extend the constraints to smaller mass scales than we achieved in M31 study, so as to close the open window in the PBH fraction to the total DM. Our study with Subaru/HSC is hard to probe microlensing events by PBHs with mass  $M_{\text{PBH}} \lesssim 10^{-12} M_\odot$ , due to finite source size effect and wave effect. One strategy to overcome these effects is to monitor distant objects by high cadence observation with shorter-wavelength. For example, as presented in Bai & Orlofsky (2018), one can fulfill this requirement by monitoring pulsars with X-ray satellite. Although current constraint from by RXTE (10d)<sup>1</sup> is still too weak to put meaningful constraint on PBH abundance, future experiments such by Athena/Lynx (100d) (Barcons et al. 2015; Lynx Team Collaboration et al. 2018), AstroSat (100d) (Singh et al. 2014) and LOFT (300d) (LOFT Collaboration et al. 2012) are expected to set meaningful constraint about  $M_{\text{PBH}} \sim 10^{-14} M_\odot$  by observation of SMC X-1.

Another way to explore is to extend our constraints to heavier mass scales. If we could repeat observations of M31 with HSC every few months over 10 years, say 10 minutes observation for each observation run, we should be able to improve the constraints at heavier mass scales. These long-term observations would be very powerful to make comparison with population synthesis of black holes probed by future gravitational wave experiments Raidal et al. (2018). We can also go more stringent constraint by combining multiple observation of M31 and the Galactic bulge. Future space-based missions such as WFIRST (Spergel et al. 2015) and Euclid (Penny et al. 2013), can also improve the statistics of microlensing events.

---

<sup>1</sup>see [https://heasarc.gsfc.nasa.gov/docs/xte/RXTE\\_tech\\_append.pdf](https://heasarc.gsfc.nasa.gov/docs/xte/RXTE_tech_append.pdf)

# Appendix A

## Properties of transient candidates detected in HSC-M31 observation

In this section we discuss properties of secure candidates which include unique features in their light curves (flash, contiguous variation, etc.). Our classification of variable stars is based on our eye-ball checks of the shape of the light curves from  $r$ -band observations. In order to study the stellar properties for those candidates, we take advantage of the color property to identify their stellar types. In addition to the  $r$ -band data summarized in Table 4.2, we have access to the  $g$ -band data of M31 taken in 2013, 2015, and 2017 with the Subaru/HSC. For these dataset, we created the coadd images from these  $g$ -band images in every epoch, and measure the photometry for the candidate. We then used the Kurucz (1993) to model their stellar type with  $g-r$  color by taking into account the HSC filter responses. In the following, we summarize the properties of variable stars detected from our analysis, and also give some examples of light curves.

### A.1 Properties of variable stars

- Eclipsing binary

This type of candidates display a light curve with eclipse dip, during a given duration, and then such a transient feature repeats with a given period. We classify these kinds of candidates as an eclipse binary of stars, where two stars are rotating around each other and either of the two stars causes an eclipse on another star, leading a dip in the light curve of their total flux. The depth of ellipse, time duration and period are different from candidate to candidate. All the candidates seem to be M-type stars based on their  $g-r$  colors. Among the eclipsing binaries we found a unique candidate

as shown in Fig. A.9, where one dark star totally hide the other bright star so that the flux of bright star gets totally dark. This kind of binary system is generally composed by a white dwarf and a brown dwarf.

- Binary stars

For candidates that have pulsating light curves, we classify those as candidates of binary stars. If the two amplitudes of light curve within one period are similar, the stars have almost same mass and size stars. Their  $g-r$  colors indicate that almost all binary systems are M-type stars. About 10 systems have a period shorter than our observation duration (about 7 hours), and the shortest period is about 1.2 hours. These short period binary systems would be a contact binary system, where the two stars share the common envelope. Some examples of binary systems are shown in Fig. A.5.

- Cepheid variable stars

We have around 1000 candidates which display a constant rising or declining light curve over the 7-hour observation. We classify them as Cepheid variable star candidates. Most of the Cepheid candidates are found along the disk region of M31, and the distribution seems to be consistent with the distribution of classical  $\delta$  Cep variable stars found by PAndromeda project (Kodric et al. 2013). Due to the limited time observation, we can't measure an entire period of the light curve, so can't determine the period of each candidate. Their  $g-r$  colors indicate that most candidates are A- or F-type stars.

- Stellar flare

We find around 30 stars which shows a sudden magnification in brightness, followed by an almost exponential decay. We classify the candidates as a stellar flare. Their  $g-r$  colors indicate that most of the candidates are M-type stars, which is consistent with the properties of the normal prominent star flares. Hence, these flare stars are likely to be in the MW halo region. We did not find secure candidates for G-type flare stars. This is consistent with the previous work, which shows that M-stars have more frequent flare events because energetics in the atmosphere is more affected by their magnetic field compared to G-type stars (Moffett 1974; Lacy et al. 1976; Henry & Newsom 1996). On the other hand, there is still one candidate which has suddenly becomes  $\sim 22$  magnitude in brightness from complete dark, as in Fig. A.1. This flare event can be a G-type star in M31, because those stars should be bright enough to be detected by our observation if they exist in MW halo.

- Moving objects: asteroids in the Solar system

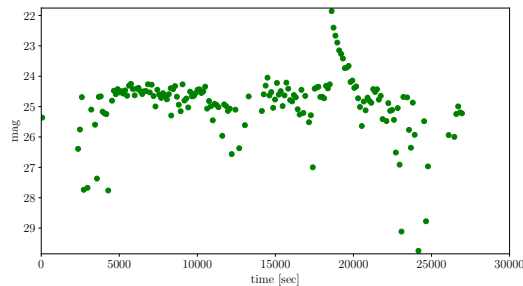


Figure A.1: Light curve of flare candidate in 2017. This target does not show up clearly in the 2014 observation.

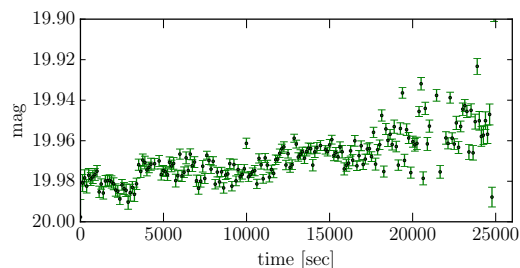


Figure A.2: Light curve of a nova candidate which indicate small magnification in 2014.

There exist a Gaussian-shape curve at the fixed WCS position. Since they display a clear trail in the postage-stamp image region, we consider these candidates as asteroids or comets in the Solar system. These moving objects also works as a main confusion component to our microlensing search. We have so far found two promising candidates of asteroids.

- RR-Lyrae stars

We find about 1,000 candidates which have a peak magnification around the best-seeing epochs. Since exposures with the best-seeing epochs have the deepest photometry, we may be probing some very faint stars around the limiting magnitude. Most candidates have a similar shape of light curve with peak magnitude of  $r \sim 24.5-25$ , and also locate in the halo region of M31. These candidates can be considered as RR-Lyrae variable stars, which have an absolute magnitude of  $r \sim 1\text{mag}$ , the apparent magnitude is consistent with the hypothesis that the RR-Lyrae stars are in 750 kpc distance. However, the color properties of these stars suggests that many of them are M-type or K-type stars, which is inconstant with empirical law that RR-Lyrae variables tend to be A-type or F-type stars. Still, there exists more than 100 candidates classified as A-type or F-type stars among these samples.

- R Coronae Borealis-type stars

We are finding that some types of stars “disappear” within a year timescale. We believe that these stars belong to a similar class of variable stars to the R Coronae Borealis star (hereafter RCB) that is a peculiar low-mass yellow supergiant star in the constellation of Coronae Borealis, displays non-periodic variability, and fade by several magnitudes at irregular intervals. The origin and nature of RCB-type star is poorly understood, but one scenario is that the time-variability is caused by a build-up mass loss of carbon-rich dust in the stars atmosphere. There is a heterogeneous sample of about 100 RCB stars in MW that have been constructed by various datasets. The HSC/Subaru data led us to find about 1500 candidates of RCB-type stars about 300 of which fade from 21 to 26 mag. Comparing the candidates with the PHAT HST star catalogs, almost all the candidate stars display properties of post-AGB stars in terms of their color and absolute magnitudes. The search of RCB-type stars is relatively easy, because we need to look for relatively bright stars that appear or disappear between the two images. The HSC data from the requested observation will allow us to build a homogeneous sample of RCB-type stars in M31, and develop a better understanding of the nature of these stars. These stars could give a new channel to carbon enrichment in galaxy evolution, as advocated in the literature (e.g., Karakas et al. (2015)). Our preliminary estimate indicates that RCB-type stars give dust enrichment by a rate of  $\sim 10^{-4}M_{\odot}/\text{yr}$ , which is not that different from the rate from AGB stars (e.g. Matsuura et al. (2009)).

- A star before nova (M31 LRN 2015)

A candidate of red nova was discovered in M31 in January 2015, about three months after our observation in 2014 (Williams et al. 2015). The candidate is identified as a rare and enigmatic luminous red nova (LRN), which is characterized by a reddening color as they fade. However, the mechanism of explosion has not been revealed because of their limited number of samples observed. Here we look into the photometric data of this candidate to reveal the status before explosion (See Hirochi et al. (2016) for more detail). Fig. A.2 shows the light curve and image of the target star from our 2014 observation. The coordinate of candidate is 00h 42m 07.99s +40d 55m 01.1s in RADEC, which is close to M31 bulge. This object is not detected with our selection criteria of variable stars, probably due to its small change of flux. Photometry of the LRN also gives 22.8mag in r-band in 2015, while it totally disappears in 2017 observation.

## A.2 Flare events

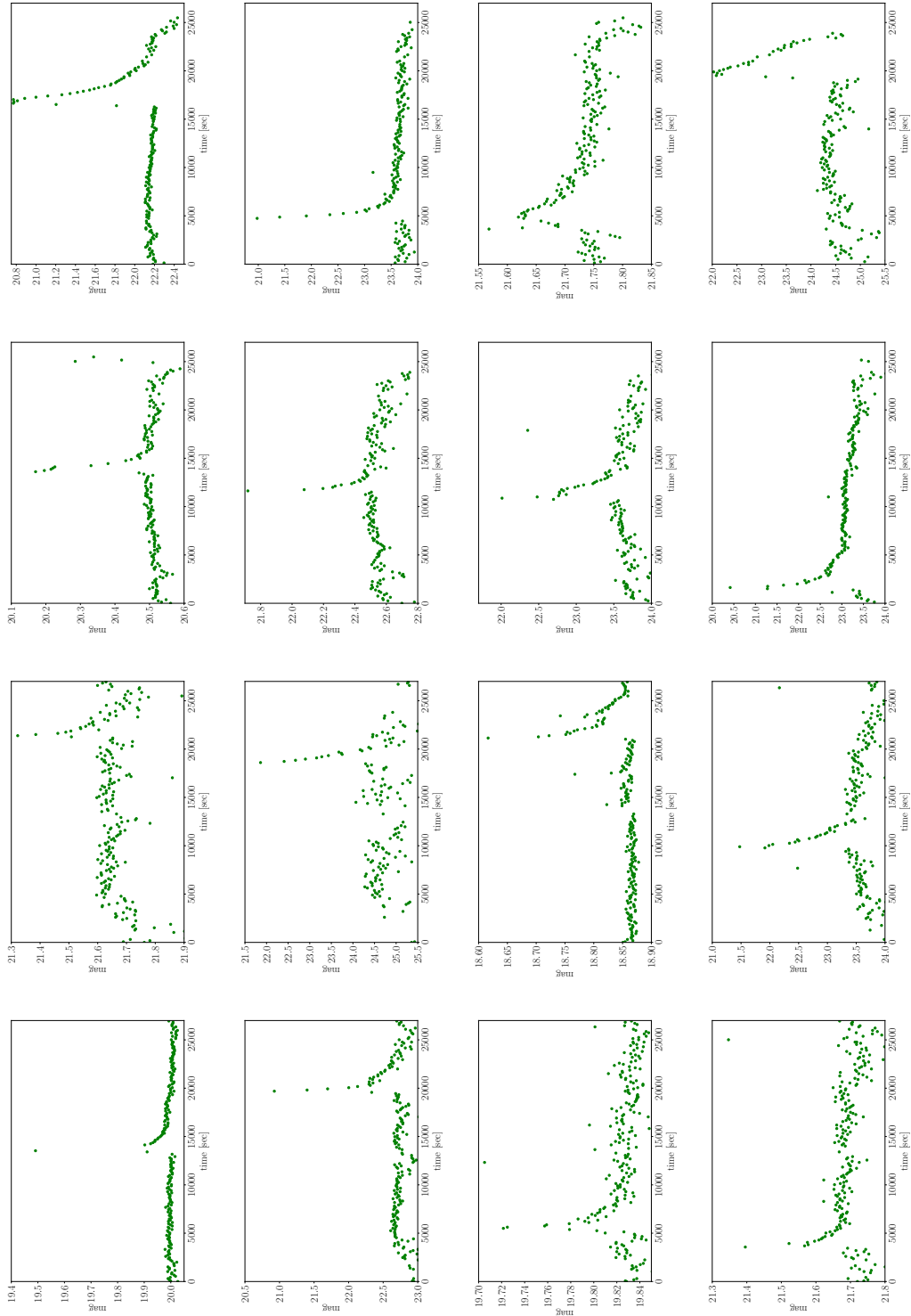


Figure A.3: Example of light curves of flare events, with magnification either in 2014 or 2017.

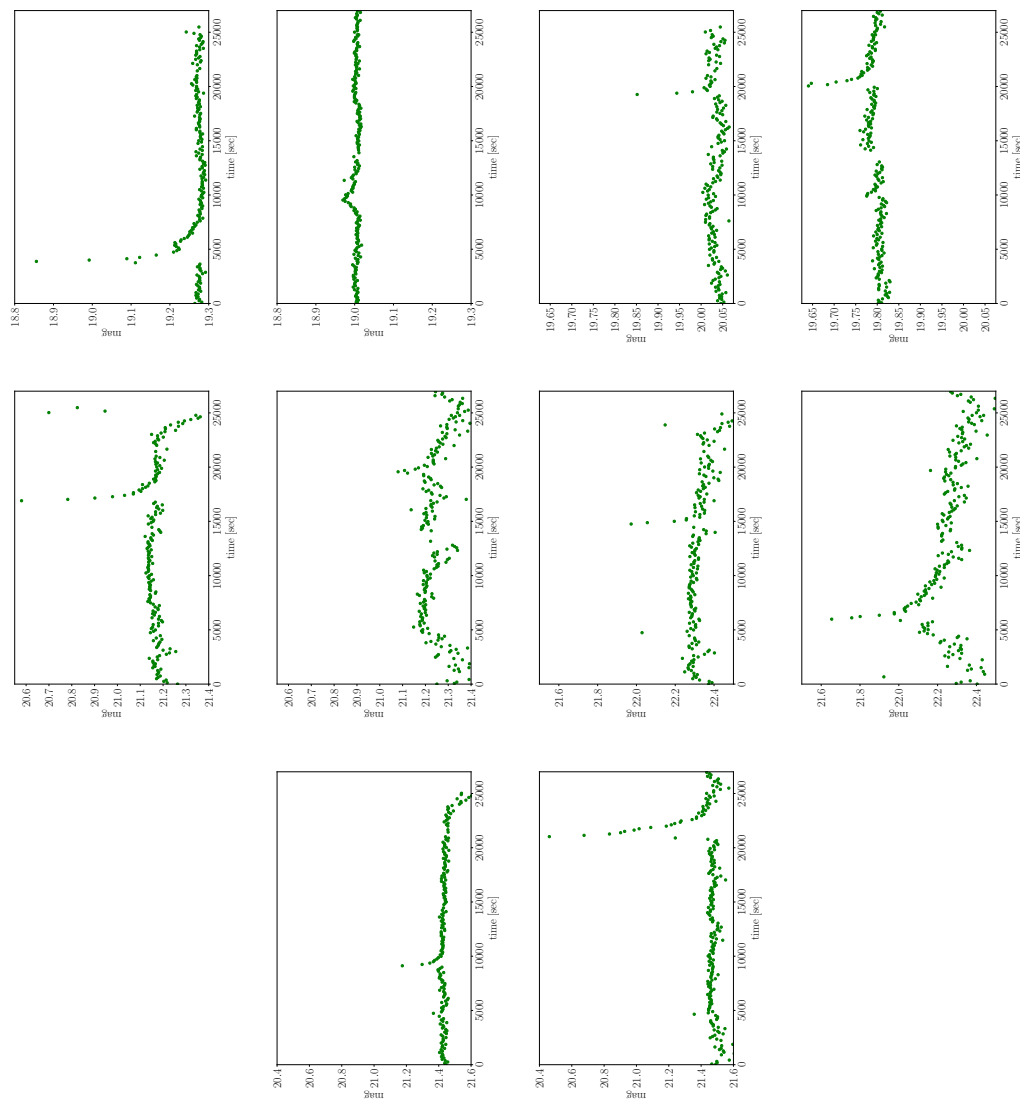


Figure A.4: Light curves of flare-star candidates which show magnification both in 2014 and 2017. Among images in each row, the first and second images from the left comes from the photometry of the same star, and each represents a light curve from the HSC-M31 observation in 2014 and 2017, respectively. The same is true for the rightmost and the second image from the right, which also represents the photometry of a common star. The order of these figures correspond to the serial number in Table A.1, ordering from left to right, and from top to bottom (here corresponds from #17 to #21). (Following figures from Fig. A.5 to Fig. A.9 also follows this display rule. )

Appendix A. *Properties of variable stars detected by our HSC-M31 observation*

---

# of events	RA	DEC	$m_r$ [mag], 2014	$m_{r2}$ [mag], 2017	timing of flare
1	11.5412243375	41.3971608494	22.171	22.114	2014
2	11.393000757	40.7105289417	23.605	23.615	2014
3	11.3139236649	40.7412265793	21.734	21.805	2014
4	11.3012595387	41.158699046	24.271	24.503	2014
5	10.7370329514	40.8903654558	20.495	20.400	2014
6	10.6258500158	41.8272977176	22.401	22.516	2014
7	10.5291547964	41.7643068792	23.095	23.524	2014
8	10.3761204743	41.4770522067	19.348	18.806	2014
9	11.3291033623	41.6402684426	21.795	21.619	2017
10	11.1868050062	41.4385607476	24.681	24.381	2017
11	11.1859271346	41.4724914305	19.480	18.856	2017
12	11.1114120629	41.6800459557	23.263	23.474	2017
13	11.0962946906	41.926482595	20.569	19.985	2017
14	10.6921263554	41.8637754591	22.647	22.613	2017
15	10.6858782707	41.8673085101	19.890	19.828	2017
16	9.9669723303	40.7986947613	21.759	21.668	2017
17	11.0004733481	40.6595469432	19.285	19.013	2014/2017
18	11.0074713445	40.9352814739	20.027	19.795	2014/2017
19	10.7265116069	40.8950261902	21.135	21.190	2014/2017
20	10.8886686488	41.7745915397	22.293	22.207	2014/2017
21	10.3301651385	41.7931961196	21.418	21.429	2014/2017

Table A.1: Coordinates of flare events, corresponding to Fig. A.3 and Fig. A.4.

### A.3 Binary stars with short period

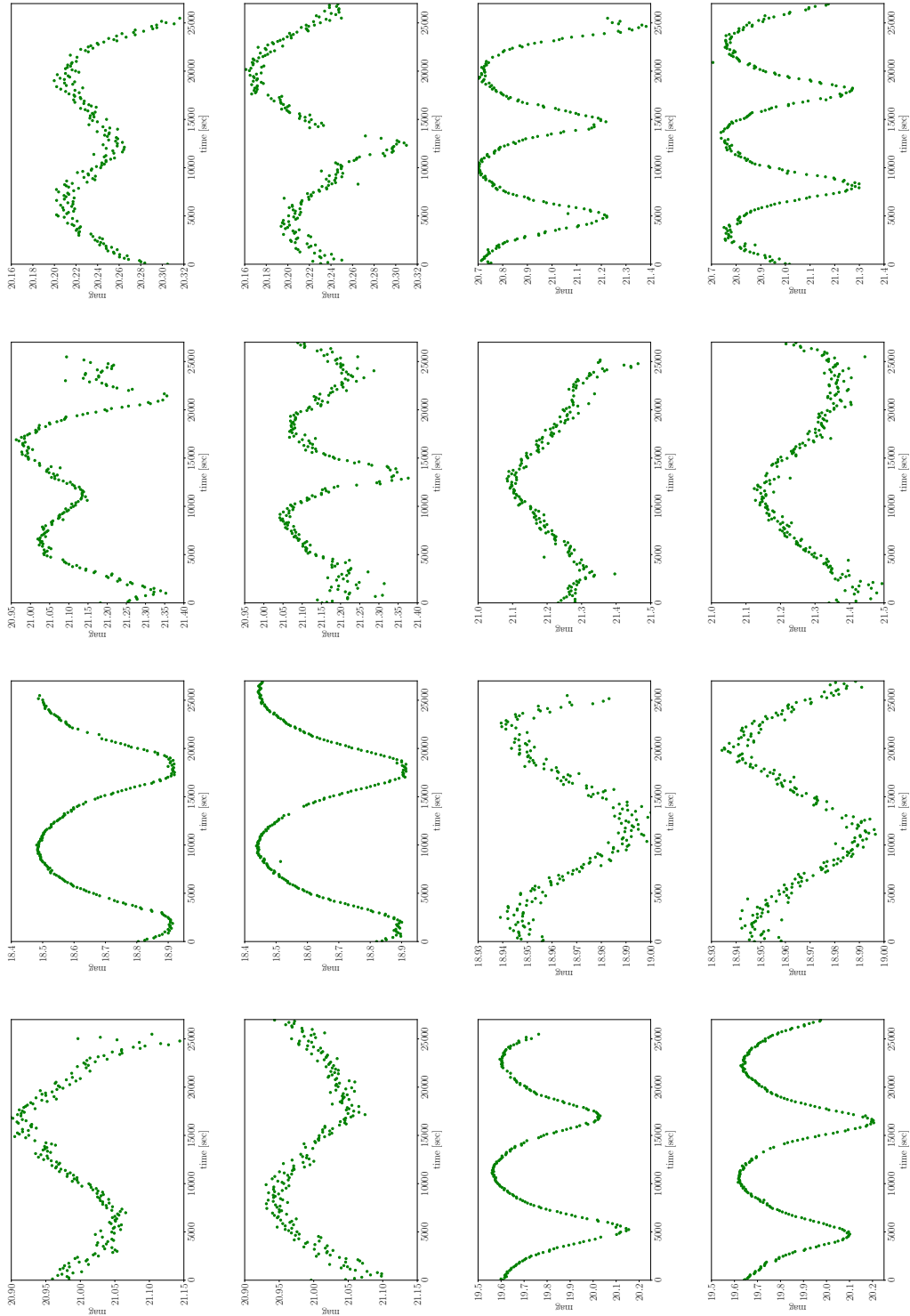


Figure A.5: Light curves of binary-star candidates with  $< 0.5$ days period.

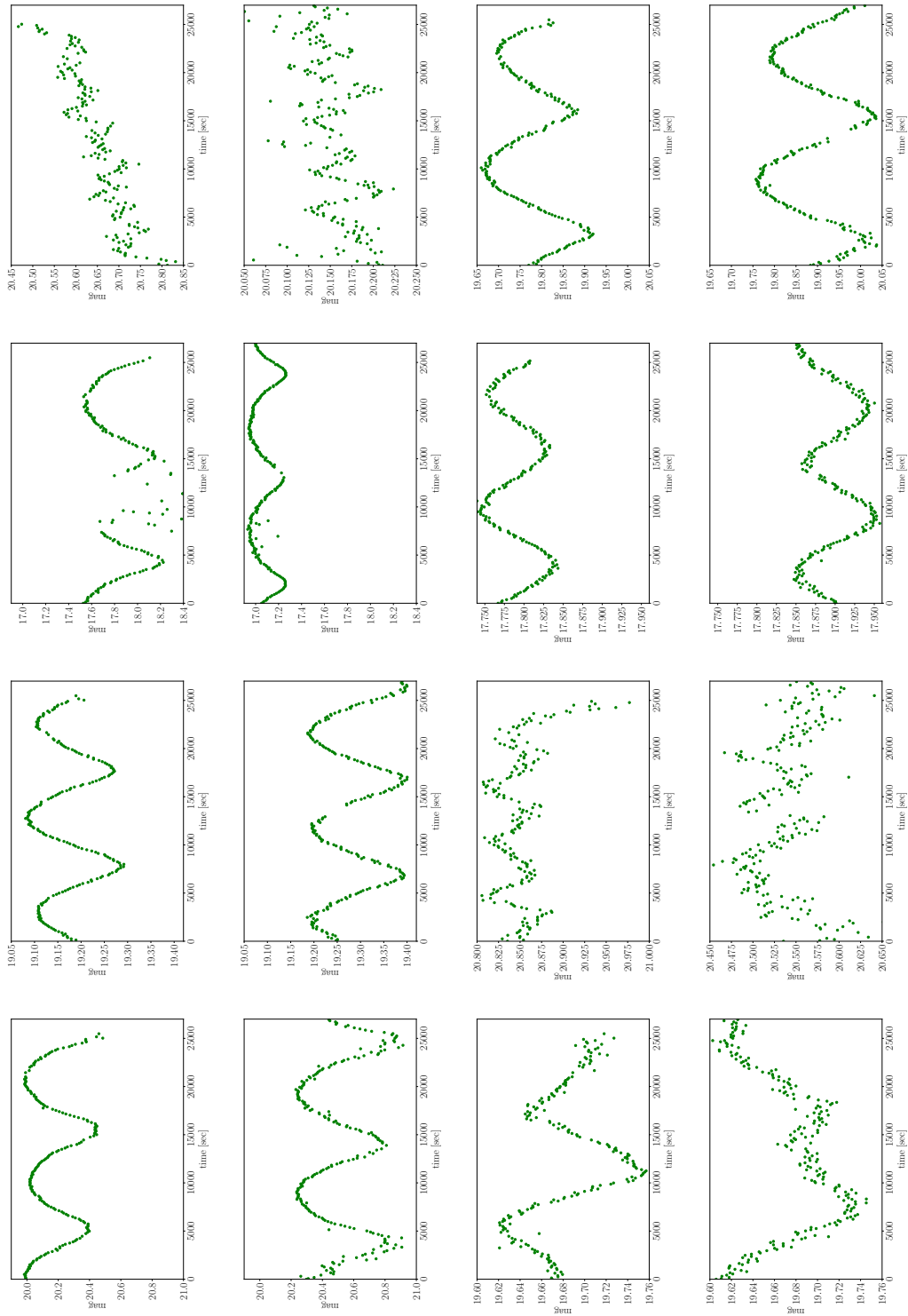


Figure A.6: Light curves of binary-star candidates with  $< 0.5$ days period (cont'd).

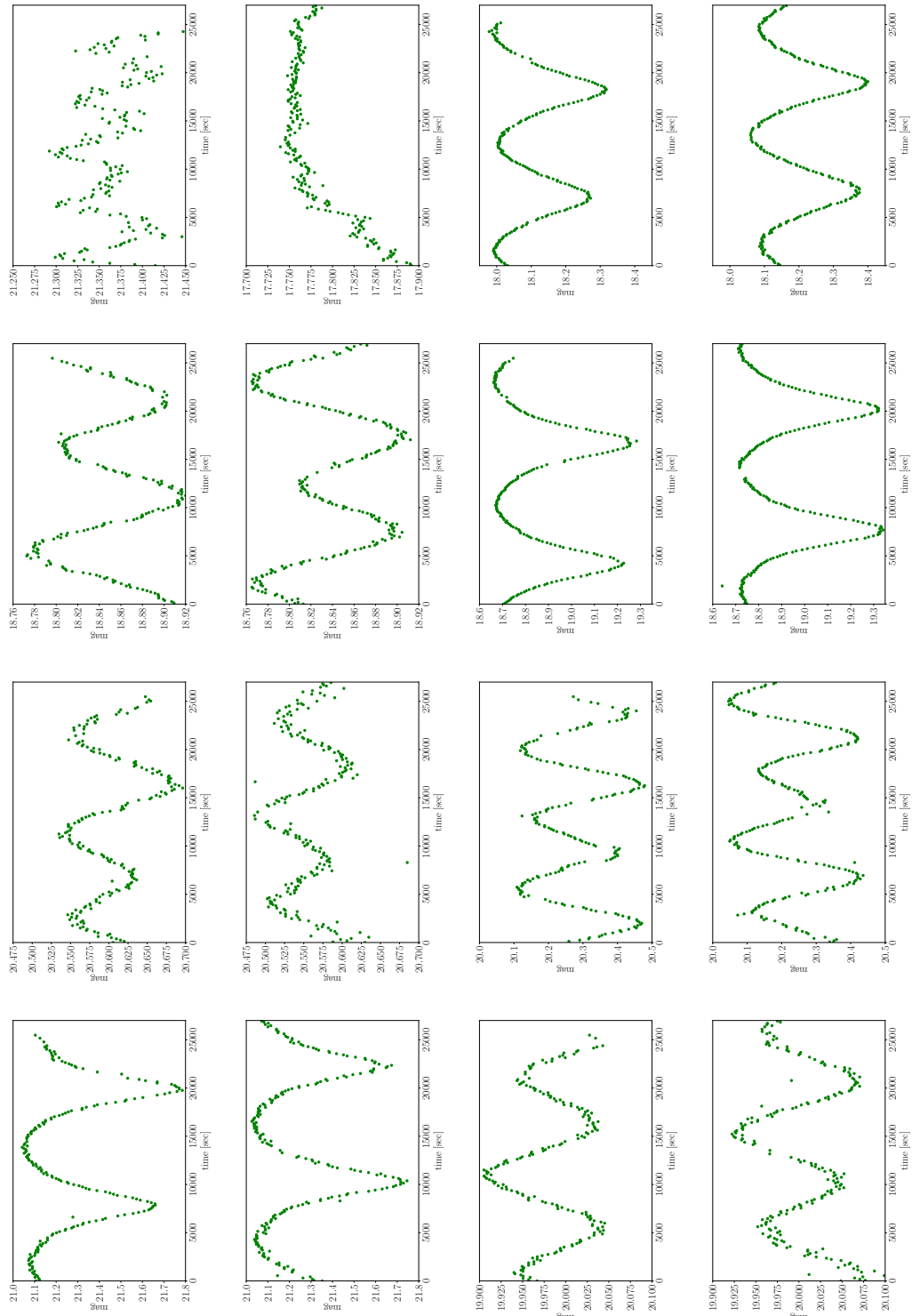


Figure A.7: Light curves of binary-star candidates with  $< 0.5$ days period (cont'd).

Appendix A. *Properties of variable stars detected by our HSC-M31 observation*

---

# of events	RA	DEC	$m_r$ [mag], 2014	$m_{r2}$ [mag], 2017	Figure
1	11.4544580378	41.0724194699	20.250	20.217	A.5
2	11.3613925945	41.4399798626	20.740	20.855	A.5
3	11.3424058582	41.4049005181	21.120	21.120	A.5
4	11.3730373361	41.7324054517	21.111	21.240	A.5
5	10.9972899731	40.8010048889	18.506	18.591	A.5
6	11.0517168744	41.5291107259	18.992	18.965	A.5
7	11.0334352565	41.5484507549	20.980	20.980	A.5
8	11.0811761058	41.6740238454	19.574	19.901	A.5
9	11.0339595747	41.8482462356	20.690	20.140	A.6
10	10.9180098152	40.8900349064	19.689	19.791	A.6
11	10.8204104054	40.9462218981	19.117	17.540	A.6
12	10.8475499417	41.8790422723	17.760	17.830	A.6
13	10.5475596619	41.5421396385	19.129	19.215	A.6
14	10.6102177325	41.9193046729	20.834	20.539	A.6
15	10.4347282405	40.6102561978	20.049	20.298	A.6
16	10.3102330942	41.7518386402	19.745	19.727	A.6
17	10.1015757893	41.0675861952	21.334	18.504	A.7
18	10.0215405021	41.1109749894	18.043	18.121	A.7
19	10.193663404	41.479567314	18.911	18.892	A.7
20	9.95941178853	40.8563016946	18.691	18.946	A.7
21	9.81843250039	41.4840653543	20.550	20.550	A.7
22	9.71134555541	41.3294391638	20.249	20.324	A.7
23	9.70316324049	41.3640774656	21.162	21.123	A.7
24	9.68958110388	41.4426975874	19.918	19.967	A.7

Table A.2: Coordinates of binary-star candidates, corresponding to Fig. A.5, A.6 and A.7.

## A.4 Eclipsing binary stars

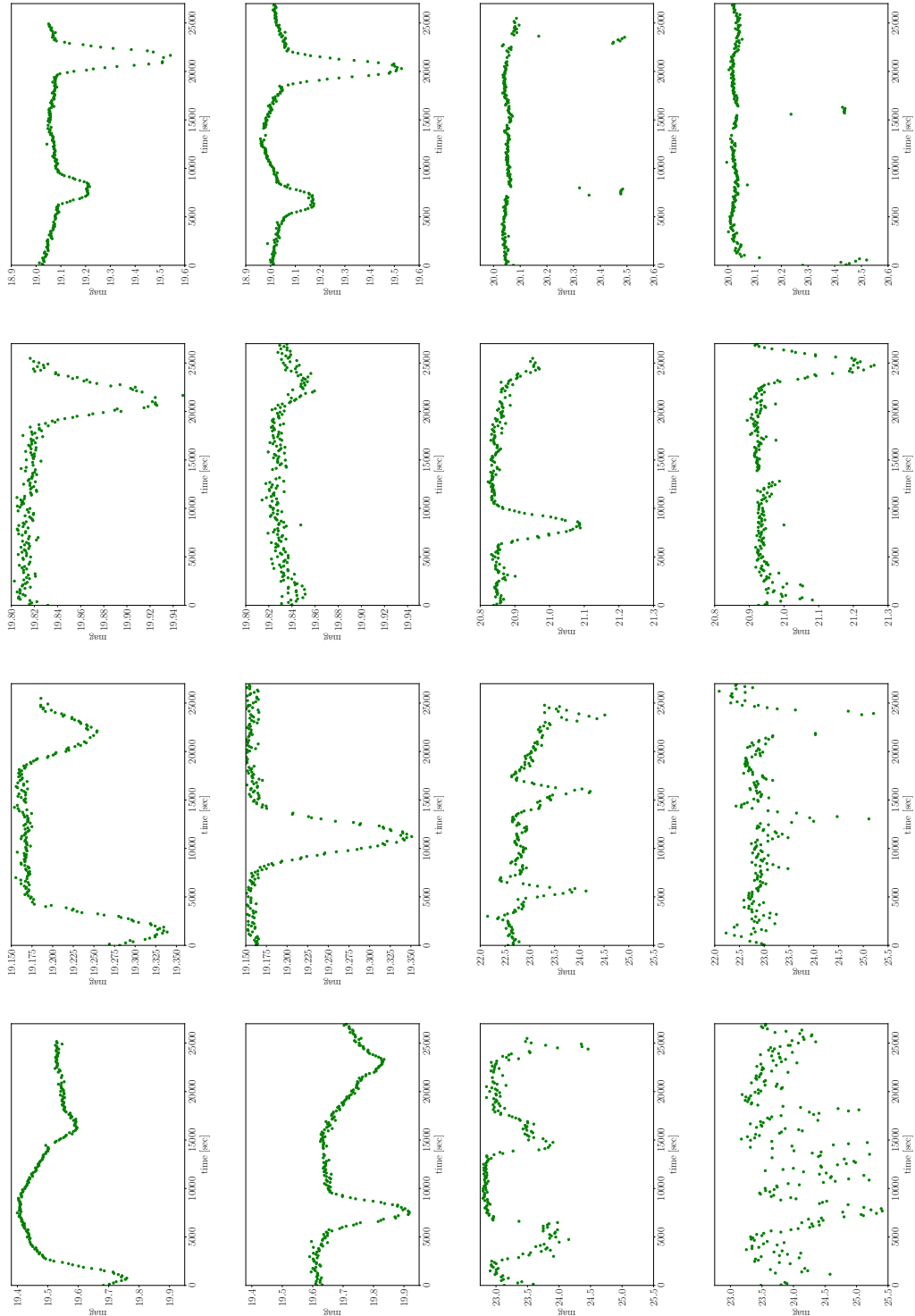


Figure A.8: Light curves of eclipsing binary candidates with dip structures both in 2014 and 2017.

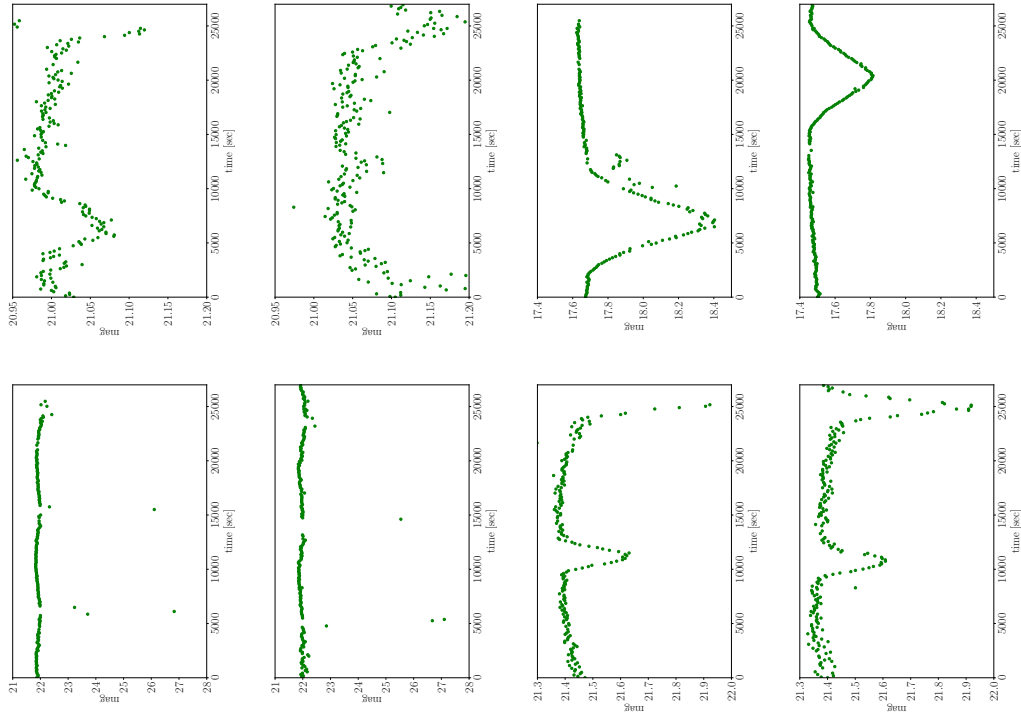


Figure A.9: Light curves of eclipsing binary candidates with dip structures both in 2014 and 2017 (cont'd).

# of events	RA	DEC	$m_r$ [mag], 2014	$m_{r,2}$ [mag], 2017	Figure
1	11.5973834218	40.9113943591	19.077	19.085	A.8
2	11.272306997	40.9966128856	20.052	20.021	A.8
3	11.1844915391	40.7418192411	19.813	19.835	A.8
4	11.0032482866	40.9003822393	20.840	20.929	A.8
5	10.7290724677	40.5643149165	19.168	19.158	A.8
6	10.7554814292	41.793357782	22.835	22.521	A.8
7	10.7466086947	41.9359969811	19.440	19.565	A.8
8	10.5196226158	41.7562567376	22.824	23.117	A.8
9	10.2535074052	41.2699913159	20.978	21.013	A.9
10	10.1831727378	40.8530373679	17.762	17.578	A.9
11	10.0014656481	40.9601501214	21.843	23.178	A.9
12	9.82277563673	41.3887700087	21.517	21.358	A.9

Table A.3: Coordinates of eclipse binary candidates, corresponding to Fig. A.8 and Fig. A.9.

# Appendix B

## Reduction of imaging data targeting dense stellar field using hscPipe

A precise photometry requires a correction of various systematic effects such as night glow, instrument noise, vignetting of the camera, and variations in responses between different CCD pixels. In this section we describe our analysis method regarding the reduction of HSC images targeting at dense stellar fields. We refer to hscPipe<sup>1</sup> and Niikura et al. (2016)<sup>2</sup> for more detail of each procedure.

- Bias, dark current subtraction and flat-field determination

Raw CCD data contain various contaminations, and need processing of bias subtraction, dark current subtraction, and flat-field determination. We also need to subtract background contamination due to light diffusion of the atmosphere or other unknown source. Here we correct these corrections by hscPipe like in the following command:

```
$ hscProcessCcd.py /mydirectry/ --rerun myrerun --id visit=xxxxxx ccd=0..103 --  
calib=/CALIBdirectry/ --clobber-config -C config_reduceFrames.py
```

where we basically use the config file “config\_reduceFrames.py” as in the following (Note that we need to adjust the values of processCcd.calibrate.background.binSize, processCcd.calibrate.background.approxOrder, and processCcd.calibrate.measurePsf.starSelector parameters when we have difficulty in solving the astrometry in each CCD).

---

<sup>1</sup>[https://hsc.mtk.nao.ac.jp/pipedoc\\_e/](https://hsc.mtk.nao.ac.jp/pipedoc_e/)

<sup>2</sup>[http://hep.phys.s.u-tokyo.ac.jp/wordpress/wp-content/uploads/2016/06/mth2016\\_niikura.pdf](http://hep.phys.s.u-tokyo.ac.jp/wordpress/wp-content/uploads/2016/06/mth2016_niikura.pdf)

```

=====
try:
    processCcd = root.processCcd
except AttributeError:
    processCcd = root
processCcd.isr.doWrite=True #\
processCcd.calibrate.repair.doCosmicRay=False #\
processCcd.calibrate.background.binSize=64 #\
processCcd.calibrate.background.useApprox=True #\
processCcd.calibrate.background.approxOrder=6 #\
processCcd.calibrate.detection.includeThresholdMultiplier=5.0 #\
processCcd.calibrate.measurePsf.starSelector['objectSize'].widthMin=1.05
=====

```

Note that we skipped cosmic ray removal here for simplicity, and will discuss the residual effect later. For latest HSC data (especially taken later than 2017) we need to skip analysis on CCD=9 and 33 because we cannot estimate bias or other corrections for those CCDs.

- WCS determination

The HSC pipeline provide us with a useful feature, the so-called “SkyMap”, which defines a conversion of the celestial sphere to the flat coordinate system, “SkyMap coordinate”, based on a tiling or tessellation. The largest region in the coordinate is called a “Tract”, and it contains a “Patch” (see Fig. 3.4 for a example of patch and CCD correspondence). These processes performed a warping of each exposure to determine the common WCS of the SkyMap.

By using the star catalog of Pan-Starrs survey as the input catalog for the M31 region, we solved astrometry solution of every 11 images, 30 sec exposure plus time-sequential 10 exposures taken from the science  $\sim$  200 exposures by *mosaic.py*.

- Coadd

In the analysis of M31 data taken with HSC, we combine multiple images to create a single coadd image by the median stack. This process involves corrections of satellite tails, ghosts, and cosmic rays, and those outliers are needed to be clipped. Then the example code is as in the following:

```
$ stack.py /mydirectry --output=/outdirectry --id tract=0 filter=HSC-R2 patch=x,x --
selectId visit=xxxxxx -C simpleCoaddConfig.py -c assembleCoadd.doSigmaClip=True
assembleCoadd.clipIter=3 assembleCoadd.sigmaClip=1.5 doOverwriteCoadd=True --
clobber-config --batch-type=smp --cores=4
```

where we use the config file “simpleCoaddConfig.py” as in the following:

```
=====
from lsst.pipe.tasks.assembleCoadd import SafeClipAssembleCoaddTask
root.assembleCoadd.retarget(SafeClipAssembleCoaddTask)
root.assembleCoadd.doMatchBackgrounds=False
root.assembleCoadd.badMaskPlanes=['BAD', 'EDGE', 'SAT', 'INTRP', 'NO_DATA']
=====
```

Note that this process also involves correction of flux scale of each visit and ccd. We also need to clip the cosmic rays carefully in the dense stellar field.

# Bibliography

- Abbott, B. P. et al. 2016, Phys. Rev. Lett. 116, 061102
- Adams, A. W. & Bloom, J. S., ArXiv e-prints: 0405266
- Addison, G. E., Hinshaw, G., & Halpern, M., 2013, MNRAS, 436, 1674
- Afshordi, N., McDonald, P. & Spergel, D. N., 2003, 594, 71
- Aihara, H. et al. 2018, PASJ, 70S, 4
- Aihara, H. et al. 2018, PASJ, 70S, 8
- Alard, C. 2000, A&AS, 144, 363
- Alard, C., Lupton, R.H. 1998, ApJ, 503, 325
- Ali-Haïmoud, Y., Kovetz, E. D. & Kamionkowski, M., 2017, ArXiv e-prints: 1709.06576
- Ali-Haïmoud, Y. & Kamionkowski, M. 2017, Phys. Rev. D95, 043534
- Alcock, C. et al., 2001, ApJ, 550, 169
- Alcock, C. et al. (The MACHO Collaboration), 2000, ApJ, 542, 281
- Alcock, C. et al. 1998, ApJ, 499, 9
- Alcock, C. et al. 1998, ApJ, 461, 84
- Alcock, C. et al., 1995, ApJ, 449, 28
- Anderson et al., 2014, MNRAS, 441, 24
- Arina, C. 2018, arXiv e-prints: 1805.04290
- Aurière, M. et al., 2001, ApJ, 553, 137

- Axelrod, T. and Kantor, J. and Lupton, R. H. and Pierfederici, F. 2010, *Software and Cyberinfrastructure for Astronomy*, 7740E, 15
- Bahcall, J. N., 1986, *Annual Review of Astronomy and Astrophysics*, 24, 577
- Bai, Y. & Orlofsky, N., 2018, ArXiv e-prints: 1812.01427
- Baillon, P. and Bouquet, A. and Giraud-Heraud, Y. and Kaplan, J. 1993, *A&A*, 277, 1
- Baltz, E.A., & Silk, J. *ApJ*, 530, 578
- Barcons, X., Nandra, K., Barret, D., den Herder, J.-W. , Fabian, A. C., Piro, L., Watson, M. G., & the Athena team, 2015, *Journal of Physics, Conference Series* 610, 1, 012008
- Barnacka, A., Glicenstein, J.-F., & Moderski, R. 2012, *Phys.Rev. D*86, 043001
- Bartelmann, M. 1996, *A&A*, 313, 697
- Bartelmann, M. & Schneider, P. 2001, *Physics Reports*, 340, 291
- Battistelli, E. S., Fulcoli, V. & Macculi, C., 2000, *New Astronomy*, 5, 77
- Becker, M. R. & Kravtsov, A. V. 2011, *ApJ*, 740, 25
- Bennett, D. P., 2005, *ApJ*, 633, 906
- Bertin, E. 2011, *Astronomical Society of the Pacific Conference Series*, 442, 435
- Betoule, M. et al, 2014, *A&A*, 568, 22
- Bhattacharya, S., Habib, S., Heitmann, K. & Vikhlinin, A. 2013, *ApJ*, 766, 32
- Bird, S. and Cholis, I. and Muñoz, J. B. and Ali-Haïmoud, Y. and Kamionkowski, M. and Kovetz, E. D. and Raccanelli, A. & Riess, A. G. 2016, *Phys. Rev. Lett.* 116, 201301
- Böhringer, H., et al. 2004, *A&A*, 425, 367
- Bosch, J. et al. 2018, *PASJ*, 70S, 5
- Brandt, T. D., 2016, *ApJ*, 824, 31
- Bringmann, T. & Weniger, C., 2012, *Physics of the Dark Universe*, 1, 194
- Broadhurst, T., Takada, M., Umetsu, K., Kong, X., Arimoto, N., Chiba, M. & Futamase, T. 2005, *ApJ*, 619, L143

- Burrows, A., Hubbard, W. B., Lunine, J. I. & Liebert, J., 2001, *Reviews of Modern Physics*, 73, 719
- Bullock, J. S., Kolatt, T. S., Sigad, Y., Somerville, R. S., Kravtsov, A. V., Klypin, A. A., Primack, J. R., & Dekel, A. 2001, *MNRAS*, 321, 559
- Calchi Novati, S. et al. 2014, *ApJ*, 783, 86
- Calchi Novati, S. 2010, *General Relativity and Gravitation*, 42, 2101
- Calchi Novati, S. et al. 2009, *ApJ*, 695, 442
- Calchi Novati, S. et al. 2005, *A&A*, 443, 911
- Caldwell, J. A. R., & Coulson, I. M.. 1986, *MNRAS*, 218, 223
- Callingham, T., Cautun, M., Deason, A. J., Frenk, C. S., Wang, W., Gómez, F. A., Grand, R. J. J., Marinacci, F. & Pakmor, R., 2018, arXiv e-prints: 1808.10456
- Capela, F., Pshirkov, M. & Tinyakov, P. 2013, *Phys.Rev. D*87, 023507
- Capela, F., Pshirkov, M. & Tinyakov, P. 2013, *Phys.Rev. D*87, 123524
- Carr, B., Raidal, M., Tenkanen, T., Vaskonen, V. & Veermäe, H., 2017, *Phys. Rev. D*, 96, 023514
- Carr, B. and Kühnel, F. and Sandstad, M. 2016, *Phys.Rev. D*94, 083504C
- Carr, B. J., Kohri, K., Sendouda, Y., & Yokoyama, J. 2010, *Phys.Rev. D*81, 104019
- Carr, B. J. and Sakellariadou, M., 1999, *ApJ*, 516, 195
- Carr, B. J., 1975, *ApJ*, 201, 1
- Carr, B. J. & Hawking, S. W. 1974, *MNRAS* 168, 399
- Cieplak, A. M. & Griest, K. 2013, *ApJ* 767, 145
- Clowe, D., Bradač, M., Gonzalez, A. H., Markevitch, M., Randall, S. W., Jones, C. & Zaritsky, D. 2006, *ApJ*, 648, 109
- Conrad, J. & Reimer, O. 2017, *Nature Physics*, 13, 224
- Cooke, R. J., Pettini, M. & Steidel, C. C., 2018, *ApJ*, 855, 102

- Crotts, A. P. S. & Tomaney, A. B., 1996, *ApJ*, 473, 87
- Crotts, A. P. S. 1992, *ApJ*, 399, 43
- Cusano, F., Garofalo, A., Clementini, G., Cignoni, M., Federici, L., Marconi, M., Musella, I., Ripepi, V., Speziali, R., Sani, E. & Merighi, R. 2015, *ApJ*, 806, 200
- Dalal, N., Lithwick, Y., & Kuhlen, M. 2010, *ArXiv e-prints*:1010.2539
- Dalcanton, J. J. et al. 2012, *ApJS*, 200, 18
- Davis, M., Efstathiou, G., Frenk, C. S. & White, S. D. M. 1985, *ApJ*, 292, 371
- de Blok, W. J. G., McGaugh, S. S.; Bosma, A., & Rubin, V. C., 2001, *ApJ*, 552, 23
- de Jong, J.T.A. et al. (The MEGA collaboration) 2006, *A&A*, 446, 855
- Demers, S., Battinelli, P., & Letarte, B., 2003, *AJ*, 125, 3037
- Deng, H. & Vilenkin, A., 2017, *Journal of Cosmology and Astroparticle Physics*, 12, 044
- Deng, H., Garriga, J., & Vilenkin, A., 2017, *Journal of Cosmology and Astroparticle Physics*, 04, 050
- Diego, J. M., 2018, *ApJ*, 857, 25
- Diemer, B. & Kravtsov, A. V. 2014a, *ArXiv e-prints*:1407.4730 (DK14)
- . 2014b, *ApJ*, 789, 1
- Dodelson, S., “Gravitational Lensing” 2017, Cambridge University Press
- Dodelson, S., “Modern Cosmology” 2003, Academic. Press
- Dodelson, S. & Liguori, M., 2006, *Phys. Rev. Lett.* 97, 231301
- Duffy, A. R., Schaye, J., Kay, S. T., & Dalla Vecchia, C. 2008, *MNRAS*, 390, L64
- Ebeling, H., Edge, A. C., Allen, S. W., Crawford, C. S., Fabian, A. C. & Huchra, J. P. 2000, *MNRAS*, 318, 333
- Ebeling, H., Edge, A. C., Bohringer, H., Allen, S. W., Crawford, C. S., Fabian, A. C., Voges, W. & Huchra, J. P. 1998, *MNRAS*, 301, 881
- Eisenstein, D. J., 2005, *ApJ*, 633, 560

- Fixsen, D. J., 2009, *ApJ*, 707, 916
- Futamase, T., 1995, *Progress of Theoretical Physics*, 93, 3, 647
- Garriga, J., Vilenkin, A. & Zhang, J., 2016, *Journal of Cosmology and Astroparticle Physics*, 02, 064
- Garriga, J. & Vilenkin, A., 1993, *Phys. Rev. D.*, 47, 3265
- Geehan, J. J., Fardal, M. A., Babul, A. & Guhathakurta, P. 2006, *MNRAS*, 366, 996
- Gentile, G., Salucci, P., Klein, U., Vergani, D. & Kalberla, P., 2004, *MNRAS*, 351, 903
- Golse, G. & Kneib, J.-P. 2002, *A&A*, 390, 821
- Gondolo, P. 1999, *ApJ*, 510, 29
- Green, A. M., 2016, *Phys. Rev. D*, 94, 063530
- Gould, A., 2000, *ApJ*, 535, 928
- Gould, A. 1996, *ApJ*, 470, 201
- Gould, A. 1992, *ApJ*, 386, 5
- Graham, P. W., Rajendran, S. & Varela, J., 2015, *Phys. Rev. D*, 2015, 92, 063007
- Griest, K., Cieplak, A.M. & Lehner, M J. 2014, *ApJ*, 786, 158
- Griest, K., Lehner, M. J., Cieplak, A. M. & Jain, B., 2011, *Phys. Rev. Lett.*, 107, 231101
- Griest, K., et al. (The MACHO Collaboration) 1991, *ApJ*, 372, 79
- Han, C. & Gould, A., 2003, *ApJ*, 592, 172
- Han, C. & Gould, A., 1996, *ApJ*, 467, 540
- Han, C. & Gould, A., 1995, *ApJ*, 447, 53
- Hawking, S. W. 1989, *Phys. Rev. B.*, 231, 237
- Hawking, S. W. 1974, *Nature* 248, 30.
- Hawking, S. W. 1971, *MNRAS* 152, 75
- Henry G. W. & Newsom M. S., 1996, *PASP*, 108, 242

- Hinshaw et al., 2013, ApJS, 208, 19
- Hinshaw et al., 2003, ApJS, 148, 63
- Hirochi et al., 2016, discussion in <http://user.keio.ac.jp/~mariko/conference/16binary.proceedings/28.hirochi.pdf>
- Hooper, D. 2018, arXiv e-prints: 1812.02029
- Hu, W. & Kravtsov, A. V. 2003, ApJ, 584, 702
- Huang, S. et al. 2017, PASJ, 70S, 6
- Inomata, K., Kawasaki, M., Mukaida, K. & Yanagida, T. T. , 2018, Phys. Rev. D97, 043514
- Inomata, K. and Kawasaki, M. and Mukaida, K. and Tada, Y. and Yanagida, T. T. 2017, Phys. Rev. D95, 123510
- Inomata, K., Kawasaki, M., Mukaida, K., Tada, Y. & Yanagida, T. T. 2017, Phys. Rev. D96, 043504
- Ivezic, Z. et al. 2018, ApJ, 750, 99
- Jungman, G., Kamionkowski, M. and Griest, K. 1996, Physics Reports, 267, 195
- Jurić, M. et al. 2015, ArXiv e-prints:1512.07914
- Kaiser, N. 1986, MNRAS, 222, 323
- Karakas, A. I., Ruiter, A. J., & Hampel, M., 2015, ApJ, 809, 184
- Katz, A., Kopp, J., Sibiryakov, S. & Xue, W., 2018, ArXiv e-prints: 1807.11495
- Kawanomoto, S., Uraguchi, F., Komiyama, Y., Miyazaki, S., Furusawa, H., Finet, F., Hattori, T., Wang, S-Y., Yasuda, N., Suzuki, N., 2018, PASJ, 70, 66
- Kawasaki, M., Mukaida, K. & Yanagida, T. T. 2016, Phys. Rev. D94, 063509
- Kawasaki, M., Kusenko, A., Tada, Y. & Yanagida, T. T. 2016, Phys. Rev. D94, 083523
- Kelly, P. L. et al., 2018, Nature Astronomy, 2, 334
- Kent, S. M., 1992, ApJ, 387, 181

## References

---

- Kerins, E., Carr, B. J., Evans, N. W., Hewett, P., Lastennet, E., Le Du, Y., Melchior, A.-L., Smartt, S. J. & Valls-Gabaud, D. 2001, *MNRAS*, 323, 13
- Kiraga, M. & Paczyński, B., 1994, *ApJ*, 430, 101
- Klasen, M., Pohl, M. & Sigl, G. 2015, *Progress in Particle and Nuclear Physics* 85, 1K
- Klypin, A., Zhao, H., & Somerville, R S. 2002, *ApJ*, 573, 597K
- Kneib, J.-P. et al. 2003, *ApJ*, 598, 804
- Kodric, M. et al. 2013, *AJ*, 145, 106
- Komatsu, E., 2011, *ApJS*, 192, 18
- Kouvaris, C., *Phys.Rev.Lett.* 2012, 108, 191301
- Kouvaris, C. & Tinyakov, P. 2011, *Phys. Rev. Lett.* 107, 091301
- Kouvaris, C., & Tinyakov, P. 2011, *Phys.Rev.* D83, 083512
- Kroupa, P., 2001, *MNRAS*, 322, 231
- Kühnel, F. & Freese, K., 2017, *Phys. Rev. D*, 95, 083508
- Kühnel, F., Rampf, C. & Sandstad, M., 2015, *European Physical Journal C*, 76, 93
- Kuhlen, M., Diemand, J. & Madau, P., 2008, 686, 262
- Kurucz, R. 1993, CD-ROM No.13 (Cambridge, Mass.: Smithsonian Astrophysical Observatory), 13
- Lacy C. H., Moffett T. J. & Evans D. S., 1976, *ApJS*, 30, 85
- Lane, R. R. and Kiss, L. L. and Lewis, G. F. and Ibata, R. A. and Siebert, A. and Bedding, T. R. and Székely, P. 2009, *MNRAS*, 400, 917L
- Lee, C.-H. et al., 2012, *The Astronomical Journal*, 143, 89
- LOFT Collaboration et al. 2012, *Experimental Astronomy*, 34, 415
- LSST Science Collaboration et al. 2009, ArXiv e-prints: 0912.0201
- Lynx Team Collaboration et al. 2018, ArXiv e-prints: 1809.09642

- Magnier et al. 2013, ApJS, 205, 20
- Mamon, G. A., & Soneira, R. M. 1982, ApJ, 255, 181
- Mandelbaum, R. et al. 2013, ApJS, 212, 5
- Mao, Y.-Y., Strigari, L. E. & Wechsler, R. H., 2014, Phys. Rev. D, 89, 063513
- Mao, S & Paczyński, B., 1996, ApJ, 473, 57
- Matsunaga, N. & Yamamoto, K. 2006, Journal of Cosmology and Astroparticle Physics, 01, 023
- Matsuura et al., 2009, MNRAS, 396, 918
- Meylan, G., Jetzer, P., North, P., Schneider, P., Kochanek, C. S. & Wambsganss, J., “Gravitational Lensing: Strong, Weak and Micro”, 2006, Springer
- Mediavilla, E., Muñoz, J. A., Falco, E., Motta, V., Guerras, E., Canovas, H., Jean, C., Oscoz, A. & Mosquera, A. M., 2009, ApJ, 706, 1451
- Melbourne, J. et al., 2012, ApJ, 748, 47
- Meneghetti, M., Rasia, E., Merten, J., Bellagamba, F., Ettori, S., Mazzotta, P., Dolag, K. & Marri, S. 2010, A&A, 514, A93
- Meneghetti, M., et al. 2014, ArXiv e-prints:1404.1384
- Merten, J., et al. 2014, ArXiv e-prints:1404.1376
- Miyama, S. & Sato, K., 1978, Progress of Theoretical Physics, 59, 1012
- Miyatake, H., More, S., Takada, M., Spergel, D. N., Mandelbaum, R., Rykoff, E. S. & Rozo, E. 2015, ArXiv e-prints: 1506.06135
- Miyazaki, S. et al. 2018, PASJ, 70, 1
- Miyazaki, S., et al. 2015, PASJ, 807, 22
- Mo, H., van den Bosch, F. & White, S. “Galaxy Formation and Evolution” 2010, Cambridge University Press
- Moffett T. J. 1974, ApJS, 29, 1

- More, S., Miyatake, H., Mandelbaum, R., Takada, M., Spergel, D. N., Brownstein, J. R., & Schneider, D. P., 2015, *ApJ*, 806, 2
- Mróz, P. et al. 2018, arXiv e-prints:1811.00441
- Mróz, P. et al. 2017, *Nature*, 548, 183
- Musco, I., Miller, J. C. & Polnarev, A. G., *Classical and Quantum Gravity*, 26, 235001
- Nakamura, T. T. 1998, *Phys. Rev. Lett* 80, 1138
- Nakamura, T., Sasaki, M., Tanaka, T. & Thorne, K. S., 1997, *ApJ*, 487, 139
- Navarro, J. F., Frenk, C. S., & White, S. D. M. 1996, *ApJ*, 462, 563
- Navarro, J. F., Frenk, C. S., & White, S. D. M., 1997, *ApJ*, 490, 493
- Navarro, J. F., et al. 2004, *MNRAS*, 349, 1039
- Nesti, F. & Salucci, P. 2013, *JCAP*, 07, 016
- Newman, A. B., Treu, T., Ellis, R. S., Sand, D. J., Nipoti, C., Richard, J. & Jullo, E. 2013, *ApJ*, 765, 24
- Niikura, H., Takada, M., Yokoyama, S., Sumi, T. & Masaki, S., ArXiv e-prints: 1901.07120
- Niikura, H., Takada, M., Yasuda, N., Lupton, R. H., Sumi, T., More, S., Kurita, T., Sugiyama, S., More, A., Oguri, M. & Chiba, M., ArXiv e-prints: 1701.02151
- Niikura, H. 2016, Master thesis, “Probing properties of dark matter with Subaru imaging data of massive clusters and Andromeda Galaxy”
- North, J. R., Davis, J., Bedding, T. R., Ireland, M. J., Jacob, A. P., O’Byrne, J., Owens, S. M., Robertson, J. G., Tango, W. J. & Tuthill, P. G. 2007, *MNRAS*, 380, 80
- Oguri, M., Diego, J. M., Kaiser, N., Kelly, P. L. & Broadhurst, T., 2018, *Phys. Rev. D*, 97, 023518
- Oguri, M., Bayliss, M. B., Dahle, H., Sharon, K., Gladders, M. D., Natarajan, P., Hennawi, J. F. & Koester, B. P. 2012, *MNRAS*, 420, 3213
- Oguri, M., & Takada, M. 2011, *Phys. Rev. D*, 83, 023008
- Oguri, M., Takada, M., Umetsu, K. & Broadhurst, T. 2005, *ApJ*, 632, 841

- Oguri, M. & Hamana, T. 2011, MNRAS, 414, 1851
- Oguri, M. 2002, Master thesis, “Resolving the Central Density Profile of Dark Matter Halos with Gravitational Lensing Statistics”,
- Oguri, M. 2004, Doctor thesis, “Strong Gravitational Lenses in a Cold Dark Matter Universe”,
- Oh, S.-H., Brook, C., Governato, F., Brinks, E., Mayer, L., de Blok, W. J. G., Brooks, A., & Walter, F., 2011, The Astronomical Journal, 142, 24
- OMeara, J. M., Tytler, D., Kirkman, D., Suzuki, N., Prochaska, J. X., Lubin, D. & Wolfe. A. M. 2001 ApJ, 552, 718
- Paczynski, B. 1986, ApJ, 304, 1
- Paczynski, B., Udalski, A., Szymanski, M., Kubiak, M., Pietrzynski, G., Soszynski, I., Wozniak, P. & Zebrun, K., 1999, Acta Astronomica, 49, 319
- Page, D. N. & Hawking, S. 1976, ApJ, 206, 1
- Page, D. N., 1976, Phys. Rev. D., 14, 3260
- Penny, M. T. et al., 2013, MNRAS, 434, 2
- Penzias, A. A., & Wilson, R. W., 1965, ApJ, 142, 419
- Percival, W. J., et al, 2010, MNRAS, 401, 2148
- Perlmutter, S. et al., 1999, ApJ, 517, 565
- Peterson, J. B. & Falk, T., 1991, ApJL, 374, 5
- Planck Collaboration et al. 2018, ArXiv e-prints: 1807.06209
- Planck Collaboration et al. 2015, ArXiv e-prints
- Polnarev, A. & Zembowicz, R., 1991, Phys. Rev. D., 43, 1106
- Power, C., Navarro, J. F., Jenkins, A., Frenk, C. S., White, S. D. M., Springel, V., Stadel, J. & Quinn, T. 2003, MNRAS, 338, 14
- Quinn, D. P., Wilkinson, M. I., Irwin, M. J., Marshall, J., Koch, A. & Belokurov, V., 2009, MNRAS, 396, 11

- Raidal, M., Spethmann, C., Vaskonen, V. & Veermäe, H., 2018, ArXiv e-prints: 1812.01930
- Ricotti, M. and Ostriker, J. P. and Mack, K. J. 2008, ApJ, 680, 829
- Riess, A. G. et al. Astronomical Journal, 1998, 116,1009
- Riffeser, A., Seitz, S., & Bender, R. 2008, ApJ, 684, 1093
- Riffeser, A., Fliri, J., Seitz, S., & Bender, R. 2006, ApJS, 163, 225
- Rowe, B. T. P. et al., 2015, Astronomy and Computing, 10, 121
- Rubin, V. C., Thonnard, N. & Ford, Jr., W. K., 1978, ApJ, 225, 107
- Roulet, E. & Mollerach, S., 1997, Physics Reports, 279, 67
- Schlaafy, E. F. et al. 2012, ApJ, 756, 158
- Schneider, P. 1996, IAUS, 168, 209
- Schneider, P. 2006, in Saas-Fee Advanced Course 33: Gravitational Lensing: Strong, Weak and Micro, ed. G. Meylan, P. Jetzer, P. North, P. Schneider, C. S. Kochanek, & J. Wambsganss, 1-89
- Sasaki, M. and Suyama, T. and Tanaka, T. and Yokoyama, S., 2018, Classical and Quantum Gravity, 35, 063001
- Sasaki, M., Suyama, T., Tanaka, T. & Yokoyama, S. 2016, Phys. Rev. Lett. 117, 061101S
- Seitz, S. & Schneider, P. 1996, A&A, 305, 383
- Seto, N. & Cooray, A., 2004, Phys. Rev. D., 70, 3512
- Schlaafy, E. F. et al., 2012, ApJ, 756, 158
- Schneider, P., Ehlers, J. & Falco, E.E., 1992. Gravitational Lenses. Springer, Heidelberg.
- Singh, K. P. et al. Astrosat mission, 2014, Proc.SPIE, 9144, 15
- Smith, G. P., Kneib, J.-P., Smail, I., Mazzotta, P., Ebeling, H. & Czoske, O. 2005, MNRAS, 359, 417

## References

---

- Smoot, G. F., Bennett, C. L., Kogut, A., Wright, E. L., Aymon, J., Bogges, N. W., Cheng, E. S., de Amici, G., Gulkis, S., Hauser, M. G., Hinshaw, G., Jackson, P. D., Janssen, M., Kaita, E., Kelsall, T., Keegstra, P., Lineweaver, C., Loewenstein, K., Lubin, P.; Mather, J., Meyer, S. S., Moseley, S. H., Murdock, T., Rokke, L., Silverberg, R. F., Tenorio, L., Weiss, R. & Wilkinson, D. T. *ApJ*, 1992, 396
- Spergel, D. et al., 2015, ArXiv e-prints: 1503.03757
- Spergel, D. et al., 2013, *ApJS*, 148, 175
- Springel, V., White, S. D. M., Frenk, C. S., Navarro, J. F., Jenkins, A., Vogelsberger, M., Wang, J., Ludlow, A. & Helmi, A., 2008, *Nature*, 456, 73
- Springel, V. 2005, *MNRAS*, 364, 1105
- Springel, V., Yoshida, N. & White, S. D. M. 2001, *New Astron.*, 6, 79
- Sreekumar, P. et al. (EGRET Collaboration), 1998, *ApJ*, 494, 523
- Stanek, R., Rasia, E., Evrard, A. E., Pearce, F. & Gazzola, L. 2010, *ApJ*, 715, 1508
- Sumi, T. et al. 2003, *ApJ*, 591, 204
- Sumi, T. et al. 2011, *Nature* 473, 349
- Suzuki, N. et al. 2012, *ApJ*, 746, 85
- Takada, M. & Spergel, D. N. 2014, *MNRAS*, 441, 2456
- Takada, M., 2014, Subaru Proposal, S14B98
- Takada, M. & Jain, B. 2002, *MNRAS*, 340, 580
- Takahashi, R., Sato, M., Nishimichi, T., Taruya, A. & Oguri, M. 2012, *ApJ*, 761, 152
- Takahashi, R. & Nakamura, T., 2003, *ApJ*, 595, 1039
- Tashiro, H. & Sugiyama, N. 2008, *Phys.Rev. D*78, 023004
- Tisserand, P. et al. 2004, *A&A*, 424, 245
- Tisserand, P. et al. (The EROS collaboration) 2007, *A&A*, 467, 387
- Tonry, J., L. et al. 2012, *ApJ*, 750, 99

- Tyson, J. A. & Fischer, P. 1995, *ApJ*, 446, L55
- Udalski, A., Szymański, M. K. & Szymański, G., 2015, *Acta Astronomica*, 65, 1
- Udalski, A., Szymanski, M., Kaluzny, J., Kubiak, M., Mateo, M. & Krzeminski, W., 1994, *ApJ*, 426, 69
- van den Bosch, F. C., More, S., Cacciato, M., Mo, H. & Yang, X. 2013, *MNRAS*, 430, 725
- Venumadhav, T., Dai, L. & Miralda-Escudé, J., 2017, *ApJ*, 850, 49
- von der Linden, A., et al. 2014, *MNRAS*, 439, 2
- Vogelsberger, M., Helmi, A., Springel, V., White, S. D. M., Wang, J., Frenk, C. S., Jenkins, A., Ludlow, A., & Navarro, J. F., 2009, *MNRAS*, 395, 797
- Walsh, D., Carswell, R. F. & Weymann, R. J. 1979, *Nature*, 279, 381
- Walterbos, R. A. M. & Kennicutt, Jr., R. C., 1988, *A&A*, 198, 61
- Wambsganss, J., 2006, *ArXiv e-prints*: 0604278
- Wechsler, R. H., Bullock, J. S., Primack, J. R., Kravtsov, A. V., & Dekel, A. 2002, *ApJ*, 568, 52
- Wegg, C., Gerhard, O., & Portail, M. 2016, *MNRAS*, 463, 577
- Wilkinson, P. N., Henstock, D. R., Browne, I. W., Polatidis, A. G., Augusto, P., Readhead, A. C., Pearson, T. J., Xu, W., Taylor, G. B. & Vermeulen, R. C., 2001, *Phy. Rev. Lett.* 86, 584
- Williams, S. C., Darnley, M. J., Bode, M. F., & Steele, I. A., 2015, *ApJ*, 805, 18
- Williams, B. F. et al. 2014, *ApJS*, 215, 9
- Witt, H. J. and Mao, S. 1994, *ApJ*, 430, 505
- Wyrzykowski, L. et al., 2010, *MNRAS*, 407, 189
- Wyrzykowski, L. et al., 2009, *MNRAS*, 397, 1228
- Zel'dovich, Y. B. and Novikov, I. D. 1967, *Sov. Astron.* 10, 602
- Zhang, Y.-Y., et al. 2010, *ApJ*, 711, 1033

## *References*

---

- Zhang, Y.-Y., Finoguenov, A., Böhringer, H., Kneib, J.-P., Smith, G. P., Kneissl, R., Okabe, N. & Dahle, H. 2011, *A&A*, 527, C3
- Zhao, D. H., Jing, Y. P., Mo, H. J., & Börner, G. 2009, *ApJ*, 707, 354
- Zhao, D. H., Mo, H. J., Jing, Y. P., & Börner, G. 2003, *MNRAS*, 339, 12
- Zitrin, A., et al. 2014, *ArXiv e-prints*:1411.1414
- Zoccali, M., Cassisi, S., Frogel, J. A., Gould, A., Ortolani, S., Renzini, A., Rich, R. M. & Stephens, A. W. 2000, *ApJ*, 530, 418
- Zwicky, F. 1937, *ApJ*, 86, 217